



**HAL**  
open science

# Study and implementation of nonlinear equalizers using artificial neural networks for coherent optical transmission systems

Abraham Sergio Sotomayor Fernandez

► **To cite this version:**

Abraham Sergio Sotomayor Fernandez. Study and implementation of nonlinear equalizers using artificial neural networks for coherent optical transmission systems. Networking and Internet Architecture [cs.NI]. Ecole nationale supérieure Mines-Télécom Atlantique, 2024. English. NNT : 2024IMTA0426 . tel-04848927

**HAL Id: tel-04848927**

**<https://theses.hal.science/tel-04848927v1>**

Submitted on 19 Dec 2024

**HAL** is a multi-disciplinary open access archive for the deposit and dissemination of scientific research documents, whether they are published or not. The documents may come from teaching and research institutions in France or abroad, or from public or private research centers.

L'archive ouverte pluridisciplinaire **HAL**, est destinée au dépôt et à la diffusion de documents scientifiques de niveau recherche, publiés ou non, émanant des établissements d'enseignement et de recherche français ou étrangers, des laboratoires publics ou privés.

# THÈSE DE DOCTORAT DE

L'ÉCOLE NATIONALE SUPÉRIEURE  
MINES-TÉLÉCOM ATLANTIQUE BRETAGNE  
PAYS DE LA LOIRE – IMT ATLANTIQUE

ÉCOLE DOCTORALE N° 648  
*Sciences pour l'Ingénieur et le Numérique*  
Spécialité : *Télécommunication*

Par

**Abraham Sergio SOTOMAYOR FERNANDEZ**

**Etude et Implémentation des Egaliseurs Non-linéaires utilisant des Réseaux de Neurones Artificiels pour les Systèmes de Transmission Optique Cohérente**

Thèse présentée et soutenue à IMT Atlantique, Brest, le 10 octobre 2024

Unité de recherche : LabSTICC (UMR CNRS 6285)

Thèse N° : 2024IMTA0426

## Rapporteurs avant soutenance :

Ghaya REKAYA Professeure, Télécom Paris  
Christophe FINOT Professeur, Université de Bourgogne

## Composition du Jury :

Président :	Christelle AUPETIT-BERTHELEMOT	Professeure, ENSIL-ENSCI
Rapporteurs :	Ghaya REKAYA	Professeure, Télécom Paris
	Christophe FINOT	Professeur, Université de Bourgogne
Examineurs :	Sergei TURITSYN	Professeur, Aston University
	Raphaël LE BIDAN	Enseignant Chercheur, IMT Atlantique
Dir. de thèse :	Jean-Louis DE BOUGRENET DE LA TOCNAVY	Professeur, IMT Atlantique
Co-dir. de thèse :	Vincent CHOQUEUSE	Maître de conférences, ENIB
Encadrant de thèse :	Michel MORVAN	Enseignant Chercheur, IMT Atlantique

## Invité(s) :

Encadrant Industriel : Erwan PINCEMIN Ingénieur R&D, Orange



# ACKNOWLEDGMENT

---

I would like to express my gratitude to my supervisors, as this thesis would not have been possible without their invaluable support. To Erwan Pincemin from Orange, who always believed in me and whose insightful advice greatly aided my progress; to Vincent Choqueuse from ENIB, whose strong involvement and valuable lessons I was fortunate to receive; to Michel Morvan from IMT Atlantique, whose teaching skills and guidance I deeply appreciated; to Jean-Louis de Bougrenet de la Tocnaye from IMT Atlantique, who facilitated funding for my expenses at an international conference; and to all the staff of the doctoral school and Labsticc.

I would also like to thank the members of the “Comité de Suivi Individuel” (CSI), Yves Jaouen from Télécom Paris and Roland Gautier from UBO, for taking the time to monitor my progress and for their valuable technical advice that contributed significantly to this achievement.

Special thanks to the manuscript examiners Ghaya Rekaya from Télécom Paris and Christophe Finot from the Université de Bourgogne for reviewing my manuscript and allowing me to defend my thesis, as well as for their encouraging comments. I also extend my gratitude to my oral defense examiners Christelle Aupetit-Berthelemot from ENSIL-ENSCI, Sergei Turitsyn from Aston University, and Raphaël Le Bidan from IMT Atlantique for their insightful questions and comments during my doctoral defense, and for awarding me the doctoral degree.

I would also like to extend my gratitude to my friends and colleagues at Orange, including team manager Nicolas Brochier, department director Ibrahim Houmed, and research program manager Géraldine Calvignac, who always worried about my progress and my personal and professional issues, and welcomed to continue my career at Orange. I appreciate my team colleagues for their support and advice, as well as the ancient and current PhD students and interns who accompanied me during my studies in Lannion.

Finally, I dedicate this achievement to my family for their invaluable support: to my mother, Gisella, and my father, Carlos; to my brothers, Carlos, Guillermo, and Ricardo; and to my sisters, Gisela, Sofia, and Tania, who, despite the distance, supported me daily with their advice and love. I would also like to express my heartfelt gratitude and dedicate this work to my fiancée, Fiorella, for her unwavering support and love.



# TABLE OF CONTENTS

---

<b>List of Figures</b>	<b>v</b>
<b>List of Tables</b>	<b>xi</b>
<b>Acronyms</b>	<b>xiii</b>
<b>Notations</b>	<b>xvii</b>
<b>Résumé de la thèse en français</b>	<b>xix</b>
1 Introduction . . . . .	xix
2 Effets Non-linéaires dans les Fibres Optiques . . . . .	xx
3 Équation Non-linéaire de Schrödinger . . . . .	xxii
4 Traitement Numérique des Signaux pour les Systèmes de Transmission Optique Cohérente . . . . .	xxii
5 Algorithmes d'Égalisation Non-linéaire . . . . .	xxiii
5.1 Digital Backpropagation . . . . .	xxiii
5.2 Séries de Volterra . . . . .	xxiv
5.3 Compromis entre Performance et Complexité Calculatoire . . . . .	xxiv
6 Égaliseurs Non-linéaires basés sur des Réseaux de Neurones Artificiels . . . . .	xxv
6.1 Perceptron Multicouche (MLP) . . . . .	xxvi
6.2 Processus d'apprentissage . . . . .	xxvii
6.3 Sélection des hyper-paramètres et Traitement des données . . . . .	xxviii
6.4 Résultats des égaliseurs basés sur NN . . . . .	xxviii
7 L'effet MMSE-scatterplot: constellation en forme de grille . . . . .	xxix
7.1 Modèle mathématique du phénomène MMSE-scatterplot . . . . .	xxx
7.2 Technique de mitigation de l'effet MMSE-scatterplot . . . . .	xxxii
7.3 Résultats de l'usage de la technique de mitigation proposée . . . . .	xxxiii
8 Conclusion et Perspectives . . . . .	xxxv
<b>1 Introduction</b>	<b>1</b>
1.1 Context and Motivation . . . . .	1
1.2 Objectives and Methodology . . . . .	3
1.3 Contributions . . . . .	4
1.4 Workshops and Publications . . . . .	4
1.5 Thesis Outline . . . . .	5
<b>2 Fundamental of Optical Communications</b>	<b>7</b>
2.1 Dual-Polarization Transmitter . . . . .	8
2.1.1 Laser Sources . . . . .	8
2.1.2 Modulation Formats . . . . .	9
2.1.3 Digital Modulation . . . . .	10

TABLE OF CONTENTS

---

2.1.4	Dual Polarization IQ Modulator . . . . .	12
2.1.5	Pulse Shaping . . . . .	13
2.2	Dual-Polarization Coherent Receiver . . . . .	14
2.3	Optical Fibers . . . . .	15
2.3.1	Fiber Loss . . . . .	16
2.3.2	Chromatic Dispersion . . . . .	16
2.3.3	Polarization Mode Dispersion . . . . .	17
2.3.4	Nonlinear Impairments . . . . .	20
2.3.5	Optical Amplifiers . . . . .	24
2.4	Nonlinear Schrödinger Equation . . . . .	25
2.5	Split-Step Fourier Method . . . . .	26
2.6	Summary . . . . .	30
<b>3</b>	<b>Nonlinear Impairments in Coherent Optical Systems: Numerical and Experimental Investigations</b>	<b>33</b>
3.1	Digital Signal Processing and Numerical Investigations of Nonlinear Effects . . .	33
3.1.1	Channel Equalization . . . . .	35
3.1.2	Adaptive Equalization . . . . .	40
3.1.3	Frequency Offset Compensation . . . . .	44
3.1.4	Carrier Phase Recovery . . . . .	45
3.1.5	Nonlinear Effects for Different Transmission Configurations . . . . .	47
3.2	Nonlinear Impairments Compensation Techniques . . . . .	50
3.2.1	Digital Backpropagation . . . . .	50
3.2.2	Volterra Nonlinear Equalizer . . . . .	52
3.2.3	Computational Complexity . . . . .	54
3.3	Experimental Setup . . . . .	56
3.3.1	Optical Back-to-Back . . . . .	57
3.3.2	Optical Fiber Transmission . . . . .	59
3.3.3	Nonlinearity Compensation . . . . .	61
3.4	Summary . . . . .	62
<b>4</b>	<b>Neural Networks Based Nonlinear Equalizers for Optical Transmission Systems</b>	<b>65</b>
4.1	Fundamentals of Machine Learning . . . . .	65
4.1.1	Model Selection . . . . .	66
4.1.2	Learning Process . . . . .	67
4.1.3	Hyperparameters Tuning . . . . .	69
4.2	Neural Networks . . . . .	70
4.2.1	Single Artificial Neuron Model . . . . .	70
4.2.2	Multilayer Perceptron . . . . .	71
4.3	Nonlinear Equalizers using Neural Networks . . . . .	73
4.3.1	State of the Art . . . . .	73
4.3.2	Implementation and Tests using a Numerical Setup . . . . .	78
4.3.3	Study of the position of the MLP . . . . .	86
4.3.4	Implementation and Tests using the Experimental Setup . . . . .	89

---

4.4	Summary . . . . .	92
<b>5</b>	<b>MMSE-driven Signal Constellation Scatterplot Effect</b>	<b>93</b>
5.1	MMSE-Driven Signal Constellation Scatterplot . . . . .	94
5.2	Origin of the MMSE-scatterplot . . . . .	97
5.2.1	MSE Loss Function . . . . .	97
5.2.2	MMSE estimate . . . . .	97
5.3	Mitigation Techniques of the MMSE-scatterplot effect . . . . .	98
5.3.1	Related works . . . . .	100
5.3.2	Soft Thresholding-based Output Layer . . . . .	100
5.4	Description of the Numerical Setup . . . . .	102
5.4.1	Transmission setup . . . . .	103
5.4.2	Datasets . . . . .	104
5.4.3	NN hyperparameters and Training Process . . . . .	105
5.5	Results . . . . .	105
5.6	Summary . . . . .	108
	<b>Conclusion and Perspectives</b>	<b>111</b>
	<b>A Quality of Transmission Assessment Metrics</b>	<b>113</b>
A.1	Signal-to-Noise Ratio . . . . .	113
A.2	Optical Signal to Noise Ratio . . . . .	113
A.3	Generalized Signal-to-Noise Ratio . . . . .	114
A.4	Symbol Error Rate . . . . .	114
A.5	Bit Error Rate . . . . .	115
A.6	Q-Factor . . . . .	116
	<b>B Information Theory</b>	<b>117</b>
B.1	Entropy . . . . .	117
B.2	Conditional Entropy . . . . .	118
B.3	Mutual Information . . . . .	118
	<b>Bibliography</b>	<b>121</b>



# LIST OF FIGURES

1	Évolution du produit bit-rate et distance de transmission sur des fibres optiques [1] © . . . . .	xix
2	Dépendance de la capacité d'un système de transmission optique sur la puissance du signal optique en bleu. La ligne noire pointillée représente la capacité de Shannon et la ligne rouge pointillée est la capacité maximale du système fixée à la puissance optimale [2] © . . . . .	xx
3	Constellation 16QAM reçue à 32-GBaud et 1-dBm après $20 \times 100$ km de SSMF.	xxi
4	Chaîne d'algorithmes de traitement numérique des signaux utilisés dans le récepteur cohérent. BPD: photodiodes balancées, ADC: convertisseur analogique-numérique. . . . .	xxiii
5	Schéma illustrant la méthode de la DBP à $\frac{L}{h}$ steps par span. $\mathbf{E}(L, t)$ représente les signaux reçus à la fin du segment de longueur $L$ , $h$ est la longueur du pas, et $\hat{\mathbf{D}}$ et $\hat{\mathbf{N}}$ représentent des opérateurs linéaires et non-linéaires, respectivement. $\xi$ est un paramètre à optimiser. . . . .	xxiii
6	Schéma d'un égaliseur non linéaire basé sur les séries de Volterra avec des noyaux d'ordre 3. $E_x$ et $E_y$ représentent les composantes de $\mathbf{E}$ , $N$ est le nombre de spans, FFT est la transformée de Fourier rapide et IFFT est la FFT inverse, $H_{CD}^k$ représente la compensation de la CD cumulée sur $k$ spans, $\xi$ est un paramètre à optimiser [3] ©2012, IEEE. . . . .	xxiv
7	Performances du système en utilisant un égaliseur linéaire (CDC), des égaliseurs non-linéaires DBP et VNLE avec $\xi$ optimal pour une transmission DP-16QAM à 32-GBaud sur $14 \times 100$ km de SSMF. . . . .	xxv
8	Placement du réseau de neurones après le bloc de compensation de phase. . . . .	xxvi
9	Architecture du NN Perceptron Multicouche (MLP). . . . .	xxvi
10	Modèle d'un neurone artificiel. . . . .	xxvii
11	Performances du système en incluant le NN pour une transmission DP-16QAM sur $14 \times 100$ km de SSMF. Plus violets : SER optimisé. Étoiles cyan : MSE optimisé. . . . .	xxix
12	Diagrammes de constellation des signaux égalisés avec la MLP avec des hyperparamètres qui optimisent le SER (première ligne), et qui optimisent le MSE (deuxième ligne). . . . .	xxx
13	Cas général d'un système de transmission avec égalisation du canal par un réseau de neurones NN. . . . .	xxxii
14	Système de transmission sur canal AWGN avec égalisation du canal par un réseau de neurones NN. . . . .	xxxii
15	Constellations d'entrée $R$ , sortie du NN $Y$ et sortie de la fonction STH pour des signaux 16-QAM quadratique et des signaux 8-QAM non rectangulaire ©2024, IEEE. . . . .	xxxii
16	Système de transmission avec égaliseur basé sur le NN et en incluant la fonction STH à la fin. . . . .	xxxii

17	Système de transmission DP-64QAM à 32-Gbaud sur $14 \times 50$ km de SSMF ©2024, IEEE. . . . .	xxxiii
18	Résultats de BER et de MI pour différents niveaux de puissance par canal P/ch ©2024, IEEE. . . . .	xxxiv
19	Constellations des signaux d'entrée $R$ et des signaux égalisés $Y = f(R)$ . (a) P/ch = -4dBm, (b) P/ch = -2dBm, (c) P/ch = 0dBm, (d) P/ch = 2dBm ©2024, IEEE. . . . .	xxxiv
1.1	Broadband traffic between 2019 and 2022 [7]. . . . .	1
2.1	Block Diagram of a Dual-Polarization coherent optical transmission system. DAC: digital-to-analog converter, IQM: IQ modulator, BA: Booster Amplifier, EDFA: Erbium-doped Fiber Amplifier, LO: local oscillator, O/E: Optical-to-Electrical, ADC: Analog-to-Digital Converter. Blue lines are electrical signals, and red lines are optical signals. . . . .	7
2.2	Dual-Polarization Transmitter. DAC: Digital-to-Analog Converter, RFDA: RF Driver Amplifier (linear amplifier), PBC: Polarization Beam Combiner, BA: Booster Amplifier. . . . .	8
2.3	PSK and QAM constellations. . . . .	10
2.4	QPSK and 16QAM constellations using Gray encoding. . . . .	11
2.5	BER vs. $E_b/N_0$ for PSK and QAM constellations in an AWGN channel with optimal source encoding. . . . .	11
2.6	16QAM constellation with differential encoding [56] ©2009, IEEE. . . . .	12
2.7	Coherent Receiver with phase diversity using a $90^\circ$ Hybrid. . . . .	14
2.8	Dual Polarization coherent receiver using two nested $90^\circ$ Hybrids. . . . .	15
2.9	Fiber loss coefficient and wavelength dependence [60] ©2010, IEEE. . . . .	16
2.10	Evolution of the state of polarization when the incident light is linearly polarized at $45^\circ$ with respect to the slow and fast axis [18] ©2001, 1995 by ACADEMIC PRESS. . . . .	18
2.11	Modeling of the PMD [24] ©2010, IEEE. . . . .	18
2.12	Poincaré sphere. . . . .	19
2.13	Maxwellian distribution of the DGD. . . . .	20
2.14	Decomposition of Kerr Nonlinear effects [60]. NLPN: Nonlinear Phase Noise, SPM: Self-Phase Modulation, XPM: Cross-Phase Modulation, FWM: Four-Wave Mixing, IXPM: Intrachannel XPM, IFWM: Intrachannel FWM, XPolM: Cross-Polarization Modulation. . . . .	21
2.15	16QAM received constellation after $20 \times 100$ km with full loss compensation using EDFA. . . . .	23
2.16	Asymmetric SSFM. . . . .	27
2.17	Symmetric SSFM. . . . .	28
3.1	Comparison of SSFM versions for a DP-16QAM 32 GBaud over $14 \times 100$ km of single-mode fiber. . . . .	34
3.2	DSP algorithms used in the DP Coherent Receiver. BPD: balanced photodiodes, ADC: analog-to-digital converter, RRC: root-raised cosine, FSE: Fractionally-spaced equalizer, MIMO: multiple-input-multiple-output. . . . .	35

3.3	Impulse response of CD equalization FIR filters for an accumulated dispersion $D = 1700\text{ps/nm}$ , symbol rate $R_s = 32\text{GBaud}$ , corresponding to $N = 55$ taps. The blue lines are for the real part and the red lines are- for the imaginary part.	37
3.4	BER vs. P/ch using different CD equalizers (FD and TD) for a DP-16QAM 32 Gbaud over 14x100 km of SSMF. N is the number of FIR filter taps. . . . .	38
3.5	Simplified DSP for a single polarization transmission and only accounting for the CD and the NLI. . . . .	38
3.6	BER vs. P/ch using different CD equalizers (FD and TD) for a SP-16QAM 32 Gbaud over 10x100 km of SSMF. N is the number of FIR filter taps. . . . .	38
3.7	2x2 MIMO equalizer with Fractionally-Spaced Equalizer (FSE). . . . .	40
3.8	FSE performs by FIR $\mathbf{h}_{ij}$ . . . . .	41
3.9	Radii employed in adaptive equalization using CMA/RDE. . . . .	42
3.10	MSE calculated during MIMO equalization. . . . .	43
3.11	Equalized outputs (steady state). Blue points: X polarization, red points: Y polarization. . . . .	43
3.12	Carrier frequency Offset estimation and compensation. . . . .	44
3.13	CFO compensation. Blue points: X polarization, red points: Y polarization. . . .	45
3.14	Viterbi-and-Viterbi algorithm for carrier phase recovery. . . . .	45
3.15	(Top) CPE feed-forward blind algorithm with B phase blocks [56]. (Bottom) inside the blocks. . . . .	46
3.16	CPE. Blue points: X polarization, red points: Y polarization. . . . .	47
3.17	BER vs. OSNR (0.1 nm) for a BtB configuration. . . . .	48
3.18	Performance BER vs. P/ch using the DSP depicted in Fig. 3.2. . . . .	48
3.18	Performance BER vs. P/ch using the DSP depicted in Fig. 3.2 (cont.). . . . .	49
3.19	Asymmetric DBP. . . . .	50
3.20	Symmetric DBP. . . . .	51
3.21	BER as a function of the P/ch and the nonlinear rotation parameter $\xi$ and using the CDC and the DBP. . . . .	51
3.22	Volterra series based nonlinear equalization scheme [3] ©2012, IEEE. . . . .	53
3.23	BER as a function of the P/ch and the nonlinear rotation parameter $\xi$ using the CDC and the VNLE. . . . .	54
3.24	Computational complexity (CC) in RMpS and processing time in Logarithmic scale. . . . .	55
3.25	Experimental setup with the Dual Polarization (DP) Transmitter, the optical fiber consisted of $N_{\text{spans}} \times 100$ km spans of Standard Single-Mode Fiber (SSMF), the DP receiver, and the Offline-DSP. AWG: Arbitrary Waveform Generator, ECL: External Cavity Laser, PBC: Polarization Beam combiner, vOA: Variable Optical Attenuator, EDFA: Erbium-Doped Fiber Amplifier, OSA: Optical Spectrum Analyzer, PC: Polarization Controller, PBS: Polarization Beam Splitter, LO: Local Oscillator, BPD: Balanced Photo-Detectors, DSO: Digital Storage Oscilloscope. .	56

3.26	(a) Filtered CUT at 1552 nm at the receiver observed in the OSA, (b) general view of the DP-TX and DP-Coherent RX comprising the AWG which generates DP-16QAM modulated samples at 92 GSa/s, the ECL with a low-noise EDFA, the DP-IQ Modulator, an optical switch to select the number of fiber spans and the PC, (c) OSA showing the wavelengths combs multiplexed with the CUT with two aside channels off, (d) DSO operating at 80 GSa/s to recover the XI, XQ, YI, and YQ components, (e) workstation with the Keysight software and the MATLAB programs for offline DSP. . . . .	57
3.27	(a) AWG at 92 GSa/s, DP-IQ modulator and DSO operating at 80 GSa/s, (b) Spools of 100-km of SSMF and EDFA after each span. . . . .	58
3.28	Back-to-Back DP-16QAM 32GBaud. . . . .	58
3.29	DSP results of a DP-16QAM signal constellations after 5x100 km SSMF: X-Pol (blue), Y-Pol (red). CDC: Chromatic dispersion Compensation, MSE: Mean Squared Error, MIMO: Multiple-Input-multiple-output, CFOC: Carrier Frequency Offset Compensation, CPE: Carrier Phase Estimation. . . . .	59
3.29	DSP results of a DP-16QAM signal constellations after 5x100 km SSMF: X-Pol (blue), Y-Pol (red). CDC: Chromatic dispersion Compensation, MSE: Mean Squared Error, MIMO: Multiple-Input-multiple-output, CFOC: Carrier Frequency Offset Compensation, CPE: Carrier Phase Estimation (cont.). . . . .	60
3.30	BER vs. P/ch of experimental DP-16QAM 32 GBaud signal over 5x100 km of SSMF. . . . .	60
3.31	BER as a function of the P/ch and the nonlinear rotation parameter $\xi$ using the CDC and the DBP. . . . .	61
3.32	BER as a function of the P/ch and the nonlinear rotation parameter $\xi$ using the CDC and the VNLE. . . . .	62
3.33	Results of experimental DP-16QAM 32 GBaud signal over 5x100 km of SSMF using the DBP and the VNLE. Dash-dot lines: interpolation curves. . . . .	62
4.1	Artificial neuron model. . . . .	70
4.2	Common nonlinear activation functions. . . . .	71
4.3	Multiplayer Perceptron. . . . .	72
4.4	Estimation of published papers on optical fiber nonlinearity compensation/mitigation using neural networks. Source: Google Scholar *up to May 2024. . . . .	74
4.5	DSP with NN nonlinear equalizer after the CPR algorithm. . . . .	78
4.6	DSP receiver used for Manakov-equation based model without CFO and LPN. . . . .	80
4.7	SER per trial using the hyperparameter optimization framework Optuna in a DP-16QAM system at 3 dBm over $14 \times 100$ km of SSMF. $N$ represent memory taps, $L$ is number of hidden layers, $N_h$ is number of hidden units in layer $h$ , and $lr$ for learning rate. The dashed red line is the level of SER without NN. . . . .	81
4.8	MSE loss function in training (blue) and validation (red) datasets per epoch, and SER (green) in the validation dataset. . . . .	82
4.9	BER vs. P/ch using the trained MLP at each P/ch for a DP-16QAM over $14 \times 100$ km of SSMF and comparison with the DBP and the VNLE. . . . .	82
4.10	IQ constellation diagrams using only CDC (first row) and the MLP (second row). . . . .	83

4.11	Computational complexity in RMpS and processing time in Logarithmic scale including the MLP. . . . .	84
4.12	MSE loss per trial using the hyperparameter optimization framework Optuna in a DP-16QAM system at 2 dBm over $14 \times 100$ km of SSMF. $N$ represent memory taps, $L$ is number of hidden layers, $N_h$ is number of hidden units in layer $h$ , and $lr$ for learning rate. . . . .	85
4.13	MSE loss function in training (blue) and validation (red) datasets per epoch. . .	85
4.14	BER vs. P/ch using the trained MLP at each P/ch for a DP-16QAM over $14 \times 100$ km of SSMF. . . . .	86
4.15	IQ constellation diagrams using only CDC the MLP. . . . .	86
4.16	Receiver configurations. A) MLP acting at 1sps with CD equalized signal, B) MLP acting at 2 sps with CD equalized signal, C) MLP acting at 2 sps with non-equalized signal. sps: samples/symbol, RRC: Root Raised Cosine, LPF: Low Pass Filter, CDC: Chromatic Dispersion Compensation ©2023, IEEE. . . . .	87
4.17	Results BER vs. P/ch for scenarios (A),(B),(C),(D). CDC and a, 1StPS and 2StPS DBP results were added as a reference. The insets represent the IQ constellations of the predicted signal in the optimal power ©2023, IEEE. . . . .	89
4.18	Computational complexity for scenarios (A),(B),(C). Results with CDC and a 1StPS DBP and 2StPS DBP were added as a reference ©2023, IEEE. . . . .	90
4.19	(a) LFSR-2 and (b) LFSR-4 used to generate PRBS-N [147] © . . . . .	91
4.20	Followed approach to train an Neural Networks (NN) using a dataset containing PRBS. To avoid the NN always observing the same first third of the PRBS that constitute the Training dataset, at each epoch, we randomly rotate the symbols inside each third (only in the Training dataset) a multiple of $\pi/2$ ( $n, m, \dots, l$ are randomly and uniformly selected from $\{0,1,2,3\}$ ). . . . .	91
5.1	Classical transceiver model with an NN-based nonlinear equalizer (regressor) in an AWGN channel represented by Z ©2024, IEEE. . . . .	94
5.2	MMSE-scatterplot effect on signal constellations in an AWGN channel ©2024, IEEE. . . . .	96
5.3	Soft and Hard-thresholding functions for a PAM4 constellation with alphabet $\mathcal{X} = \{x_1, x_2, x_3, x_4\}$ ©2024, IEEE. . . . .	99
5.4	Estimate of $X$ using the STH function in (5.5), where $R$ are the inputs in Fig. 5.2a, 5.2c, 5.2e and 5.2g ©2024, IEEE. . . . .	99
5.5	Proposed NN followed by the STH function. Flatten: reshapes input $r$ into a vector of shape $(B, :)$ , where $B$ is the mini-batch size. Color blue indicates only training mode, red indicates only evaluation mode, and purple indicates both training and evaluation modes ©2024, IEEE. . . . .	101
5.6	Dual-Polarization Transmission Setup. SpS: samples per symbol, RRC: root-raised cosine, PBC: polarization beam combiner, EDFA: erbium-doped fiber amplifier, LPF: low pass filter, CDC: chromatic dispersion compensation, DBP: digital backpropagation, MIMO: multiple-input multiple-output, CFOE: carrier frequency offset estimation, CPR: carrier phase recovery ©2024, IEEE. . . . .	103
5.7	Curve of losses (average of training batches per epoch) for each equalizer for P/ch = 0 dBm ©2024, IEEE. . . . .	106

5.7	Curve of losses (average of training batches per epoch) for each equalizer for $P/\text{ch} = 0$ dBm (cont.) ©2024, IEEE. . . . .	107
5.8	Symbol constellation diagrams of the received signal (NN input) $R$ and constellations of equalized signal $Y = f(R)$ for each NN-based equalizer and using a DBP 1 StPS. (a) $P/\text{ch} = -4$ dBm, (b) $P/\text{ch} = -2$ dBm, (c) $P/\text{ch} = 0$ dBm, (d) $P/\text{ch} = 2$ dBm ©2024, IEEE. . . . .	107
5.9	Performances obtained for each equalizer ©2024, IEEE. . . . .	108
A.1	Eye diagram for Q-factor computation in binary signals using (A.18), where $u_{1,0}$ and $\sigma_{1,0}$ are the mean and standard deviations, respectively for level 1 and level 0 [177] ©2012, IEEE. . . . .	116

# LIST OF TABLES

---

3.1	Transmission Configurations using QPSK, 16QAM and 64QAM modulation formats at different Baud rates and for different fiber lengths. . . . .	47
4.1	Loss functions. . . . .	67
4.2	Summary of most relevant and impressive studies that covered fiber nonlinearity compensation using neural networks in coherent communications. . . . .	74
4.3	MLP architectures for $N_{span} = 5$ and $N_{span} = 10$ of 100km SSMF. $n_i$ , $n_h$ ( $h = 1, 2$ ), and $n_o$ are the number of neurons in the input, hidden, and output layers, respectively. . . . .	87
5.1	NN architecture and training specifications used in Section 5.1 for an AWGN channel. . . . .	95
5.2	Parameters of numerical simulation. . . . .	104
5.3	Number of batches and symbols used in training and validation. . . . .	104
5.4	Architecture of the NN-based nonlinear equalizer. . . . .	105
5.5	Parameter $\sigma^2$ utilized in NNs with MSE-X and NN+STH with MSE. . . . .	106



# ACRONYMS

---

**ADC** Analog-to-Digital Converters  
**AI** Artificial Intelligence  
**AIR** Achievable Information Rate  
**ASE** Amplified Spontaneous Emission  
**ASIC** Application-Specific Integrated Circuit  
**AWG** Arbitrary Waveform Generator  
**AWGN** Additive White Gaussian Noise  
**BER** Bit Error Rate  
**biLSTM** bidirectional LSTM  
**BPD** Balanced Photo-Detectors  
**BtB** Back-to-Back  
**CC** Computational Complexity  
**CD** Chromatic Dispersion  
**CFO** Carrier Frequency Offset  
**CMA** Constant Modulus Algorithm  
**CNLSE** coupled NLSE  
**CNN** Convolutional Neural Networks  
**CPE** Carrier Phase Estimation  
**CPR** Carrier Phase Recovery  
**CUT** Channel Under Test  
**CW** Continuous-Wave  
**DAC** Digital-to-Analog Converters  
**DBP** Digital Backpropagation  
**DD-LMS** decision-directed least mean squared  
**DFB** Distributed Feedback Laser  
**DFT** Discrete Fourier Transform  
**DGD** Differential Group Delay  
**DL** Deep Learning  
**DML** Direct-Modulated Laser  
**DOF** Degrees of Freedom  
**DOP** Degree of Polarization  
**DP** Dual Polarization

**DSF** Dispersion Shifted Fiber  
**DSO** Digital Storage Oscilloscope  
**DSP** Digital Signal Processing  
**EAM** Electro-Absorption Modulator  
**ECL** External Cavity Laser  
**EDFA** Erbium-Doped Fiber Amplifiers  
**FD** Frequency-Domain  
**FDE** Frequency-Domain Equalizer  
**FEC** Forward Error Correction  
**FFT** Fast Fourier Transform  
**FIR** Finite Impulse Response  
**FP** Fabry–Pérot  
**FSE** Fractionally-Spaced Equalizer  
**FWM** Four Wave Mixing  
**GMI** Generalized Mutual Information  
**GN** Gaussian Noise  
**GSNR** Generalized Signal-to-Noise Ratio  
**GVD** Group Velocity Dispersion  
**IDFT** Inverse Discrete Fourier Transform  
**IF** Intermediate Frequency  
**IFFT** Inverse Fast Fourier Transform  
**IFWM** intrachannel Four-Wave Mixing  
**IM/DD** Intensity Modulation and Direct-Detection  
**IQ** In-Phase/Quadrature  
**IS-SSFM** iterative symmetric SSFM  
**ISI** Intersymbol Interference  
**IXPM** intrachannel Cross-Phase Modulation  
**LEAF** Large Effective Area Fiber  
**LFSR** Linear Feedback Shift Register  
**LO** Local Oscillator  
**LPN** Laser Phase Noise  
**LS** Least-Square  
**LSB** Least Significant Bits  
**LTSM** Long Short-Term Memory  
**MI** Mutual Information  
**MIMO** Multiple-Input-Multiple-Output

**ML** Machine Learning  
**MLP** Multilayer Perceptron  
**MMSE** Minimum MSE  
**MSB** Most Significant Bits  
**MSE** Mean Squared Error  
**MZM** Mach-Zehnder Modulators  
**NF** Noise Figure  
**NLI** Nonlinear Impairments  
**NLPN** Nonlinear Phase Noise  
**NLSE** Nonlinear Schrödinger Equation  
**NN** Neural Networks  
**NS-SSFM** non-iterative symmetric SSFM  
**OFDM** Orthogonal Frequency Division Multiplexing  
**OSNR** Optical Signal-to-Noise Ratio  
**PAM** Pulse Amplitude Modulation  
**PAS** Probabilistic Amplitude Shaping  
**PBC** Polarization Beam Combiner  
**PBS** Polarization Beam Splitter  
**PC** Polarization Controller  
**PCS** Probabilistic Constellation Shaping  
**PMD** Polarization Mode Dispersion  
**PRBS** Pseudo-Random Binary Sequences  
**PSD** power spectral density  
**PSK** Phase-Shift Keying  
**PSP** Principal States of Polarization  
**QAM** Quadrature Amplitude Modulation  
**QoT** Quality of Transmission  
**RC** Raised-Cosine  
**RDE** Radius-Directed Equalizer  
**ReLU** Rectified Linear Unit  
**RLS** recursive least squares  
**RM** Real Multiplications  
**RMpS** real multiplications per symbol  
**RNN** Recurrent Neural Networks  
**RRC** Root Raised-Cosine  
**SC** Single Channel

<b>SD</b>	Soft-Decision
<b>SER</b>	Symbol Error Rate
<b>SGD</b>	Stochastic Gradient Descent
<b>SNR</b>	Signal-to-Noise Ratio
<b>SOI</b>	Symbol of Interest
<b>SOP</b>	States of Polarization
<b>SP</b>	Single Polarization
<b>SPM</b>	Self-Phase Modulation
<b>SpS</b>	samples per symbol
<b>SSF</b>	Split-Step Fourier Method
<b>SSMF</b>	Standard Single-Mode Fiber
<b>STH</b>	Soft-Thresholding
<b>StPS</b>	steps per span
<b>TD</b>	Temporal-Domain
<b>TDE</b>	Time-Domain Equalizer
<b>TL</b>	Transfer Learning
<b>VNLE</b>	Volterra Nonlinear Equalizer
<b>WDM</b>	Wavelength Division Multiplexing
<b>XPM</b>	Cross-Phase Modulation
<b>XPolM</b>	Cross-Polarization Modulation

# NOTATIONS

---

## Optical amplifier parameters

- $F_n$  Optical amplifier noise factor  
 $G$  Optical amplifier gain  
 $n_{sp}$  Spontaneous emission noise factor

## Optical fiber parameters

- $\alpha$  Fiber loss coefficient  $Km^{-1}$   
 $\beta_2$  Group Velocity Dispersion  $[ps^2/km]$   
 $\gamma$  Nonlinear coefficient  $[W^{-1} \cdot km^{-1}]$   
 $a$  Core radius  
 $D$  Chromatic Dispersion coefficient  $[ps/(nm \cdot km)]$   
 $n_1$  Core refractive index  
 $n_2$  Cladding refractive index

## Physics constants

- $c$  Speed of light in vacuum  $[299792458 \text{ m/s}]$   
 $h$  Planck constant  $[6.62607015e-34 \text{ J} \cdot \text{Hz}^{-1}]$

## Signal notations

- $\mathbf{E}(t)$  Dual-Polarization optical field  
 $\mathbf{s}_m$  m-th modulated complex symbol of an M-ary constellation  
 $S(f)$  Frequency domain signal  
 $s(t)$  Continuous signal  
 $s[k]$  Discrete signal  
 $x_n$  n-th modulated transmitted symbol

## Transmission parameters

- $\Delta\nu$  Sum linewidth signal and LO lasers  
 $\lambda$  Wavelength  
 $\omega_c$  Angular carrier frequency  
 $\phi_s(t)$  Laser phase noise  
 $\rho$  Roll-off factor

## NOTATIONS

---

$f_c$	Carrier frequency
$K$	Oversampling factor
$k_0$	Wave number
$T$	Sampling Period
$T_s$	Symbol Period
SpS	Samples per symbol

# RÉSUMÉ DE LA THÈSE EN FRANÇAIS

## 1 Introduction

Les réseaux de transmission optique subissent une évolution constante, car ils doivent s'adapter aux nouveaux besoins des utilisateurs. En particulier, les capacités de transmission utilisant des fibres optiques se sont largement développées depuis les premiers systèmes à modulation d'intensité de l'impulsion optique et détection directe (IM/DD) à 10 Gbits/s par paire de fibres, jusqu'aux tout derniers systèmes à multiplexage de longueur d'onde (WDM) à détection cohérente. Très récemment, l'utilisation du multiplexage par division spatiale (SDM) avec des fibres multi-cœurs ou multi-modes, a permis d'atteindre des records de transmission de, par exemple, 1,4 Exabits/s · km [1] (Fig. 1).

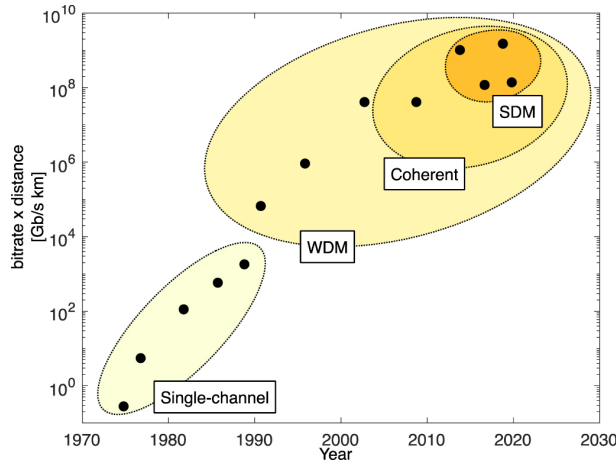


Figure 1 – Évolution du produit bit-rate et distance de transmission sur des fibres optiques [1] © .

Cependant, ces capacités seront encore insuffisantes au regard de l'avenir de la 6G et des nouvelles technologies immersives, comme la réalité virtuelle, qui vont nécessiter une grande bande passante et donc des capacités de transmission aussi élevées. Dans ce contexte, il est essentiel de comprendre quelles sont les limites fondamentales à l'atteinte de la capacité maximale dans les systèmes optiques actuels. Pour cela, nous devons nous retourner en 1948. Dans cette année-là, Claude Shannon a énoncé, dans son célèbre travail “A Mathematical Theory of Communication”, que la capacité maximale atteignable  $C$  sur un canal additif et blanc avec bruit gaussien (AWGN) répond à l'expression suivante :

$$C = 2 \cdot B \cdot \log_2(1 + SNR), \quad (1)$$

où  $2B$  est la bande passante du signal complexe et  $SNR$  est le rapport signal sur bruit  $SNR = \frac{P_s}{P_n}$  où  $P_s$  et  $P_n$  représentent la puissance du signal et la puissance du bruit, respectivement.

Dans le contexte des fibres optiques, dans les systèmes actuels de transmission, les pertes de la fibre sont compensées par des amplificateurs optiques et notamment dans la bande C (1530 nm

- 1565 nm), nous utilisons les amplificateurs à fibre dopée à l’erbium (EDFA). Ces amplificateurs génèrent un bruit AWGN qui est dû au phénomène d’émission spontanée amplifiée (ASE). A fortes puissances du signal  $P_s$ , le  $SNR$  n’est plus linéaire avec  $P_s$ , mais un facteur dépendant de  $P_s^3$  s’ajoute à la puissance de bruit gaussien  $P_{ASE}$  classique dû aux amplificateurs optiques, c’est-à-dire  $P_n = P_{ASE} + P_{NLI}$ , où  $P_{NLI} = \eta P_s^3$  et  $\eta$  dépend de la configuration du système. Cette formulation devient d’un modèle appelé “Gaussian Noise (GN)”, où le terme additionnel  $P_{NLI}$  est considéré comme un bruit additif gaussien dû aux interférences non-linéaires (NLI). Ce bruit est inhérent aux transmissions optiques, mais il est plus visible à fortes puissances optiques. De ce fait, classiquement, le point d’opération optimal est choisi comme le point auquel la capacité est maximale et le niveau de puissance correspondant est fixé pour maintenir cette capacité maximale, comme c’est montré dans la Fig. 2.

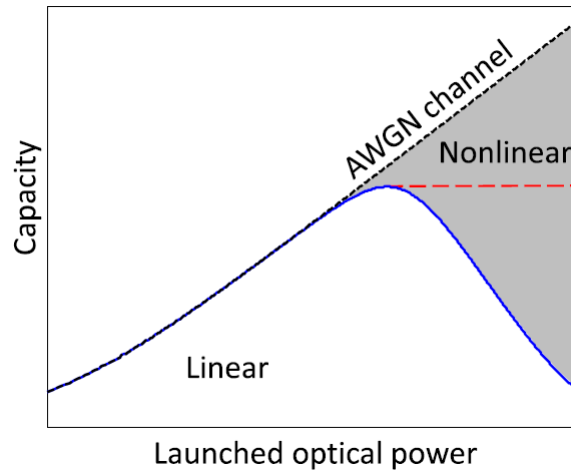


Figure 2 – Dépendance de la capacité d’un système de transmission optique sur la puissance du signal optique en bleu. La ligne noire pointillée représente la capacité de Shannon et la ligne rouge pointillée est la capacité maximale du système fixée à la puissance optimale [2] © .

## 2 Effets Non-linéaires dans les Fibres Optiques

Le bruit dû aux NLI est provoqué par la non-linéarité de la fibre. Ce phénomène désigne le comportement non-linéaire de l’indice de réfraction  $\tilde{n}$  de la fibre lorsque la puissance optique devient grande. En particulier, les effets non-linéaires de Kerr sont ceux dans lesquels la non-linéarité est proportionnelle à l’intensité de l’impulsion optique,

$$\tilde{n}(\omega, I) = n(\omega) + n_2 I, \tag{2}$$

où  $n(\omega)$  est un terme linéaire,  $n_2$  est appelé coefficient d’indice non-linéaire et  $I$  représente l’intensité de l’impulsion optique.

La dépendance de  $\tilde{n}$  avec  $I$  est à l’origine de différents effets non-linéaires, parmi lesquels les plus importants sont :

- L’auto-modulation de phase (SPM)
- La modulation de phase croisée (XPM)

- Le mélange à quatre ondes (FWM)

La SPM désigne le phénomène par lequel la réfraction non-linéaire affecte la phase du signal due à sa propre intensité. Comme l'intensité de l'impulsion optique varie dans le temps lors de la propagation, le déplacement de phase non-linéaire amorce ainsi un déplacement instantané de la fréquence autour de la fréquence centrale qui reste inchangée. Si nous considérons seulement la SPM, nous observons un élargissement symétrique du spectre du signal dû aux harmoniques générées à cause de la NLI. D'autre part, avec la présence de la dispersion chromatique (CD) et quand elle est positive, l'effet résultant est un rétrécissement de l'impulsion dans les domaines temporel et spectral.

Le bruit d'ASE, dû aux amplificateurs optiques, et la SPM induisent un bruit de phase non-linéaire,

$$\phi_{NL} = \gamma L_{eff} \sum_{i=1}^{N_{sp}} |E + \sum_{k=1}^i n_k|^2, \quad (3)$$

où  $\gamma$  est appelé coefficient non-linéaire de la fibre,  $L_{eff}$  est appelé longueur effective du span,  $E$  représente le champ électromagnétique,  $n_k$  sont des variables aléatoires i.i.d. de type Gaussien dues au bruit d'ASE, et  $N_{sp}$  est le nombre de spans de fibre à longueur uniforme. À titre d'exemple, nous pouvons observer dans la Fig. 3 l'effet du bruit de phase non-linéaire sur une transmission à  $20 \times 100$  km de fibres monomodes standard (SSMF) avec des EDFA après chaque span.

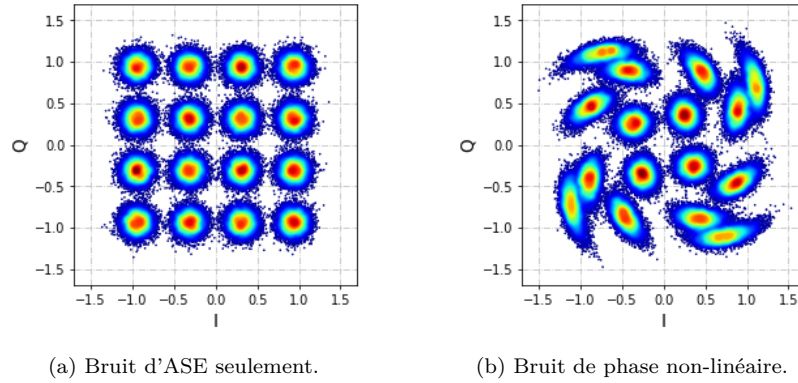


Figure 3 – Constellation 16QAM reçue à 32-GBaud et 1-dBm après  $20 \times 100$  km de SSMF.

La XPM a le même principe que la SPM, sauf que le déplacement de phase du champ électrique d'une impulsion est provoqué par une impulsion voisine. Quand ces impulsions appartiennent au même canal, la XPM est appelée intra-XPM (IXPM). Au contraire de la SPM, la XPM provoque un élargissement asymétrique du spectre avec un changement de la fréquence centrale. Comme les différentes harmoniques générées à l'intérieur du spectre se déplacent à des vitesses différentes, cela cause un "gigue de collision".

Au contraire de la SPM et de la XPM, le FWM implique un échange d'énergie pour générer une nouvelle composante fréquentielle à partir de trois harmoniques. Le FWM est plus susceptible de se produire dans les transmissions WDM et même à l'intérieur d'un même canal (intra-FWM (IFWM)). Plus la CD est large, les impulsions optiques qui arrivent à différents moments (en raison de la CD) peuvent s'interférer entre elles et causer du FWM.

### 3 Équation Non-linéaire de Schrödinger

L'équation qui décrit la propagation du champ électromagnétique vectoriel  $\mathbf{E} = [E_1, E_2]$  à travers la fibre optique est connue sous le nom d'équation non-linéaire couplée (ou vectorielle) de Schrödinger (CNLSE). Cette équation, dérivée des équations de Maxwell, est simplifiée comme ceci, lorsqu'on considère que la biréfringence du matériau qui compose la fibre est linéaire :

$$\frac{\partial E_1}{\partial z} = \left( -\frac{\alpha}{2} - \beta_1 \frac{\partial}{\partial t} - \frac{j\beta_2}{2} \frac{\partial^2}{\partial t^2} \right) E_1 + j\gamma \left( |E_1|^2 + \frac{2}{3}|E_2|^2 \right) E_1, \quad (4)$$

$$\frac{\partial E_2}{\partial z} = \left( -\frac{\alpha}{2} - \beta_1 \frac{\partial}{\partial t} - \frac{j\beta_2}{2} \frac{\partial^2}{\partial t^2} \right) E_2 + j\gamma \left( |E_2|^2 + \frac{2}{3}|E_1|^2 \right) E_2, \quad (5)$$

où  $\alpha$ ,  $\beta_1$ ,  $\beta_2$  et  $\gamma$  représentent respectivement le coefficient d'atténuation de la fibre, la dispersion modale de polarisation (PMD), la CD et le coefficient non-linéaire de la fibre.

Dans les fibres actuelles, la biréfringence peut changer assez rapidement, et donc la longueur de battement<sup>1</sup>  $L_B$  est beaucoup plus petite que la longueur non-linéaire<sup>2</sup>  $L_{NL}$ . La CNLSE devient l'équation de Manakov-PMD suivante :

$$\frac{\partial \mathbf{E}}{\partial z} = \left( -\frac{\alpha}{2} - \beta_1 \frac{\partial}{\partial t} - \frac{j\beta_2}{2} \frac{\partial^2}{\partial t^2} \right) \mathbf{E} + j\frac{8}{9}\gamma|\mathbf{E}|^2\mathbf{E}. \quad (6)$$

### 4 Traitement Numérique des Signaux pour les Systèmes de Transmission Optique Cohérente

En raison des différents effets linéaires et non-linéaires, ainsi que des imperfections des composants optiques et électriques, comme le décalage de la fréquence du laser et celui de l'oscillateur local, ainsi que le bruit de phase des lasers, dans les systèmes cohérents actuels, la compensation de ces effets est effectuée électroniquement via des algorithmes de traitement numérique des signaux (DSP). Concrètement, dans ce travail, nous avons considéré une chaîne d'algorithmes DSP, comme illustré dans la Fig. 4.

Les algorithmes DSP ont comme tâche la récupération des signaux transmis avec le moins d'erreurs possible. Il existe une grande variété d'algorithmes, l'un plus performant que l'autre, mais ça peut entraîner une complexité d'implémentation et de calcul plus grande. Dans ce travail, nous considérons une chaîne DSP standard qui performe une synchronisation et un rééchantillonnage à deux fois la fréquence symbole, pour respecter le critère de Nyquist. Ensuite, nous utilisons un filtre de mise en forme du type racine carrée de cosinus surélevé (RRC) juste avant l'égalisation du canal. L'algorithme suivant correspond à un égaliseur adaptatif pour récupérer les deux polarisations orthogonales, en plus que nous récupérons les signaux à la fréquence symbole. Ce qui reste, c'est la compensation du décalage de la fréquence et le bruit de phase des lasers.

---

1. La longueur de fibre dans laquelle les états de polarisation sur les axes orthogonaux sont retardés de  $2\pi$ .  
2. La longueur dans laquelle la non-linéarité de la fibre est significatif.

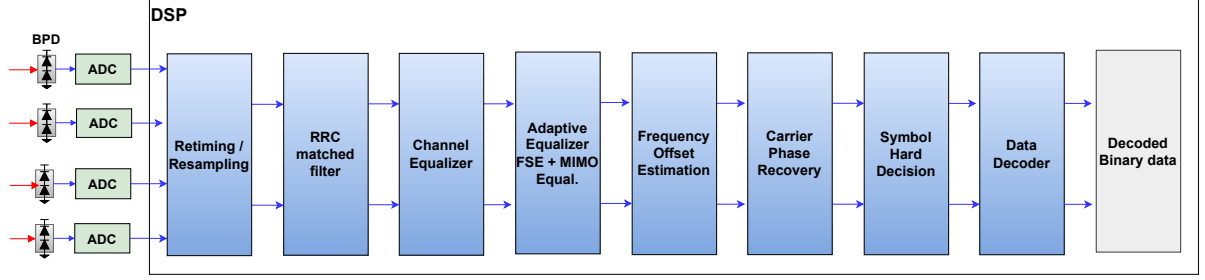


Figure 4 – Chaîne d’algorithmes de traitement numérique des signaux utilisés dans le récepteur cohérent. BPD: photodiodes balancées, ADC: convertisseur analogique-numérique.

Les récepteurs actuels utilisent comme égaliseur de canal des algorithmes pour compenser la CD, car la PMD est compensée avec l’égaliseur adaptatif. La compensation de la NLI a mobilisé un grand nombre de travaux de DSP, parce que la complexité calculatoire additionnelle est très significative. Les chercheurs ont proposé une série d’algorithmes DSP pour compenser la NLI, en essayant à réduire cette complexité afin que ces algorithmes puissent être implémentés en hardware. L’algorithme de Digital Backpropagation (DBP) est vu comme la méthode la plus performante pour compenser la NLI.

## 5 Algorithmes d’Égalisation Non-linéaire

### 5.1 Digital Backpropagation

La DBP est basée sur la méthode de Split-Step Fourier (SSFM). Cette méthode consiste à numériquement rétro propager les signaux reçus en employant une compensation linéaire suivie d’une compensation de la NLI par petits pas de fibre de longueur  $h$ , comme illustré dans la Fig. 5, où  $\hat{D}$  et  $\hat{N}$  représentent les opérateurs linéaires et non-linéaires, respectivement.

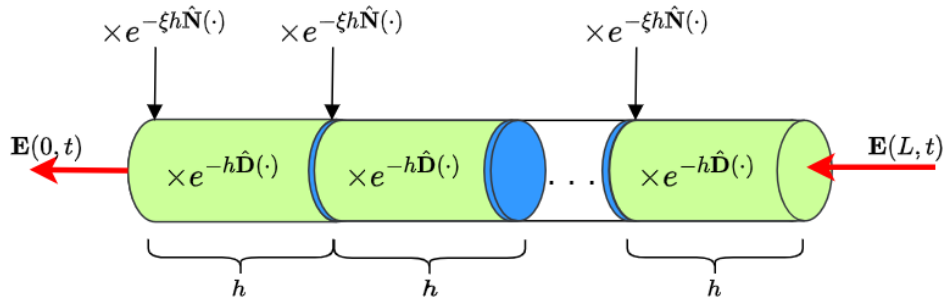


Figure 5 – Schéma illustrant la méthode de la DBP à  $\frac{L}{h}$  steps par span.  $\mathbf{E}(L, t)$  représente les signaux reçus à la fin du segment de longueur  $L$ ,  $h$  est la longueur du pas, et  $\hat{D}$  et  $\hat{N}$  représentent des opérateurs linéaires et non-linéaires, respectivement.  $\xi$  est un paramètre à optimiser.

En effet, avec des longueurs infinitésimales de fibre, il est possible de considérer que les effets linéaires et non-linéaires agissent indépendamment, ce qui n’est pas valable si on considère

plusieurs kilomètres de fibre par exemple. Il est compréhensible, donc, que la précision de cette méthode augmente avec la diminution du pas  $h$ . Néanmoins, réduire le pas  $h$  fait aussi augmenter le nombre d'opérations nécessaires à effectuer, rendant la méthode très complexe en termes de complexité calculatoire.

## 5.2 Séries de Volterra

Une autre méthode possible est basée sur les séries de Volterra (VNLE). La fibre optique, en tant que système non-linéaire, peut être modélisée par des séries de Volterra. En prenant le système à l'inverse, il est possible d'estimer l'entrée (les signaux originalement transmis) par rapport à la sortie (les signaux reçus) avec un ordre du noyau de Volterra suffisant. De la même que la DBP, la méthode est plus performante avec noyaux d'ordre plus élevé. Un ordre du noyau entre 3 ou 5 est raisonnable. La Fig. 6 illustre la méthode de séries de Volterra avec noyaux d'ordre 3.

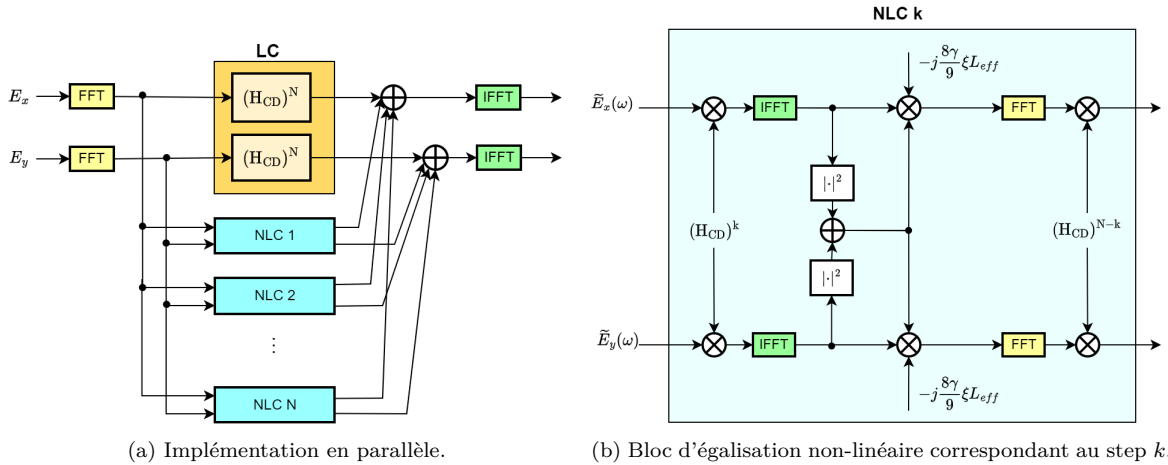


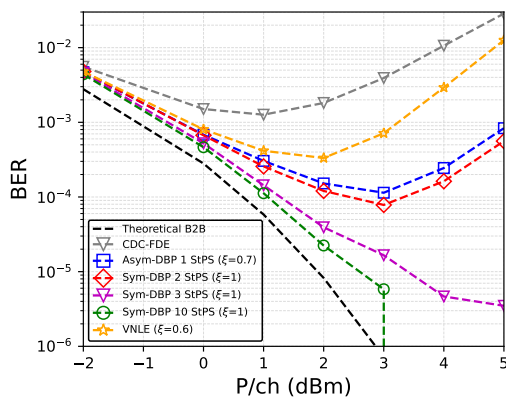
Figure 6 – Schéma d'un égaliseur non linéaire basé sur les séries de Volterra avec des noyaux d'ordre 3.  $E_x$  et  $E_y$  représentent les composantes de  $\mathbf{E}$ ,  $N$  est le nombre de spans, FFT est la transformée de Fourier rapide et IFFT est la FFT inverse,  $H_{CD}^k$  représente la compensation de la CD cumulée sur  $k$  spans,  $\xi$  est un paramètre à optimiser [3] ©2012, IEEE.

## 5.3 Compromis entre Performance et Complexité Calculatoire

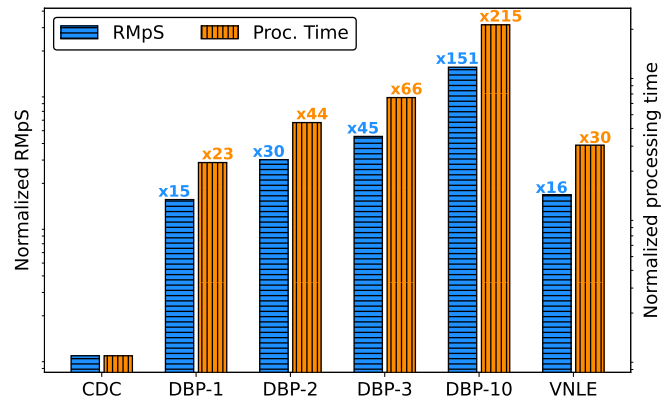
Prenons l'exemple d'une transmission d'un signal à double polarisation DP-16QAM à 32-GBaud sur  $14 \times 100$  km de longueur de span, ce qui est raisonnablement la configuration d'un système de transmission actuel à l'exception de la longueur de span uniforme. À ce stade, nous nous intéressons à investiguer la performance de la DBP et du VNLE, ainsi que les performances d'un égaliseur linéaire, c'est-à-dire la compensation de la CD seulement.

Nous investiguons les performances en termes de taux d'erreur binaire (BER). Les résultats du BER sont montrés dans la Fig. 7a. Nous pouvons vérifier que la DBP est plus performante tant qu'elle donne le meilleur taux d'erreur, encore en utilisant 1 step par span (StPS). Remarquons que nous utilisons la version asymétrique à 1 StPS et la version symétrique à  $\geq 2$  StPS, car ces derniers donnent une meilleure performance que les versions asymétriques. Mais la

comparaison n'est pas juste si nous ne regardons pas la complexité calculatoire de ces égaliseurs. Nous mesurons la complexité calculatoire en termes du nombre d'opérations mathématiques nécessaires lors de l'égalisation, concrètement le nombre de multiplications réelles par symbole traité (RMpS). De plus, nous mesurons le temps qui prend à traiter un symbole (processing time). La complexité calculatoire, de notre exemple, est illustrée dans la Fig. 7b. Au-dessous de chaque bar, il est indiqué le nombre de fois plus grand par rapport aux résultats d'égaliseur linéaire (CDC). Ces résultats montrent que la DBP à 1 StPS et le VNLE ont, à peu près, la même complexité, mais la DBP étant plus performante en termes de BER. Néanmoins, la DBP et le VNLE sont trop gourmands en calcul et ça, c'est un problème pour être actuellement implémenté au niveau hardware.



(a) BER vs. P/ch.



(b) Complexité calculatoire (CC) en multiplications réelles par symbole égalisé (RMpS) et temps de traitement.

Figure 7 – Performances du système en utilisant un égaliseur linéaire (CDC), des égaliseurs non-linéaires DBP et VNLE avec  $\xi$  optimal pour une transmission DP-16QAM à 32-GBaud sur  $14 \times 100$  km de SSMF.

Nous visons, à travers cette étude, à vérifier si des techniques simples basées sur des réseaux de neurones artificiels (ANN ou NN) peuvent surmonter ces défis de complexité calculatoire en permettant encore une réduction du BER significatif.

## 6 Égaliseurs Non-linéaires basés sur des Réseaux de Neurones Artificiels

Les techniques basées sur l'apprentissage automatique (ML) pour l'égalisation du canal optique exploitent le fait que nous pouvons avoir accès aux données avec une certaine facilité, que ce soit des données simulées ou des données expérimentales. En effet, le succès du ML repose sur l'utilisation des mégadonnées (*big data* en anglais) pour construire des modèles qui permettent de représenter une fonction ou une transformation d'une entrée vers une sortie.

Les réseaux de neurones artificiels sont des techniques du ML construits à partir du concept d'apprentissage profond (*Deep Learning* (DL) en anglais), dans lequel la représentation du modèle se fait par couches, où chaque couche est dédiée à l'extraction des caractéristiques communes à toutes les données d'entrées. Ces caractéristiques sont souvent abstraites dans les couches de début et plus intuitives dans les couches de sortie.

De manière générale, nous avons inclus le NN après la sortie du bloc de compensation de phase, comme illustré dans la Fig 8.

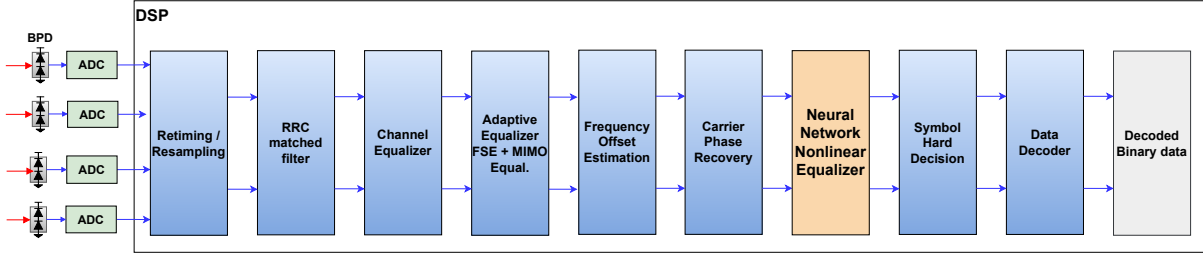


Figure 8 – Placement du réseau de neurones après le bloc de compensation de phase.

Dans notre travail, nous nous sommes focalisés sur les NN du type Perceptron Multicouche.

### 6.1 Perceptron Multicouche (MLP)

Les NN MLP sont les modèles les plus généraux et peuvent représenter n’importe quelle fonction. Le MLP est illustré dans la Fig. 9.

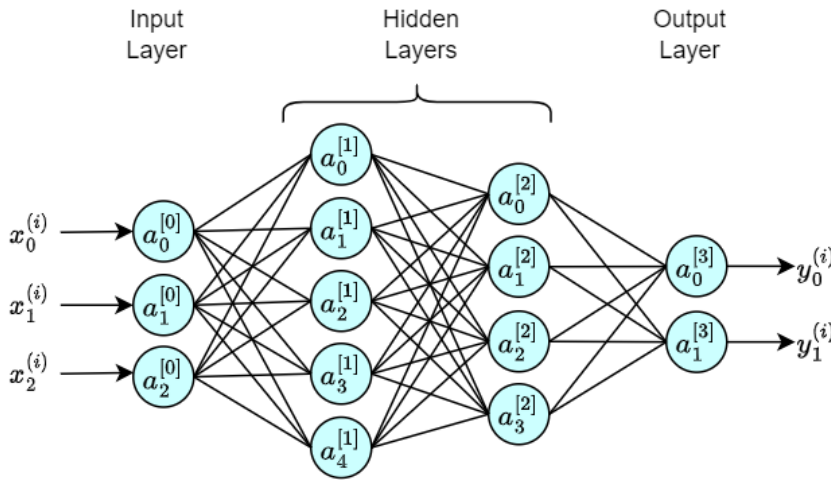


Figure 9 – Architecture du NN Perceptron Multicouche (MLP).

En général, le but du réseau consiste à trouver la vraie valeur de  $\mathbf{y}$ , c’est-à-dire  $\mathbf{y}_{\text{true}}$  en ayant comme information  $\mathbf{x}$ .

Le réseau MLP consiste en multiples couches, où chaque couche est composée d’un nombre défini de neurones. Notamment, la première couche est la couche d’entrée et la dernière couche est la couche de sortie. Les couches au milieu sont appelées couches cachées. Chaque neurone reçoit toutes les entrées de la couche précédente. La valeur résultante est transmise vers tous les neurones de la couche suivante. La Fig. 10 montre le modèle du neurone artificiel.

D’après ce modèle, la sortie de chaque neurone est une combinaison linéaire de ses entrées plus un terme de biais, avec sa sortie transformée via une fonction d’activation non-linéaire  $\phi$  :

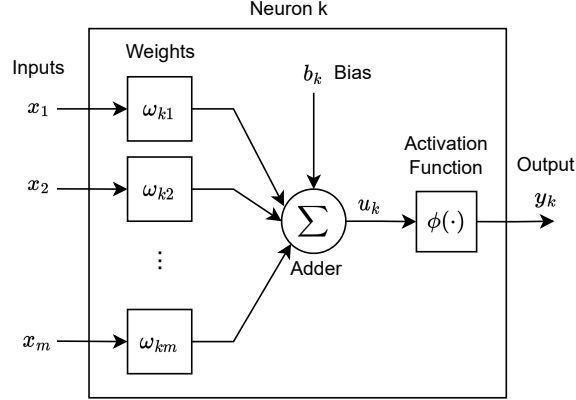


Figure 10 – Modèle d'un neurone artificiel.

$$u_k = \boldsymbol{\omega}_k \mathbf{x}^\top + b_k, \quad (7a)$$

$$y_k = \phi(u_k), \quad (7b)$$

où  $\boldsymbol{\omega}_k = [\omega_{k1}, \omega_{k2}, \dots, \omega_{km}]$  est l'ensemble de poids  $\omega_{km}$  pour chaque entrée  $x_m$ ,  $\mathbf{x} = [x_1, x_2, \dots, x_m]$  représentent les  $m$  entrées,  $b_k$  est le terme de biais,  $u_k$  est une combinaison linéaire et  $y_k$  est la valeur de sortie du neurone.

Pour le réseau complet illustré en Fig. 9, le vecteur de sortie  $\mathbf{y}$  est représenté comme ceci :

$$\mathbf{y} = f(\mathbf{x}; \boldsymbol{\theta}), \quad (8)$$

où  $f$  représentent l'ensemble d'opérations linéaires et non-linéaires, et  $\boldsymbol{\theta}$  est l'ensemble de poids  $\mathbf{W}^{[l]}$  et  $\mathbf{b}^{[l]}$  pour  $1 \leq l < L$  et appelé les paramètres du réseau MLP,

$$\boldsymbol{\theta} = \mathbf{W}^{[1]}, \mathbf{b}^{[1]}, \dots, \mathbf{W}^{[L-1]}, \mathbf{b}^{[L-1]}. \quad (9)$$

## 6.2 Processus d'apprentissage

Comme le but du réseau MLP est de rapprocher  $\mathbf{y}$  à  $\mathbf{y}_{\text{true}}$ , nous devons, lors de l'apprentissage, mettre à jour les valeurs de  $\boldsymbol{\theta}$  de façon à ce que la différence entre  $\mathbf{y}$  et  $\mathbf{y}_{\text{true}}$  diminue. Cette différence instantanée est nommée Fonction de coût ou de pertes et est notée comme  $l(\mathbf{y}, \mathbf{y}_{\text{true}})$ . La mise à jour de  $\boldsymbol{\theta}$  est un problème d'optimisation, et donc, des algorithmes classiques comme l'algorithme du gradient stochastique (SGD) et ses variantes (ADAM, Adagrad, RMSProp) sont souvent utilisés. L'algorithme de SGD consiste à faire varier les valeurs de  $\boldsymbol{\theta}$  à partir du gradient d'une valeur représentative de  $l(\mathbf{y}, \mathbf{y}_{\text{true}})$ , donc l'espérance mathématique, notée comme  $\mathcal{L}(\boldsymbol{\theta})$ , par rapport à  $\boldsymbol{\theta}$ , c'est-à-dire :

$$\boldsymbol{\theta} \leftarrow \boldsymbol{\theta} - \varepsilon \nabla_{\boldsymbol{\theta}} \mathcal{L}(\boldsymbol{\theta}), \quad (10)$$

où  $\varepsilon$  est nommée taux d'apprentissage et  $\nabla_{\boldsymbol{\theta}}$  est le gradient de  $\mathcal{L}(\boldsymbol{\theta})$  par rapport à  $\boldsymbol{\theta}$ .

Les fonctions de coût considérées sont habituellement l'erreur quadratique, la valeur absolue,

la fonction d'Huber, etc. Pour la fonction quadratique, il est classiquement utilisé l'erreur quadratique moyenne (MSE), calculée comme ceci :

$$MSE(\mathbf{y}, \hat{\mathbf{y}}) = \mathbb{E}(l(\mathbf{y}, \mathbf{y}_{\text{true}})) = \frac{1}{N} \sum_{i=1}^N (y_i - y_{\text{true},i})^2, \quad (11)$$

où  $\mathbb{E}$  représente l'espérance mathématique, et  $y_i$  et  $y_{\text{true},i}$  sont respectivement les neurones  $i$  pour  $1 \leq i \leq N$  de la sortie  $\mathbf{y}$  et du target  $\mathbf{y}_{\text{true}}$ .

### 6.3 Sélection des hyper-paramètres et Traitement des données

Le MLP est défini par le nombre de couches cachées, le nombre de neurones pour chaque couche et les fonctions d'activation non-linéaires à la sortie de chaque couche. Ces paramètres de réseau sont appelés hyper-paramètres. En plus, lors de l'apprentissage, d'autres paramètres doivent aussi être définis, comme le taux d'apprentissage  $\varepsilon$ . Quand on utilise la SGD, l'optimisation est souvent faite par groupes ou Batches de données, et quand tous les batches de données ont été traités, nous parlons de l'achèvement d'un Epoch. Ces deux paramètres, la taille des batches et le nombre d'epochs sont également des hyper-paramètres.

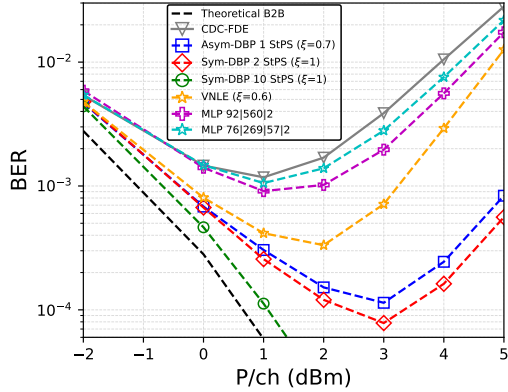
Le choix des hyper-paramètres peut être fait de manières différentes. Nous avons adopté une stratégie basée sur la méthode de l'estimateur de Parzen à structure arborescente (TPE). Pour ce faire, nous devons définir une fonction objective, que celle que nous souhaitons optimiser. Nous identifions deux fonctions : le taux d'erreur binaire (ou symboles) et la fonction de coût MSE.

Un autre point à considérer concerne le traitement des données à fournir au MLP. Comme illustré dans la Fig. 8, l'entrée du réseau sont les symboles après le compensateur de phase et la sortie correspond aux symboles égalisés. Comme l'objectif du réseau est d'obtenir les symboles originalement transmis, les symboles transmis correspond au target. En ce qui suit, nous considérons trois sets de données différents : l'une pour l'apprentissage du réseau, l'autre pour la validation des résultats lors de l'apprentissage, et finalement une dernière pour des tests finaux.

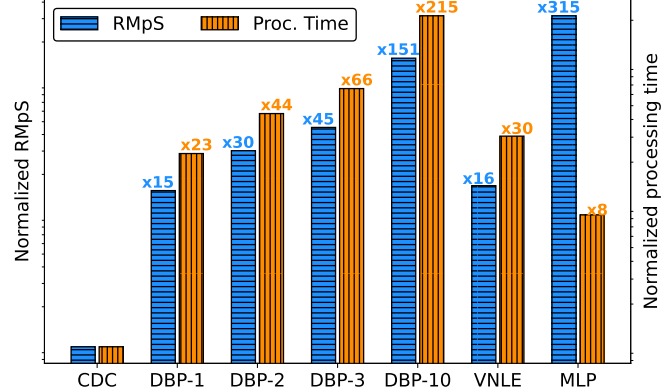
### 6.4 Résultats des égaliseurs basés sur NN

En prenant l'exemple précédent d'une transmission DP-16QAM à 32-GBaud sur  $14 \times 100$  km de SSMF, nous avons trouvé les hyper-paramètres qui minimisent le taux d'erreur symbole (SER) et le MSE, les deux métriques en utilisant les données de validation. Une fois l'architecture des réseaux choisie, nous utilisons les réseaux entraînés dans une phase de test. Nous avons calculé le taux d'erreur binaire (BER) pour chaque cas (SER optimisé et MSE optimisé). Le MLP avec SER optimisé compte 92 neurones d'entrée, 560 neurones dans la première couche cachée, et 2 neurones de sortie, tandis que le MLP avec MSE optimisé compte 76 neurones d'entrée, 269 et 57 neurones respectivement dans la première et la deuxième couche cachée, et 2 neurones de sortie. Les résultats sont montrés dans la Fig. 11a. La complexité calculatoire est également calculée comme le nombre de multiplications réelles nécessaires pour égaliser un symbole (RMpS) et le temps de traitement. Ces deux dernières valeurs, RMpS et temps de

traitement, sont montrées dans la Fig. 11b dans le cas du NN avec SER optimisé qui a la plus petite taille parmi les deux.



(a) BER vs. P/ch.



(b) Complexité calculatoire (CC) en multiplications réelles par symbole égalisé (RMpS) et temps de traitement. MLP correspond à MLP 92|560|2 (SER optimisé).

Figure 11 – Performances du système en incluant le NN pour une transmission DP-16QAM sur  $14 \times 100$  km de SSMF. Plus violets : SER optimisé. Étoiles cyan : MSE optimisé.

Nous observons que les valeurs de BER sont moins bonnes que celles de la DBP et le VNLE. En plus, un réseau avec hyper-paramètres choisis pour optimiser le SER donne de meilleurs résultats (plus violets) que ceux d'un réseau avec hyper-paramètres choisis pour optimiser le MSE (étoiles cyan). La complexité calculatoire, qui correspond au réseau avec SER optimisé, montre aussi une quantité d'opérations supérieure à celle de la DBP et le VNLE mais avec un moindre temps de traitement. Cela s'explique facilement en regardant le réseau comme une succession de matrices, où les multiplications de lignes et de colonnes peuvent se faire en parallèle.

Les diagrammes de constellation 16QAM des symboles égalisés sont montrés dans la Fig. 12. Noter que les symboles égalisés avec un MLP (MSE optimisé, deuxième ligne) prennent une allure en forme de grille sur les lignes horizontales et verticales à  $-0.95, -0.32, +0.32, +0.95$ . Ce phénomène, qui apparaît très légèrement dans les diagrammes de la première ligne avec SER optimisé, est analysée dans la section suivante.

Nous avons vu, donc, que malgré une optimisation des paramètres du réseau, soit en utilisant le SER ou le MSE comme métrique d'optimisation, le MLP n'est pas capable de compenser la non-linéarité de la fibre aussi bien que la DBP ou le VNLE, au moins pour les systèmes de transmission cohérents sur des longues distances de SSMF.

## 7 L'effet MMSE-scatterplot: constellation en forme de grille

Lorsque les réseaux neuronaux sont utilisés comme égaliseur non-linéaire avec un critère de minimisation basé sur le MSE (MMSE) lors de l'apprentissage, nous avons observé que les constellations subissent une déformation, en adoptant une forme de grille (dans les cas des constellations QAM rectangulaires). Ce phénomène observé correspond bien à une égalisation non-linéaire où la fonction de coût est basée sur le MSE, et pour cette raison, nous l'avons appelé

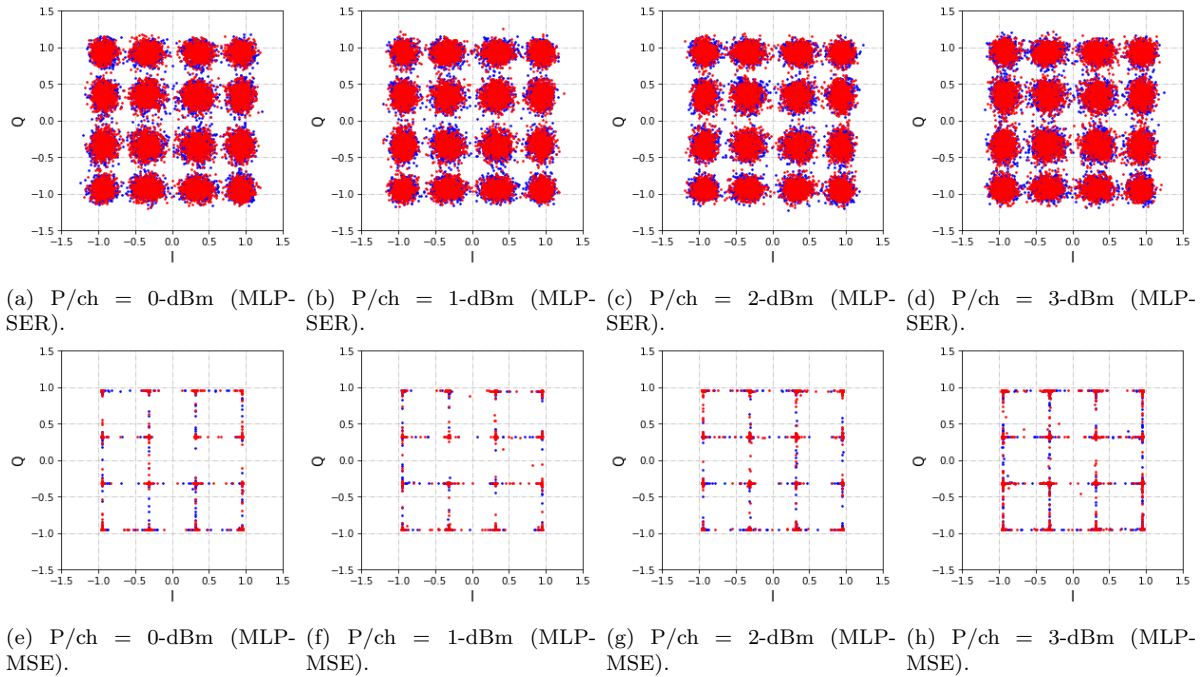


Figure 12 – Diagrammes de constellation des signaux égalisés avec la MLP avec des hyper-paramètres qui optimisent le SER (première ligne), et qui optimisent le MSE (deuxième ligne).

l’effet “MMSE-scatterplot”. Nous l’observons notamment dans le cas où nous avons optimisé les hyper-paramètres du réseau en tenant compte de la minimisation du MSE. Néanmoins, ce phénomène apparaît également dans le premier cas, où nous optimisons les hyper-paramètres en tenant compte de minimiser le SER (voir comment les points ont une certaine tendance à se diffuser vers les lignes verticales et horizontales). En général, ce phénomène apparaîtra sur tous les égaliseurs non-linéaires entraînés avec une fonction de coût basée sur le MSE. Ce qui va changer d’un résultat à l’autre, c’est le niveau d’égalisation du réseau avant d’originer une déformation de la constellation. Ce niveau d’égalisation va dépendre principalement de la capacité du réseau, c’est-à-dire du nombre des paramètres, du taux d’apprentissage, du temps d’entraînement, de la taille des données et de la représentativité des données.

Mais concrètement, en quoi l’effet MMSE-scatterplot est problématique pour la correcte récupération de bits transmis ? Pour répondre à cette question, il faut savoir qu’actuellement, les schémas de correction d’erreurs sont basés sur une décision dite “soft”, qui s’appuie sur des probabilités d’avoir reçu le bit correct plutôt que de décider au préalable la valeur du bit avant de le corriger. La première approche correspond au schéma de Soft-Decision Forward Error Correction (SD-FEC) tant que la deuxième correspond au schéma de Hard-Decision FEC (HD-FEC). Considérons maintenant la présence de ce phénomène de grille. Clairement, cette allure correspond à une décision du type “Hard”, puisque les symboles égalisés ont déjà pris une décision (soit les symboles réels prennent les valeurs  $-0.95$ ,  $-0.32$ ,  $+0.32$  ou  $+0.95$  dans l’exemple précédent). Il n’est donc pas adapté aux schémas de SD-FEC qui est la méthode la plus optimale aujourd’hui.

Dans cette étude-là, nous nous sommes focalisés sur la compréhension de ce phénomène et sur le modèle mathématique qui explique l’apparition de ce phénomène. En plus, en prenant avan-

tage de ce modèle, nous avons proposé une technique pour éviter l'apparition de ce phénomène de grille.

## 7.1 Modèle mathématique du phénomène MMSE-scatterplot

Considérons le cas général du système de transmission illustré dans la Fig. 13 avec un bloc d'égalisation par un réseau de neurones NN, où  $X$  est la séquence des symboles émis,  $R$  est la séquence des symboles reçus, et  $Y$  est l'estimation de  $X$  par le réseau de neurones.

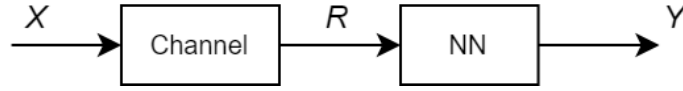


Figure 13 – Cas général d'un système de transmission avec égalisation du canal par un réseau de neurones NN.

Il a été démontré que la valeur estimée de  $X$ , sous le critère de minimisation du  $MSE = \mathbb{E}[|X - Y|^2]$ , est atteinte de façon optimale quand  $Y = \mathbb{E}[X|R]$ .

Considérons maintenant le cas d'un système de transmission sur un canal AWGN, comme illustré dans la Fig. 14, où le bruit du canal AWGN est représenté par  $Z \sim \mathcal{CN}(0, \sigma^2)$ ,  $\sigma^2$  est la variance du bruit, les signaux transmis sont représentés par  $X$  qui ont une probabilité d'occurrence uniforme  $p(X) = \frac{1}{M}$ , où  $M$  est la taille de l'alphabet  $\chi$ , et  $R$  représente les signaux reçus  $R = X + Z$ .

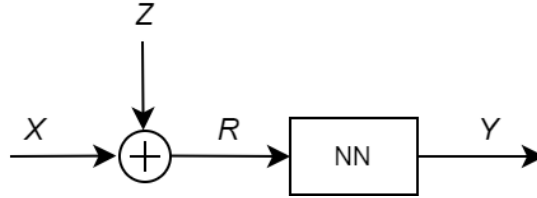


Figure 14 – Système de transmission sur canal AWGN avec égalisation du canal par un réseau de neurones NN.

La valeur optimale de  $Y$ , en utilisant  $Y = \mathbb{E}[X|R]$  et  $p(R|X) = \frac{1}{\pi\sigma^2} e^{-\frac{|r-x|^2}{\sigma^2}}$ , entraîne :

$$y = \mathcal{S}_\chi(r; \sigma^2) = \frac{\sum_{x \in \chi} x e^{-\frac{|r-x|^2}{\sigma^2}}}{\sum_{x \in \chi} e^{-\frac{|r-x|^2}{\sigma^2}}}, \quad (12)$$

où la fonction nommée  $\mathcal{S}_\chi(r; \sigma^2)$  avec des paramètres d'entrée  $r$  et  $\sigma^2$ , est appelée ici fonction de Soft-Thresholding (STH).

L'utilisation directe de la fonction STH sur les signaux  $R$  donne des constellations avec une distribution similaire à celle d'un réseau entraîné avec le critère de MMSE, comme il est montré dans la Fig. 15.

Cela veut dire que le NN, quand il est appris en utilisant la fonction de coût MSE, est équivalent à la fonction STH, qui introduit l'effet MMSE-scatterplot.

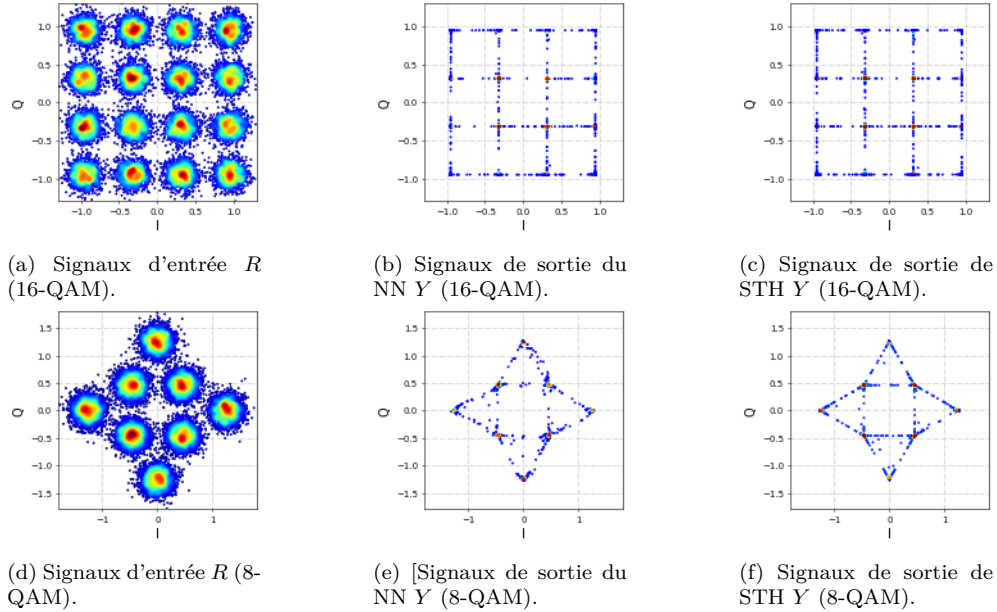


Figure 15 – Constellations d’entrée  $R$ , sortie du NN  $Y$  et sortie de la fonction STH pour des signaux 16-QAM quadratique et des signaux 8-QAM non rectangulaire ©2024, IEEE.

## 7.2 Technique de mitigation de l’effet MMSE-scatterplot

Nous avons proposé une technique pour empêcher l’apparition de l’effet MMSE-scatterplot, en incluant la fonction de STH tout à la fin du réseau de neurones NN, comme illustré dans la Fig. 16 dans le cas d’un canal AWGN.

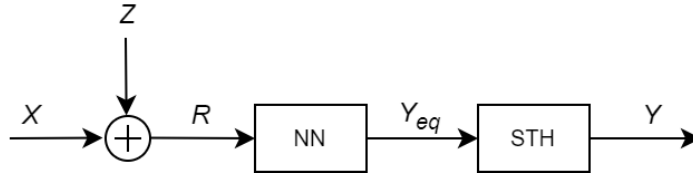


Figure 16 – Système de transmission avec égaliseur basé sur le NN et en incluant la fonction STH à la fin.

En effet, nous savons que, sous le critère de MMSE, le NN converge vers l’effet MMSE-scatterplot (constellation en forme de grille). Cependant, selon les paramètres d’entraînement du réseau (taux d’apprentissage, taille des batches, nombre d’epochs, etc.), cette convergence n’est pas immédiate, et par conséquent, le réseau est capable de faire de l’égalisation avant qu’il ne converge vers l’effet MMSE-scatterplot. Nous proposons, donc, de dire au réseau de ne faire que de l’égalisation pure, tant que l’effet MMSE-scatterplot sera fait par la fonction STH ajoutée à la fin du réseau. Les signaux égalisés  $Y_{eq}$  seront les signaux à la sortie du NN (ou à l’entrée de la fonction STH). La fonction de coût est calculée avec  $Y$  et  $X$  à chaque itération. Cette méthode peut entraîner une descente de gradient évanescence. Nous résoudrons cela en ajoutant  $Y_{eq}$  à  $Y$ , donnant comme valeur  $Y = Y + Y_{eq}$ . Cet artifice est connu comme connexion résiduelle.

Même si le phénomène de MMSE-scatterplot est clairement distinctif, il vaut mieux calculer une métrique qui nous permet de mesurer la réduction de la quantité d’information de  $X$  étant

donné  $Y$ . Cette métrique est l'information Mutuelle (MI). En effet, plus le phénomène MMSE-scatterplot est présent, plus nous perdons de l'information de  $X$  sachant  $Y$ , puisque les valeurs de  $Y$  deviennent plus largement décorréliées de celles de  $X$ , et donc, en diminuant la MI.

### 7.3 Résultats de l'usage de la technique de mitigation proposée

Pour examiner les résultats de la méthode proposée, nous prenons le cas d'une transmission DP-64QAM à 32-Gbaud sur  $14 \times 50$  km de SSMF. Le schéma détaillé du système de transmission pour ce test est illustré dans la Fig. 17.

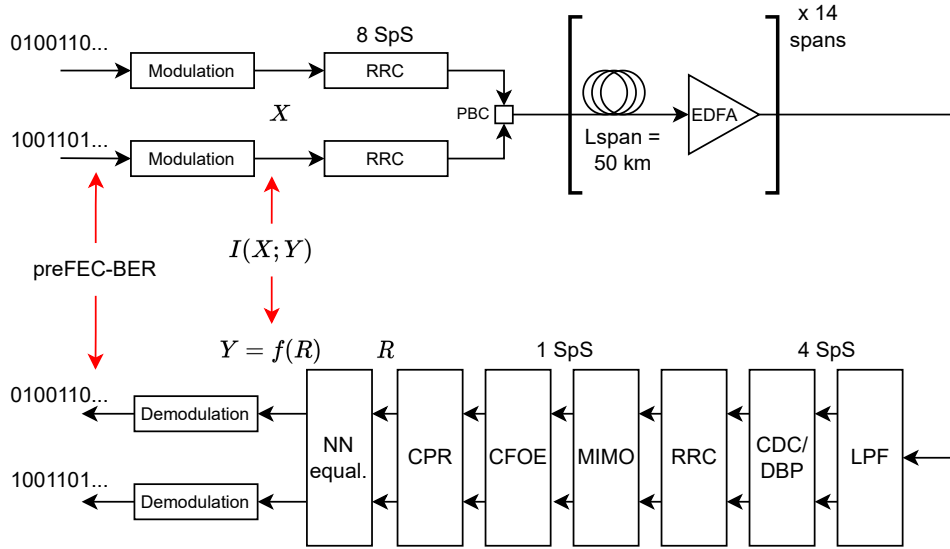


Figure 17 – Système de transmission DP-64QAM à 32-Gbaud sur  $14 \times 50$  km de SSMF ©2024, IEEE.

Les valeurs de BER (preFEC-BER) et de la MI sont calculées par des différents niveaux de puissance des signaux. Les résultats sont montrés dans la Fig. 18. Noter que nous avons ajouté les résultats de compensation linéaire classique par DSP (CDC), ceux du NN avec fonction de coût MSE, notre proposition du NN + STH toujours avec la fonction de coût MSE, ceux du NN avec la fonction de coût MSE-X, et ceux de la DBP à 1 StPS comme référence. La fonction de coût MSE-X est une fonction dérivée de la minimisation de l'entropie conditionnelle de  $X$  étant donné  $Y$  [4].

Nous observons que les résultats de la technique proposée NN + STH (en bleu pointillé avec cercles) montrent une diminution du BER, comme le NN classique (en vert pointillé avec losanges) et le MSE-X (en rouge pointillé avec triangles inversés), tout en empêchant une diminution de la MI, ce qui est fait aussi par la MSE-X, mais pas pour le NN classique, comme attendu. Noter que la DBP est supérieure à toutes ces méthodes.

Nous affichons également les constellations à l'entrée du NN et à la sortie du NN + STH pour vérifier si le MMSE-scatterplot a été bien limité. Les différents résultats sont montrés dans la Fig. 19 pour quatre niveaux de puissance par canal différents.

Nous constatons que les constellations à la sortie du NN + STH ne sont pas affectées par l'effet MMSE-scatterplot, ce qui est en accord avec la moindre diminution de la MI, montrée dans la Fig. 18b. L'autre méthode MSE-X permet également de limiter l'effet MMSE-scatterplot.

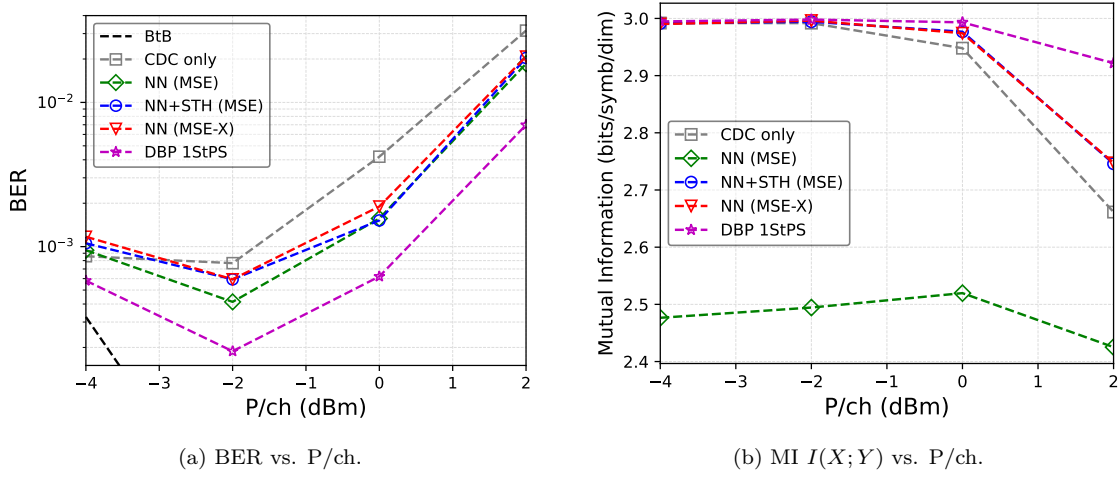


Figure 18 – Résultats de BER et de MI pour différents niveaux de puissance par canal  $P/ch$  ©2024, IEEE.

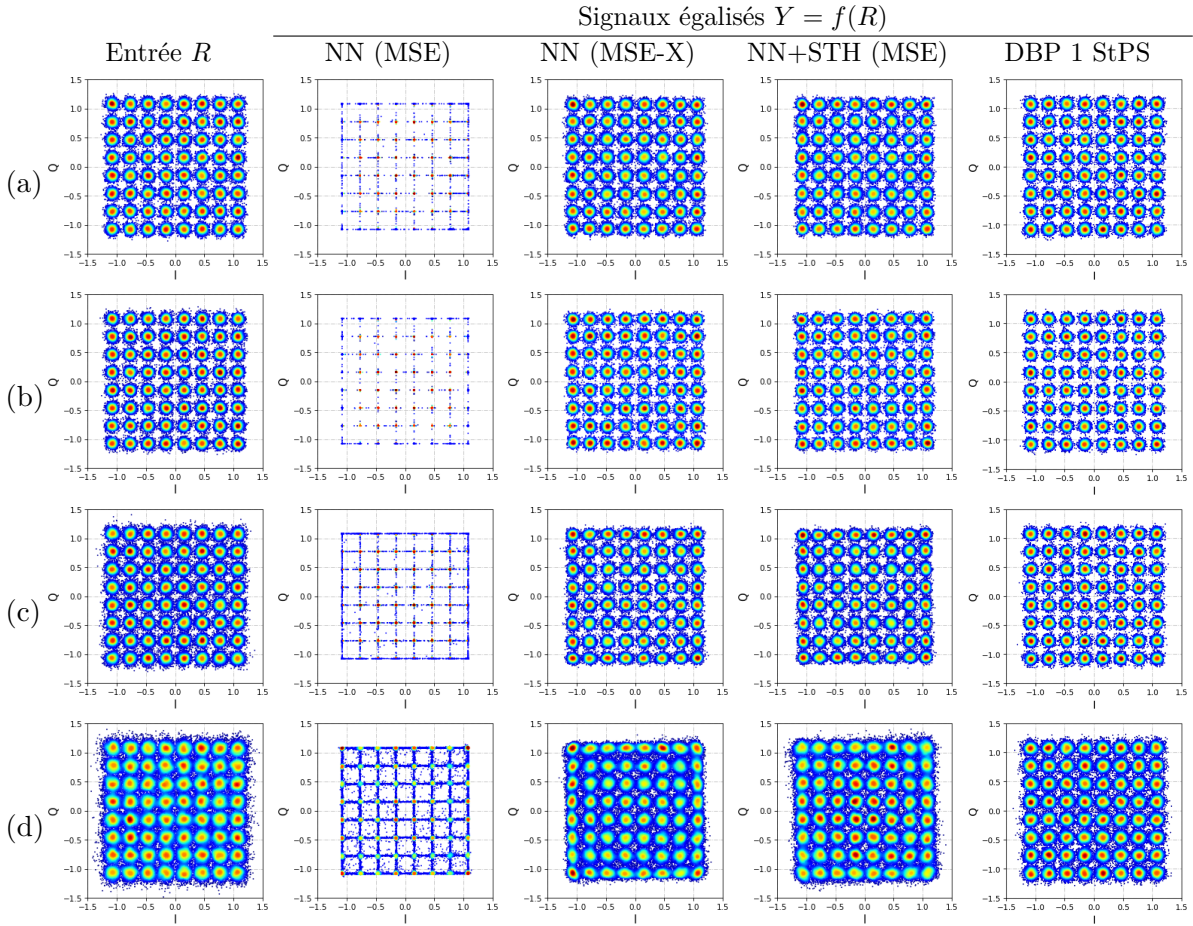


Figure 19 – Constellations des signaux d'entrée  $R$  et des signaux égalisés  $Y = f(R)$ . (a)  $P/ch = -4dBm$ , (b)  $P/ch = -2dBm$ , (c)  $P/ch = 0dBm$ , (d)  $P/ch = 2dBm$  ©2024, IEEE.

## 8 Conclusion et Perspectives

Cette étude se concentre sur l'évaluation des avantages des réseaux de neurones (NN) en tant que techniques de compensation des impairments non-linéaires (NLI) dans les transmissions optiques cohérentes à haut débit. Le modèle de NN choisi est le Perceptron Multicouche (MLP), qui a la capacité théorique d'approximer n'importe quelle fonction non linéaire.

Dans ces travaux, nous avons considéré le scénario d'un seul canal, révélant une capacité de compensation de la NLI plus limitée par rapport aux méthodes classiques de référence, telles que la Digital Backpropagation (DBP) et l'égaliseur basé sur des séries de Volterra (VNLE), mais avec un temps de traitement inférieur.

Nous avons également abordé un phénomène observé dans les diagrammes de constellation lors de l'utilisation de NN entraînés avec la fonction de coût d'erreur quadratique moyenne (MSE). Ce phénomène est particulièrement impactant pour les techniques avancées de correction d'erreur (SD-FEC). Nous avons nommé ce phénomène MMSE-scatterplot. Nous avons expliqué le modèle mathématique de l'effet MMSE-scatterplot à l'aide de la fonction appelée Soft-Thresholding (STH). En utilisant cette fonction STH à la fin du NN, nous pouvons obtenir un signal égalisé sans ce phénomène de MMSE-scatterplot.

L'étude conclut que la question des avantages des NN comme égaliseur non linéaire reste ouverte et nécessite l'implication de divers acteurs, notamment les fournisseurs du hardware pour les communication optique. Bien que des avancées aient été réalisées, des recherches futures devraient se concentrer sur l'intégration de techniques comme la Learned DBP (LDBP) dans des configurations de transmission réelles, tout en garantissant la reproductibilité des méthodes et leur implémentation hardware.



# INTRODUCTION

## 1.1 Context and Motivation

During the last years, the traffic rate through the internet has greatly increased [5], [6] (Fig. 1.1), with an estimated increment from 2019 to 2023 of 30% of estimated annual average growth [7] in fixed and mobile networks. During the COVID-19 pandemic, the growth rate was more pronounced, slightly decreasing in post-COVID times but still with positive growth rates. Several factors have contributed to this trend, for instance, video devices for high definition (HD), ultra HD, and 4K video-streaming, connected devices in industrial environments using the Internet of Objects (IoT), mobile technologies 4G and 5G, and it is expected that this trend will continue with the advent of the 6G in 2030 [8].

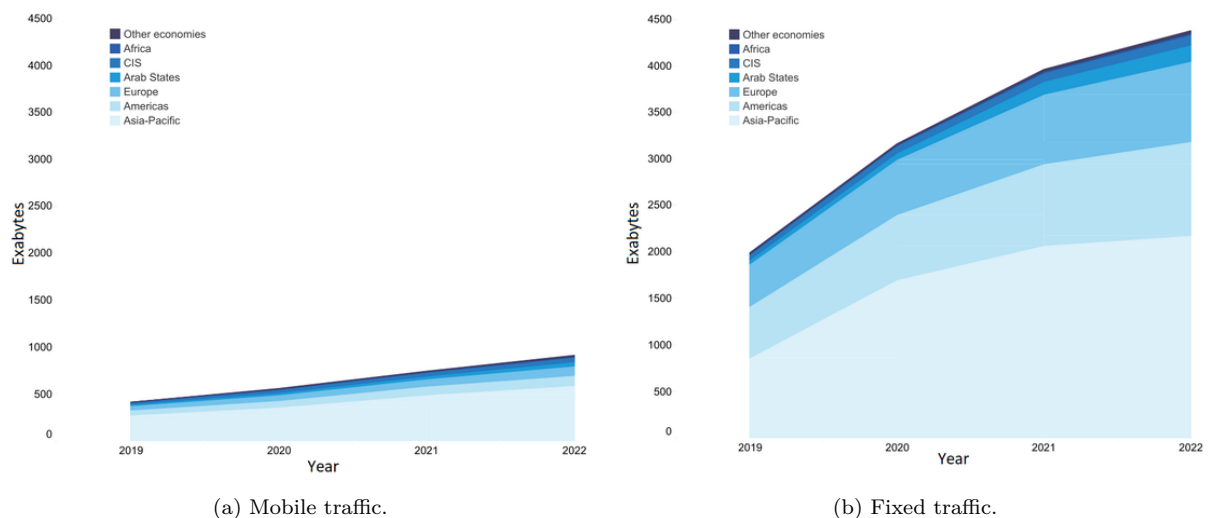


Figure 1.1 – Broadband traffic between 2019 and 2022 [7].

This traffic increase has obliged network operators to upgrade their telecommunication infrastructures, including the backbone network, which is a critical part of a network operator’s operation. Indeed, the backbone or back-haul network physically interconnects large metropolitan areas<sup>1</sup> allowing the transport of vast amounts of data. The physical support of back-haul transmission networks is the optical fiber due to its high bandwidth and low attenuation. These characteristics made the optical fiber the best cost-effective solution against other technologies, such as coaxial cable systems, which required more repeaters due to its highest attenuation, and microwave systems that are limited in capacity [9].

1. Separated from a few kilometers to thousand kilometers as is the case of intercontinental distances.

Modern optical fibers widely used today in network operators are those made of silica, particularly the SSMF ITU-T G.652D. The SSMF was adopted due to its low attenuation, allowing a transmission for longer distances and, therefore, less number of optical amplifiers. Since the invention of modern optical fibers, several improvements are continuously being conducted, for instance, using novel materials such as the newest hollow-core fiber with a core essentially made of air [10] with low attenuation of  $\sim 0.11$  dB/km in 1550 nm. Still, the silica-based optical fibers continue to prevail and might continue at least in the back-haul networks until the manufacturing process of these novel optical fibers becomes economically affordable for telecom operators.

In addition to the evolution of optical fiber, electronic and optical components have also evolved to permit the transmission of higher data rates over long distances. Indeed, the employed technology for the optical transmission system has evolved from Intensity Modulation and Direct-Detection (IM/DD) schemes with lower spectral efficiency and low data rates towards coherent communications with high spectral efficiency and high data rates. IM/DD with dispersion-managed systems was suitable for 10Gb/s data bit rate transmissions. To achieve higher data bit rates, from 40Gb/s per channel up to 1.6 Tb/s per channel, it was necessary to use more complex modulation formats and, hence, more complex receiver architectures. Notably, coherent communications have enabled the use of two orthogonal polarizations transmitted simultaneously using the same spectrum but also more efficient modulation schemes to encode more bits per symbol [11], approaching the optimal Gaussian constellations [12]. In conjunction with optical Erbium-Doped Fiber Amplifiers (EDFA), suitable for C-band (1530 nm - 1565 nm) and later L-band (1565 nm - 1625 nm), to increase the transmission distance, and the Wavelength Division Multiplexing (WDM) to send multiple channels using a single fiber, it has been possible to increase the product capacity  $\times$  distance. In recent years, other novel solutions have also been proposed to continue increasing the channel capacity. For instance, the use of the other bands of the optical spectrum [13], [14], namely O-band (1260 nm - 1360 nm), E-band (1360 nm - 1460 nm), S-band (1460 nm - 1530 nm), and U-band (1625 nm - 1675 nm), more efficient constellation shaping techniques such as the Probabilistic Constellation Shaping (PCS) and Probabilistic Amplitude Shaping (PAS) [15], [16], and recently the used of digital sub-carriers multiplexing schemes [17].

An ultimate barrier to reaching Shannon's capacity is the optical fiber Nonlinear Impairments (NLI), which are detrimental effects produced by a nonlinear behaviour of silica fibers when high light intensity crosses the optical fiber, altering the refraction index of the optical fiber material [18]. Particularly, the Kerr nonlinear effects produce that the refractive index changes proportionally to light intensity levels. Indeed, the Kerr nonlinear effects could significantly limit the transmission distances and the transmission capacity at high Optical Signal-to-Noise Ratio (OSNR), as is needed for high order modulation formats [19], [20]. Several techniques based on Digital Signal Processing (DSP) have been proposed to compensate for the Kerr nonlinear effects [21]. For instance, techniques that are based on the propagation equation, namely the Nonlinear Schrödinger Equation (NLSE), such as the Digital Backpropagation (DBP) [22]–[24]. Other techniques with lower computational complexity have also been proposed, such as the Volterra Nonlinear Equalizer (VNLE) [3], [25], and Perturbation based methods [26]. Nonetheless, applying these techniques embedded in an Application-Specific Integrated Circuit (ASIC) has remained challenging due to the additional and prohibited complexity added to the actual transceivers [27]. Decreasing the complexity of these methods often leads to lower performance in real-world conditions, causing a loss of interest in practical implementations.

Recently, with the gain in popularity of Machine Learning (ML) and Artificial Intelligence (AI), novel techniques for NLI compensation have been proposed to achieve a significant gain in performances with reduced complexity efficiently. Indeed, ML has proven to be very effective in other fields, such as image recognition, computer vision, speech recognition, natural language processing, and recently generative AI using large language models and many other applications [28], [29].

In communication systems, the use of ML has been extensively studied. Indeed, such “data-driven” techniques, which are capable of learning from an “input-output” relationship [30], have demonstrated superior efficiency compared to traditional adaptive methods. In wireless systems, ML has found a lot of interest since more than two decades ago [31]–[33] and [34, & references therein], so much so that the intensive research in this area is still very recent [35], [36]. Similarly, in optical communications, ML also has attracted a lot of interest, particularly in signal equalization due to the linear and nonlinear impairments. ML using NN has been widely and extensively studied during the last years, proving to be useful and superior to the classical techniques based on DSP. Indeed, NN are a general purpose ML technique capable of solving complex problems. For instance, different types of NN, such as the Multilayer Perceptron (MLP) [37], [38], Convolutional Neural Networks (CNN) [39], Recurrent Neural Networks (RNN) [40], [41], and CNN + RNN [42], have been tested in various numerical and experimental scenarios. A comparison of different NN architectures in terms of statistical performance and complexity was presented in [43]. In [44], an NN architecture was proposed for optical/electrical nonlinearity compensation, while [45] proposed NN for digital pre-distortion at the transmitter side. Additionally, several physics-based complex-values NN, such as the Learned DBP (LDBP), were proposed in [46]–[48].

Responding to the necessity of still further investigations about the capabilities of NN in NLI compensation in optical transport networks, Orange Labs, IMT Atlantique, and the École Nationale d’Ingénieurs de Brest (ENIB)<sup>2</sup>, associated with preparing a PhD thesis to investigate this topic deeply.

## 1.2 Objectives and Methodology

This thesis aimed to investigate the use of NN for NLI compensation in long-haul and high data bit rate coherent optical transmission systems. From an industrial point of view, we focused our study on use cases that are typical in an existing deployed optical transport network, i.e., a full DSP based receiver for channel equalization and carrier phase recovery, using SSMF with typical span lengths of 100 km and multiple number of spans, using DP configurations and a symbol mapping using Quadrature Amplitude Modulation (QAM) formats. In punctual scenarios, we have lightened these configurations to investigate the factors that limit the performance of NN, for instance, decreasing the span length or using Single Polarization (SP) transmission scenarios.

The main steps carried out during the thesis are the following:

- Study of the NLI impact on the classical coherent optical system through a numerical and experimental investigation. The numerical investigation was done via simulations of

---

2. Later, this collaboration, that has been done for several decades also with the École Nationale Supérieure des Sciences Appliquées et de Technologie (ENSSAT) de Lannion, originated the foundation of the Lab’Optic, a joint lab dedicated to optical communications research.

the whole coherent optical system (dual polarization transmitter, dispersive and nonlinear optical channel accounting for Chromatic Dispersion (CD), Polarization Mode Dispersion (PMD) and NLI, and the DSP algorithms of the dual-polarization coherent receiver) using Python. Orange has a laboratory equipped with modern transmitters and coherent receivers ideal for research and several spools of SSMF, which jointly have permitted us to implement a point-to-point optical coherent link for our experiments. The laboratory also has several equipments for metrology.

- Study and implementation of NN for NLI compensation using Pytorch, which is a ML framework in Python. The NN coded in Pytorch are integrated as an additional DSP algorithm into the DSP blocks. The NN are primarily trained and tested using numerical data- for various scenarios. In a second stage, we used the experimental data for punctual scenarios.

### 1.3 Contributions

Our principal contributions are listed below:

- Using NN, as nonlinear equalizers, provokes a transformation on the signal constellation, adopting a grid shape in the case of rectangular QAM formats. As some authors also indicated, we attributed this transformation to using the Mean Squared Error (MSE) loss function during the NN training. Due to an extensive investigation and deep analysis, we found the theoretical explanation of this previously mentioned grid shape effect in the signal constellations, that for a more general case, we named Minimum MSE (MMSE) driven signal constellation scatterplot and abbreviated as “MMSE-scatterplot”. Our contribution relies on explicitly associating a mathematical expression derived from the MMSE analysis in previous works with the MMSE-scatterplot effect. This equation is called the Soft-Thresholding (STH) function. We showed that the signal constellation after the NN training using the MMSE criterion and the signal constellation using the STH function have the same characteristic distribution of symbols.
- Additionally, to avoid the MMSE-scatterplot emergence on the equalized symbols, we propose including the STH function as a nonlinear activation function after the NN during the training stage.

### 1.4 Workshops and Publications

#### Workshops

- A. Sotomayor, “Neural Networks applied to Nonlinearity mitigation in Long Haul Optical Transmission Systems” in Seminaire ASMP, ENIB, 07 Oct. 2021.
- A. Sotomayor, “Neural Networks applied to Nonlinearity mitigation in Coherent Long Haul Optical Transmission Systems” in Salon Optical Networks, Orange, 18 May 2022.
- A. Sotomayor, “Neural Networks applied to Nonlinearity mitigation in Coherent Long-Haul Optical Transmission Systems” in Ambient Connectivity PhD students sharing sessions, Orange, 18 November 2022.

## Journal Papers

- E. Pincemin, Y. Loussouarn, A. Sotomayor, et al., “End-to-End Interoperable 400-GbE Optical Communications Through 2-km 400GBASE-FR4,  $8 \times 100$ -km 400G-OpenROADM and 125-km 400-ZR Fiber Lines” in *Journal of Lightwave Technology*, vol. 41, no. 4, pp. 1250-1257, 15 Feb.15, 2023, doi: 10.1109/JLT.2022.3204731.
- A. Sotomayor, V. Choqueuse, E. Pincemin and M. Morvan, “MMSE-Driven Signal Constellation Scatterplot Using Neural Networks-Based Nonlinear Equalizers” in *Journal of Lightwave Technology*, doi: 10.1109/JLT.2024.3421927.

## International Conferences

- E. Pincemin, Y. Loussouarn, A. Sotomayor, et al., “927-km End-to-End Interoperable 400-GbEthernet Optical Communications through 2-km 400GBASE-FR4,  $8 \times 100$ -km 400G-OpenROADM and 125-km 400-ZR Fiber Lines” in *Optical Fiber Communication Conference (OFC) 2022, Technical Digest Series (Optica Publishing Group, 2022)*, paper Th4A.3.
- A. Sotomayor, E. Pincemin, V. Choqueuse, and M. Morvan, “Optimized Cost Function of Multi-Layer Perceptron for Fibre Non-Linear Impairment Mitigation in Coherent 200-Gbps DP-16QAM Transmission System” in *Optica Advanced Photonics Congress 2022, Technical Digest Series (Optica Publishing Group, 2022)*, paper JTU2A.41.
- A. Sotomayor, E. Pincemin, V. Choqueuse and M. Morvan, “A Comparison of Machine Learning Techniques for Fiber Non-Linearity Compensation: Multilayer Perceptron vs. Learned Digital BackPropagation” in *2023 23rd International Conference on Transparent Optical Networks (ICTON), Bucharest, Romania, 2023*, pp. 1-4, doi: 10.1109/ICTON59386.2023.10207458.

## 1.5 Thesis Outline

The remainder of this thesis manuscript is organized as follows:

- In chapter 2, we present the fundamentals of optical communications with a particular focus on coherent systems. We detail the characteristics of the three elements that compose a coherent optical transmission system: a dual-polarization transmitter, the optical channel, and the dual-polarization coherent receiver.
- In chapter 3, we focus on the DSP based techniques employed in standard optical transceivers for channel equalization, adaptive equalization, frequency offset compensation, and carrier phase recovery. We described in detail each of these algorithms and their practical implementations. We also show step-by-step the effects of these algorithms in data from simulation scenarios as well as for data from the experimental setup.
- In chapter 4, we briefly introduce ML and specially NN, showing the reasons why NN achieved a great success in many tasks. After that, we summarize the state of the art of NN used as nonlinear equalizers in optical coherent systems. This part is followed by our implementations and results of the MLP using the numerical and experimental setup for different use cases. Here, we also show the MMSE-scatterplot effect and propose the Huber loss function to avoid its appearance partially.

- In chapter 5, we deeply analyze the MMSE-scatterplot effect from a theoretical point of view, presenting its equivalent mathematical equation derived from the MMSE analysis. Taking advantage of this equation, we also propose a novel technique to avoid its total appearance. These results are compared against the MSE-X loss function recently proposed in the literature.

# FUNDAMENTAL OF OPTICAL COMMUNICATIONS

Coherent communication has been pivotal in accelerating the growth of transmission capacity and global Internet communications. This technology is also increasingly being utilized in optical access networks. [49].

Various technologies have converged to enable the popularity of coherent systems. While optical fiber was initially designed to permit large bandwidth transmissions, one of the limitations was the optical and electrical components needed to efficiently transmit more information within the same spectral bandwidth with the highest quality. The introduction of coherent technology in optical communications in the first decade of the new millennium [11] has made it possible. Coherent technology, jointly with powerful DSP techniques embedded in ultra-rapid ASIC based on CMOS technology [50], coherent transmissions have gained great popularity, especially in optical transport networks.

Fig. 2.1 illustrates a classical block diagram of an optical transmission system that uses coherent technology. We distinguish the dual-polarization transmitter, multiple optical fiber spans with full loss compensation using EDFA after each span, and the dual-polarization coherent receiver.

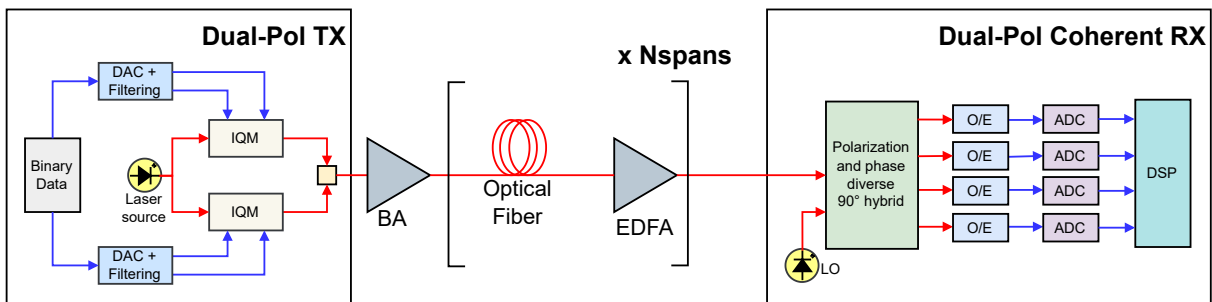


Figure 2.1 – Block Diagram of a Dual-Polarization coherent optical transmission system. DAC: digital-to-analog converter, IQM: IQ modulator, BA: Booster Amplifier, EDFA: Erbium-doped Fiber Amplifier, LO: local oscillator, O/E: Optical-to-Electrical, ADC: Analog-to-Digital Converter. Blue lines are electrical signals, and red lines are optical signals.

This chapter details the structure of the classical optical transmission system. In Section 2.1, we describe the dual-polarization transmitter. Section 2.2 is dedicated to the dual-polarization coherent receiver. Then, in Section 2.3, we describe the optical channel. Section 2.4 presents the Nonlinear Schrödinger equation (NLSE) that describes the optical signal propagation. Section 2.5 introduces the Split-Step Fourier method to solve the NLSE numerically. Lastly, Section 2.6 summarizes the chapter.

## 2.1 Dual-Polarization Transmitter

Coherent communications have enabled more Degrees of Freedom (DOF) to encode the information on the Transmitter. Unlike the first technologies based on IM/DD, coherent technology has made it possible to encode the binary information digits in both phase and amplitude in the complex plane. The number of symbols in the complex plane defines how efficiently the optical channel bandwidth is used by means of the number of transmitted bits per symbol. Additionally, using two orthogonal polarization states for the carrier lightwave further enhances spectral efficiency by transmitting twice the quantity of information. Indeed, by using two In-Phase/Quadrature (IQ) modulators, the generated signals could be combined, doubling the data rate. Fig. 2.2 illustrates the dual-polarization transmitter and its components: a source of lightwave, the DP-IQ modulators, the binary data encoder or bits-to-symbols mapping, the Digital-to-Analog Converters (DAC) and the filters for pulse shaping.

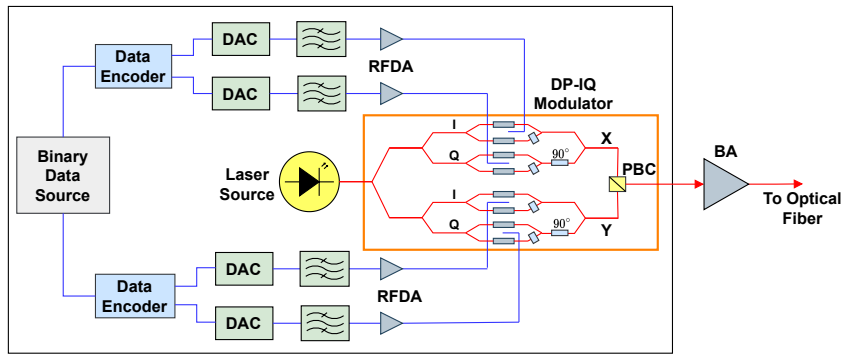


Figure 2.2 – Dual-Polarization Transmitter. DAC: Digital-to-Analog Converter, RFDA: RF Driver Amplifier (linear amplifier), PBC: Polarization Beam Combiner, BA: Booster Amplifier.

### 2.1.1 Laser Sources

The coherent light source is crucial for spectrally efficient coherent systems in optical networks. In optical communications, laser sources are typically based on semiconductors. A laser, which stands for light amplification by stimulated emission of radiation, is a device that emits coherent light with narrow linewidth due to a process of stimulated emission of radiation. Depending on the cavity structure, the lasers could be of the type: Fabry–Pérot (FP) lasers, Distributed Feedback Laser (DFB) lasers, or External Cavity Laser (ECL).

A FP laser consists of two highly reflective mirrors in which light is confined. After several reflections, light in phase is constructively added. The frequencies at which this happens are known as cavity modes. The wavelengths of the generated optical lightwave depend on the distance of the mirrors, which is the principle of tunable lasers. FP lasers are very susceptible to phase fluctuations, thus leading to laser phase noise.

As modern optical transceivers need to operate in a single frequency with narrow linewidth, an alternative is using DFB lasers. A DFB laser contains a Bragg grating inside the cavity that functions as a distributed mirror. The wavelength is selected by thermally changing the period of the grating. One inconvenience of DFB lasers is that laser gain occurs in the same region

of wavelength selection, the latter affecting the process of laser gain. Also, DFB lasers have a broad linewidth of some MHz, which is not suitable for modern transceivers.

A tunable laser with narrower linewidth is the ECL, which separates the cavity laser from the gain medium. In the gain medium, multiple modes are generated and passed to an etalon filter with a very narrow profile to select the desired wavelength. Ultra-compact ECL are commonly used due to their characteristics, e.g., a narrow linewidth of  $< 100$  kHz [51].

The laser linewidth is a critical parameter for modern coherent systems based on phase diversity. A broader spectrum of the laser beam leads to increased quantum fluctuations affecting the phase of the optical field. In the classical coherent transceiver, DSP techniques for higher modulation schemes typically require a narrow laser linewidth for optimal functioning [52].

The Laser Phase Noise (LPN) arises due to spontaneous emission into the semiconductor lasers [53] and is modeled as a Wiener process [54]–[57]. In a discrete-time model:

$$\phi_s[k] = \phi_s[k-1] + w[k], \quad (2.1)$$

where  $\phi_s[k]$  is the phase noise of the  $k$ -th symbol and  $w[k]$  is the source frequency noise assumed to be stationary Gaussian [54] with zero mean and variance  $\sigma^2 = 2\pi\Delta fT_s$ , being  $\Delta f$  the sum linewidth of signal and Local Oscillator (LO) lasers and  $T_s$  is symbol duration [55], [56], [58].

### 2.1.2 Modulation Formats

The binary sequences<sup>1</sup> are mapped into signal waveforms that could be transmitted through the channel. This process is called Digital Modulation. The signal waveforms could vary in amplitude, phase, or frequency. This study focuses on amplitude and phase-based modulation formats, namely Phase-Shift Keying (PSK) and Quadrature Amplitude Modulation (QAM). These two are the most commonly used formats in optical transport networks. PSK modulation is based on the phase diversity, while QAM is based on the amplitude and phase diversity. The signal waveforms are represented in the complex plane. The set of unique complex numbers used to represent the binary information is known as the constellation alphabet [59].

The PSK modulated symbols are represented by two-dimensional vectors:

$$\mathbf{s}_m = \left[ A \cos \frac{2\pi}{M}(m-1), A \sin \frac{2\pi}{M}(m-1) \right], \quad m = 1, 2, \dots, M, \quad (2.2)$$

where  $A$  is the amplitude, and  $M$  is the order of the PSK modulation or the possible phases to encode the information.

$M$ -ary QAM results from combining two Pulse Amplitude Modulation (PAM) signals,  $M_1$ -PAM and  $M_2$ -PAM, in quadrature, so that  $M = M_1M_2$ . The M-QAM modulated symbols are represented as follows:

$$\mathbf{s}_m = [A_{m,s}, A_{m,c}], \quad m_s = 1, 2, \dots, M_1, \quad m_c = 1, 2, \dots, M_2, \quad (2.3)$$

where  $A_{m,s} = (2m_s - 1 - M_1)d_1$  and  $A_{m,c} = (2m_c - 1 - M_2)d_2$  are the signal amplitudes of the quadrature components, where  $2d_1$  and  $2d_2$  are the distance between adjacent signal amplitudes for each PAM constellations that conform the M-QAM [59].

---

1. In this work, we assume that binary information is already compressed (source encoding) and with redundancy (channel encoder). Thus, the binary information sequences are code words [59].

For illustration purposes, Fig. 2.3 illustrates examples of PSK and QAM constellations.

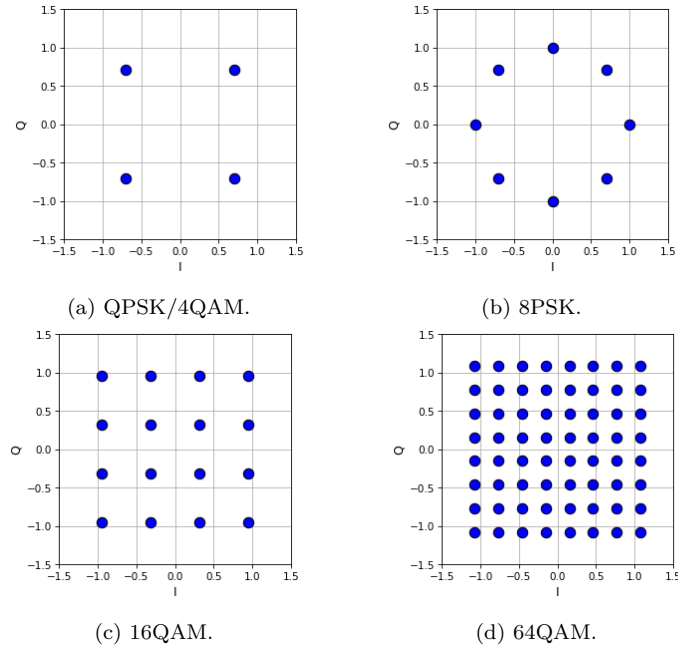


Figure 2.3 – PSK and QAM constellations.

### 2.1.3 Digital Modulation

The main objective of digital modulation is to map the code words into signal waveforms. The modulator encodes a sequence of  $b$  information bits using  $M = 2^b$  distinct waveforms, one for each of the possible sequences of  $b$  bits [59]. A digital modulator is also known as bit-to-symbol encoder or mapper. In our study, we used two mapping schemes: Gray encoding and Differential encoding.

#### Gray Encoding

This scheme is known as the optimal encoding and is based on the assumption that an error is more likely to occur between neighboring symbols. The idea behind this is that neighboring symbols must differ by the fewest number of bits. Gray encoding maps the code words into symbols so that only one bit differs between neighbors in their corresponding code words. Therefore, if there is a mistake in detection due to noise, the error associated will only affect one bit (at least for high SNR) [59], [60]. For example, in a QPSK and 16QAM, Gray encoding maps the code words as illustrated in Fig. 2.4.

In a PSK constellation composed of  $M$  symbols ( $M$ -PSK), the symbols are closer to each other than in a QAM of  $M$  symbols ( $M$ -QAM) of the same order  $M$  for  $M > 4$ . As a result, the probability of binary errors, referred to as Bit Error Rate (BER), is higher in  $M$ -PSK modulation formats than in  $M$ -QAM for  $M > 4$ . To illustrate this point, we can estimate the probability of error for different orders of PSK and QAM when varying the Signal-to-Noise Ratio (SNR) per transmitted bit  $E_b/N_0$ . The formulas used to calculate this error probability are indicated in

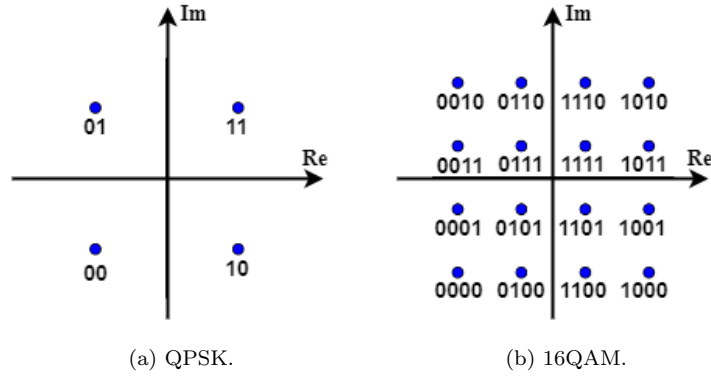
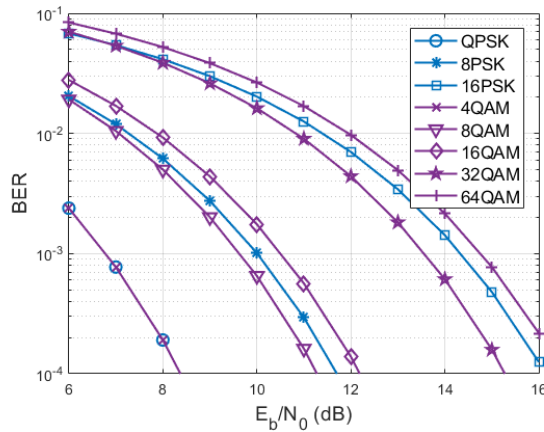


Figure 2.4 – QPSK and 16QAM constellations using Gray encoding.

Appendix A. Fig. 2.5 depicts the BER with respect to  $E_b/N_0$  for the PSK and QAM modulation formats of different orders in a Additive White Gaussian Noise (AWGN) channel using Gray encoding.

Figure 2.5 – BER vs.  $E_b/N_0$  for PSK and QAM constellations in an AWGN channel with optimal source encoding.

### Differential Encoding

At the receiver, typical DSP algorithms for carrier phase recovery are blind<sup>2</sup>, resulting in a phase ambiguity in case of phase shifts or cycle slips [62], [63]. There are at least two ways to solve this issue: 1) by inserting periodic pilot symbols in the information data and 2) by using differential encoding. The first method has shown good results in solving the ambiguity problem with a lower BER penalty than the differential encoding [64]. Still, the required pilot symbols could potentially decrease the useful data payload, which, in turn, reduces the spectral efficiency. On the other hand, differential encoding solves the phase ambiguity problem with a penalty in BER, which is minimal in high SNR [56].

<sup>2</sup>. Blind algorithms are those which rely on signal statistics, in contrast with data-aided algorithms which work with training sequences [61].

In this work, we have chosen the differential encoding approach. However, some studies have shown the superiority of data-aided approaches, for instance, in [61], where it was performed a comparison between blind equalizers and data-aided equalizers.

In differential encoding, the two Most Significant Bits (MSB) of the code word of  $b$  bits represent one of the four quadrants of the complex plane and are differentially encoded, i.e., the phase difference of symbol  $i$  and symbol  $i - 1$  encodes the information. Specifically, if the two MSB used for symbol  $i$  are “00”, the quadrant of symbol  $i$  and symbol  $i - 1$  is the same. If the two MSB used for symbol  $i$  are “01”, the quadrant of symbol  $i$  is the next quadrant counterclockwise. If the two MSB used for symbol  $i$  are “10”, the quadrant of symbol  $i$  is the next quadrant clockwise. If the two MSB used for symbol  $i$  are “11”, the quadrant of symbol  $i$  is the second next quadrant counterclockwise. The remaining bits represent the points within the quadrant and are Gray encoded to minimize errors [62]. For example, in 16QAM, the differential encoding technique is used to map the data, as shown in Fig. 2.6. The two MSB represent the quadrant change, while the two Least Significant Bits (LSB) within the quadrants are Gray encoded. Notice that in QPSK, the two bits of the symbols are differentially encoded.

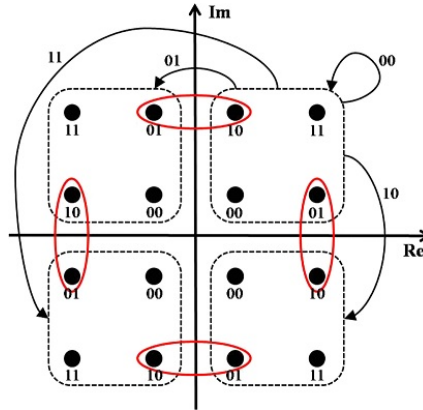


Figure 2.6 – 16QAM constellation with differential encoding [56] ©2009, IEEE.

### 2.1.4 Dual Polarization IQ Modulator

Higher-order modulation schemes use efficient modulators to encode as much information as possible into a light wave. The Direct-Modulated Laser (DML) is typically used for short distances and low data bit rates. A DML comprises the laser source and the modulator. The output power is directly modulated by changing the pump current of the laser gain medium. The DML is limited in extinction ratio, which is the current range in which the optical output power is linear with the pump current. Another problem of the DML is the modulation chirp, which denotes the time dependence of the transmitted frequency.

Other kind of modulators are those based on an external cavity to the laser source. An Electro-Absorption Modulator (EAM) belongs to this category. An EAM is made by a semiconductor waveguide, in which an electric signal is applied perpendicular to the optical wave direction via electrodes. The optical power is modulated by changes in the optical absorption spectrum due to the current applied to the semiconductor waveguide. An EAM can also be integrated with a DFB laser on the same chip.

Both the DML and the EAM modulate the optical power. Phase modulators are needed to achieve more efficient modulation schemes. Phase modulation is achieved with the use of electro-optic crystals. A current applied to the electro-optic crystal changes the phase delay of the propagating light.

An optical modulator that combines both amplitude and phase is the Mach-Zehnder Modulators (MZM). The structure consists of two phase modulators, where each arm modulates half of the light wave. A bias electrode is applied in one of the arms to shift the operating point to the sinusoidal region of the power transfer function. This bias induces a  $90^\circ$  phase shift between the two arms, which are combined at the output. An IQ modulator consists of two MZM-based amplitude modulators. The modulated signals are then combined with a  $90^\circ$  phase difference to form the complex field. A DP-IQ modulator consists of two IQ modulators whose outputs are combined via a Polarization Beam Combiner (PBC) [52].

### 2.1.5 Pulse Shaping

The electrical pulse waveforms are generated using a set of DAC and pulse shapers to generate the band-limited waveforms [60], reducing spectral occupancy for high spectral efficiency. In an AWGN channel, it has been demonstrated that the Raised-Cosine (RC) is an optimal choice for pulse shaping as the RC filter significantly reduces the Intersymbol Interference (ISI) [50]<sup>3</sup>. The RC filter is given by:

$$P_{RC}(f) = \begin{cases} T_s & , 0 \leq |f| \leq \frac{1-\rho}{2T_s} \\ \frac{T_s}{2} \left( 1 + \cos \left( \frac{\pi T_s}{\rho} \left| f - \frac{1-\rho}{2T_s} \right| \right) \right) & , \frac{1-\rho}{2T_s} \leq |f| \leq \frac{1+\rho}{2T_s} \\ 0 & , |f| > \frac{1+\rho}{2T_s}, \end{cases} \quad (2.4)$$

where  $\rho$  is the roll-off factor  $0 < \rho \leq 1$ , and  $T_s$  is the symbol period.

In practice, the RC filter response is shared between the transmitter and receiver using an Root Raised-Cosine (RRC) filter on each side for maximum SNR [50]. The RRC filter frequency response is the square root of  $P_{RC}(f)$ , resulting in the following impulse response [66]:

$$p_{RRC}(t) = \frac{4\rho}{\pi\sqrt{T_s}} \frac{\cos\left((1+\rho)\pi\frac{t}{T_s}\right) + \frac{\sin\left((1-\rho)\pi\frac{t}{T_s}\right)}{4\rho\frac{t}{T_s}}}{1 - \left(4\rho\frac{t}{T_s}\right)^2}, \quad t \in \mathbb{R}. \quad (2.5)$$

In a discrete model, the pulse shaper  $p(t)$  in (2.5) is not realizable due to its anti-causal nature and because it is infinite in time. Therefore, if we want to implement this filter using a Finite Impulse Response (FIR) filter, it is necessary to make it causal and with finite size. For instance, truncating the filter and shifting the half size of the filter, as follows:

$$p[k] = \frac{4\rho}{\pi\sqrt{K}} \frac{\cos\left((1+\rho)\pi\frac{k-LK}{K}\right) + \frac{(1-\rho)\pi}{4\rho} \text{sinc}\left((1-\rho)\frac{k-LK}{K}\right)}{1 - \left(4\rho\frac{k-LK}{K}\right)^2}, \quad k \in [0; 2LK], \quad (2.6)$$

where the filter size is  $2LK + 1$ ,  $L$  is the half-size of the filter in taps per symbol, and  $K$  is the

3. For nonlinear channels, it has been shown that the RC filter is not optimal. However, in practice, it is still largely used. In [65], other alternatives have been proposed that are more adapted to nonlinear optical channels.

oversampling factor.

Let us represent the dual-polarization transmitted time-varying optical field as  $\mathbf{E}(t)$  after the pulse shaping  $p(t)$  as [55]:

$$\mathbf{E}(t) = \begin{bmatrix} E_1(t) \\ E_2(t) \end{bmatrix} = \sqrt{P_{tx}} \sum_n \mathbf{x}_n p(t - nT_s) e^{j(\omega_c t + \phi_s(t))}, \quad (2.7)$$

where  $P_{tx}$  is the average transmitted power,  $\mathbf{x}_n = [x_{1,n}, x_{2,n}]^T$  are the  $n$ -th modulated symbols in both polarization,  $T$  means the transpose operator,  $T_s$  is the symbol period,  $\omega_c = 2\pi f_c$  is the carrier frequency, and  $\phi_s(t)$  is the laser phase noise.

The digitized transmitted signal  $\mathbf{E}[k]$  takes the form:

$$\mathbf{E}[k] = \begin{bmatrix} E_1[k] \\ E_2[k] \end{bmatrix} = \sqrt{P_{tx}} \sum_n \mathbf{x}_n p(kT - nT_s) e^{j(\omega_c kT + \phi_s(kT))}, \quad (2.8)$$

where  $k$  is the discrete time index and  $T = \frac{T_s}{K}$  is the sampling period.

## 2.2 Dual-Polarization Coherent Receiver

In conjunction with the DP transmitter, the DP coherent receiver is the other key component enabling efficient communications. A figure illustrating the coherent receiver is shown in Fig. 2.7 for a polarization  $p$ , where an identical one is used in parallel for the other polarization. The incoming signal  $E_r$  and the Continuous-Wave (CW) LO  $E_{LO}$  are the input of a  $90^\circ$  Hybrid which is a 2-input 4-output passive device that generates the four combinations between the complex envelopes  $E_{r,p}$  and  $E_{LO}$ , for each polarization  $p$ . Four Balanced Photo-Detectors (BPD) convert the optical signals into electrical ones containing the I and Q components of the Intermediate Frequency (IF) signals.

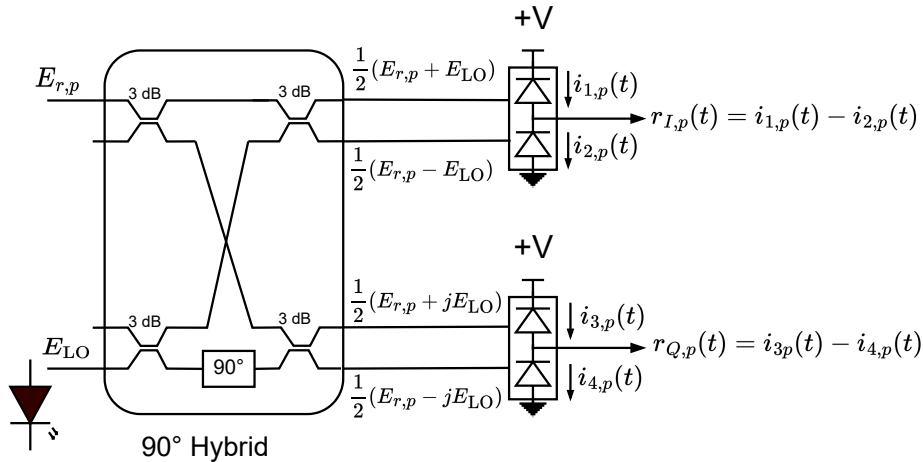


Figure 2.7 – Coherent Receiver with phase diversity using a  $90^\circ$  Hybrid.

The components I and Q are given by:

$$r_{I,p}(t) = \mathcal{R}\sqrt{P_{LO}(t)P_{r,p}(t)}\cos(\phi_{r,p}(t) - \phi_{LO}(t)), \quad (2.9)$$

$$r_{Q,p}(t) = \mathcal{R}\sqrt{P_{LO}(t)P_{r,p}(t)}\sin(\phi_{r,p}(t) - \phi_{LO}(t)), \quad (2.10)$$

where  $R$  is the responsivity of the photodiode,  $P_{LO}$  and  $P_{r,p}$  are the power of the LO and the power of the incoming signal in polarization  $p$ , respectively. The cosine and sinus contain the phase information of the incoming signal and the LO.

The DP receiver consists of two nested  $90^\circ$  Hybrid, one for each polarization, as shown in Fig. 2.8.

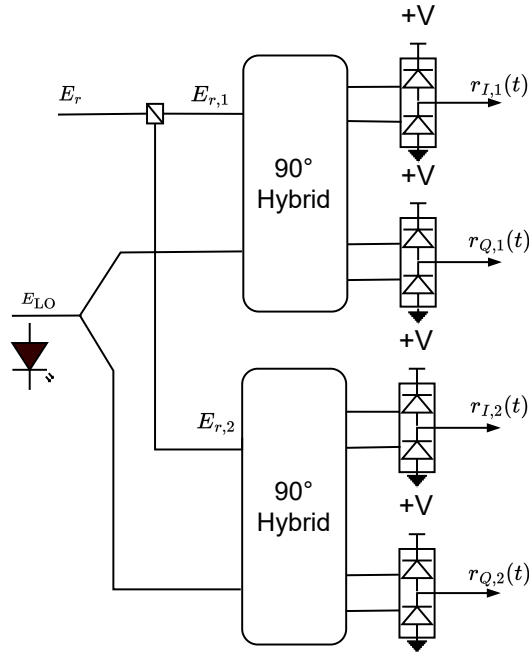


Figure 2.8 – Dual Polarization coherent receiver using two nested  $90^\circ$  Hybrids.

The resulting electrical signals are converted to digital signals through four Analog-to-Digital Converters (ADC) for further offline digital signal processing.

## 2.3 Optical Fibers

The principle of optical fibers is the total internal refraction of light inside the optical fiber core during light propagation. This phenomenon occurs due to the difference in refraction index between the core of the optical fiber and the cladding and the incident angle of light. The index refraction is an intrinsic property of a material that determines how much of the incident light is refracted by the medium [18].

Let  $n_1$  and  $n_2$  be the refractive index of the core and the cladding of a step-index optical fiber, respectively. The refractive index difference, denoted by  $\Delta$ , equals  $\Delta = \frac{n_1 - n_2}{n_1}$ . A parameter  $V$  determines the number of modes that propagate inside the fiber, which is defined as follows:

$$V = k_0 a \sqrt{n_1^2 - n_2^2}, \quad (2.11)$$

where  $k_0 = 2\pi/\lambda$  is the wave number,  $\lambda$  is the wavelength of light, and  $a$  is the core radius. For step-index fibers, single-mode propagation corresponds to  $V < 2.405$ .

### 2.3.1 Fiber Loss

When a signal travels through an optical fiber, the transmitted power  $P_0$  decreases over a distance  $z$ . This decay can be described by  $P(z) = P_0 e^{-\alpha z}$ , where  $\alpha$  is the fiber loss coefficient measured in decibels per kilometer (dB/km) and  $z$  is the distance in km [18].

The fiber loss coefficient is optical fiber material dependent, and it was characterized for different types of fiber along the different frequency bands used in telecommunications. Fig. 2.9 shows the fiber loss coefficients characterized in telecommunications bands: O-band (1260 nm - 1360 nm), E-band (1360 nm - 1460 nm), S-band (1460 nm - 1530 nm), and U-band (1625 nm - 1675 nm). EDFA is also shown in the C-band (1530 nm - 1565 nm).

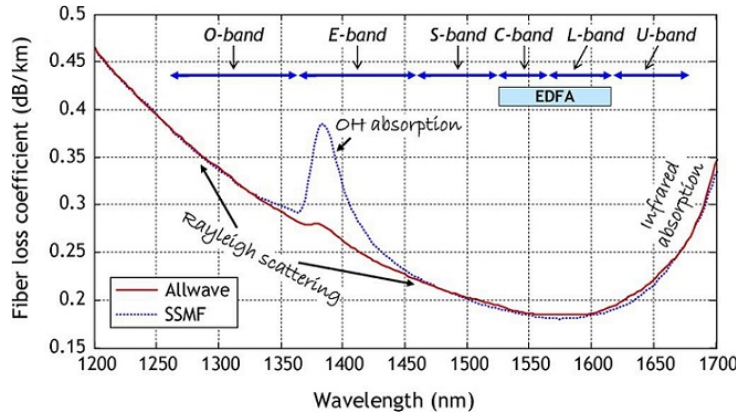


Figure 2.9 – Fiber loss coefficient and wavelength dependence [60] ©2010, IEEE.

A typical SSMF reaches its minimum value of  $< 0.2$  dB/km in around the C-band and L-band.

Sometimes, it is useful to convert the fiber attenuation coefficient from (dB/km) to a linear scale. Using the definition of the fiber loss, we can find the following relationship:

$$\alpha(\text{km}^{-1}) = \frac{\text{Ln}(10)}{10} \alpha(\text{dB/km}) \approx 0.23 \alpha(\text{dB/km}). \quad (2.12)$$

### 2.3.2 Chromatic Dispersion

The CD is a phenomenon that occurs due to the dispersion characteristics of the optical fiber. The refractive index  $n$  is actually frequency-dependent  $n(\omega)$  and causes different spectral components of the pulse to travel at different velocities  $c/n(\omega)$  along the propagation. This results in generating a pulse broadening [18].

The effects of dispersion are mathematically analyzed using the Taylor series expansion of the mode-propagation constant  $\beta$  about the center frequency  $\omega_0$  [18]:

$$\beta(\omega) = n(\omega)\frac{\omega}{c} = \beta_0 + \beta_1(\omega - \omega_0) + \frac{1}{2}\beta_2(\omega - \omega_1)^2 + \dots, \quad (2.13)$$

where  $\beta_m = \left. \frac{d^m \beta}{d\omega^m} \right|_{\omega=\omega_0}$  for  $m=0,1,2,\dots$

$\beta_1$  is the inverse of the group velocity  $v_g$ , and  $\beta_2$  [ps<sup>2</sup>/km] is the Group Velocity Dispersion (GVD) parameter and is responsible for pulse broadening. Commonly, a parameter  $D$  [ps/(nm · km)] called CD coefficient is widely used to represent the CD and is given by:

$$D = \frac{d\beta_1}{d\lambda} = \frac{d\beta_1}{d\omega} \frac{d\omega}{d\lambda} = -\frac{2\pi c}{\lambda^2} \beta_2. \quad (2.14)$$

An interesting property is that  $D$  depends on the fiber design. The wavelength for which  $D$  is zero is represented as  $\lambda_D$ . For instance,  $\lambda_D$  for an SSMF is around 1.31  $\mu\text{m}$ , while in 1.55  $\mu\text{m}$ ,  $D$  is around 17 ps/(nm · km). A special fiber with  $\lambda_D$  null in 1.55  $\mu\text{m}$  is the Dispersion Shifted Fiber (DSF). The interest of an DSF is the absence of CD, but other undesired transmission effects must be considered due to the zero CD in the C-band. [18], [67].

In the absence of nonlinear effects, the Frequency-Domain (FD) transfer function of the CD for a distance  $z$ , represented by  $G_{CD}(\omega)$  is given by [68],

$$G_{CD}(\omega) = \exp\left(-j\frac{D\lambda^2 z}{4\pi c}\omega^2\right), \quad (2.15)$$

where  $D$  is the CD parameter,  $\lambda$  is the central wavelength,  $z$  is the propagation distance, and  $\omega$  is the frequency component with respect to the central carrier frequency.

The sign of  $\beta_2$  defines two regimes: a normal-dispersion regime when  $\beta_2 > 0$  (or equivalently  $D < 0$ ) and an anomalous-dispersion regime when  $\beta_2 < 0$  (or equivalently  $D > 0$ ). In the normal-dispersion regime, the highest spectral components (or equivalently, lowest wavelengths) travel slower than the lower frequencies (or equivalently, higher wavelengths), while the anomalous-dispersion regime is the opposite.

### 2.3.3 Polarization Mode Dispersion

Single-mode fibers can support two degenerate modes that are polarized in two orthogonal directions [18]. When a lightwave is launched in these two orthogonal polarizations, the two components travel at different group velocities, provoking a delay between the two components, resulting in a pulse broadening. This phenomenon is referred to as PMD. The PMD occurs in optical fibers due to random birefringence caused by inherent imperfections in fiber manufacturing and stresses and vibrations from the external environment [55] that results in a mixing of the two orthogonal polarization modes.

Another effect of optical fiber birefringence is the random rotation/transformation of the States of Polarization (SOP) as the light propagates through the fiber. The SOP describes all the surface of the Poincaré sphere after a fiber length called beat length. The beat length is defined as [18]:

$$L_B = \frac{2\pi}{|\beta_x - \beta_y|} = \frac{\lambda}{B}, \quad (2.16)$$

where  $B = |n_x - n_y|$  is the modal birefringence, and  $n_x$  and  $n_y$  are the effective mode indices of the two orthogonal polarization states. Fig. 2.10 illustrates the evolution of SOP when the incident light is linearly polarized at  $45^\circ$  with respect to the slow and fast axis.

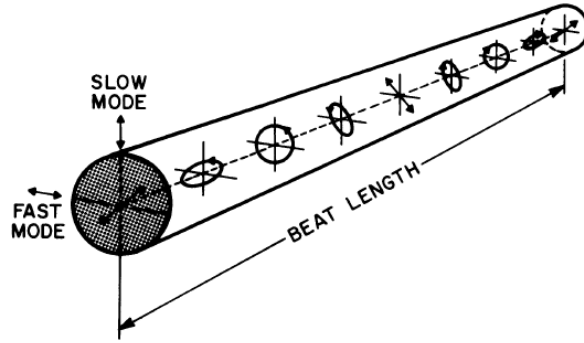


Figure 2.10 – Evolution of the state of polarization when the incident light is linearly polarized at  $45^\circ$  with respect to the slow and fast axis [18] ©2001, 1995 by ACADEMIC PRESS.

The modal birefringence causes pulse distortion due to a propagation delay between the two Principal States of Polarization (PSP). The PSP are two orthogonal polarization states at the input and output of the fiber to which the pulse broadening is minimal. One PSP corresponds to a minimum propagation time, and the other corresponds to a maximum propagation time [69]. In effect, the effective refractive index becomes different for each polarization state, resulting in different velocities. The delay of arrival time of these polarization states is known as Differential Group Delay (DGD) and results in a slow and fast axis. In areas of weak birefringence, the state of polarization (SOP) changes with minimal DGD. Conversely, in areas of strong birefringence, significant DGD is introduced, and the SOP is maintained over the beat length.

To model the PMD, the fiber span is divided into small sections with the first-order PMD<sup>4</sup> remaining constant in each section and with random rotations of the PSP between each section [24]. This approach is valid if we only consider the first-order PMD and neglect higher orders. Fig. 2.11 illustrates this modeling approach.

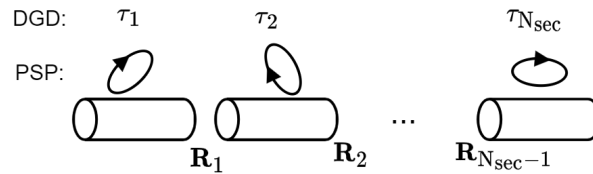


Figure 2.11 – Modeling of the PMD [24] ©2010, IEEE.

The rotation matrices  $\mathbf{R}_k \in \text{SU}(2)$  after the section  $k$ , where  $\text{SU}(2)$  is a type of special unitary matrix of degree 2, are the Jones representations of the Stokes vector of the Rotational matrix  $3 \times 3$ , and are in the form [71]:

4. First-order PMD refers to the DGD, i.e., considering small frequency ranges and therefore non-frequency dependence of the DGD [70].

$$\text{SU}(2) = \left\{ \begin{bmatrix} a & b \\ -b^* & a^* \end{bmatrix} : a, b \in \mathbb{C}, |a|^2 + |b|^2 = 1 \right\}. \quad (2.17)$$

The Stokes vectors, represented as  $s_1$ ,  $s_2$  and  $s_3$ , lead to all possible SOP of light, which are represented by the Poincaré sphere

In the more general case,  $\mathbf{R}_k$  is a combination of three  $2 \times 2$  matrices, one for each axis in the Poincaré sphere, illustrated in Fig. 2.12.

$$\mathbf{R}_k^{(1)}(\phi) = \begin{bmatrix} e^{-j\phi/2} & 0 \\ 0 & e^{j\phi/2} \end{bmatrix}, \quad \mathbf{R}_k^{(2)}(\psi) = \begin{bmatrix} \cos\psi & -j\sin\psi \\ -j\sin\psi & \cos\psi \end{bmatrix}, \quad \mathbf{R}_k^{(3)}(\theta) = \begin{bmatrix} \cos\theta & -\sin\theta \\ \sin\theta & \cos\theta \end{bmatrix}, \quad (2.18)$$

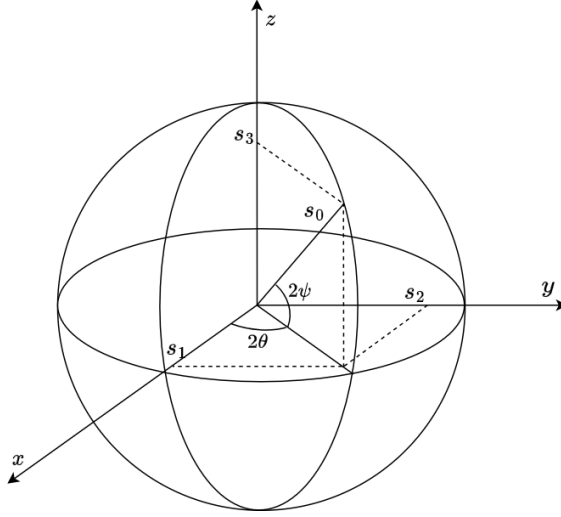


Figure 2.12 – Poincaré sphere.

where  $\mathbf{R}_k^{(1)}(\phi)$  represents a birefringent matrix that randomly change the phase difference  $\phi$  between the slow and fast axis of the PSP [69], [72],  $\mathbf{R}_k^{(2)}(\psi)$  represents the ellipticity  $2\psi$  variation [24], and  $\mathbf{R}_k^{(3)}(\theta)$  a rotation of the azimuth angle  $2\theta$  around the  $z$ -axis [24], [69].

The rotation matrices are not unique and can adopt different forms, according to considerations of the polarization of the PSP, the angle rotations, correlations between adjacent sections, or if the DGD is constant for all sections [73]:

- Considering a neglected phase difference between the slow and fast axis ( $\phi = 0$ ), the matrix  $\mathbf{R}_k(\theta, \psi)$  can be simplified as [24]:

$$\mathbf{R}_k(\theta, \psi) = \begin{bmatrix} \cos\theta\cos\psi - j\sin\theta\sin\psi & -\sin\theta\cos\psi + j\cos\theta\sin\psi \\ \sin\theta\cos\psi + j\cos\theta\sin\psi & \cos\theta\cos\psi + j\sin\theta\sin\psi \end{bmatrix}, \quad (2.19)$$

where  $2\theta$  and  $2\psi$  are the azimuth and ellipticity angles on the Poincaré sphere, respectively. The angle  $\theta$  is uniformly distributed over the range  $(-\pi/2, \pi/2)$  and  $\psi$  in  $(-\pi/4, \pi/4)$ .

- Considering only linear polarizations ( $2\psi = 0$  or  $\pm\pi$ ) [73], [74] the matrix  $\mathbf{R}$  becomes:

$$\mathbf{R}_k(\theta, \psi) = \begin{bmatrix} \cos\theta & e^{-j\psi}\sin\theta \\ -e^{j\psi}\sin\theta & \cos\theta \end{bmatrix}. \quad (2.20)$$

- From the previous case, considering  $\phi = 0$ , the matrix  $\mathbf{R}$  becomes real-valued [58], [75]:

$$\mathbf{R}_k(\theta) = \begin{bmatrix} \cos\theta & \sin\theta \\ -\sin\theta & \cos\theta \end{bmatrix}. \quad (2.21)$$

The transfer function of the PMD for a section  $k$  has the form [24], [58], [70], [73] :

$$H_{PMD}(\omega) = \mathbf{R}_k \mathbf{T}(\omega) \mathbf{R}_k^H, \quad (2.22)$$

where  $\mathbf{T}(\omega)$  is a diagonal matrix accounting for the DGD in the form:

$$\mathbf{T}(\omega) = \begin{bmatrix} e^{\frac{j\omega\tau}{2}} & 0 \\ 0 & e^{-\frac{j\omega\tau}{2}} \end{bmatrix}, \quad (2.23)$$

and  $\tau$  follows a Maxwellian distribution [24] with probability density function:

$$f_T(\tau) = \begin{cases} \frac{8}{\pi^2 \Delta\tau} \left(\frac{2\tau}{\Delta\tau}\right)^2 e^{-\left(\frac{2\tau}{\Delta\tau}\right)^2/\pi} & ; \tau \geq 0, \\ 0 & ; \tau < 0, \end{cases} \quad (2.24)$$

where  $\Delta\tau$  is the PMD and is the mean DGD (ps). For instance, for a PMD coefficient  $\delta = 0.05\text{ps}/\sqrt{\text{km}}$ , a section  $\Delta z = 1\text{km}$ , and  $\Delta\tau = \delta\sqrt{\Delta z}$ , the DGD follows the Maxwellian distribution showed in Fig. 2.13:

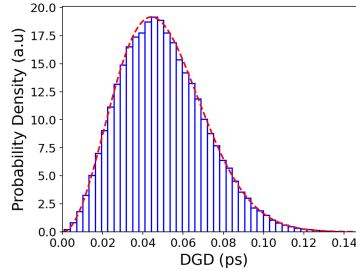


Figure 2.13 – Maxwellian distribution of the DGD.

The maximum PMD value is  $\sim 3.3 \times \text{PMD}$ . An optical fiber link with a PMD of 12-ps can generate maximum values of  $\sim 36$ -ps. At 10-Gbps with IM/DD technology, the maximum PMD is  $\sim 12$ -ps, corresponding to a maximum allowable DGD of  $\sim 36$ -ps.

Another effect of PMD is the temporal variation of PSP of a fiber link. This impairment is a second-order effect of PMD.

### 2.3.4 Nonlinear Impairments

The intensity dependence of the optical fiber refractive index originates nonlinear refractions [18], [21], [55]. This phenomenon is called the Kerr effect and is considered the principal source

of nonlinear impairments in optical communications [76].

The Kerr effect induces both intra-channel and inter-channel nonlinearities [55], [60], as shown in Fig. 2.14. In turn, the intra-channel and inter-channel nonlinear effects are divided based on whether they are produced by signal-noise or signal-signal interactions.

Signal-noise interactions generate Nonlinear Phase Noise (NLPN), while signal-signal interactions generate nonlinear effects due to interactions between frequency components produced inside or outside the channel. Among the intrachannel nonlinearities due to signal-signal interactions, we find the Self-Phase Modulation (SPM), the intrachannel Cross-Phase Modulation (IXPM), and the intrachannel Four-Wave Mixing (IFWM). For interchannel nonlinear effects, we can find the Cross-Phase Modulation (XPM), the Four Wave Mixing (FWM), and the Cross-Polarization Modulation (XPolM) [18], [21], [60].

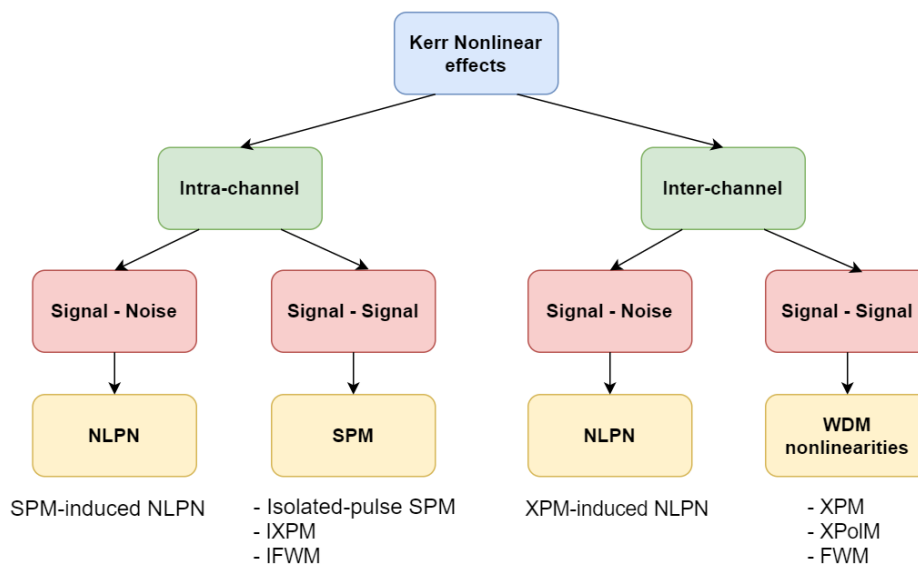


Figure 2.14 – Decomposition of Kerr Nonlinear effects [60]. NLPN: Nonlinear Phase Noise, SPM: Self-Phase Modulation, XPM: Cross-Phase Modulation, FWM: Four-Wave Mixing, IXPM: Intrachannel XPM, IFWM: Intrachannel FWM, XPolM: Cross-Polarization Modulation.

### Self-Phase Modulation

This phenomenon occurs due to nonlinear refractions that affect a signal due to its own intensity [18]. To reflect this intensity dependency, the refractive index is expressed as:

$$\tilde{n}(\omega, I) = n(\omega) + n_2 I, \quad (2.25)$$

where  $n(\omega)$  is a linear frequency-dependence term,  $I$  is the optical intensity inside the fiber given by  $I = \frac{P}{A_{eff}}$ , being  $P$  the optical power and  $A_{eff}$  the effective core area, and  $n_2$  is the nonlinear index coefficient. The latter is related to a parameter called nonlinear coefficient  $\gamma$  in the form:

$$\gamma = \frac{n_2 \omega_0}{c A_{eff}}, \quad (2.26)$$

where  $\omega_0$  is the carrier frequency,  $c$  is the speed of light in vacuum, and  $A_{eff}$  is known as the effective core area. Typical values for a SSMF in  $\lambda = 1.55\mu\text{m}$  are  $n_2 \approx 2.7 \cdot 10^{-20}\text{m}^2/\text{W}$ ,  $A_{eff} \approx 80\mu\text{m}^2$ , resulting in  $\gamma \approx 1.4\text{W}^{-1} \cdot \text{km}^{-1}$ .

The phase shift of the signal, due to the SPM, changes according to:

$$\phi = \tilde{n}k_0L = (n + n_2I)k_0L, \quad (2.27)$$

where  $k_0 = 2\pi/\lambda$  is the wave number,  $L$  is the fiber length, and the SPM term is due to the nonlinear phase-shift  $\phi_{NL} = n_2k_0LI$ .

The SPM causes a spectral broadening of the optical pulse, yielding a symmetric spectrum with new frequency components (multi-peaks). The nonlinear phase shift, which is proportional to the optical pulse intensity, induces an instantaneous frequency shift from the central frequency across the pulse. This effect is known as frequency chirp. However, the pulse shape and central frequency remain unchanged, preserving the pulse velocity as well [18].

An important point to mention is the behavior of pulses when CD and SPM are combined. In the anomalous dispersion regime ( $\beta_2 < 0$ ), it was shown that the combination of CD and SPM leads to a pulse temporal compression [18], as the high frequencies created at the end of the pulses are speedier than the low frequencies generated at the beginning of the pulses. In very particular conditions, when there is a balance between the effects of SPM and CD, the pulses propagate without any deformation both in the temporal and spectral domain. These very particular pulses are named ‘‘Solitons’’, a solitary wave propagating without any deformation despite the CD.

### SPM-induced Nonlinear Phase noise

In the presence of Amplified Spontaneous Emission (ASE) noise, and nor CD neither PMD, the SPM results in NLPN. The phase shift due to the NLPN for a system of  $N$  uniformly spaced identical amplifiers is given by [55]:

$$\phi_{NL} = \gamma L_{eff} \sum_{i=1}^N |E + \sum_{k=1}^i n_k|^2, \quad (2.28)$$

where  $\gamma$  is the nonlinearity coefficient,  $L_{eff} = \frac{1-e^{-\alpha L}}{\alpha}$  is the effective length of each span, and  $n_k$  are i.i.d normal distributed random variables representing the ASE noise contribution for each amplifier.

We can observe this effect in the received constellation. Due to the NLPN, the received complex symbols with more amplitude experience more significant phase shifts than those with lower amplitude. This results in received symbols adopting a spiral-shaped constellation, as shown in Fig. 2.15b in the case of a 16QAM constellation. Fig. 2.15a shows the same constellation considering only the accumulated ASE noise.

### Cross-Phase Modulation

When two different wavelengths propagate through the same optical fiber, they can interfere with each other. If two electromagnetic waves,  $E_1$  and  $E_2$ , at frequencies  $\omega_1$  and  $\omega_2$ , traverse the same optical fiber, the nonlinear refraction  $n(\omega_1)$  depends on the intensity of both  $E_1$  and  $E_2$ , and vice versa. This phenomenon is known as XPM.

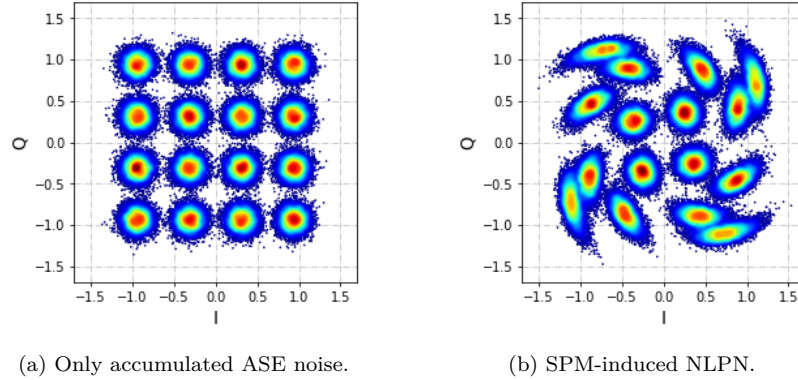


Figure 2.15 – 16QAM received constellation after  $20 \times 100$  km with full loss compensation using EDFA.

$E_2$  has an effect on  $E_1$ , resulting in a nonlinear phase rotation  $\phi_{NL_1}$  similar to the one caused by SPM. XPM is always accompanied by SPM, as demonstrated in (2.29) and (2.30).

$$\phi_{NL_1} = n_2 k_{0,1} L (I_1 + 2I_2), \quad (2.29)$$

$$\phi_{NL_2} = n_2 k_{0,2} L (I_2 + 2I_1), \quad (2.30)$$

where  $k_{0,1}$  and  $k_{0,2}$  are the wave number corresponding to  $E_1$  and  $E_2$ , respectively, and  $I_1$  and  $I_2$  are the optical intensity of  $E_1$  and  $E_2$ . Also,  $E_1$  and  $E_2$  are assumed to be both linearly polarized along the same axis. The first terms are due to SPM. Notice that the XPM does not involve an energy exchange between the two waves and that the respective phase of the interfering signal does not play any role in the XPM phenomenon.

When the interaction of two electromagnetic waves that originate nonlinear refraction is produced inside the same channel, for instance, two neighboring pulses or spectral components, this phenomenon is called IXPM.

On the other hand, when the XPM is originated due to a coupling between two polarization components of the same optical wave, the phase shifts are given by:

$$\phi_{NL_1} = n_2 k_0 L \left( I_1 + \frac{2}{3} I_2 \right), \quad (2.31)$$

$$\phi_{NL_2} = n_2 k_0 L \left( I_2 + \frac{2}{3} I_1 \right), \quad (2.32)$$

where  $E_1$  and  $E_2$  are the two orthogonal polarizations of the same optical wave,  $k_0 = \frac{2\pi}{\lambda}$ ,  $\lambda$  is the central wavelength, and the factor  $\frac{2}{3}$  is characteristics of these kind of coupling.

In the presence of ASE noise, the XPM originates NLPN [55].

The XPM, like the SPM, is responsible for generating new frequency components within the pulse spectrum, resulting in asymmetric spectral broadening, a change in the central frequency (unlike SPM, which does not alter the pulse frequency), and modification of the pulse velocity. XPM produces a timing jitter, named “collision jitter”, which is due to the frequency-shifted spectral components of the pulse because of the temporal overlapping with neighboring pulses [55], [77]. These spectral components travel at different velocities, producing the timing

jitter. When the channel spacing is reduced, or the CD is lower, the walk-off between interfering pulses is longer, and XPM becomes more critical. XPM can significantly limit WDM systems using low-dispersion optical fibers, e.g. ITU-T G653 or G655 fibers[18], [21].

### Four-Wave Mixing

Another phenomenon originated by nonlinear interactions is the FWM. This phenomenon arises when three optical frequencies  $f_1$ ,  $f_2$  and  $f_3$  generates a new frequency  $f_4$  [78] in the form:

$$f_4 = f_1 + f_2 - f_3. \quad (2.33)$$

Unlike the SPM and the XPM, the FWM involves a transfer of energy for the generation of component  $f_4$ . Interestingly, this process necessitates a phase matching to be carried out. The phase matching condition refers to specific frequencies and refractive index that could rarely occur [18]. However, when the spacing between the three frequencies reduces or when the CD is low, the possibility of provoking a FWM increases. For this reason, this effect is particularly sensitive in WDM transmissions [78]. Nevertheless, it could also happen in single-channel transmissions when multiple pulses overlap each other (due to a temporal broadening coming from the CD), leading to interference between three spectral components that are temporally synchronous. This phenomenon, called IFWM [55], generates pulse amplitude fluctuations and creation of “ghost” pulses in the “zeros” of the binary sequence.

FWM is less susceptible for large CD values, being an SSMF at  $1.55\mu\text{m}$  more robust against the FWM occurrence, but much more susceptible if multiple channels are closer to each other[79].

### Cross-Polarization Modulation

Finally, another phenomenon that could affect the quality of a WDM transmission is the XPolM. Specifically, because of the nonlinearity, the SOP of a DP optical field change degrading the Degree of Polarization (DOP) of the signal [80]. If this phenomenon is not carefully managed, the PMD compensators, which rely on slowly varying polarization changes, could fail, degrading the overall transmission quality [81].

In the context of Kerr nonlinearity in long-haul coherent optical systems, the CD reduces the impact of nonlinear impairments, particularly in the multi-channel or WDM transmission system configuration [23], [24]. At 1550 nm, the CD is highly positive, generating that different channels move at different velocities, decreasing the walk-off between two pulses of different wavelengths or the time during which the two pulses are colliding. This results in a reduction of the inter-channel nonlinearity [21]. For this reason, in multi-channel coherent systems, it is preferable to compensate for the CD electronically at the receiver with DSP techniques than periodically compensating the CD after each fiber span [68].

### 2.3.5 Optical Amplifiers

Due to the fiber loss, the signal amplitude needs to be regularly amplified. Current configurations use EDFA in C and L bands, which have the lowest attenuation among the other bands of the optical spectrum. These EDFA introduce an in-band white Gaussian noise that degrades the signal, especially in higher-order modulation formats that are very sensitive to noise.

The amplification process takes place by a process called Stimulated Emission, which refers to a random multiplication factor of the incident signal photon. When an incident photon collides with an Erbium ion, it emits a photon with the same coherent properties, and this process is successively repeated, leading to signal amplification. At the same time, another process takes place, which is called Spontaneous Emission. The latter refers to when an Erbium ion passes from an excited state to a lower energy state, emitting a photon. The spontaneous emission is random and is responsible for generating noise within the amplifier. The whole process, stimulated emission and spontaneous emission, are summarized under the term ASE.

The ASE noise degrades the SNR and the quantity that quantifies this degradation is the amplifier Noise Figure (NF)  $F_n = 2\eta_{sp}(G - 1)/G \approx 2\eta_{sp}$ , where  $G$  is the gain and considering  $G \gg 1$ , and  $\eta_{sp}$  is the spontaneous emission noise factor [60], [82]. The typical NF in EDFA ranges from 4dB to 6 dB.

The noise produced by ASE is additive and can be considered Gaussian. Therefore, it is an AWGN source with power spectral density, per polarization, equals to:

$$N_{ASE} = (G - 1)h\nu\eta_{sp}, \quad (2.34)$$

where  $h = 6.626 \cdot 10^{-34} \text{J}\cdot\text{Hz}^{-1}$  is the Plank constant and  $\nu$  is the optical frequency.

## 2.4 Nonlinear Schrödinger Equation

The propagation of the optical signal through the optical fiber is described by the vectorial NLSE [24], [73], [83]. This equation has the form:

$$\frac{\partial \mathbf{E}}{\partial z} = \left[ \left( -\frac{\alpha}{2} - \frac{j\beta_2}{2} \frac{\partial^2}{\partial t^2} \right) \mathbf{I} - \beta_1 \frac{\partial}{\partial t} \right] \mathbf{E} + j\gamma \left[ |\mathbf{E}|^2 \mathbf{I} - \frac{1}{3} (\mathbf{E}^H \boldsymbol{\sigma}_3 \mathbf{E}) \boldsymbol{\sigma}_3 \right] \mathbf{E}, \quad (2.35)$$

where

- $\mathbf{E} = [E_1, E_2]^T$  is the Jones vector of the electromagnetic field,
- $\alpha$  is the attenuation coefficient,
- $\beta_2$  accounts for the GVD,
- $\mathbf{I}$  is the  $2 \times 2$  matrix identity.
- $\beta_1$  is a  $2 \times 2$  matrix that represents the PMD. For a section  $k$ ,  $\beta_{1,k} = \mathbf{R}_k \left( \frac{\tau}{2} \boldsymbol{\sigma}_1 \right) \mathbf{R}_k^H$ , where  $\mathbf{R}_k$  are the rotation matrices per each axis defined in (2.18),  $\tau$  is the DGD, and  $\boldsymbol{\sigma}_1 = \begin{bmatrix} 1 & 0 \\ 0 & -1 \end{bmatrix}$ .
- $\gamma$  is the nonlinear parameter,
- $\boldsymbol{\sigma}_3$  is the Pauli spin matrix  $\begin{bmatrix} 0 & -j \\ j & 0 \end{bmatrix}$ .

We neglected the dispersion slope term  $\beta_3$ , and we consider that  $\alpha$  and  $\beta_2$  are constant over the frequency band.

Equation (2.35) can be decomposed in two terms. The first term represents the linear part of the equation and is represented by the linear operator  $\hat{\mathbf{D}}$ , and the second term represents the nonlinear part and is represented by the nonlinear operator  $\hat{\mathbf{N}}$ , giving as a result:

$$\frac{\partial \mathbf{E}}{\partial z} = (\hat{\mathbf{D}} + \hat{\mathbf{N}})\mathbf{E}, \quad (2.36a)$$

$$\hat{\mathbf{D}} = \left( -\frac{\alpha}{2} - \frac{j\beta_2}{2} \frac{\partial^2}{\partial t^2} \right) \mathbf{I} - \beta_1 \frac{\partial}{\partial t}, \quad (2.36b)$$

$$\hat{\mathbf{N}} = j\gamma \left[ |\mathbf{E}|^2 \mathbf{I} - \frac{1}{3} (\mathbf{E}^H \boldsymbol{\sigma}_3 \mathbf{E}) \boldsymbol{\sigma}_3 \right]. \quad (2.36c)$$

Simplified versions of the NLSE are obtained under certain considerations:

- Assuming constant linear birefringence, the NLSE is reduced to a pair of equations with a factor  $\frac{2}{3}$  due to the nonlinear coupling between the two polarizations, called coupled NLSE (CNLSE) [72], [73], [83], [84].

$$\frac{\partial E_1}{\partial z} = \left( -\frac{\alpha}{2} - \beta_1 \frac{\partial}{\partial t} - \frac{j\beta_2}{2} \frac{\partial^2}{\partial t^2} \right) E_1 + j\gamma \left( |E_1|^2 + \frac{2}{3} |E_2|^2 \right) E_1, \quad (2.37)$$

$$\frac{\partial E_2}{\partial z} = \left( -\frac{\alpha}{2} - \beta_1 \frac{\partial}{\partial t} - \frac{j\beta_2}{2} \frac{\partial^2}{\partial t^2} \right) E_2 + j\gamma \left( |E_2|^2 + \frac{2}{3} |E_1|^2 \right) E_2. \quad (2.38)$$

- Considering the rapid changes in birefringence in a length scale much smaller than the one of nonlinearity, the nonlinearity is averaged over all possible polarization states in the Poincaré sphere. The CNLSE, thus, reduces to the Manakov-PMD equation [83], [85].

$$\frac{\partial \mathbf{E}}{\partial z} = \left( -\frac{\alpha}{2} - \beta_1 \frac{\partial}{\partial t} - \frac{j\beta_2}{2} \frac{\partial^2}{\partial t^2} \right) \mathbf{E} + j\frac{8}{9}\gamma |\mathbf{E}|^2 \mathbf{E}. \quad (2.39)$$

However, let us indicate that the original term was provided without the attenuation coefficient  $\alpha$  and with a term called nonlinear PMD, which is usually neglected.

- Also, it is common that the PMD be neglected; in that case, this is referred to as the Manakov equation.

$$\frac{\partial \mathbf{E}}{\partial z} = \left( -\frac{\alpha}{2} - \frac{j\beta_2}{2} \frac{\partial^2}{\partial t^2} \right) \mathbf{E} + j\frac{8}{9}\gamma |\mathbf{E}|^2 \mathbf{E}. \quad (2.40)$$

## 2.5 Split-Step Fourier Method

To solve the NLSE, an iterative method called the Split-Step Fourier Method (SSFM) is commonly employed. This technique is based on the assumption that the dispersive and nonlinear effects act independently. When this is not true in reality, this approximation becomes valid for small distances  $h$  for which the accumulated CD is low.[18].

Specifically, when setting  $\hat{\mathbf{D}} = 0$  and applying only the nonlinear operator  $\hat{\mathbf{N}}$ , and then  $\hat{\mathbf{N}} = 0$  and applying only the linear operator  $\hat{\mathbf{D}}$ , we obtain [18], [24]:

$$\mathbf{E}(z+h, t) \approx \exp(h\hat{\mathbf{D}})\exp(h\hat{\mathbf{N}})\mathbf{E}(z, t). \quad (2.41)$$

Fig. 2.16 illustrates the SSFM considering a step size  $h$  and span length  $L$ .

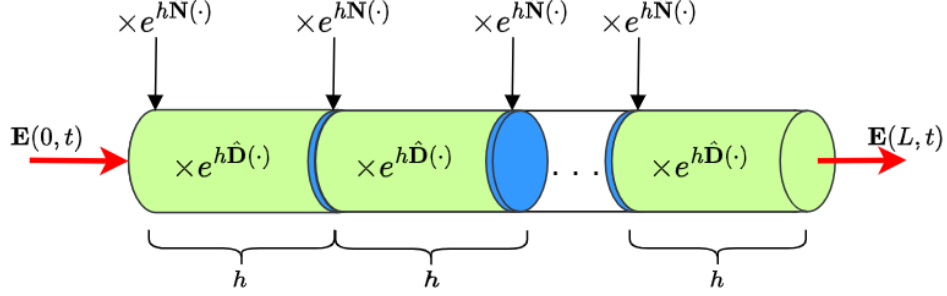


Figure 2.16 – Asymmetric SSFM.

Due to the temporal derivatives, it is easier to compute the linear part in the frequency domain since  $\partial/\partial t$  becomes  $j\omega$  when using the Fourier transform. Therefore, the linear operator  $\hat{\mathbf{D}}$  in frequency domain becomes:

$$\hat{\mathbf{D}}(\omega) = \left( -\frac{\alpha}{2} + \frac{j\beta_2\omega^2}{2} \right) \mathbf{I} - j\omega\beta_1. \quad (2.42)$$

And the term  $\exp(h\hat{\mathbf{D}})$  simplifies to:

$$\exp(h\hat{\mathbf{D}}(\omega)) = \exp \left[ \left( -\frac{\alpha}{2} + \frac{j\beta_2\omega^2}{2} \right) h\mathbf{I} \right] \exp(-j\omega h\beta_1), \quad (2.43)$$

where the last term  $\exp(-j\omega h\beta_1) = \exp(-\mathbf{R}j\frac{\omega\tau}{2}\boldsymbol{\sigma}_1\mathbf{R}^H)$ , where  $\boldsymbol{\sigma}_1 = \begin{bmatrix} 1 & 0 \\ 0 & -1 \end{bmatrix}$ . Since  $\mathbf{R}$  is invertible, i.e.  $\mathbf{R} \cdot \mathbf{R}^H = \mathbf{R}^H \cdot \mathbf{R} = \mathbf{I}$ ,

$$\exp(-j\omega h\beta_1) = \mathbf{R} \exp \left( -j\frac{\omega\tau}{2}\boldsymbol{\sigma}_1 \right) \mathbf{R}^H \quad (2.44)$$

The reader could notice that (2.44) is equivalent to (2.22).

Finally, the linear operator  $\hat{\mathbf{D}}(\omega)$  becomes:

$$\exp(h\hat{\mathbf{D}}(\omega)) = \mathbf{R} \exp \left[ \left( -\frac{\alpha}{2} + \frac{j\beta_2\omega^2}{2} \right) h\mathbf{I} \right] \exp \left( -j\frac{\omega\tau}{2}\boldsymbol{\sigma}_1 \right) \mathbf{R}^H. \quad (2.45)$$

On the other hand, the nonlinear operator  $\hat{\mathbf{N}}$  is computed in the time domain. When using the CNLSE,  $\hat{\mathbf{N}}$  becomes:

$$\hat{\mathbf{N}}(E_j) = j\gamma \left( |E_j|^2 + \frac{2}{3}|E_{3-j}|^2 \right); j = 1, 2. \quad (2.46)$$

Similarly, when using the Manakov-PMD equation,  $\hat{\mathbf{N}}$  has the form:

$$\hat{\mathbf{N}} = j\frac{8}{9}\gamma|\mathbf{E}|^2. \quad (2.47)$$

The SSFM in (2.41) is known as the asymmetric version. The algorithm 1 details the procedure.

---

**Algorithm 1** Asymmetric Split-Step Fourier Method
 

---

- 1:  $z \leftarrow 0$
  - 2: **while**  $z \leq L_{span} - h$  **do**
  - 3:   **Nonlinear Step:**
  - 4:    $\mathbf{E}(z, t) \leftarrow \exp(h\hat{\mathbf{N}}(z))\{\mathbf{E}(z, t)\}$  ▷ Nonlinear operator
  - 5:   **Linear Step:**
  - 6:   Compute  $\mathbf{E}(z, w) \leftarrow \mathcal{F}\{\mathbf{E}(z, t)\}$  ▷ Fourier transform
  - 7:    $\mathbf{E}(z + h, w) \leftarrow \exp(h\hat{\mathbf{D}}(w))\{\mathbf{E}(z, w)\}$  ▷ Linear operator
  - 8:    $\mathbf{E}(z + h, t) \leftarrow \mathcal{F}^{-1}\{\mathbf{E}(z + h, w)\}$  ▷ Inverse Fourier Transform
  - 9:   Update  $z \leftarrow z + h$
  - 10: **end while**
  - 11: **Return**  $\mathbf{E}(z, t)$
- 

Since this version leads to less accuracy, it is commonly employed a symmetric version of the SSFM that improves the precision. The symmetric version of the SSFM has the form:

$$\mathbf{E}(z + h, t) \approx \exp\left(\frac{h}{2}\hat{\mathbf{D}}\right) \exp\left(\int_z^{z+h} \hat{\mathbf{N}}dz\right) \exp\left(\frac{h}{2}\hat{\mathbf{D}}\right) \mathbf{E}(z, t), \quad (2.48)$$

where the linear operator  $\hat{\mathbf{D}}$  is applied for half the step size  $h/2$ , followed by the nonlinear operator  $\hat{\mathbf{N}}$  on the middle of the step ( $z + \frac{h}{2}$ ) for the complete step size  $h$ , and finally the linear operator  $\hat{\mathbf{D}}$  for the remaining half step size  $h/2$ .

Fig. 2.17 illustrates the symmetric SSFM for a step size  $h$  and span length  $L$ .

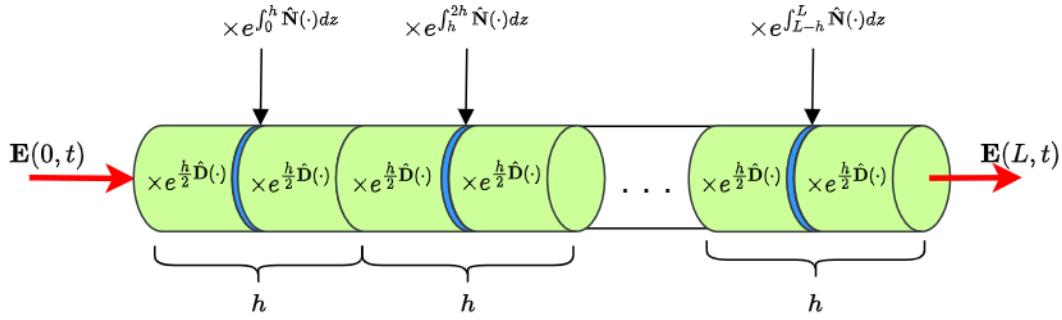


Figure 2.17 – Symmetric SSFM.

While the computation of  $\hat{\mathbf{D}}$  in the frequency domain according to (2.45) is straightforward, the nonlinear operator  $\hat{\mathbf{N}}$  necessitates operating an integral. To simplify this operation, a common approach is to approximate the integral using the trapezoidal rule:

$$\exp\left(\int_z^{z+h} \hat{\mathbf{N}}dz\right) = \exp\left(\frac{h}{2}(\hat{\mathbf{N}}(z+h) + \hat{\mathbf{N}}(z))\right). \quad (2.49)$$

Nevertheless, the main concern is the necessity of prior knowledge in the middle of the step of  $\hat{\mathbf{N}}(z+h)$ . Therefore, to simulate the signal propagation using the symmetric SSFM is usually employed an iterative method called iterative symmetric SSFM (IS-SSFM). The idea is to initially set  $\hat{\mathbf{N}}(z+h) = \hat{\mathbf{N}}(z)$  and through an iterative process estimate  $\hat{\mathbf{N}}(z+h)$ . The algorithm 2 details this procedure.

---

**Algorithm 2** Iterative Symmetric Split-Step Fourier Method
 

---

```

1:  $z \leftarrow 0$ 
2:  $N_{iter} \leftarrow 2$  ▷ number of iterations per step
3: while  $z \leq L_{span} - h$  do
4:    $i \leftarrow 1$  ▷ Init iteration
5:    $\hat{\mathbf{N}}(z+h) \leftarrow \hat{\mathbf{N}}(z)$  ▷ Initialize  $\hat{\mathbf{N}}(z+h)$ . Used in line 13 when i=1
6:    $\mathbf{E}(z_0, t) \leftarrow \mathbf{E}(z, t)$  ▷ Save initial  $\mathbf{E}$  to repeat at each iteration
7:   while  $i \leq N_{iter}$  do
8:     Linear Step:
9:     Compute  $\mathbf{E}(z, w) \leftarrow \mathcal{F}\{\mathbf{E}(z_0, t)\}$  ▷ Fourier Transform
10:     $\mathbf{E}(z + \frac{h}{2}, w) \leftarrow \exp(\frac{h}{2}\hat{\mathbf{D}}(\omega))\{\mathbf{E}(z, w)\}$  ▷ Linear operator
11:     $\mathbf{E}(z + \frac{h}{2}, t) \leftarrow \mathcal{F}^{-1}\{\mathbf{E}(z + \frac{h}{2}, w)\}$  ▷ Inverse Fourier Transform
12:    Nonlinear Step:
13:     $\mathbf{E}(z + \frac{h}{2}, t) \leftarrow \exp(\frac{h}{2}(\hat{\mathbf{N}}(z+h) + \hat{\mathbf{N}}(z)))\{\mathbf{E}(z + \frac{h}{2}, t)\}$  ▷ Nonlinear operator using trapezoidal rule
14:    Linear Step:
15:    Compute  $\mathbf{E}(z + \frac{h}{2}, w) \leftarrow \mathcal{F}\{\mathbf{E}(z + \frac{h}{2}, t)\}$  ▷ Fourier Transform
16:     $\mathbf{E}(z + h, w) \leftarrow \exp(\frac{h}{2}\hat{\mathbf{D}}(\omega))\{\mathbf{E}(z + \frac{h}{2}, w)\}$  ▷ Linear operator
17:     $\mathbf{E}(z + h, t) \leftarrow \mathcal{F}^{-1}\{\mathbf{E}(z + h, w)\}$  ▷ Inverse Fourier Transform
18:    Update  $\hat{\mathbf{N}}(z+h)$  with  $\mathbf{E}(z+h, t)$ 
19:    Update  $i \leftarrow i + 1$ 
20:  end while
21:  Update  $z \leftarrow z + h$ 
22: end while
23: Return  $\mathbf{E}(z, t)$ 
    
```

---

This method is computationally expensive, but the advantage is that we can increase the step size  $h$  without losing accuracy [18]. On the other hand, if  $h$  is sufficiently small, the integral could be replaced by simply  $h\hat{\mathbf{N}}(z + \frac{h}{2})$ , assuming that  $\hat{\mathbf{N}}(z+h) \approx \hat{\mathbf{N}}(z + \frac{h}{2}) \approx \hat{\mathbf{N}}(z)$ . This version is called non-iterative symmetric SSFM (NS-SSFM), detailed in the algorithm 3.

Finally, to increase the accuracy of the asymmetric SSFM, we can use  $h_{eff}$  instead of  $h$  in the nonlinear part [24], where  $h_{eff}$  takes into account the loss after  $h$ , and is given by:

$$h_{eff} = \frac{1 - \exp(-\alpha h)}{\alpha}. \quad (2.50)$$

**Algorithm 3** Non-iterative Symmetric Split-Step Fourier Method

---

```

1:  $z \leftarrow 0$ 
2: while  $z \leq L_{span} - h$  do
3:   Linear Step:
4:   Compute  $\mathbf{E}(z, w) \leftarrow \mathcal{F}\{\mathbf{E}(z, t)\}$  ▷ Fourier Transform
5:    $\mathbf{E}(z + \frac{h}{2}, w) \leftarrow \exp(\frac{h}{2}\hat{\mathbf{D}}(\omega))\{\mathbf{E}(z, w)\}$  ▷ Linear operator
6:    $\mathbf{E}(z + \frac{h}{2}, t) \leftarrow \mathcal{F}^{-1}\{\mathbf{E}(z + \frac{h}{2}, w)\}$  ▷ Inverse Fourier Transform
7:   Nonlinear Step:
8:    $\mathbf{E}(z + \frac{h}{2}, t) \leftarrow \exp(h(\hat{\mathbf{N}}(z + \frac{h}{2})))\{\mathbf{E}(z + \frac{h}{2}, t)\}$  ▷ Nonlinear operator using trapezoidal rule
9:   Linear Step:
10:  Compute  $\mathbf{E}(z + \frac{h}{2}, w) \leftarrow \mathcal{F}\{\mathbf{E}(z + \frac{h}{2}, t)\}$  ▷ Fourier Transform
11:   $\mathbf{E}(z + h, w) \leftarrow \exp(\frac{h}{2}\hat{\mathbf{D}}(\omega))\{\mathbf{E}(z + \frac{h}{2}, w)\}$  ▷ Linear operator
12:   $\mathbf{E}(z + h, t) \leftarrow \mathcal{F}^{-1}\{\mathbf{E}(z + h, w)\}$  ▷ Inverse Fourier Transform
13:  Update  $z \leftarrow z + h$ 
14: end while
15: Return  $\mathbf{E}(z, t)$ 

```

---

## 2.6 Summary

This chapter has covered the basis of optical communication systems with a focus on coherent technology that is suitable for long haul and high data bit rate optical transmissions. We have presented the three classical blocks that compose an optical coherent link: the dual-polarization transmitter, the optical channel, and the dual-polarization coherent receiver.

The dual-polarization transmitter must encode and transmit as much information as possible, exploiting the states of the light wave (amplitude, phase, states of polarization). A laser source with narrow linewidth, thus a lower laser phase noise, is required to achieve higher performances. The binary information is encoded into two orthogonal components (in-phase and quadrature) modulating in amplitude and in phase the optical signal. A dual-polarization IQ-modulator permits to encode the information in two orthogonal polarization states in the same bandwidth doubling the spectral efficiency.

On the other extreme, a dual-polarization coherent receiver permits the recovery of the phase information of the optical signal using a local oscillator with similar characteristics to the laser source, two 90° hybrid circuits, and four balanced photodetectors.

The transmission medium, composed of several optical fiber spans, induces several impairments to the optical signal. Notably, the signal undergoes attenuation, chromatic dispersion (CD), polarization mode dispersion (PMD), and nonlinear impairments (NLI). The attenuation is compensated using optical amplifiers. The CD and PMD generate both pulse broadening due to spectral components propagating at different velocities. In the case of PMD, the pulse broadening is due to an arrival time delay due to the different propagation velocities of the two orthogonal polarization states at the input of the fiber. The nonlinear impairments originate due to nonlinear refraction because of high optical intensity. Among the different effects provoked by nonlinear impairments, we have shown notably the nonlinear phase noise due to the interaction with amplified spontaneous emission (ASE) noise, self-phase modulation (SPM), cross-phase

modulation (XPM), and four-wave mixing (FWM) in intra and inter-channel configurations.

The equation that describes the signal propagation through the optical fiber is the Nonlinear Schrödinger Equation (NLSE) and adopts different forms according to the assumptions of the impairments affecting the signal. Since there is no direct solution for this equation in its more complete form, it is generally solved using the Split-Step Fourier (SSFM) method. The SSFM iteratively solves the NLSE by mathematically decoupling the fiber span in small sections when we can consider that the CD, PMD, and NLI act independently of each other.



# NONLINEAR IMPAIRMENTS IN COHERENT OPTICAL SYSTEMS: NUMERICAL AND EXPERIMENTAL INVESTIGATIONS

---

The previous chapter covered the classical coherent system, in which the dual-polarization coherent receiver permits the recovery of the optical signal phase via the LO, the two  $90^\circ$  hybrid circuits, and the four balanced photo-detectors. The next component of the coherent receiver is a set of DSP algorithms implemented in modern transceivers to reconstruct the transmitted signal and recover the transmitted bits fully.

In this chapter, we show the effects of fiber nonlinearity using numerical and experimental setups. In Section 3.1, we describe in detail the set of DSP algorithms employed in signal equalization using static and adaptive algorithms, as well as the algorithms for carrier phase recovery and frequency offset compensation. Section 3.2 introduces two algorithms for nonlinearity compensation commonly employed in the literature: the Digital Backpropagation (DBP) and the Volterra Nonlinear Equalizer (VNLE). In Section 3.3, we present the experimental setup that simulates a complete modern transceiver, and the multiple spans of SSMF permit us to study the effects of optical fiber impairments, particularly uncompensated nonlinearity. We also employ the algorithms for nonlinearity compensation described in Section 3.2 in the experimental testbed. Finally, Section 3.4 summarizes this chapter.

## 3.1 Digital Signal Processing and Numerical Investigations of Nonlinear Effects

The numerical setup reproduces the Single Channel (SC) Dual-Polarization (DP) transmission system depicted in Fig. 2.1. Specifically, the DP transmitter, the optical channel, and the DP coherent receiver were simulated using MATLAB first and Python lastly. The developed programs coded in MATLAB were helpful for understanding the signal propagation via the SSFM implementation and the capabilities of a classical offline DSP. Later, we implemented and optimized those programs using Python for at least two reasons: i) Python is an open-source language with a large community of contributors that facilitates the programming task, and ii) when we implemented NN, we used Tensorflow and PyTorch, which are two ML frameworks in Python. Therefore, having all the tools used in the same environment seemed easier.

For the numerical setup, we consider an ECL emitting an optical carrier at the wavelength  $\lambda_c=1552\text{nm}$ . We use an oversampling factor of 8 samples per symbol (SpS) to simulate the

digital-to-analog conversion in forward propagation. To simulate the signal’s propagation, we numerically solve the NLSE (or the Manakov-PMD equation) using the split-step Fourier method (SSFM). We consider a  $14 \times 100$ km of SSMF with parameters: attenuation coefficient  $\alpha = 0.2$ dB/km, CD coefficient  $D = 17$ ps/(nm · km), DGD =  $0.05$ ps/ $\sqrt{\text{km}}$ , and nonlinear coefficient  $\gamma = 1.4$ W<sup>-1</sup> · km<sup>-1</sup>. Each span loss is fully compensated at the end of the span using EDFA with NF = 4.5dB. The pulse shapers at the transmitter and received side are RRC filters with roll-off factor  $\rho=0.1$  and with filter length equal to 40 taps delayed the symbol duration  $T_s$ . The ECL and the LO are considered identical with laser linewidth 100 kHz, and with a Carrier Frequency Offset (CFO) equals 200 MHz.

To simulate the optical channel, we consider linear impairments such as fiber loss, CD and PMD, as well as nonlinear effects like SPM, SPM-induced NLPN, and XPolM, all of these resulting from NLI. We ignored the effects of IFWM since the phase matching condition for new frequencies generation is rarely satisfied unless special considerations are made [18].

The choice of the SSFM version depends on the desired level of accuracy and the available computational resources. We performed a non-exhaustive comparison of the SSFM versions. Specifically, we compared the Iterative-Symmetric SSFM (IS-SSFM) using two iterations/step and step-size  $h = 4$  km, the Non-iterative-Symmetric SSFM (NS-SSFM) using the Coupled Non-linear Schrödinger equation (CNLSE) and the Manakov-PMD approximation with step-size  $h = 1$  km, and the asymmetric-SSFM also using the CNLSE and the Manakov-PMD approximation with step-size  $h = 1$  km. To make the comparison, we used the classical DSP receiver described in Section 3.1, and we calculated the BER. The results are shown in Fig. 3.1.

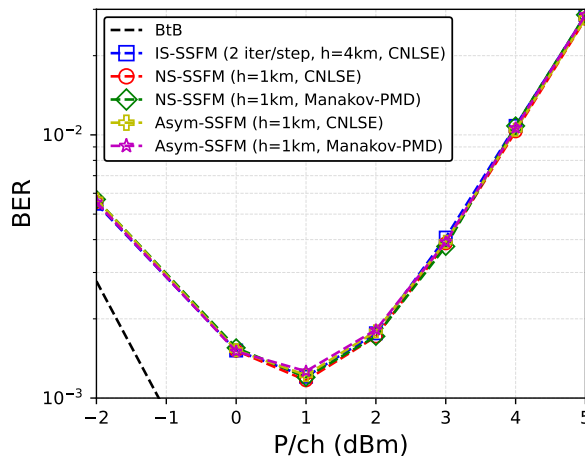


Figure 3.1 – Comparison of SSFM versions for a DP-16QAM 32 GBaud over 14x100 km of single-mode fiber.

We can observe very close results for all explored approaches. Nevertheless, the IS-SSFM processes 25 steps per span (StPS) while the other methods process 100 StPS. Under these configurations, the IS-SSFM 25 StPS, and two iterations per step, takes half of the time than the NS-SSFM 100 StPS, but the same time that the asymmetric SSFM 100 StPS.

When using the same number of steps per span, the IS-SSFM is  $\times N_{iter}$  more expensive in computational resources than the NS-SSFM versions. For instance, the IS-SSFM, with only two iterations per step, takes double the time than the NS-SSFM. Also, the asymmetric versions take half the time compared to the symmetric versions. The difference between the CNLSE

and the Manakov-PMD approximation is just one additional multiplication per symbol in the nonlinear operator. Therefore, in our study, unless another indication, we used the asymmetric SSFM approach to simulate the optical signal propagation.

Fig. 3.2 illustrates a typical set of DSP algorithms implemented in modern transceivers for a single channel.

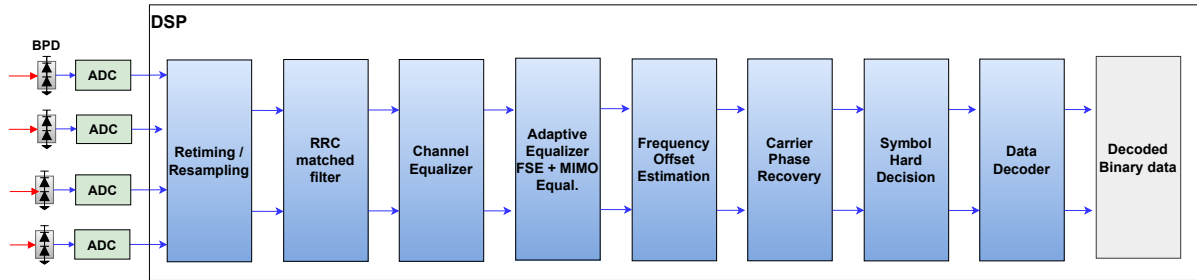


Figure 3.2 – DSP algorithms used in the DP Coherent Receiver. BPD: balanced photodiodes, ADC: analog-to-digital converter, RRC: root-raised cosine, FSE: Fractionally-spaced equalizer, MIMO: multiple-input-multiple-output.

The DSP performs interpolation and timing recovery, anti-aliasing filtering (in our work, we used a matched filter RRC), channel equalization, and adaptive equalization ( $2 \times 2$  Multiple-Input-Multiple-Output (MIMO) FIR filters) to recover the complex data of both polarizations, frequency offset estimation, carrier phase recovery, and decoding [74], [86].

We must mention that other possible configurations are proposed in the vast literature on this matter. For instance, some authors indicate that the RRC matched filter is unnecessary as long as the FIR filters for channel equalization or adaptive equalization play the role of a matched filter [74], [86], [87]. More indeed, the adaptive equalizer could also compensate static linear impairments such as the CD in addition to dynamic linear impairments [75].

The optimization of the DSP structure and the employed algorithms is out of the scope of the present work. Despite that, the reader must consider that combining different algorithms could significantly change the interpretation of determined results. Notably, the remaining nonlinear effects compensation could also be partially performed by a carrier phase recovery algorithm. We detailed more about this observation in chapter 4.

We assume that the ADCs work with an oversampling factor of at least 2 to respect the Nyquist sampling theorem and prevent aliasing. Depending on this oversampling factor, it may be necessary to perform resampling with prior retiming. A typical algorithm uses linear interpolation functions and maximizes the squared modulus of the interpolated signal [88].

### 3.1.1 Channel Equalization

The goal of an equalizer is to recover the transmitted symbols. In the case of optical channel equalizers, these could be divided into linear and nonlinear equalizers. A linear equalizer usually performs only CD equalization since this is a static (time-invariant) impairment. On the other hand, the PMD is a dynamic effect (time-variant), and commonly, traditional DSP separates both tasks. Nonlinear equalizers are necessary when working in a nonlinear regime where these effects disturb the signal phase significantly.

A linear equalizer performing CD equalization is generally implemented in the FD via a zero-forcing Frequency-Domain Equalizer (FDE). The zero-forcing FDE is performed by using an all-band pass filter  $H_{CD}(\omega)$  equal to  $1/G_{CD}(\omega)$ ,

$$H_{CD}(\omega) = \exp\left(j\frac{D\lambda^2z}{4\pi c}\omega^2\right). \quad (3.1)$$

The FDE is performed using the Discrete Fourier Transform (DFT) and Inverse Discrete Fourier Transform (IDFT) via Fast Fourier Transform (FFT) and Inverse Fast Fourier Transform (IFFT) algorithms, respectively. For real-time implementations, where the number of samples is vast, the DFT and IDFT are sequentially processed in small blocks. The DFT corresponds to a circular convolution in the time domain [89]. As we require linear convolutions, we can employ the overlap-and-save or the overlap-add methods. In the overlap-and-save method, the small blocks overlap previous  $M - 1$  samples, while in the overlap-add method, each block is appended with  $M - 1$  zeros. Afterward, the overlapped samples are discarded, and the sequence reconstructed [90], [91].

In [68], it was proposed a Temporal-Domain (TD) approach based on the inverse Fourier transform of the CD transfer function, given by:

$$h_{CD}(t) = \sqrt{\frac{c}{jD\lambda^2z}} \exp\left(\frac{j\pi c}{D\lambda^2z}t^2\right). \quad (3.2)$$

Similar to the RRC filter, the impulse response for the CD is infinite and non-causal. To make it causal and finite,  $h_{CD}(t)$  is truncated to  $N$  taps ( $N$  odd).

Let  $\mathbf{h} = [a_0, a_1, \dots, a_{N-1}]$  be the vector containing the  $N$  FIR filter taps  $a_k$ . In [68], an upper bound of  $N$  was derived and given by:

$$N = 2 \left\lfloor \frac{|D|\lambda^2z}{2cT^2} \right\rfloor + 1, \quad (3.3)$$

where  $T$  is the sampling period, and  $\lfloor x \rfloor$  states for the greatest integer less than or equal to  $x$ .

The coefficients  $a_k$  are calculated as follows:

$$a_k = \sqrt{\frac{jcT^2}{D\lambda^2z}} \exp\left(-\frac{jc\pi T^2}{D\lambda^2z}k^2\right), \quad -\left\lfloor \frac{N}{2} \right\rfloor \leq k \leq \left\lfloor \frac{N}{2} \right\rfloor. \quad (3.4)$$

Alternatively, in [92] was also proposed a FIR filter based on the Least-Square (LS) of the error between the ideal CD transfer function and the transfer function of the proposed FIR filter. This method offers the advantage of achieving even better performance with fewer FIR taps. The key lies in considering a limited bandwidth beyond the pulse shaper, effectively reducing the required taps. The resulting FIR filter is calculated as follows:

$$\mathbf{h} = (\mathbf{Q} + \epsilon \mathbf{I}_N)^{-1} \mathbf{d}, \quad (3.5)$$

where  $\epsilon$  is a penalty factor  $\sim 10^{-14}$ ,  $\mathbf{I}_N$  is a  $N \times N$  Identity matrix, and  $\mathbf{Q}$  is a Hermitian Toeplitz matrix of  $N \times N$  and equals:

$$Q(n, m) = \begin{cases} \frac{\Omega_2 - \Omega_1}{2\pi} & n = m, \\ \frac{e^{-j(-n+m)\Omega_1} - e^{-j(-n+m)\Omega_2}}{2j\pi(-n+m)} & n \neq m, \end{cases} \quad (3.6)$$

where  $\omega T \in [\Omega_1, \Omega_2]$ , and  $0 \leq n \leq N - 1$ ,  $0 \leq m \leq N - 1$ .

On the other hand,  $\mathbf{d}$  is given by:

$$\mathbf{d}(n) = \frac{e^{-j\left(\frac{n^2}{4K} + \frac{3\pi}{4}\right)}}{4\sqrt{\pi K}} \left( \operatorname{erf}\left(\frac{e^{j\frac{3\pi}{4}}(2K\pi - n)}{2\sqrt{K}}\right) + \operatorname{erf}\left(\frac{e^{j\frac{3\pi}{4}}(2K\pi + n)}{2\sqrt{K}}\right) \right), \quad -\frac{N-1}{2} \leq n \leq \frac{N-1}{2}, \quad (3.7)$$

where  $K = \frac{D\lambda^2 z}{2\pi c T^2}$ .

In Fig. 3.3, we show the impulse response for the ideal FIR filters, the FIR of [68], and the FIR of [92] for a single span of 100km corresponding to  $N = 55$  taps according to (3.3).

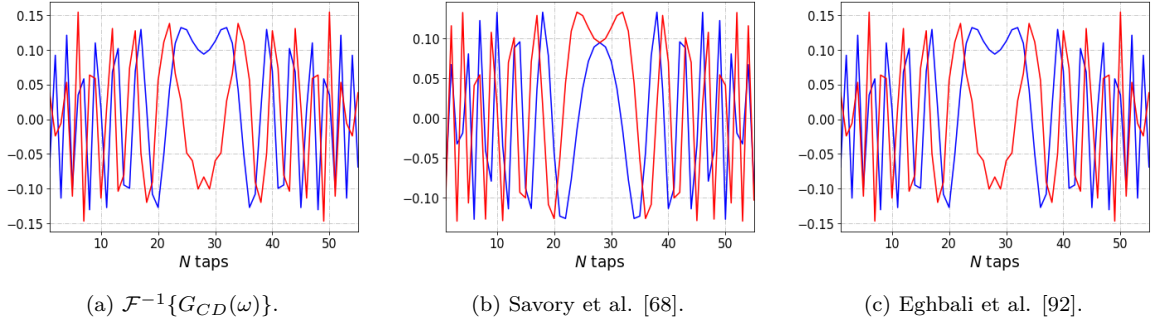


Figure 3.3 – Impulse response of CD equalization FIR filters for an accumulated dispersion  $D = 1700\text{ps/nm}$ , symbol rate  $R_s = 32\text{GBaud}$ , corresponding to  $N = 55$  taps. The blue lines are for the real part and the red lines are- for the imaginary part.

## Performance Comparison

We compared the methods described in Section 3.1.1: FDE and Time-Domain Equalizer (TDE): the FIR using the IFFT of the CD transfer function, the FIR filter in [68], and the FIR filter in [92] with  $N = 3133$  taps using (3.3). We calculated the BER obtained for different input channel powers. The results are shown in Fig. 3.4.

In this example, we noticed similar results for all methods at the end of the DSP chain. In [92], the authors stated that the LS-CD FIR filter performs better than the FIR filter of [68]. This statement could not be shown here, and the reason is the subsequent DSP algorithms, especially the adaptive filters, that could compensate for the residual CD.

To validate the superiority of the LS-CD FIR filter of [92] over the FIR filter of [68], it is helpful to change to a simplified scenario of a single polarization only accounting for the CD and the NLI and the CD compensation and the carrier phase recovery. The simplified DSP is shown in Fig. 3.5.

The BER using the FDE, the FIR using the IFFT of the CD transfer function, the FIR filter in [68], and the FIR filter in [92], with  $N = 559$  according to (3.3), are shown in Fig. 3.6.

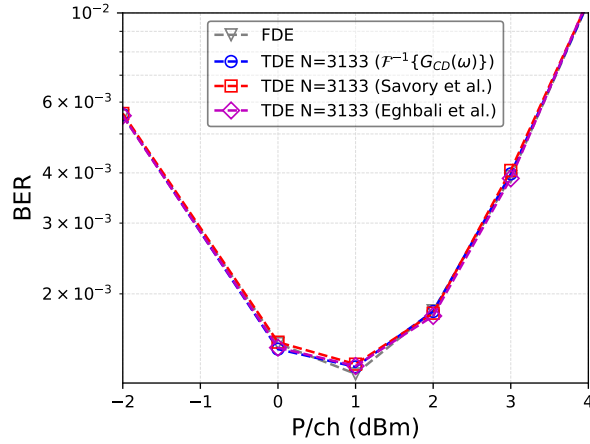


Figure 3.4 – BER vs. P/ch using different CD equalizers (FD and TD) for a DP-16QAM 32 Gbaud over 14x100 km of SSMF. N is the number of FIR filter taps.

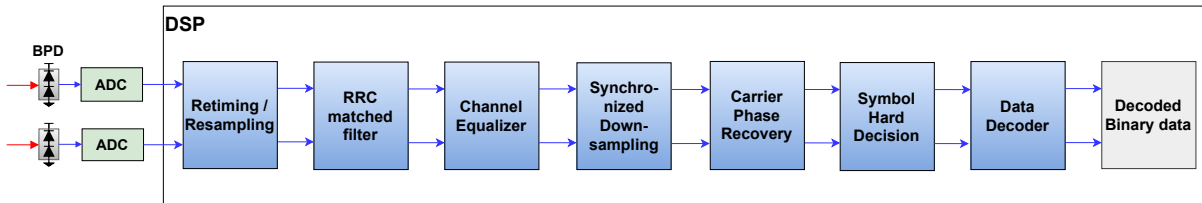


Figure 3.5 – Simplified DSP for a single polarization transmission and only accounting for the CD and the NLI.

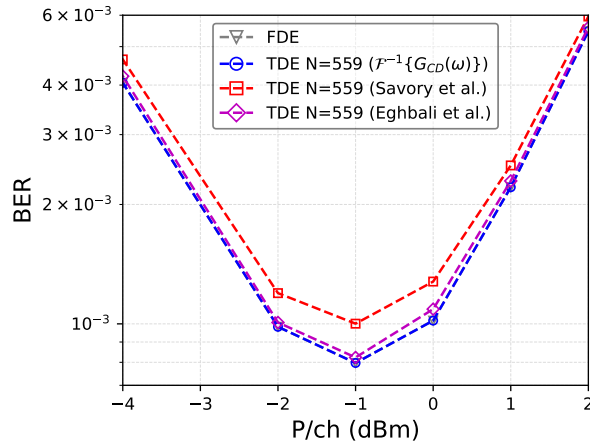


Figure 3.6 – BER vs. P/ch using different CD equalizers (FD and TD) for a SP-16QAM 32 Gbaud over 10x100 km of SSMF. N is the number of FIR filter taps.

Here, we show that using a FDE and the LS-CD FIR filter in [92] provide similar results, and certainly, we observe that the FIR filter in [68] is slightly less performant.

### Computational Complexity Comparison

A common metric to measure the Computational Complexity (CC) of an equalizer is the number of real multiplications per symbol (RMpS). This part shows the CC for the FDE and the TDE. We assume that the amount of CD was previously estimated. Therefore, its estimation does not take part in the calculations.

The FDE is based on the FFT and IFFT computation. In our Python implementations, we implemented the pair FFT/IFFT using numpy, and to speed up the processing time, we used the package pyFFTW. Both numpy and pyFFTW, are based on the Cooley-Tukey radix-2 algorithm [93] whose CC for an N-FFT block in RMpS is given by:

$$CC_{Cooley-Tukey} = 2N_{FFT} \log_2 N_{FFT}. \quad (3.8)$$

The CD-FDE requires one FFT to transform the TD to the FD, one complex multiplication with the inverse CD transfer function for CD compensation, and one IFFT to transform the signal to the TD, making a total number of RMpS given by:

$$CC_{FDE} = 4(\log_2 N_{FFT} + 1)K, \quad (3.9)$$

where  $K$  is the oversampling factor.

The overlap-save method permits efficient performance of the DFT/IDFT with a small overhead due to the overlapping part. The CC in RMpS for a  $N_{FFT}$  block length is given by:

$$CC_{FDE} = \frac{4N_{FFT}(\log_2 N_{FFT} + 1)K}{N_{FFT} - N_{CD} + 1}, \quad (3.10)$$

where  $N_{CD}$  is the overlapping part related to the CD impulse duration given by,

$$N_{CD} = \left\lceil \frac{\tau_{CD}K}{T_s} \right\rceil, \quad (3.11)$$

being  $\tau_{CD}$  the CD impulse duration and  $T_s$  the symbol interval.  $\tau_{CD}$  is estimated through  $\tau_{CD} = \frac{c}{f_c^2} |D_{acc}| B_{eff}$ , where  $c$  is the speed of light,  $f_c$  is the carrier frequency,  $D_{acc}$  is the accumulated dispersion, and  $B_{eff}$  is the effective bandwidth. By considering the RRC pulse shaper at the transmission,  $B_{eff} \approx (1 + \rho)R_s$ , where  $\rho$  is the RRC roll-off factor, and  $R_s$  is the symbol rate. In this work, we did not implement this technique since we are working with an offline DSP and we process the entire number of samples, so the real CC in an online DSP with linear filtering at once could be slightly higher due to the overlapping required part [90].

On the other hand, the TDE, using an FIR filter composed of  $N_{taps}$ , requires a total of  $N_{taps}$  complex multiplications per sample, corresponding to 4 real multiplications. Therefore the number of RMpS is given by,

$$CC_{TDE} = 4N_{taps}K. \quad (3.12)$$

The choice between the FDE and TDE will depend on the FFT points  $N_{FFT}$  for the FDE and the number of taps  $N_{taps}$  required to compensate the CD using the TDE. In general, the FDE is less complex than the TDE [90]. For instance, consider the example case of an accumulated CD of  $17 \times 14 \times 100$  ps/nm for a 32GBaud transmission at 1552 nm, an oversampling factor

$K = 2$ , and  $N_{FFT}$  equals to  $10^6$  samples. The reader could verify that the FDE requires only  $\sim 167$  RMPs while the TDE with  $N_{taps}=783$  requires 6264 RMPs, i.e., the FDE is  $\sim 37$  times faster than the TDE.

The interest of using a TDE is principally for short distances. Let us take only  $2 \times 10$  km of fiber of a transmission with the same characteristics as the previous example. In this case, the FDE is independent of the accumulated dispersion leading to the same  $\sim 167$  RMPs, while the TDE for an FIR filter of length 11 requires 88 RMPs.

### 3.1.2 Adaptive Equalization

The rotation of SOP and the PMD are time-variant effects that must be compensated dynamically. The idea is to estimate the Jones matrix of the channel, which is frequency-dependent due to the PMD. Indeed, in contrast to the CD, which is a static effect, this matrix evolves in time due to the rapid variation of the PSP [68]. Therefore, the method must be adaptive.

A classical blind technique uses a set of four FIR filters. Due to the arrangement of the four FIR filters, it takes the form of a  $2 \times 2$  MIMO filter [74], [75], which is illustrated in Fig. 3.7.

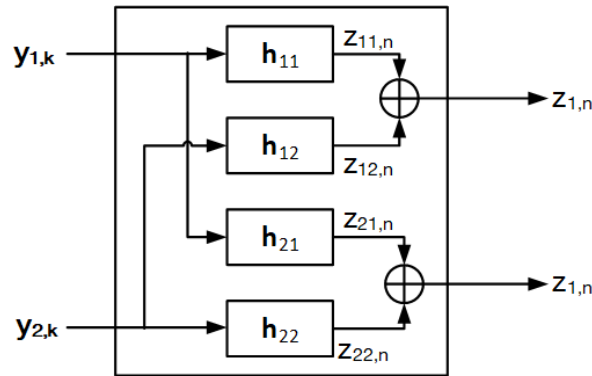


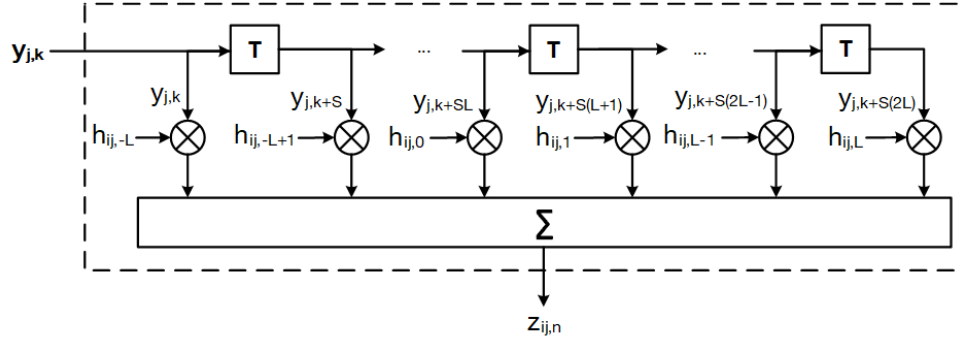
Figure 3.7 –  $2 \times 2$  MIMO equalizer with Fractionally-Spaced Equalizer (FSE).

Notice that the input is oversampled, and subsequent algorithms process data at the symbol rate. To undersample the signal at 1 sample/symbol, we used an Fractionally-Spaced Equalizer (FSE) [75] along with the  $2 \times 2$  MIMO filter.

The input at instant  $k$  are the two components  $\mathbf{r}_{1,k}$  and  $\mathbf{y}_{2,k}$  with an oversampling factor  $S$  (sampling period  $T = T_s/S$ ). The FIR filters  $\mathbf{h}_{ij}$  of length  $N = 2L + 1$  are initialized with zeros. Moreover, the central taps of  $\mathbf{h}_{11}$  and  $\mathbf{h}_{22}$  are set to one for faster convergence.

Each FIR filter is a tapped-delay filter where the delay  $T$  is the sampling period. The FIR filter performs a linear combination followed by a decimation in a factor  $S$  (i.e., the output at instant  $n$ ,  $z_{ij,n}$  is at the symbol rate) [75], [94]. Fig. 3.8 illustrates the tapped-delay filter FSE.

The recovered symbols  $z_{1,n}$  and  $z_{2,n}$  are then used to update the coefficients of the FIR filters  $\mathbf{h}_{ij}$ . This update takes advantage of the knowledge of the constellations. For example, in the case of QPSK, all the transmitted symbols have a constant modulus. Techniques such as the Constant Modulus Algorithm (CMA) have proven to be efficient in such cases.


 Figure 3.8 – FSE performs by FIR  $\mathbf{h}_{ij}$ .

### Constant Modulus Algorithm

Initially proposed by [95], this adaptive algorithm is based on the MSE minimization criteria of the signal error of both polarizations. Specifically, for a QPSK constellation with normalized symbol amplitude  $R = 1$  (see Fig. 3.9a), the objective is to minimize the MSE of the errors  $\varepsilon_{1,n} = R - |z_{1,n}|^2$  and  $\varepsilon_{2,n} = R - |z_{2,n}|^2$ . This minimization is usually achieved through a stochastic gradient descent algorithm. More precisely, let us denote the MSE of the errors as  $\langle \varepsilon_{1,n}^2 \rangle$  and  $\langle \varepsilon_{2,n}^2 \rangle$ , respectively. The FIR taps updating is performed using:

$$\frac{d\langle \varepsilon_{1,n}^2 \rangle}{d\mathbf{h}_{11}} = 0; \quad \frac{d\langle \varepsilon_{1,n}^2 \rangle}{d\mathbf{h}_{12}} = 0; \quad \frac{d\langle \varepsilon_{2,n}^2 \rangle}{d\mathbf{h}_{21}} = 0; \quad \frac{d\langle \varepsilon_{2,n}^2 \rangle}{d\mathbf{h}_{22}} = 0. \quad (3.13)$$

Replacing the gradients with their instantaneous values results in the following:

$$\mathbf{h}_{11} = \mathbf{h}_{11} + \mu \varepsilon_{1,n} z_{1,n} \mathbf{y}_{1,k}^*, \quad (3.14a)$$

$$\mathbf{h}_{12} = \mathbf{h}_{12} + \mu \varepsilon_{1,n} z_{1,n} \mathbf{y}_{2,k}^*, \quad (3.14b)$$

$$\mathbf{h}_{21} = \mathbf{h}_{21} + \mu \varepsilon_{2,n} z_{2,n} \mathbf{y}_{1,k}^*, \quad (3.14c)$$

$$\mathbf{h}_{22} = \mathbf{h}_{22} + \mu \varepsilon_{2,n} z_{2,n} \mathbf{y}_{2,k}^*, \quad (3.14d)$$

where  $\mathbf{y}_{1,k}^*$  and  $\mathbf{y}_{2,k}^*$  are the complex conjugate of  $\mathbf{y}_{1,k}$  and  $\mathbf{y}_{2,k}$ , respectively, and  $\mu$  is a convergence parameter.

In the case of multilevel constellations, additional algorithms are needed to get better performances. For instance, a decision-directed least mean squared (DD-LMS) [68], a recursive least squares (RLS), and Radius-Directed Equalizer (RDE) [58]. In this study, we have chosen the RDE, but similar results can also be obtained using the DD-LMS and the RLS [58].

### Radius Directed Equalization

Since the CMA is adapted to a constant amplitude, a better approach consists of considering multiple amplitudes (radii), which is more adapted to QAM signals. This approach is known as RDE and could be seen as a generalization of the CMA. Fig. 3.9b shows the case of a 16QAM constellation with three possible radii.

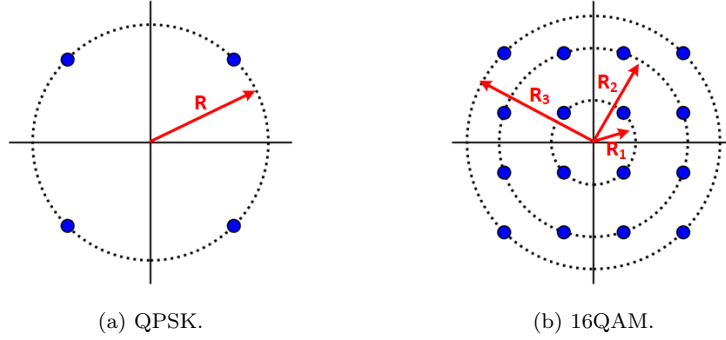


Figure 3.9 – Radii employed in adaptive equalization using CMA/RDE.

Its implementation must consider the various possible radii of the constellation. Algorithm 4 illustrates the case of a 16QAM constellation.

---

**Algorithm 4** RDE for 16QAM constellations

---

```

1: if  $|z_{l,n}| < (R_1 + R_2)/2$  then
2:    $R \leftarrow R_1$ 
3: else
4:   if  $|z_{l,n}| < (R_2 + R_3)/2$  then
5:      $R \leftarrow R_2$ 
6:   else
7:      $R \leftarrow R_3$ 
8:   end if
9: end if

```

---

For a normalize constellation ( $E_s = 1$ ) the radii for 16QAM and 64QAM are the following:

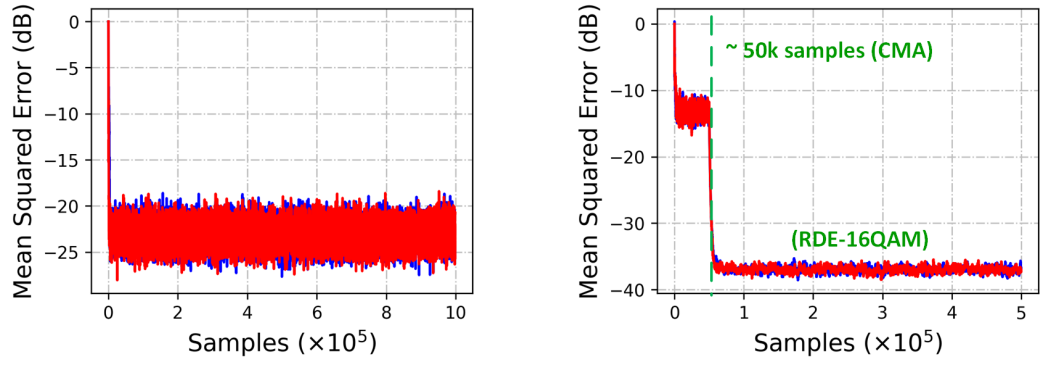
$$16\text{QAM} : R_1^2 = 0.2, R_2^2 = 1, R_3^2 = 1.8,$$

$$64\text{QAM} : R_1^2 = \frac{1}{21}, R_2^2 = \frac{5}{21}, R_3^2 = \frac{9}{21}, R_4^2 = \frac{13}{21}, R_5^2 = \frac{17}{21}, R_6^2 = \frac{25}{21}, R_7^2 = \frac{29}{21}, R_8^2 = \frac{37}{21}, R_9^2 = \frac{49}{21}.$$

The RDE requires properly initializing the FIR filter taps of the  $2 \times 2$  MIMO equalizer to avoid being trapped in a local minima. Commonly, the CMA is used as a prior algorithm to initialize the FIR taps. For higher-order modulation formats, we can also employ intermediate stages to achieve faster convergence and get better results. For instance, a 64QAM could achieve faster convergence using an intermediate RDE for 16QAM after the CMA [96].

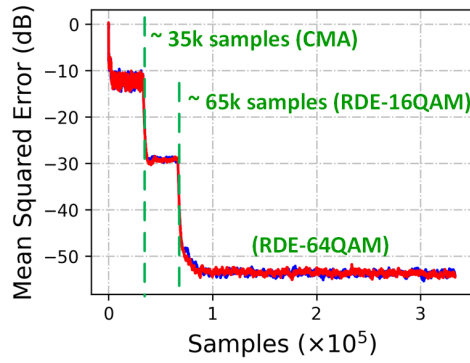
To compensate for the PMD and the SOP rotation, we used the  $2 \times 2$  MIMO equalizer combined with an FSE for optimal undersampling described in Section 3.1.2.

In Fig. 3.10, we show the MSE of the equalized output for a DP-QPSK, DP-16QAM, and DP-64QAM, and Fig. 3.11 shows the equalized outputs at the steady state for each case.



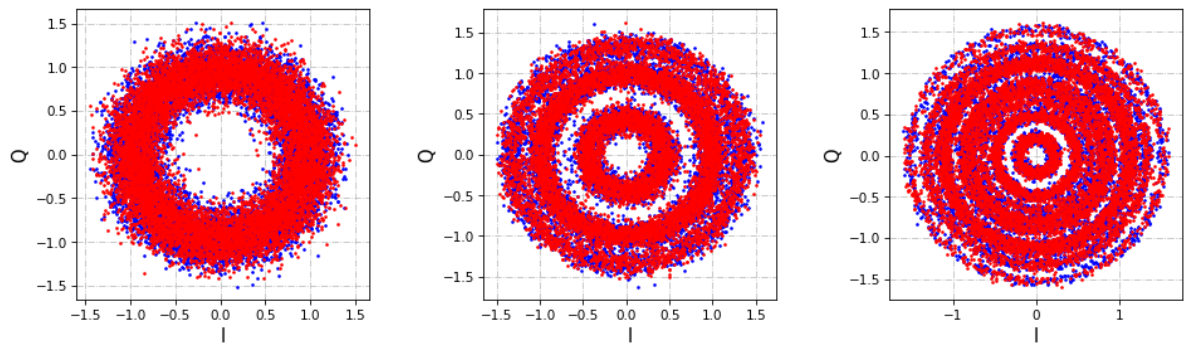
(a) DP-QPSK 64 GBaud, 30x100 km, P/ch = 3 dBm, CMA only ( $\mu = 10^{-3}$ ).

(b) DP-16QAM 32 GBaud, 10x100 km, P/ch = 1 dBm, CMA ( $\mu = 10^{-3}$ ) for taps initialization followed by RDE ( $\mu = 10^{-4}$ ).



(c) DP-64QAM 32 GBaud, 10x50 km, P/ch = -3 dBm, CMA ( $\mu = 10^{-3}$ ) and intermediate RDE ( $\mu = 10^{-4}$ ) for taps initialization followed by RDE ( $\mu = 10^{-4}$ ).

Figure 3.10 – MSE calculated during MIMO equalization.



(a) DP-QPSK 64 GBaud, 30x100 km, P/ch = 3 dBm.

(b) DP-16QAM 32 GBaud, 10x100 km, P/ch = 1 dBm.

(c) DP-64QAM 32 GBaud, 10x50 km, P/ch = -3 dBm.

Figure 3.11 – Equalized outputs (steady state). Blue points: X polarization, red points: Y polarization.

### 3.1.3 Frequency Offset Compensation

The CFO occurs due to the frequency mismatch between the LO and the beam laser source. This mismatch causes a rapid change in the signal phase proportional to the CFO  $\Delta f$ . If not correctly compensated, its detrimental effects could severely impact the performance of the system. Modern transceivers typically have a  $\Delta f$  ranging from approximately 50 to 200 MHz.

Let  $z_p[n]$  denote the electrical signal of polarization p after channel equalization and PMD compensation, assuming that nonlinear impairments are neglected. Therefore  $z_p[n]$  can be represented as:

$$z_p(n) = x_p(n)e^{j2\pi(\phi_{0,p}+n\Delta fT_s)} + b_p(n), \quad (3.15)$$

where  $x_p(n) \in \mathcal{C}$  is the complex symbol  $n$  belonging to a symbol constellation  $\mathcal{C}$ ,  $\phi_{0,p}$  is a constant phase,  $\Delta f$  is the CFO,  $T_s$  is the symbol period and  $b_p(n)$  is a residual noise.

In general, a simple CFO estimator works well with unmodulated signals. To wipe out the modulation, it is enough to raise  $z_p(n)$  to the M-th power, where M is the modulation order.

In the case of QPSK, two well-known methods are typically used. The first one consists of finding the  $\Delta f$  that maximizes the spectrum of  $z_p(n)^M$ , where  $M = 4$  and  $n \in [1, N]$  is the index sample, being N the number of symbols of the observation window [74], [97].

$$z_p^M(n) = e^{j2\pi M(\phi_{0,p}+n\Delta fT_s+b_p''(n))}, \quad (3.16)$$

where  $b_p''(n)$  is a non-Gaussian phase disturbance [97] and considering unitary amplitude for the QPSK symbols.

Therefore,  $z_p^M(n)$  is a sinusoidal shifted  $M\Delta f$  accompanied by a phase noise. Observing a peak in the spectrum allows for finding  $M\Delta f$ .

A second method is based on the phase difference of consecutive symbols. Fig. 3.12 depicts the algorithm. The raise to the M-th power ( $M = 4$ ) let only the phase difference between these two consecutive symbols, which is  $2\pi M\Delta fT_s$ . Similar to the first method, an average over a window observation is preferable for better results [98].

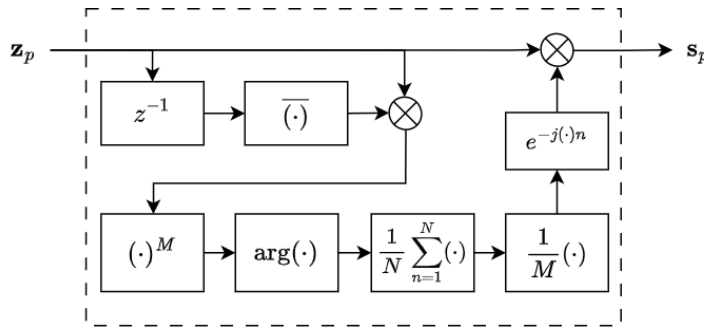


Figure 3.12 – Carrier frequency Offset estimation and compensation.

In the case of M-QAM ( $M > 4$ ), better results could be obtained using [99], which is suitable for DP M-QAM signals. This technique is based on two steps: a coarse step using spectral methods and a fine step around the estimated peak power obtained in the course step using a gradient descent-based algorithm. For more details see [99] and [100, Section 3.4].

Depending on the modulation format, we used the spectral method (adapted to QPSK) or the two-step coarse and fine method for M-QAM ( $M > 4$ ). Fig. 3.13 illustrates the constellations after the CFO compensation.

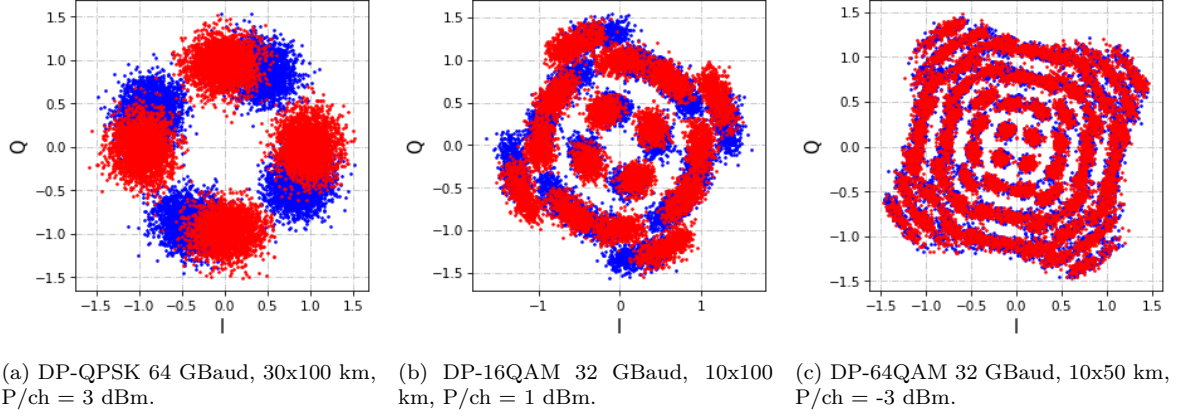


Figure 3.13 – CFO compensation. Blue points: X polarization, red points: Y polarization.

### 3.1.4 Carrier Phase Recovery

Due to the phase noise, the optical carrier phase can significantly vary, avoiding a correct detection. An algorithm of Carrier Phase Estimation (CPE) addresses the carrier phase variation. Two methods are commonly utilized: 1) data-aided, based on periodic pilot symbols, and 2) blind algorithms that employ signal statistical properties. In this study, we employ blind techniques, but we expect to modernize our DSP algorithms to be adapted to more robust data-aided carrier phase recovery techniques.

For QPSK modulation, one of the most popular is the Viterbi-and-Viterbi algorithm described in [101], [102] and illustrated in Fig. 3.14.

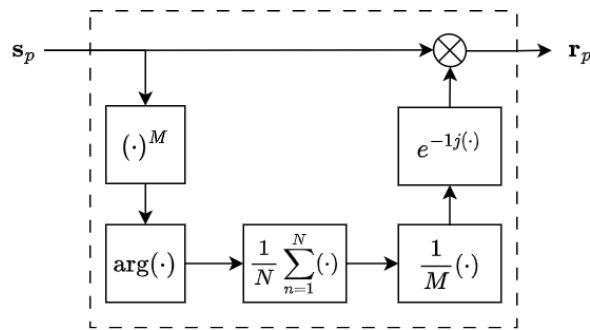


Figure 3.14 – Viterbi-and-Viterbi algorithm for carrier phase recovery.

Assuming the absence of other impairments, the process involves canceling out modulation by raising the complex symbols to the power  $M = 4$ . Subsequently, the arguments representing  $\times 4$  the estimated phase noise are summed and averaged within a window of  $N$  symbols. The resulting value is divided by 4 to obtain the estimated phase noise within that window. The compensated phase is calculated by subtracting the recovered phase noise from the initial phase.

Other algorithms have shown better performances for M-QAM signals ( $M > 4$ ), for instance, the ones using a feed-forward step. One widely known algorithm is described in [56], illustrated in Fig. 3.15.

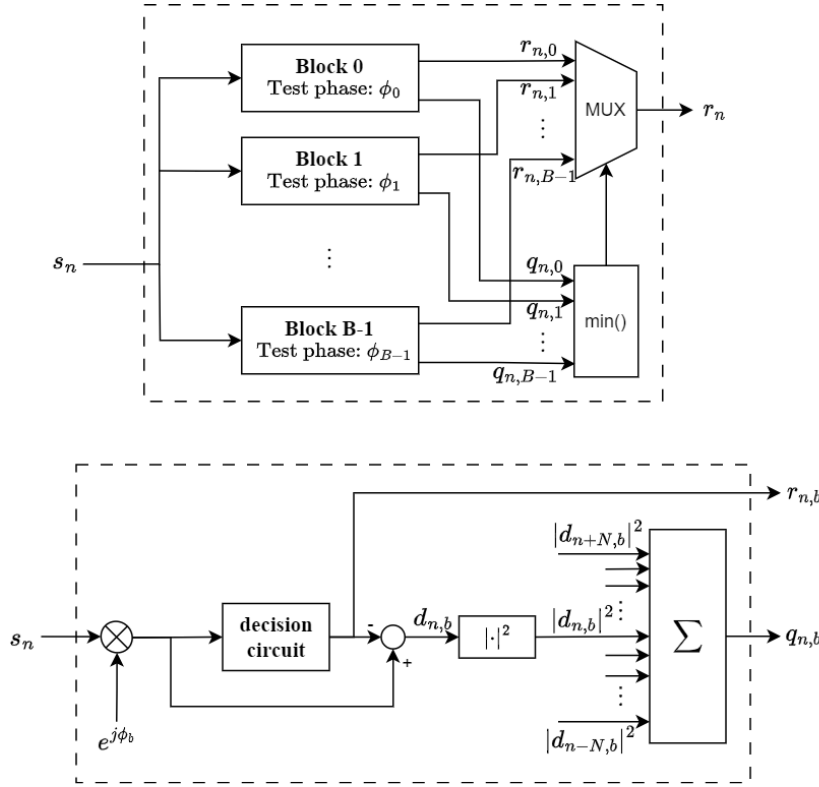


Figure 3.15 – (Top) CPE feed-forward blind algorithm with  $B$  phase blocks [56]. (Bottom) inside the blocks.

This algorithm tests  $B$ -phase rotation candidates for the received symbol  $s(n)$ . Each symbol  $s(n)$  is rotated  $B$  angles, and the distance  $d_{n,b}$  between the symbol rotated an angle  $b \in 1, B$  and the nearest constellation point  $\hat{X}_{n,b}$ , is recorded. Then, in a window of  $2N+1$  symbols, where  $N$  prior and  $N$  posterior symbols are assumed to alter the phase of the symbol in the middle, the squared distance  $|d_{n,b}|^2$  of the symbols that rotated the same angle  $b$  are summed. The sum is denoted as  $q_{n,b}$  in the figure. The angle  $b$  that minimizes  $q_{n,b}$  among the  $B$  candidates corresponds to the estimated phase rotation of the symbol  $s(n)$ .

It must be noted that to handle the 4-fold ambiguity of these methods is necessary differential encoding (if not pilot symbols used).

These algorithms are commonly susceptible to cycle slips [103]. Consequently, after recovering the phase, one must correct the phase differences greater than  $\pm\pi/4$ . An unwrap function works well in most cases. To achieve better results, more performing techniques should be considered.

Finally, the algorithms detailed in Section 3.1.4 are applied for each case. The resulting constellations are shown in Fig. 3.16.

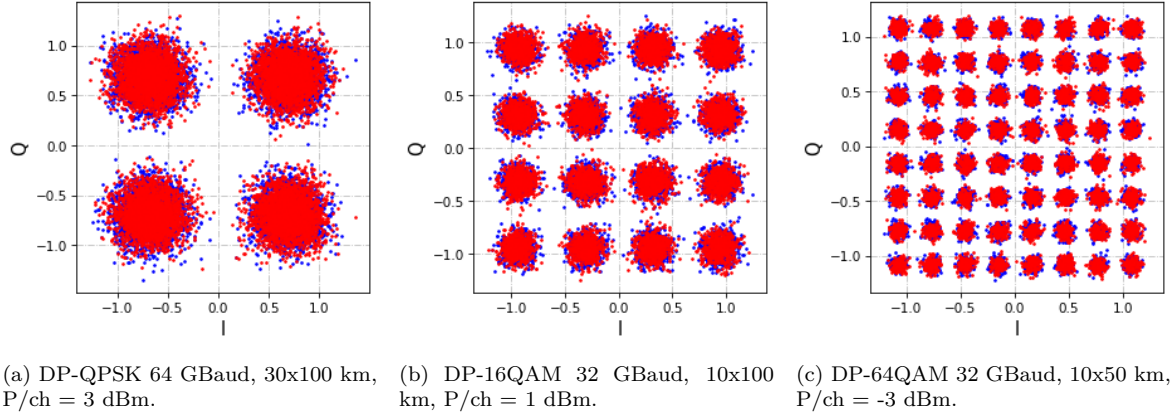


Figure 3.16 – CPE. Blue points: X polarization, red points: Y polarization.

### 3.1.5 Nonlinear Effects for Different Transmission Configurations

The classical DSP described in previous sections permits to compensate for some of the impairments that an optical signal experiences when going from the transmitter to the receiver. These impairments are due to the optical fiber and imperfect components on the transmitter and receiver sides. In this part, we want to show the NLI effects in different transmission configurations. We consider three modulation formats: QPSK, 16QAM, and 64QAM, and different data Baud rates for different spans of SSMF. The details of these scenarios are shown in Table 3.1.

Table 3.1 – Transmission Configurations using QPSK, 16QAM and 64QAM modulation formats at different Baud rates and for different fiber lengths.

	Symbol Rate (GBaud)	Bit Rate (Gbits/s)	Net Bit Rate (Gbits/s)	$N_{spans}$	$L_{spans}$ (km)
DP-QPSK	64	256	200	30, 40, 50	100
	128	512	400	25, 35, 45	100
DP-16QAM	32	256	200	10, 12, 14	100
	64	512	400	8, 10, 12	100
	128	1024	800	6, 8, 10	100
DP-64QAM	32	384	300	10, 12, 14	50
	64	768	600	8, 10, 12	50

The baselines of our simulations are the performances in Back-to-Back (BtB), i.e., only transmitter and receiver, measured using the BER per received OSNR varying only the noise level. We calculate the BER per different levels of received OSNR as shown in Fig. 3.17. Fig. 3.17a corresponds to an ideal DP transmission with only AWGN, and Fig. 3.17b corresponds to a scenario with CFO and LPN as well as the algorithms to compensate for them. The gap between theoretical, using (A.13), (A.16) and (A.17), and simulated results at low SNR in Fig. 3.17b is the penalty when employing differential encoding.

The DP-16QAM at 128 GBaud performs almost the same as the DP-64QAM at 32 GBaud. Nevertheless, the former carries a net bit rate of  $\sim 800$  Gbits/s, while the latter only  $\sim 300$

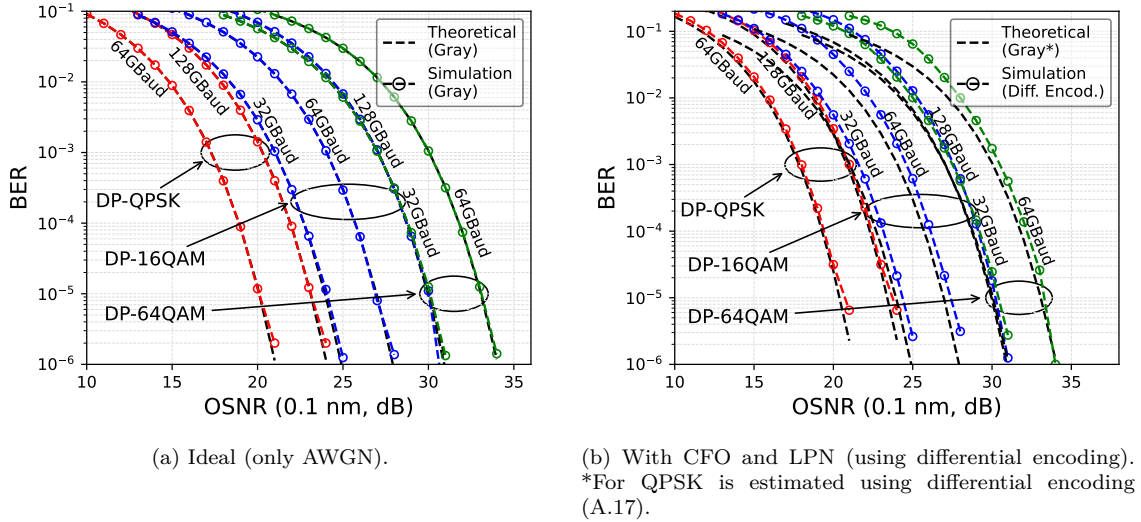


Figure 3.17 – BER vs. OSNR (0.1 nm) for a BtB configuration.

Gbits/sec (considering an overhead of 21% for FEC and synchronization).

When considering the multiple spans of optical fiber (SSMF) and the classical DSP, we obtain the results shown in Fig. 3.18.

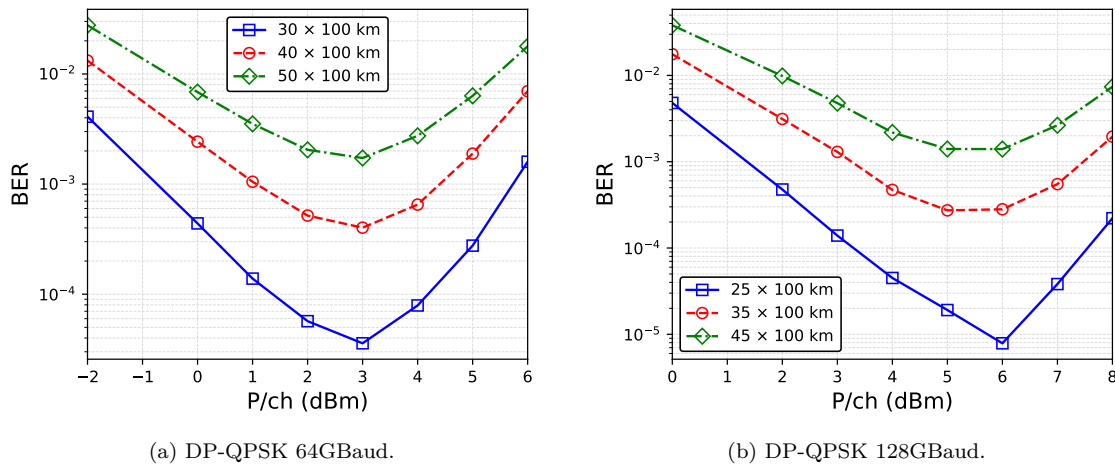
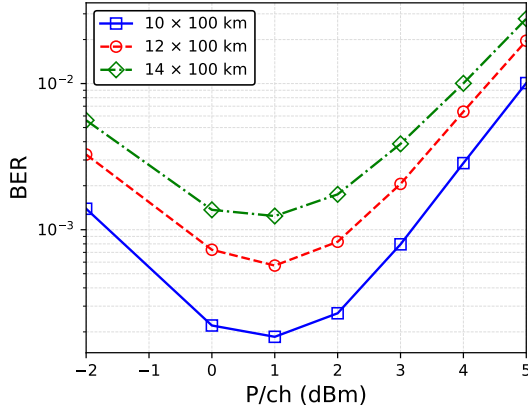


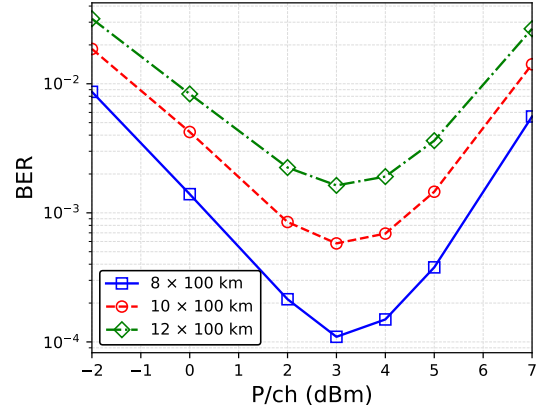
Figure 3.18 – Performance BER vs. P/ch using the DSP depicted in Fig. 3.2.

These results show the performance degradation (BER) for higher optical launch powers, which is also more detrimental for longer distances. Equivalently, the OSNR augmentation provokes an adverse effect, contrary to what happens on the left side of all figures, where the OSNR permits a BER improvement. Clearly, we can divide each curve into two regions: one corresponding to a linear regime prevalence (left side) and a second one corresponding to a nonlinear regime prevalence (right side).

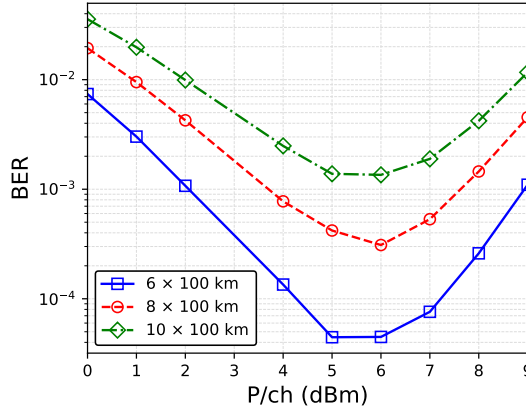
In the nonlinear regime, uncompensated NLI prevail as they become significant. Standard transceivers operate in the linear regime, close to the separation between the two regions, defined



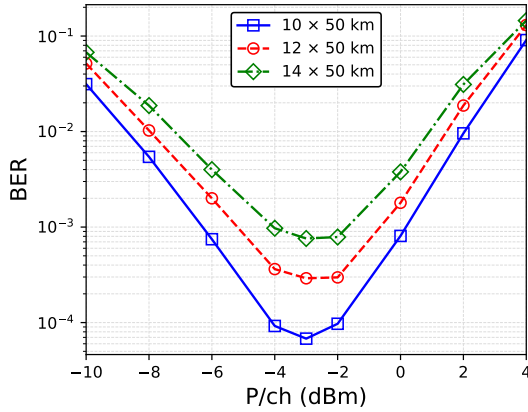
(c) DP-16QAM 32GBaud.



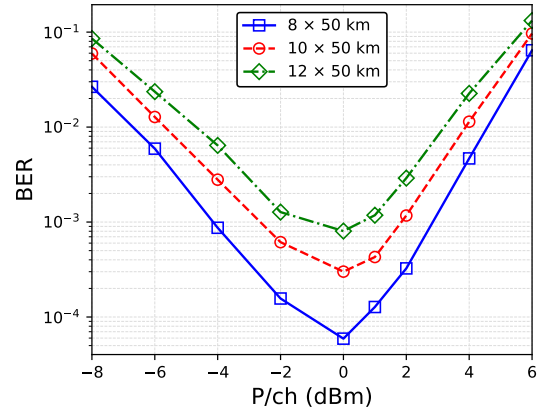
(d) DP-16QAM 64GBaud.



(e) DP-16QAM 128GBaud.



(f) DP-64QAM 32GBaud.



(g) DP-64QAM 64GBaud.

Figure 3.18 – Performance BER vs. P/ch using the DSP depicted in Fig. 3.2 (cont.).

by the optimal launch power, i.e., the launch power that minimizes the BER. As the OSNR continues increasing contrary to the BER degradation, another SNR-related metric is usually used to measure the impact of the noise on the system performance. This metric is the Generalized

OSNR (GSNR), formally defined in Appendix A.3.

In the next part, we introduce two techniques for nonlinearity compensation based on DSP. Using some of the simulated scenarios presented in Table 3.1, we quantify the benefits and drawbacks of these techniques regarding the BER improvement with respect to only linear equalizers and the additional computational resources necessary to perform the nonlinear equalization.

## 3.2 Nonlinear Impairments Compensation Techniques

Among the several nonlinearity compensation techniques found in the literature, the most popular ones are based on the inverse NLSE. In this work, we present two techniques commonly used as benchmarks for comparison purposes: the Digital Backpropagation (DBP) and the Volterra Nonlinear Equalizer (VNLE).

### 3.2.1 Digital Backpropagation

Consider the NLSE in (2.35). The inverse NLSE is given by

$$\frac{\partial \mathbf{E}}{\partial z} = (\hat{\mathbf{D}}^{-1} + \hat{\mathbf{N}}^{-1})\mathbf{E}. \quad (3.17)$$

This equation is equivalent to passing the optical signal  $\mathbf{E}$  from the receiver to the transmitter using fiber parameters with opposite sign [23], or equivalently:

$$\frac{\partial \mathbf{E}}{\partial z} = -(\hat{\mathbf{D}} + \xi \hat{\mathbf{N}})\mathbf{E}, \quad (3.18)$$

where  $\xi$  is a nonlinear rotation parameter and represents a fraction  $0 < \xi \leq 1$  of the amplitude, which is uncertain due to the amplifier noise [24]. This parameter  $\xi$  needs to be optimized empirically.

The DBP is numerically performed using the NLSE with opposite signs of the dispersion and nonlinearity operators, and whose input is the received signal after  $L$  km of fiber  $\mathbf{E}(L, t)$  to retrieve the signal before the optical fiber  $\mathbf{E}(0, t)$ . As the NLSE, the DBP is solved using the SSFM. Fig. 3.19 and 3.20 illustrate the symmetric and asymmetric versions of the DBP, respectively. The reader could notice that it is exactly the SSFM in the reverse direction (negative sign in linear and nonlinear operators) with the  $\xi$  factor in the nonlinear operator  $\hat{\mathbf{N}}$ .

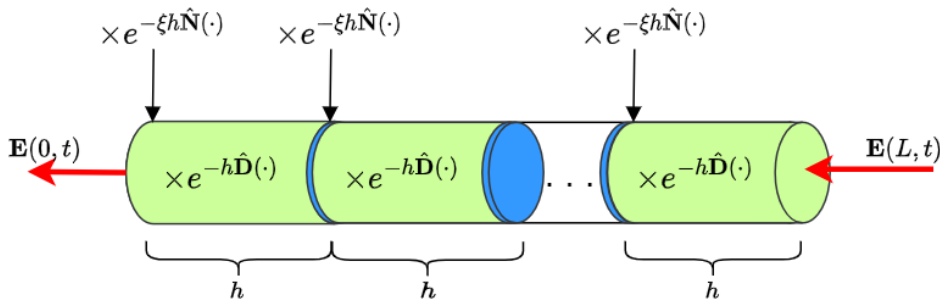


Figure 3.19 – Asymmetric DBP.

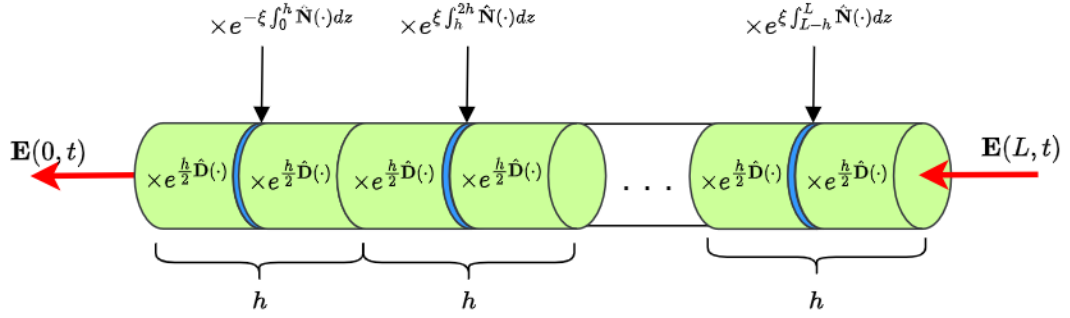
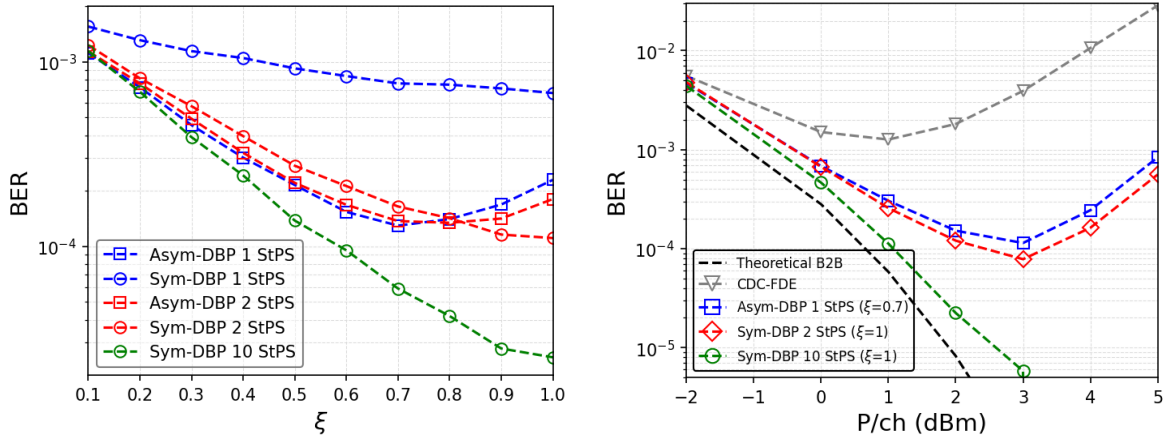


Figure 3.20 – Symmetric DBP.

The equation (3.18) could adopt multiple forms according to the NLSE employed version. In the more general case, is required a complete knowledge of the optical fiber parameters, such as the CD, the PMD, and the nonlinear coefficient  $\gamma$ . The PMD is a stochastic process commonly unknown. Therefore, the DBP is usually realized, assuming that PMD could be processed in subsequent stages. Even though a DBP addressing the PMD was also covered in several works, for instance, in [104], [105], showing good results.

Fig. 3.21 shows the DBP for 1, 2, and 10 StPS and uses the symmetric and asymmetric version with optimal nonlinear rotation parameter  $\xi$ .


 (a) Optimal  $\xi$  using the DBP for different StPS for  $P/ch = 3\text{dBm}$ .

 (b) BER vs.  $P/ch$  using the DBP at 1,2 and 10 StPS with optimal  $\xi$ .

 Figure 3.21 – BER as a function of the  $P/ch$  and the nonlinear rotation parameter  $\xi$  and using the CDC and the DBP.

In general, the asymmetric DBP works better than the symmetric DBP at 1 StPS, while increasing the number of steps per span results in similar results in both approaches. The difference between using the CNLSE or the Manakov-PMD is minimal, and empirically, the performances are the same if we optimize the parameter  $\xi$ . The results show a significant improvement with respect to CDC only and even at 1 StPS, increasing the optimal power from 1 dBm to 3 dBm with a BER reduction from  $\sim 10^{-3}$  to  $\sim 10^{-4}$  in the optimal power.

The approach followed in this work is the classical DBP. Nonetheless, during the last years, several improvements have been made to optimize the DBP, particularly in reducing its computational complexity. For instance, in [106], it was proposed using a logarithmic step size that relies on an attenuation coefficient  $k$  that depends on each transmission scenario and optical fiber parameters. This method has proved to improve performances with reduced complexity. Also, in [107] was claimed that using the Wiener-Hammerstein model<sup>1</sup> and reducing in 50% the number of considered spans, e.g., if transmission with 10 spans, only backpropagate the signal for 5 spans, permit to get similar results than the conventional DBP with 50% complexity reduction. In [108] was also proposed a Time-Domain (TD) DBP. The TD-DBP refers to the linear operators because the nonlinear operators are always in TD.

### 3.2.2 Volterra Nonlinear Equalizer

The relationship between the Fourier transform of the output  $Y(\omega)$  of a nonlinear system and the Fourier transform of the input  $X(\omega)$  could be expressed using a frequency domain Volterra series expansion [109] as follows:

$$Y(\omega) = \sum_{n=1}^{\infty} \int \dots \int H_n(\omega_1, \dots, \omega_{n-1}, \omega - \omega_1 - \dots - \omega_{n-1}) \times X(\omega_1) \dots X(\omega_{n-1}) X(\omega - \omega_1 - \dots - \omega_{n-1}) d\omega_1 \dots d\omega_{n-1}, \quad (3.19)$$

where  $H_n(\omega_1, \dots, \omega_{n-1})$  is the  $n$ -th frequency domain Volterra kernel.

The description of the nonlinear system is more accurate when using highest-order kernels, but at the same time, the complexity of the model increases. Up to the third or fifth order is commonly acceptable.

Consider the input optical field  $\mathbf{E}(\omega) = [E_x(\omega), E_y(\omega)]^T$  that corresponds to  $X(\omega)$  in (3.19). The Fourier transform of the Manakov equation in (2.40) and considering only the first three kernels<sup>2</sup> of (3.19) yield the solution [3]:

$$E_{x/y}(\omega, z) = H_1(\omega, z)E_{x/y}(\omega) + \int \int H_3(\omega_1, \omega_2, \omega - \omega_1 + \omega_2, z) \times [E_x(\omega_1)E_x^*(\omega_2) + E_y(\omega_1)E_y^*(\omega_2)] \times E_{x/y}(\omega - \omega_1 + \omega_2) d\omega_1 d\omega_2, \quad (3.20)$$

where the Volterra kernels are given by

$$H_1(\omega, z) = e^{-\frac{\alpha z}{2}} e^{-j\frac{\beta_2}{2}\omega^2 z}, \quad (3.21)$$

$$H_3(\omega_1, \omega_2, \omega - \omega_1 + \omega_2, z) = -\frac{j8\gamma/9}{4\pi^2} H_1(\omega, z) \times \frac{1 - e^{-(\alpha + j\beta_2(\omega_1 - \omega)(\omega_1 - \omega_2))z}}{\alpha + j\beta_2(\omega_1 - \omega)(\omega_1 - \omega_2)}. \quad (3.22)$$

---

1. Very similar to a symmetric DBP but with no necessarily a 50/50 step size division.  
 2. Only odd-order kernels since even-order kernels are zero due to the absence of even-order nonlinearities in optical fibers.

The linear and nonlinear impairments compensation using VNLE is achieved by the use of inverse kernels of the  $p$ th-order  $K_p$ , which are operators that nullify the second through to the  $p$ th-order Volterra kernels [110]. For an uncompensated transmission link consisting of  $N$  spans of fiber with full compensation loss, these kernels (up to order 3) are given by

$$K_1(\omega) = H_1^{-1}(\omega) = e^{j\omega^2\beta_2NL/2}, \quad (3.23)$$

$$K_3(\omega_1, \omega_2, \omega - \omega_1 + \omega_2) \approx \frac{j8\gamma/9}{4\pi^2} \times L_{eff} \times K_1(\omega) \sum_{k=1}^N e^{jk\beta_2L\Delta\omega}, \quad (3.24)$$

where  $L_{eff}$  is the effective span length, and  $\Delta\omega = (\omega_1 - \omega)(\omega_1 - \omega_2)$ .

Finally, the VNLE is built using (3.20) by replacing  $H_1$  by  $K_1$  and  $H_3$  by  $K_3$  and with input the received signal  $E_{x/y}(\omega, z)$  and output the equalized signal  $\hat{E}_{x/y}(\omega, 0)$  as follows [111]

$$\begin{aligned} \hat{E}_{x/y}(\omega, 0) &= K_1(\omega)E_{x/y}(\omega, z) + \int \int K_3(\omega_1, \omega_2, \omega - \omega_1 + \omega_2) \\ &\quad \times [E_x(\omega_1, z)E_x^*(\omega_2, z) + E_y(\omega_1, z)E_y^*(\omega_2, z)] \\ &\quad \times E_{x/y}(\omega - \omega_1 + \omega_2, z)d\omega_1d\omega_2. \end{aligned} \quad (3.25)$$

The first term in 3.25 corresponds to a linear compensation of the entire link, while the second term is a nonlinear compensator span per span. Fig. 3.22a depicts a scheme that illustrates the method. The CD is compensated in the frequency domain, and the NLI in the time domain. The linear compensator for  $k$  spans is given by

$$(H_{CD})^k = \exp(1j\beta_2/2\omega^2kL_{span}), \quad (3.26)$$

where  $L_{span}$  is the span length.

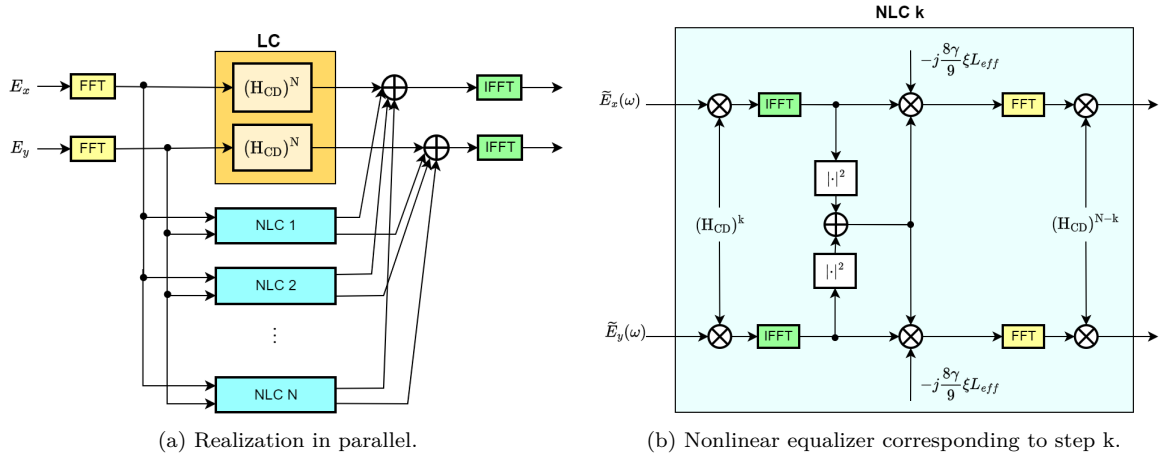


Figure 3.22 – Volterra series based nonlinear equalization scheme [3] ©2012, IEEE.

The VNLE has proven particularly useful for intrachannel nonlinearity [3]. Additionally, a parallel realization of the linear and nonlinear operators enables a lower complexity, in contrast

with the DBP, which is sequential.

Consider the use case DP-16QAM 32GBaud using 14x100 km of SSMF. Fig. 3.23a shows the BER VNLE for different  $\xi$  getting the optimal  $\xi_{opt} = 0.6$ . Fig. 3.23b shows the BER for different optical launch powers.

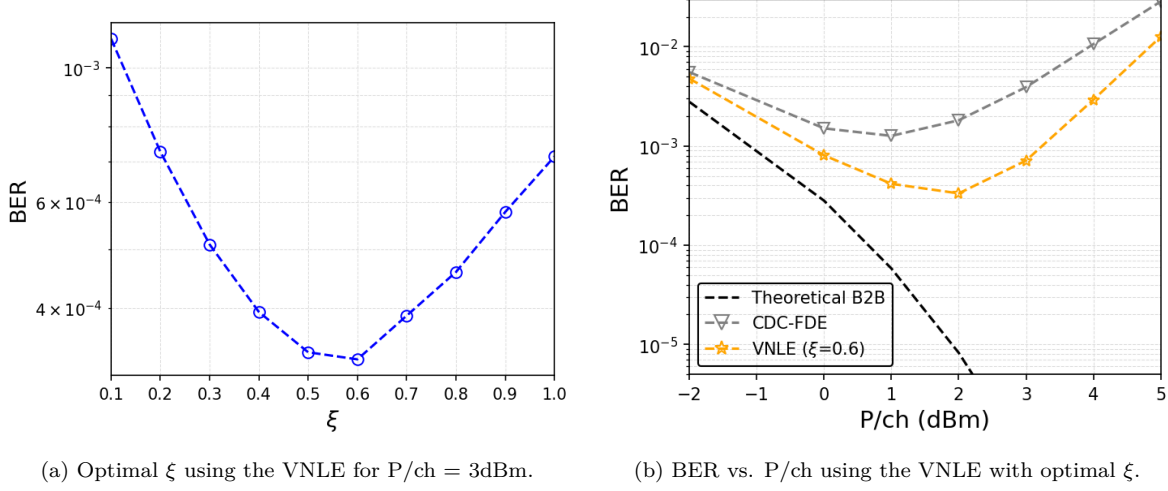


Figure 3.23 – BER as a function of the P/ch and the nonlinear rotation parameter  $\xi$  using the CDC and the VNLE.

### 3.2.3 Computational Complexity

The choice between the DBP and the VNLE must take into account not only the BER improvement capabilities but also the amount of additional computational resources required to perform the necessary operations. We focus our attention on only CD compensation and nonlinear compensation since the other algorithms described in previous sections are common in all cases.

The required RmpS for nonlinearity compensation using the DBP (using the Manakov-PMD equation), considering  $N_{step}$  StPS for a total of  $N_{span}$  spans and an oversampling factor K, is given by

$$\text{RmpS}_{\text{DBP}} = N_{span} N_{step} K (4 \log_2 N_{FFT} + 10.5), \quad (3.27)$$

where 10.5 stands for 4 Real Multiplications (RM) corresponding to one complex multiplication for the CD compensation and 6.5 RM correspond to 13 RM for both polarization accounting for: 2 RM per squared magnitude for each polarization, 1 RM by  $-j8/9\gamma h$  assuming previously calculated for both polarization, and 1 complex multiplication (4 RM) for the nonlinear phase rotation for each polarization. We assumed that the exponential function is implemented in a lookup table [23].

Consider the VNLE for the dual-polarization case. The linear compensation stage is identical to the FDE-CDC (3.9). For each of the  $N_{span}$  nonlinear compensation branches, the linear compensation per polarization accounts for 2 complex multiplication (8 RM) for CD compensation of  $k$  spans and  $N_{spans} - k$  spans,  $4 \log_2 N_{FFT}$  RmpS for one pair IFFT/FFT, 2 RM per squared

modulus, and 5 RM for nonlinear compensation accounting for the 2 polarization, thus 2.5 for each polarization. For  $N_{spans}$  and considering the oversampling factor  $K$ , the CC in RMpS for the nonlinear branches results:

$$CC_{\text{nonlin}} = N_{span}K(4\log_2 N_{FFT} + 12.5). \quad (3.28)$$

Therefore, the total CC for the entire VNLE is given by

$$CC_{VNLE} = CC_{CDC-FDE} + CC_{\text{nonlin}} \quad (3.29)$$

$$= 4(\log_2 N_{FFT} + 1)K + N_{span}K(4\log_2 N_{FFT} + 12.5). \quad (3.30)$$

Let us take the example of DP-16QAM at 32 GBaud over  $14 \times 100$  km of SSMF. The computed CC of the FDE-CDC, the Asymmetric DBP (Manakov-PMD) at 1, 2, 3, and 10 StPS, and the VNLE are shown in Fig. 3.24. We also measured the processing time of each method for the entire link for a total of  $2 \cdot 10^6$  samples<sup>3</sup>. The RMpS and the processing time are normalized to 1 for the CDC, assuming that the CDC algorithm exactly corresponds to the measured processing time. We also show the ratio with respect to the CDC for each method for both RMpS and processing time.

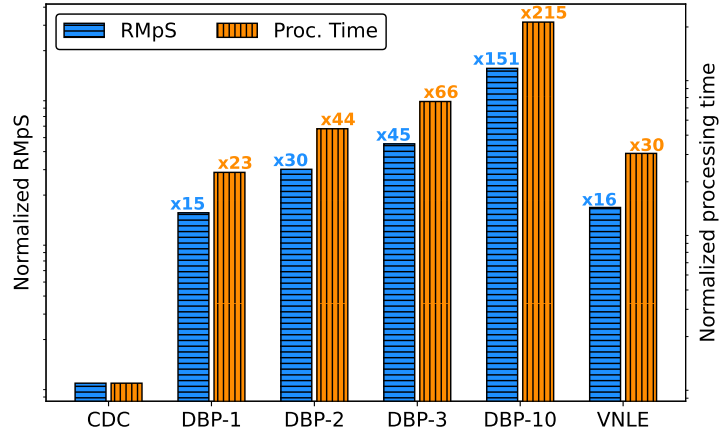


Figure 3.24 – Computational complexity (CC) in RMpS and processing time in Logarithmic scale.

We notice a good correlation between the estimated CC in RMpS and the measured processing time. The differences are related to the additions, exponential functions, and other operations performed by the processor that we did not take into account in our estimations.

This figure shows that the method with the lowest CC after the CDC is the DBP 1 StPS and the VNLE. However, these methods are still  $\sim \times 15$  more computationally expensive than the CDC. We highlight that the CC of the DBP and the VNLE could both be optimized, as proposed in some works, e.g., in [3], proposing working at the symbol rate reducing to the half the VNLE CC, in [112], where the authors proposed cascade structures for complexity reduction,

3. Using the python package “time” in a desktop with an Intel Xeon 3.60 GHz 8-core processor and 32GB RAM.

or as in [107] that proposed to work in span per steps (a single step covering more than 1 span), instead of steps per span.

### 3.3 Experimental Setup

The experimental setup of a SC-DP coherent transmission system is depicted in Fig. 3.25. A DP transmitter generates data from an Arbitrary Waveform Generator (AWG) at 92 GSa/s. In our setup, the AWG generates 16QAM symbols at a symbol rate of 32 GBaud, which are generated through several Pseudo-Random Binary Sequences (PRBS) that were Gray encoded. These symbols are band-limited by a pulse shaper RRC digital filter using a roll-off factor equal to 0.2 and conveniently oversampled to achieve the sampling rate of the AWG, i.e., 92 GSa/s. The four electrical signals XI, XQ, YI, and YQ, corresponding to the I and Q components of polarizations X and Y, are amplified by linear RF drivers. The amplified RF signals feed the two IQ modulators. An ECL at 1550.12 nm with  $\sim 100$  KHz linewidth feeds the modulators. The modulated optical carriers, corresponding to the two polarizations, are then combined using a PBC. The dual-polarization optical signal is conveniently amplified to reach the desired power level. The Channel Under Test (CUT) at 1552 nm is multiplexed with a wavelengths comb with the purpose of equalizing the optical line. A Waveshaper filter cancels each of the two side channels to simulate a single-channel configuration.

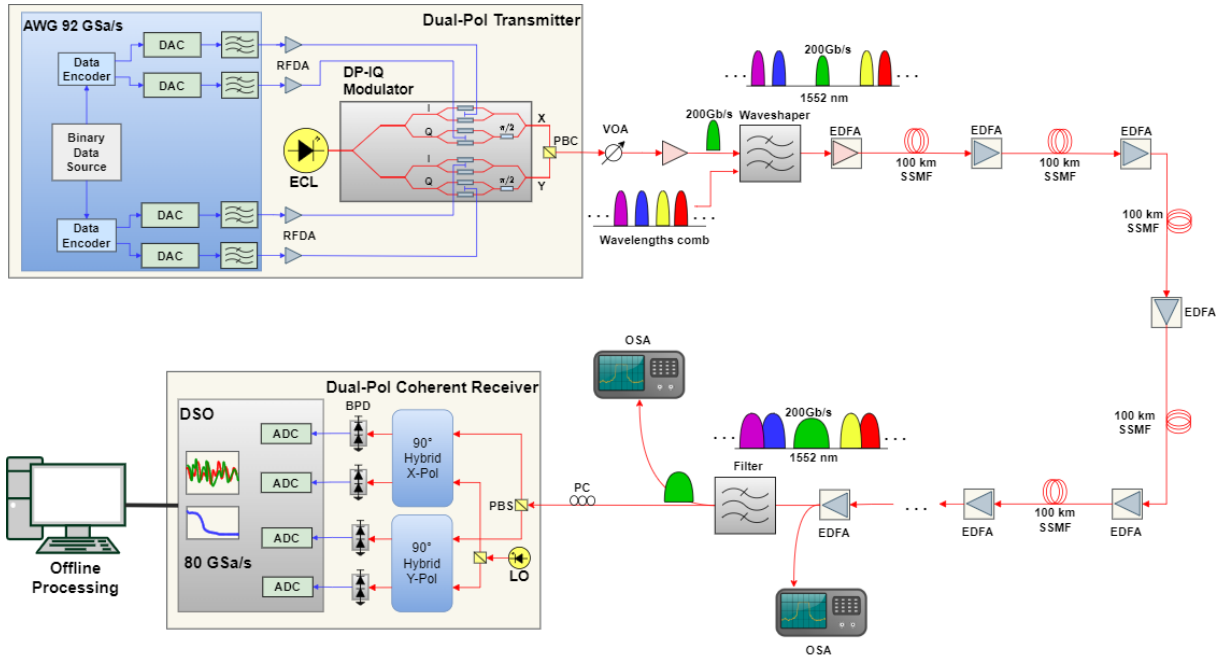


Figure 3.25 – Experimental setup with the DP Transmitter, the optical fiber consisted of  $N_{\text{spans}} \times 100$  km spans of SSMF, the DP receiver, and the Offline-DSP. AWG: Arbitrary Waveform Generator, ECL: External Cavity Laser, PBC: Polarization Beam combiner, vOA: Variable Optical Attenuator, EDFA: Erbium-Doped Fiber Amplifier, OSA: Optical Spectrum Analyzer, PC: Polarization Controller, PBS: Polarization Beam Splitter, LO: Local Oscillator, BPD: Balanced Photo-Detectors, DSO: Digital Storage Oscilloscope.

The optical fiber link comprises several spans of SSMF with a span length of 100 km. After

each span, the optical signal is amplified using EDFAs, with  $NF = \sim 4.5$  dB, to compensate for the span loss entirely.

At the receiver side the CUT is filtered. The dual-polarization coherent receiver splits the filtered signal into two orthogonal polarizations using a polarization beam splitter Polarization Beam Splitter (PBS). A polarization controller Polarization Controller (PC) is added for eventually aligning the X and Y polarization of the signal on the PSPs of the PBC. A LO, with similar parameters of the transmitter laser source, feeds the two  $90^\circ$  Hybrids that separate the I and Q components of both polarizations X and Y. Subsequently, four BPD convert the optical signals into electrical signals containing the amplitude and phase information. The four electrical signals are then sampled and digitized using ADC embedded in a Digital Storage Oscilloscope (DSO) operating at 80 GSa/s. The signal is subsequently processed using an offline DSP.

In Fig. 3.26 and 3.27, we show some pictures of the experimental setup.

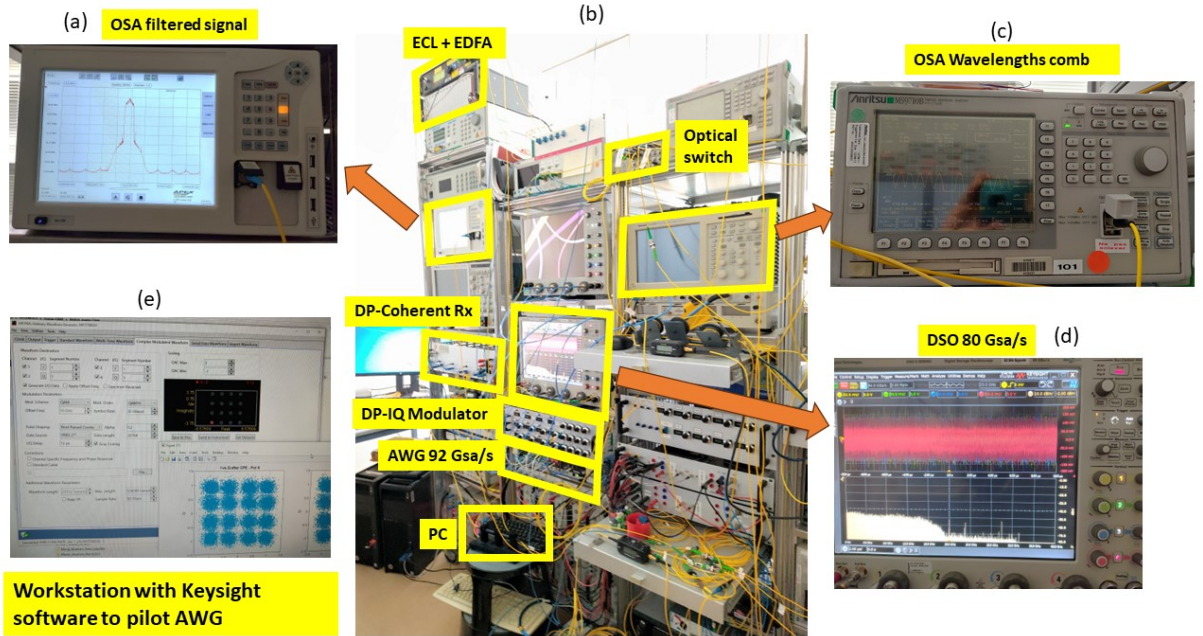


Figure 3.26 – (a) Filtered CUT at 1552 nm at the receiver observed in the OSA, (b) general view of the DP-TX and DP-Coherent RX comprising the AWG which generates DP-16QAM modulated samples at 92 GSa/s, the ECL with a low-noise EDFA, the DP-IQ Modulator, an optical switch to select the number of fiber spans and the PC, (c) OSA showing the wavelengths combs multiplexed with the CUT with two aside channels off, (d) DSO operating at 80 GSa/s to recover the XI, XQ, YI, and YQ components, (e) workstation with the Keysight software and the MATLAB programs for offline DSP.

### 3.3.1 Optical Back-to-Back

We carried out optical BtB measurements to characterize the performances of our setup, in particular, the required OSNR (ROSNR) to achieve a typical FEC threshold  $\sim 1 \times 10^{-2}$  for a DP-16QAM.

The Offline-DSP underwent retiming and resampling to convert the sampling frequency from 80 GSa/s to 128 GSa/s, which is four times the original symbol rate of 32 GBaud. The data

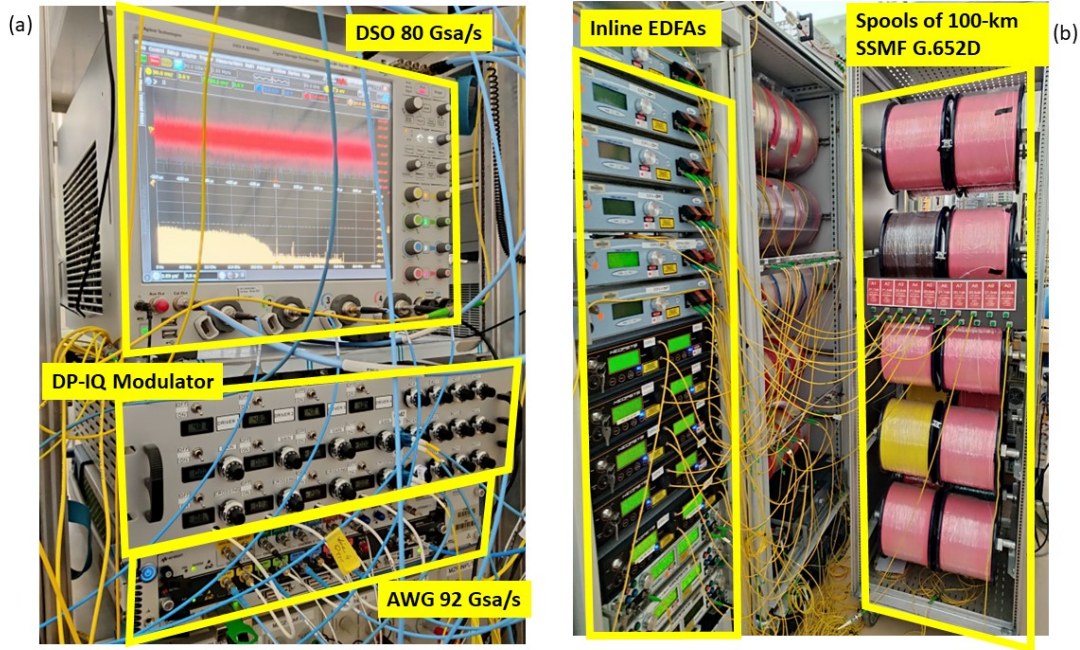


Figure 3.27 – (a) AWG at 92 GSA/s, DP-IQ modulator and DSO operating at 80 GSA/s, (b) Spools of 100-km of SSMF and EDFA after each span.

was then filtered using an RRC digital filter with the same parameters as those used in the transmitter. Subsequently, we separated the two polarizations using a  $2 \times 2$  MIMO equalizer in conjunction with an FSE to recover the signal at the symbol rate, and using sequentially the CMA and RDE. This processing was followed by estimating the frequency offset and the carrier phase. The results are shown in Fig. 3.28, where we added the theoretical BER using (A.13) and (A.16) for the recovered OSNR values.

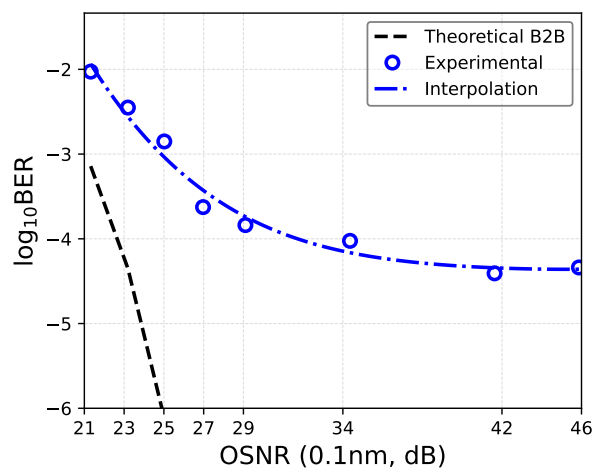


Figure 3.28 – Back-to-Back DP-16QAM 32GBaud.

### 3.3.2 Optical Fiber Transmission

In addition to the DSP algorithms conducted in the BtB scenario, the DSP must perform channel equalization. Consider only CD compensation after the RRC filter and before the  $2 \times 2$  MIMO equalizer.

Fig. 3.29 displays the signal constellations for X and Y polarizations and the power spectral density (PSD) for the DP-16QAM signal that was transmitted over  $5 \times 100$  km of SSMF, after each DSP block.

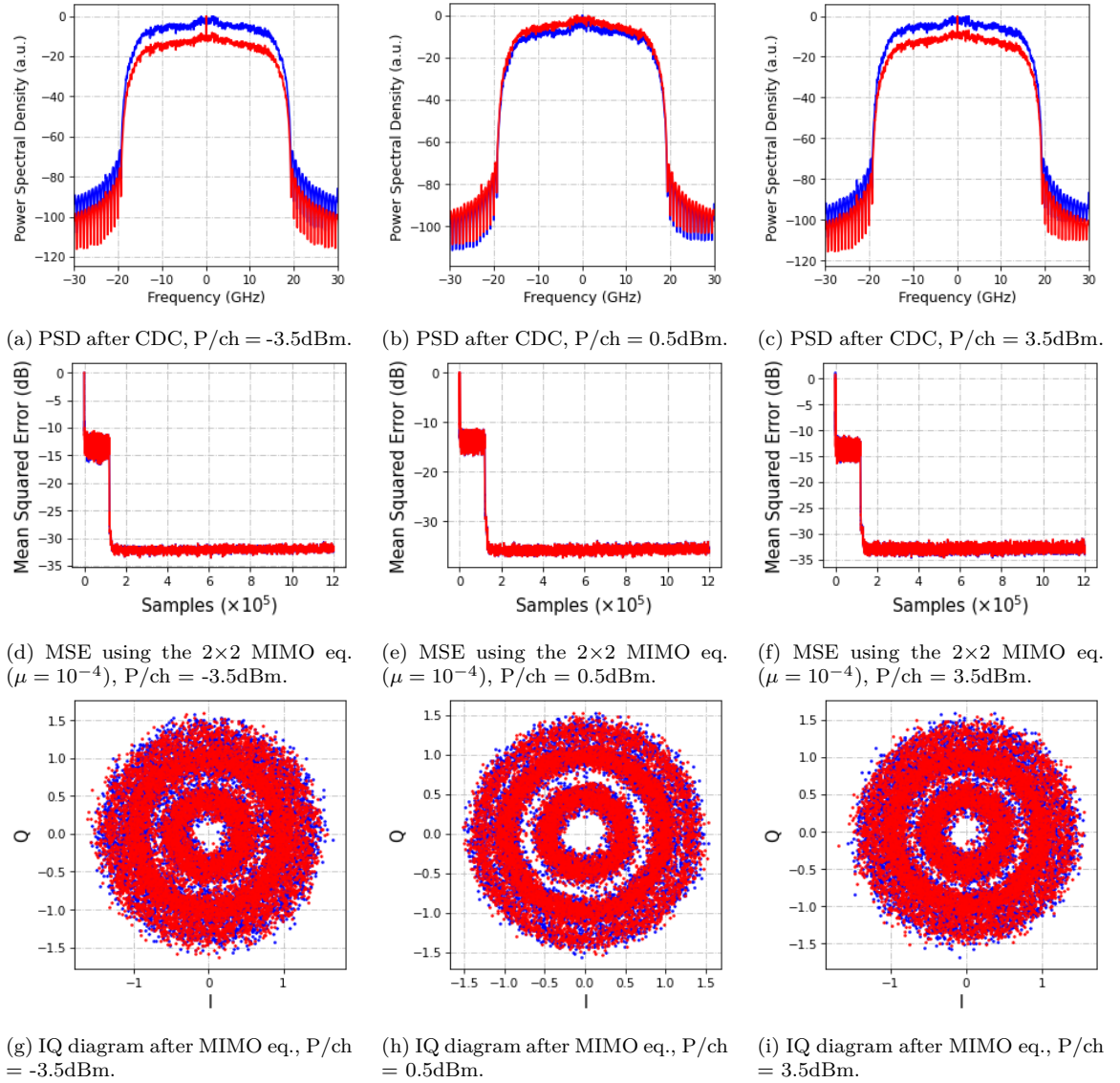


Figure 3.29 – DSP results of a DP-16QAM signal constellations after  $5 \times 100$  km SSMF: X-Pol (blue), Y-Pol (red). CDC: Chromatic dispersion Compensation, MSE: Mean Squared Error, MIMO: Multiple-Input-multiple-output, CFO: Carrier Frequency Offset Compensation, CPE: Carrier Phase Estimation.

To evaluate the overall performance of our system, we computed the BER after decoding

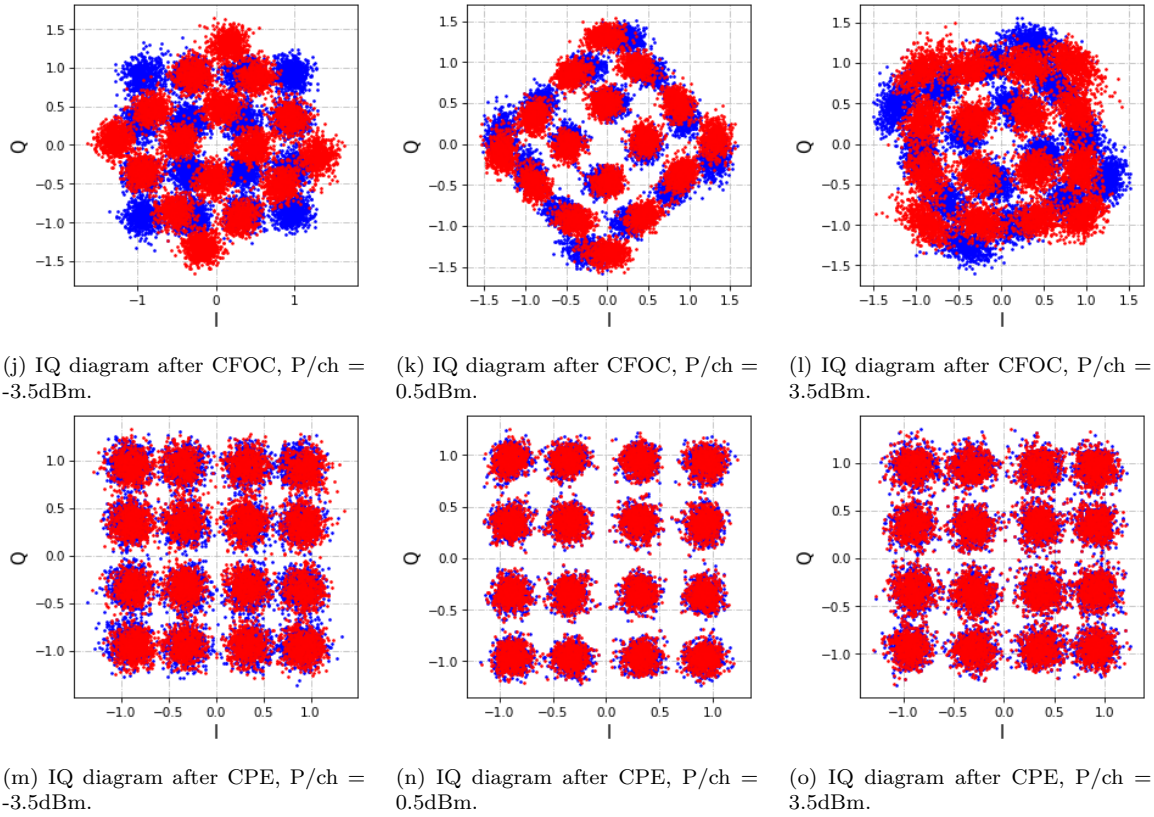


Figure 3.29 – DSP results of a DP-16QAM signal constellations after 5x100 km SSMF: X-Pol (blue), Y-Pol (red). CDC: Chromatic dispersion Compensation, MSE: Mean Squared Error, MIMO: Multiple-Input-multiple-output, CFCO: Carrier Frequency Offset Compensation, CPE: Carrier Phase Estimation (cont.).

the sequence of processed symbols. Fig. 3.30 displays the BER while varying the optical launch power  $P/ch$  for DP-16QAM 32GBaud over a distance of 5x100 km of SSMF.

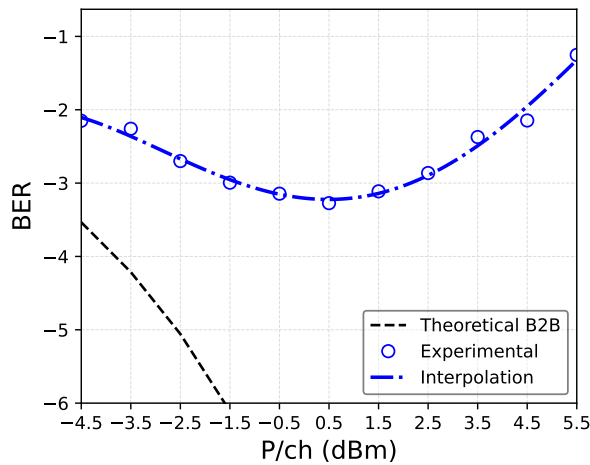
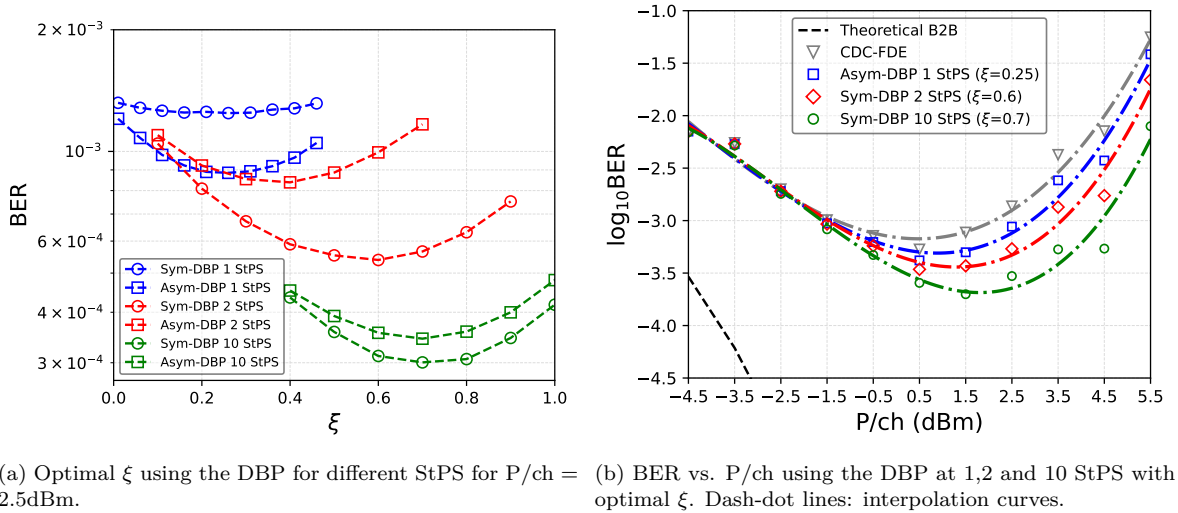


Figure 3.30 – BER vs.  $P/ch$  of experimental DP-16QAM 32 GBaud signal over 5x100 km of SSMF.

### 3.3.3 Nonlinearity Compensation

Proceeding similarly to in Section 3.2, we have performed nonlinearity compensation using the DBP and the VNLE. Both techniques necessitate the optimization of a parameter that we called  $\xi$ , which is the nonlinear rotation parameter.

The DBP necessitates specifying the number of steps per span (StPS). Since we aim at reducing the complexity algorithms, we choose 1 and 2 StPS and 10 StPS only as reference. We try both the symmetric and asymmetric DBP and choose the one that provides better results. In particular, at 1 StPS, the asymmetric version works better, being the opposite for more than 1 StPS. Notice that similar observations were made in our numerical setup. The results are shown in Fig. 3.31.



(a) Optimal  $\xi$  using the DBP for different StPS for  $P/\text{ch} = 2.5\text{dBm}$ .

(b) BER vs.  $P/\text{ch}$  using the DBP at 1, 2 and 10 StPS with optimal  $\xi$ . Dash-dot lines: interpolation curves.

Figure 3.31 – BER as a function of the  $P/\text{ch}$  and the nonlinear rotation parameter  $\xi$  using the CDC and the DBP.

We notice an increment in the optimal power, i.e. the optical launch power at which we obtain the lowest BER, from 0.5 dBm with CDC to 1 dBm using DBP-1StPS and 1.5 dBm using DBP-2StPS. Using a DBP-10StPS increments the optimal power to 2 dBm. The  $\log(\text{BER})$  also decreases from -3.2 to -3.3 in the optimal power using DBP-1StPS and to -3.4 and -3.7 using DBP-2StPS and DBP-10StPS, respectively.

Concerning the VNLE, its implementation also needs to set a parameter  $\xi$ . We selected a  $P/\text{ch} = 2.5$  dBm to find the optimal  $\xi$ . Using this optimal value, we calculated the BER for different launch powers. Fig. 3.32 shows these results. In this case, the optimal power increases up to 1 dBm with a  $\log(\text{BER})$  improvement from -3.2 to -3.4 in the optimal power.

Combining the results from the DBP and the VNLE (Fig. 3.33), we can observe that the performance of the VNLE is very similar to that of a DBP 1 StPS. However, as we have seen in Section 3.24, the DBP 1 StPS performs slightly fewer multiplications than the VNLE as well as a lower processing time (without considering optimized versions).

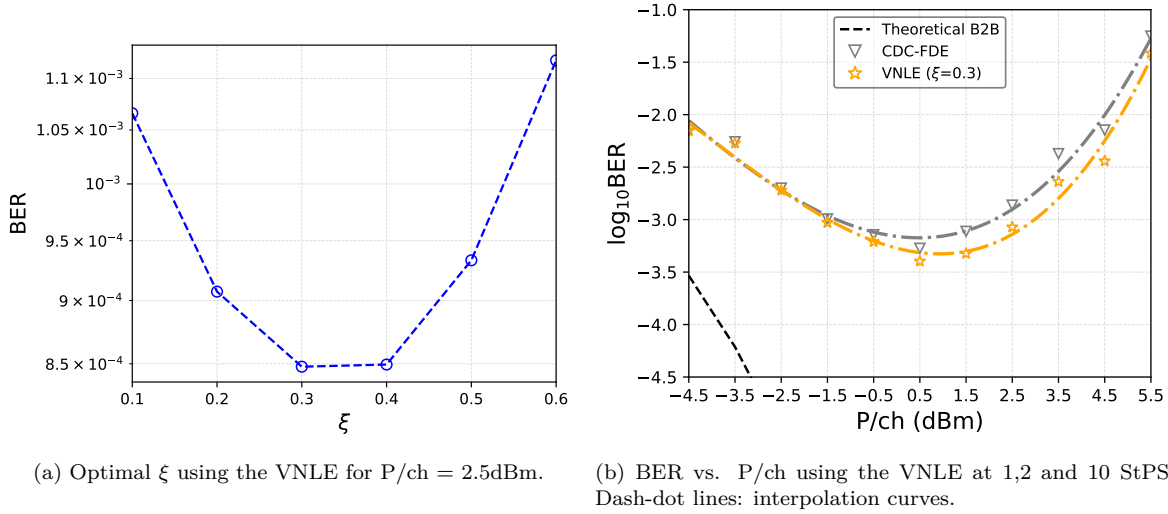


Figure 3.32 – BER as a function of the  $P/ch$  and the nonlinear rotation parameter  $\xi$  using the CDC and the VNLE.

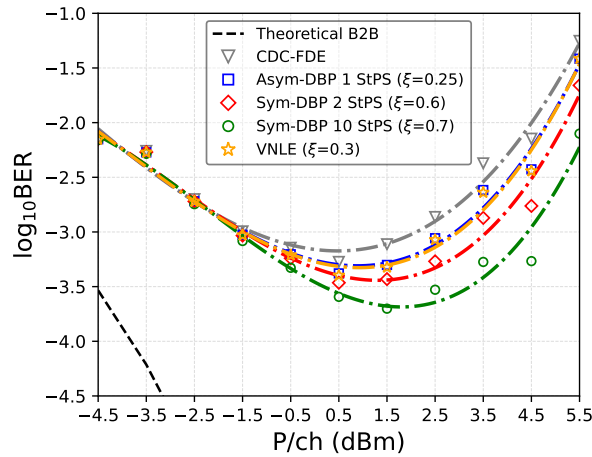


Figure 3.33 – Results of experimental DP-16QAM 32 GBaud signal over 5x100 km of SSMF using the DBP and the VNLE. Dash-dot lines: interpolation curves.

### 3.4 Summary

This chapter has covered the DSP embedded in modern transceivers. Through numerical simulations, we have introduced several DSP algorithms for channel equalization, particularly for Chromatic Dispersion (CD), and adaptive algorithms to address time-varying impairments such as the Polarization Mode Dispersion (PMD) and laser phase noise. We have also presented DSP algorithms for Carrier Frequency Offset (CFO) compensation and Carrier Phase Recovery (CPR). Using a DP-16QAM at 32GBaud, over  $14 \times 100$  km of SSMF, we have illustrated the different steps to achieve signal reconstruction to recover the original transmitted bits.

For long transmission distances for higher OSNR values, we have seen that the Nonlinear Impairments (NLI) lead to performance degradation, affecting the quality of the transmission.

To tackle this issue, we have used the Digital Backpropagation (DBP) and the Volterra Nonlinear Equalizer (VNLE). We have observed that these algorithms permit to effectively mitigate the NLI, mainly a DBP with more than 2 Step per Span (StPS) and a VNLE with similar results than a DBP at 1 StPS. However, both require a knowledge of the optical fiber parameters as well as the span length and input channel power, which in reality is very challenging to know with exactitude. Additionally, the Computational Complexity attributed to these methods is still very high for real-time scenarios.

Using an experimental setup consisting of a DP-16QAM at 32GBaud over  $5 \times 100$  km of SSMF, we obtained the detrimental effects of NLI for high input power channel and that the capabilities of the DBP and VNLE diminish when we do not have a total knowledge of the optical link. Even so, in an the experimental setup we account with more information than in a field trial or operative optical links.

Consequently, this study motivated us to study other alternatives for NLI compensation. Specifically, Neural Networks are promising techniques, as many studies also suggest. The next chapter is dedicated to the study of NN for NLI compensation in long-haul and high-data-bit-rate coherent systems.



# NEURAL NETWORKS BASED NONLINEAR EQUALIZERS FOR OPTICAL TRANSMISSION SYSTEMS

---

In this chapter, we investigate the utilization of NN for channel equalization in optical transmission systems. Specifically, to compensate for NLI. Indeed, we have seen that classical deterministic techniques such as the DBP and the VNLE permit to compensate for the dispersion and NLI jointly, but with a prohibited additional complexity that dissuades its ASIC implementation. Also, in a real scenario, its efficiency is reduced and commonly not justified for very small performance gains. Therefore, our objective here is to show how efficient and relevant could be NN for optical channel equalization, considering a coherent system and over long distances.

This chapter is composed as follows. In Section 4.1, we briefly introduce the fundamental concepts of Machine Learning (ML), including the model selection, the model hyperparameters tuning, and the learning process. Section 4.2 focuses on Neural Networks, where we present the artificial neuron model and the Multilayer Perceptron Neural Network. Section 4.3 is dedicated to NN based models employed in NLI compensation, where we present the state of the art, followed by practical implementations of NN that we employ in the numerical and the experimental setup. Section 4.4 ends the chapter by highlighting the observations and conclusions made in our study.

## 4.1 Fundamentals of Machine Learning

Frequently, ML and Deep Learning (DL) are two terms used indifferently for the same concept. However, these terms have different significance [29]. On the one hand, the ML encompasses the abilities of a machine<sup>1</sup> to learn how to do some specific task *by itself*, *based on experiences*[29]. The key terms here are *by itself*, making the difference with programmed machines, and *based on experiences*, which was a novel manner of learning for machines [113].

The characteristic of self-learning by experience is possible due to a first step called the Training phase, in which the algorithm creates a model using multiple examples that consist of pairs of inputs and expected results or targets. An input is a composition of features that represent the data. For instance, if the input is an image, the features are the pixels (in numerical representation) that conform to the image. Once the ML algorithm has learned the association input-target, we can use this model to classify or predict an outcome given input without giving

---

1. “Machine” according to the Merriam Webster dictionary: a mechanically, electrically, or electronically operated device for performing a task.

any additional instruction to the machine. This phase is called Testing or Evaluation [28].

Because the expected targets dictate the learning process, this learning approach is called Supervised Learning. Examples of supervised learning are those that perform Classification and Regression. In classification, the goal of the ML algorithm is to assign a category or class to each input, generally expressed in probabilistic terms, while in regression, we aim to predict a numerical value given some input. [28], [29].

In some problems, the targets are unknown. In those scenarios, an ML algorithm performs Unsupervised learning because no targets address the training process. Examples of unsupervised learning tasks are clustering [114], [115], which consists of grouping elements in clusters, knowing only the features that compose the inputs. Another example is anomaly detection [116], in which the goal is to efficiently identify the outliers that perturb data.

There are other learning algorithms, such as semi-supervised, in which a part of the dataset is labeled, and the remaining part is not, and reinforcement learning, which is based on awards and penalties received by an agent during the learning [29].

On the other hand, DL is a concept of learning in which a model could learn representations of data using multiple levels of abstraction, making it possible to solve complex problems using simpler representations. A teaching example is the image recognition problem, where an image is decomposed into small pieces (pixels). The first level of representation is related to shared characteristics, perhaps understandable to human eyes. A second level finds some patterns like colors or shapes, a third level finds objects like faces or wheels, and a final level represents the recognized object [117].

Finally, NN is a ML model that mimics the living being brain. For this reason, NN are also known as Artificial NN. In this work, we use only the term NN for Artificial NN without any ambiguity. We delve into the concept of NN in Section 4.2, but essentially, a NN is a composition of neurons, also called units, in which each neuron performs a mathematical operation in their inputs giving as a result an output that is sent to another neuron. The neurons are organized in layers. A deep NN comprises multiple layers using the concept of Deep Learning.

### 4.1.1 Model Selection

An ML model is chosen to provide good results in an unseen dataset, known as a testing dataset. Previously, the model is trained with several samples using a training dataset through supervised or unsupervised learning. We typically calculate the error function between the expected result, which is explicit in supervised learning and must be estimated in unsupervised learning, and the prediction. A good model can give good predictions in both training and testing datasets, an ability of the ML model called Generalization [29].

A good practice involves considering three different independent datasets for training, validation, and testing. The difference in concepts between validation and testing is minimal. Both are unseen datasets not employed for training the ML algorithm, but validation is used for predictions during the learning process, while testing is used out of the learning stage [29].

When the ML model performs well in the training dataset only, incapable of giving good predictions in the validation dataset, we say it occurs Overfitting. On the contrary, Underfitting occurs when the model cannot provide good results in the training dataset. We look for a model that could perform well in both training and validation datasets, and the latter generally will also provide good results in a testing dataset if training and validation are different and

independent [28].

This desired situation necessitates choosing an adequate model with sufficient capacity to perform the particular task correctly. Sometimes, the complexity of the model requires a more extensive variety of datasets. In such cases, the Cross-Validation technique is beneficial. This technique consists of splitting the whole available dataset into  $K$  folds or groups, where  $K - 1$  folds are used for training and the remaining for validation. This process is repeated  $K$  times, where at each time, a different fold is used for validation [28].

### 4.1.2 Learning Process

We have mentioned that a good model can generalize the results of the ML algorithm in training, validation, and testing datasets. We will see that the error function is also used to train the ML algorithm.

The learning process consists of adapting or optimizing the parameters of the ML model. The learning process differs from the hyperparameters tuning, in which we defined a set of hyperparameters to train the model. The parameters of the ML algorithm are a set of values (specifically weights and bias of each unit or neuron) learned during the learning process.

The objective of the learning process consists of finding the set of parameters, symbolized as  $\theta$ , that permits obtaining an output as close as possible to the expected result or target. More formally, let us represent the difference between the output and the target as a loss function  $l(\mathbf{y}, \mathbf{y}_{\text{true}})$ , where  $\mathbf{y}$  is the output and  $\mathbf{y}_{\text{true}}$  is the target. To find the optimal  $\theta$ , we define a loss [35]:

$$\mathcal{L}(\theta) = \mathbb{E}[l(\mathbf{y}, \mathbf{y}_{\text{true}})]. \quad (4.1)$$

Common loss functions are listed in Table 4.1 [118]:

Table 4.1 – Loss functions.

Task	Name	$l(\mathbf{y}, \mathbf{y}_{\text{true}})$
Regression	Square Loss	$(\mathbf{y} - \mathbf{y}_{\text{true}})^2$
Regression	Absolute Loss	$ \mathbf{y} - \mathbf{y}_{\text{true}} $
Regression	Huber Loss	$\begin{cases} \frac{1}{2}(\mathbf{y} - \mathbf{y}_{\text{true}})^2 & , \text{if }  \mathbf{y} - \mathbf{y}_{\text{true}}  < \delta \\ \delta \mathbf{y} - \mathbf{y}_{\text{true}}  - \frac{1}{2}\delta^2 & , \text{otherwise} \end{cases}$ where $\delta > 0$
Classification	Sigmoid Cross-Entropy Loss	$-\log \tilde{p}, \text{ where } \tilde{p} = \begin{cases} p & , \text{if } y = 1 \\ 1 - p & , \text{if } y \neq 1 \end{cases}$ $p = \sigma(f(x)) = \frac{1}{1 + e^{-f(x)}},$ where $\sigma$ is the sigmoid function
Classification	Softmax Cross-Entropy Loss	$-\log P(y x), \text{ where } P(y x) = \frac{e^{f_y(x)}}{\sum_k e^{f_k(x)}}$

The matter now becomes an optimization problem with an objective function minimizing the loss  $\mathcal{L}(\theta)$ . One common approach to this optimization problem is the Stochastic Gradient Descent (SGD) and its variants. In this context, the SGD to find the optimal set  $\theta$  that minimizes the loss  $\mathcal{L}(\theta)$  is described by:

$$\boldsymbol{\theta} \leftarrow \boldsymbol{\theta} - \varepsilon \nabla_{\boldsymbol{\theta}} \mathcal{L}(\boldsymbol{\theta}), \quad (4.2)$$

where  $\varepsilon$  is known as the Learning Rate and  $\nabla_{\boldsymbol{\theta}}$  is the gradient with respect to  $\boldsymbol{\theta}$ .

As the reader could confirm, there are no novel theoretical notions concerning previous knowledge from optimization techniques based on SGD used in classical adaptive algorithms, as the ones presented in 3.1.2. The key differences rely on the following. In the adaptive algorithms, the updating is performed sample by sample with instantaneous derivatives of the error with respect to the parameters that we want to optimize. In NN, the optimization is commonly performed in a group of examples known as mini-batches. In NN, depending on the mini-batch size, there are three types of Gradient Descent algorithms: i) Deterministic or Batch Gradient Descent, for a mini-batch size equal to the entire dataset known as Batch, ii) Stochastic or Online Gradient Descent, for a mini-batch size equal to one example, and iii) Mini-batch Stochastic Gradient Descent, for a mini-batch greater than one but lower than the entire dataset. Due to computational efficiency reasons, Batch Gradient Descent is rarely performed, mainly for large datasets, and Online Gradient Descent could also take a lot of time. For these reasons, the Mini-batch Stochastic Gradient descent is commonly utilized and very frequently simply called Stochastic Gradient Descent. Also, frequently, a mini-batch is simply termed a Batch.

Alternatively, modern optimizers utilize SGD with some modifications, e.g., ADAM optimization uses adaptive estimates of the first and second-order moments of the gradient [119].

Another difference of the objective function minimization in NN with respect to classical adaptive algorithms is the notion of Backpropagation. Indeed, an NN performs a two-step procedure: forward propagation and backward propagation or Backpropagation. On one hand, the forward propagation aims to calculate the output value and the loss. On the other hand, the Backpropagation aims to update the parameters  $\boldsymbol{\theta}$  using the gradient  $\nabla_{\boldsymbol{\theta}}$ . With this aim, the forward and backpropagation act consecutively mini-batch per mini-batch. The NN completes one Epoch when all the mini-batches complete this process

Finally, in NN, the optimization step is performed in a training dataset, in which the SGD algorithm acts to find the optimal set  $\boldsymbol{\theta}$ . However, the ultimate goal of a NN is not to find the optimal  $\boldsymbol{\theta}$  but to obtain an output  $\mathbf{y} = f(\boldsymbol{\theta}, \mathbf{x})$  as closest as possible to the true  $\mathbf{y}$  in a new and unseen dataset (testing dataset). This is clearly different from classic adaptive algorithms in which the optimal parameters are used to find the expected final outputs, i.e., no distinction between training or testing datasets. There is also a third dataset (Validation dataset), commonly considered an intermediate dataset, which is used to test an unseen dataset during the training. Still, it does not participate in the optimization step.

An ML algorithm is defined by a set of hyperparameters that controls the ML behavior and that is used for the learning process but not learned from the ML algorithm. The type of hyperparameters are vast, e.g., number of layers in deep NN, number of units or neurons in a single layer, kernel size in a convolutional layer, number of hidden units in a recurrent NN, number of trees of the random forest algorithm, etc. The learning rate, mini-batch size, and number of epochs are also considered hyperparameters because they control the learning process [29]. Finding the most suitable set of hyperparameters is not a trivial task and must not be overestimated, especially in optical communications, where the accuracy is very high<sup>2</sup>. A wrong

---

2. Most operational preFEC-BER thresholds ranging from  $\sim 10^{-3}$  to  $\sim 10^{-2}$  in current coherent transceivers [120], i.e. accuracy ranging from 99% to 99.9%.

choice of hyperparameters could also lead to poor generalization (overfitting).

The following section is dedicated to some techniques for hyperparameter selection.

### 4.1.3 Hyperparameters Tuning

There are several hyperparameter tuning approaches. Depending on the complexity of the ML algorithm and the amount of hyperparameters to be optimized, we can opt for one of these:

- Grid Search
- Random Search
- Bayesian Optimization
- Tree-structured Parzen Estimators

#### Grid Search

This technique is based on an exhaustive search of hyperparameters by taking all the possible combinations of hyperparameters in the search space. This technique is recommended for a small search space because the time to compute all the combinations could explode if the search space becomes too large.

#### Random Search

Instead of considering that all combinations have the same probability of occurrence on the search space, we could assign pre-defined probabilities of occurrence to determined combinations. In this way, only the most probable candidates in the search space will be tested. This technique is called Random Search and could be seen as an improvement of the Grid Search.

#### Bayesian Optimization

The hyperparameters search could also be seen as an optimization problem [29]. In this optimization problem, we aim to get the minimal target  $y$ , given a set of hyperparameters  $x$  using the objective function  $p(y|x)$ . This method is called Bayesian Optimization (BO). With this method, the hyperparameters search is based on two principal components: a surrogate model to model an objective function and an acquisition function to select the next set of candidates. The surrogate model is usually modeled as a Gaussian process, and the acquisition function is a function that measures the error with respect to the expected results.

#### Tree-structured Parzen Estimation

The Tree-structured Parzen Estimation (TPE) [121] is a variant of BO. Still, instead of relying on a Gaussian process in the form  $p(y|x)$  as the BO does, the TPE estimates  $p(x|y)$  using non-parametric densities. The TPE estimates  $p(x|y)$  using:

$$p(x|y) = \begin{cases} g(x) & \text{if } y > y^*, \\ b(x) & \text{otherwise,} \end{cases} \quad (4.3)$$

where  $g(x)$  stands for good distribution of the hyperparameters  $x$  in which we obtain the best  $y$  given a threshold  $y^*$ , and  $b(x)$  for bad distributions of the hyperparameters  $x$  in which we obtain the remaining  $y$ . The next combination  $x$  results from  $\operatorname{argmax}_x g(x)/b(x)$ . The distribution  $g(x)$  and  $b(x)$  are obtained using Parzen Estimators, also known as Kernel Density Estimators.

Whatever the hyperparameter tuning method is selected, we must perform a learning process to obtain the accuracy metric. The next section describes the learning process in detail.

## 4.2 Neural Networks

In this section, we focus on deep artificial NN, i.e., NN built with multiple layers, where each layer performs a specific task going from simpler to complex representations. We use the term NN for deep artificial NN for simplicity.

The concept of NN comes from the human brain’s understanding. According to [122], “A neural network is a massively parallel distributed processor made up of simple processing units, which has a natural propensity for storing experiential knowledge and making it available for use”. This processing units are called Neurons or Perceptrons. The idea behind this concept is that each neuron processes a certain amount of information and sends it to another neuron, as the actual brain does [28], [122].

### 4.2.1 Single Artificial Neuron Model

The type of processing a neuron completes is generally divided into a linear operation followed by a nonlinear function, as most problems are not purely linear. Fig. 4.1 depicts the model of an artificial neuron.

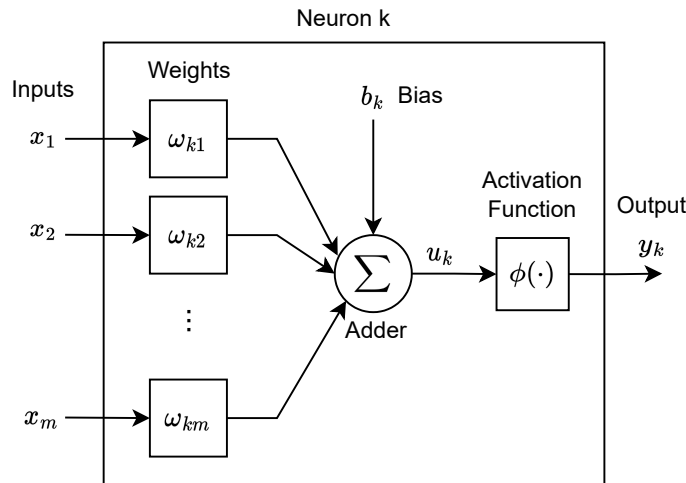


Figure 4.1 – Artificial neuron model.

Specifically, consider a neuron  $k$ , which receives information from  $m$  inputs. Each input is weighted by a factor  $\omega_{km}$  where  $k$  specifies the neuron number and  $m$  is the input number. The significance behind each weighting factor is the characterization of the strength of each input. The resulting  $m$  products are linearly combined. A bias  $b_k$  is added to this weighted

sum to adapt the value for the following activation function. This latter transforms the linear combination using a nonlinear function. The outcome  $y_k$  is the output of the neuron  $k$  [123].

The neuron model illustrated in Fig. 4.1 is equivalent to a row  $\boldsymbol{\omega}_k$  and vector  $\mathbf{x}^\top$  multiplication plus a bias  $b_k$  with a piece-wise nonlinear function  $\phi$  at the end, as follows:

$$u_k = \boldsymbol{\omega}_k \mathbf{x}^\top + b_k, \quad (4.4a)$$

$$y_k = \phi(u_k), \quad (4.4b)$$

where  $\boldsymbol{\omega}_k = [\omega_{k1}, \omega_{k2}, \dots, \omega_{km}]$  is the set of weights  $\omega_{km}$  for each input  $x_m$ ,  $\mathbf{x} = [x_1, x_2, \dots, x_m]$  is the set of  $m$  inputs,  $b_k$  is a bias,  $u_k$  is a linear combination and  $y_k$  is the output.

The purpose of a nonlinear activation function is to assign more or less importance to this output. Commonly utilized functions are the hyperbolic tangent (Tanh), the Rectified Linear Unit (ReLU), and the Sigmoid. These familiar nonlinear functions are depicted in Fig. 4.2.

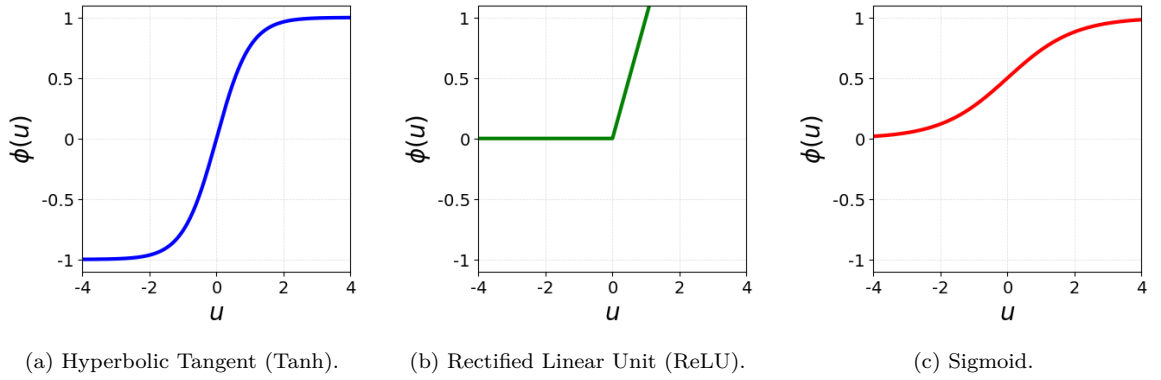


Figure 4.2 – Common nonlinear activation functions.

These nonlinear functions are defined as follows:

$$\text{Tanh}(u) = \frac{\exp(u) - \exp(-u)}{\exp(u) + \exp(-u)}, \quad (4.5a)$$

$$\text{ReLU}(u) = \max(0, u), \quad (4.5b)$$

$$\text{Sigmoid}(u) = \frac{1}{1 + \exp(-u)}. \quad (4.5c)$$

## 4.2.2 Multilayer Perceptron

An MLP is a kind of NN whose neurons are stacked in layers. An MLP is composed of more than one layer. These layers are “dense” because their neurons are “fully connected” to the neurons of the precedent and subsequent layers [29]. Therefore, they are also called Dense Neural Networks or Fully Connected Neural Networks. Fig. 4.3 shows the MLP architecture using four layers.

The first and final layers are called the Input and Output layers. The layers in the middle are called Hidden layers because they are not visible from the outside of the MLP (consider the

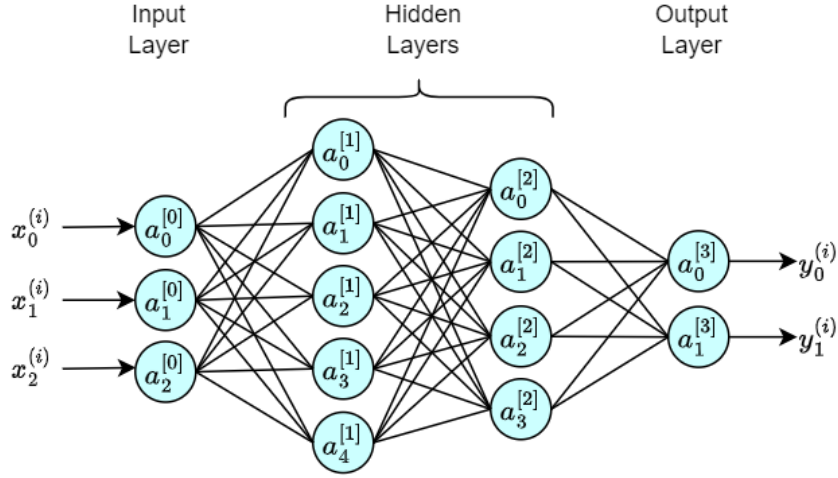


Figure 4.3 – Multiplayer Perceptron.

MLP as a “black-box”). Each circle represents a neuron that performs the operations illustrated in Fig. 4.1.

In the following, we use the following notations:

- Superscript  $(i)$  denotes the  $i$ -th training sample.
- Superscript  $[l]$  denotes the  $l$ -th layer.
- $m$  is the number of examples. This is not shown in Fig. 4.3.
- $N_i$  is the input size.  $N_i = 3$  in Fig. 4.3.
- $N_o$  is the output size.  $N_o = 2$  in Fig. 4.3.
- $N_h^{[l]}$  is the number hidden units of the layer  $l$ .  $N_h^{[1]} = 5$ ,  $N_h^{[2]} = 4$  in Fig. 4.3.
- $L$  is the number of layers.  $L = 4$  in Fig. 4.3.
- $a_k^{[l]}$  is the output of the  $k$ -th neuron in the  $l$ -th layer.

By convention, the neurons of the input layer take the training samples, i.e.,  $\mathbf{a}^{[0]} = \mathbf{x}$ , and the output of each hidden unit, similarly to (4.4), is given by,

$$a_k^{[l]} = \phi^{[l]}(\boldsymbol{\omega}_k^{[l]}(\mathbf{a}^{[l-1]})^\top + b_k^{[l]}). \quad (4.6)$$

The nonlinear activation function is assumed to be the same for all neurons in the same layer. Although there are no specific restrictions on this, it is a common practice for simplicity.

A layer with identical activation functions for all neurons is equivalent to,

$$\mathbf{a}^{[l]} = \phi^{[l]}(\mathbf{W}^{[l]}(\mathbf{a}^{[l-1]})^\top + \mathbf{b}^{[l]}), \quad (4.7)$$

where  $\mathbf{a}^{[l]}$  is the vector outputs of layer  $l$ ,  $\phi^{[l]}$  is the piece-wise nonlinear activation function,  $\mathbf{W}^{[l]}$  is the  $n_h^{[l]} \times n_h^{[l-1]}$  weight matrix whose rows are the weight vectors corresponding to each neuron, and  $\mathbf{b}^{[l]}$  is the bias vector of the  $l$ -th layer.

Consider now an MLP composed of  $L$  layers. The reader could verify that the final output  $\mathbf{y}$  is calculated through the following steps:

$$\mathbf{a}^{[0]} = \mathbf{x}, \quad (4.8a)$$

$$\mathbf{a}^{[1]} = \phi^{[1]}(\mathbf{W}^{[1]}(\mathbf{a}^{[0]})^\top + \mathbf{b}^{[1]}), \quad (4.8b)$$

$$\mathbf{a}^{[2]} = \phi^{[2]}(\mathbf{W}^{[2]}(\mathbf{a}^{[1]})^\top + \mathbf{b}^{[2]}), \quad (4.8c)$$

$$\vdots$$

$$\mathbf{a}^{[L-1]} = \phi^{[L-1]}(\mathbf{W}^{[L-1]}(\mathbf{a}^{[L-2]})^\top + \mathbf{b}^{[L-1]}), \quad (4.8d)$$

$$\mathbf{y} = \mathbf{a}^{[L-1]}. \quad (4.8e)$$

Or equivalently,

$$\mathbf{y} = f(\mathbf{x}; \boldsymbol{\theta}), \quad (4.9)$$

where  $f$  represents the successive linear and nonlinear operations from the input layer to the output layer, and  $\boldsymbol{\theta}$  is the set of all weight matrices  $\mathbf{W}^{[l]}$  and vector bias  $\mathbf{b}^{[l]}$  for  $1 \leq l < L$ , given by:

$$\boldsymbol{\theta} = \mathbf{W}^{[1]}, \mathbf{b}^{[1]}, \dots, \mathbf{W}^{[L-1]}, \mathbf{b}^{[L-1]}. \quad (4.10)$$

The set  $\boldsymbol{\theta}$  is the set of parameters of the MLP.

### 4.3 Nonlinear Equalizers using Neural Networks

Having covered the fundamentals of NN, in this section, we aim to utilize the NN as nonlinear functions for channel equalization, particularly in nonlinear equalizers. Indeed, unlike the DSP-based algorithms such as the DBP or the VNLE, NN does not rely on specific physical models or parameters [124]. For this reason, models based on NN are also called non-parametric NN. This section starts with a brief presentation of the state of the art in nonlinear equalizers using NN for compensating fiber nonlinearity. Subsequently, we present our implementations using the use cases described in Section 3.1.5.

#### 4.3.1 State of the Art

The number of research works that have investigated the use of NN for fiber nonlinearity compensation has continued growing in the last decade (with  $\sim 14$  published papers in 2014 and  $\sim 313$  in 2023), as shown in Fig. 4.4).

The early stage of these investigations was more focused on IM/DD and Orthogonal Frequency Division Multiplexing (OFDM) systems. In [125], it was numerically proved that an NN, in this work a single nonlinear layer, was able to perform similarly than a VNLE, and even more, slightly better for high data bit rate scenarios. In [126], the authors completed the study using an experimental setup. In [127], it was presented a classifier NN capable of handling nonlinearities in an IM/DD experimental setup for short distances. An interesting study of possible pitfalls when using NN in optical communications is presented in [128], having as a study

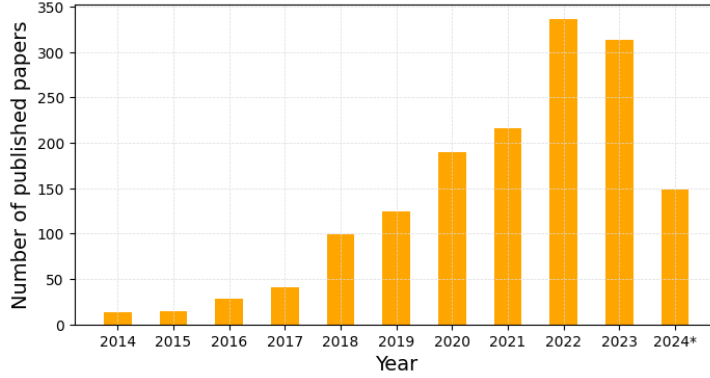


Figure 4.4 – Estimation of published papers on optical fiber nonlinearity compensation/mitigation using neural networks. Source: Google Scholar \*up to May 2024.

case the IM/DD system. Also, in [129], it was experimentally shown that an NN performing classification can compensate for fiber nonlinearity in IM/DD systems in short distances.

Focusing on coherent optical transmission systems has been intensive research in this area in recent years, as shown in Fig. 4.4. Some studies have dedicated their efforts to summarize the recent advances in this topic, for instance, in [130], [131]. In this part, we present a general review of the progress of this topic from 2018 up to now. Table 4.2 presents some of the most relevant and impressive studies we could observe. We have chosen four criteria to distinguish each other: SC or WDM channels, NN type, Regression or Classification tasks, and Simulation or Experimental setups. We have also indicated the physical channel model considered in numerical studies or even for the NN architecture building phase.

Table 4.2 – Summary of most relevant and impressive studies that covered fiber nonlinearity compensation using neural networks in coherent communications.

Ref	Author (et al.)	Year	NN	Reg/Class	SC/WDM	Physical Eq.	Sim/Exp
[37]	Sidelnikov	2018	MLP	Reg.	Both	NLSE	Sim.
[132]	Kamalov	2018	MLP	Reg.	Both		Exp.
[44]	Schadler	2019	MLP	Reg.	SC (BtB)		Exp.
[45]	Zhang	2019	MLP	Reg.	Both		Exp.
[38]	Catanese	2020	MLP	Reg.	SC	CNLSE	Sim.
[40]	Deligiannidis	2020	LSTM	Reg.	Both	Manakov	Sim.
[124]	Koike-Akino	2020	DNN-TEQ	Class.	WDM		Sim.
[133]	Nguyen	2021	MLP	Reg.	SC-PCS		Exp.
[43]	Freire	2021	MLP/Hybrids	Reg.	SC	Manakov	Both
[134]	Kamiyama	2021	MLP	Reg.	SC		Sim.
[135]	Schadler	2021	MLP	Class.	SC		Exp.
[39]	Sidelnikov	2021	CNN	Reg.	Both	CNLSE (WDM)	Sim.
[136]	Schadler	2021	biRNN	Class.	WDM		Exp.
[137]	Freire	2021	CNN + biLSTM	Reg.	SC	Manakov	Sim.
[138]	Freire	2022	MLP, biLSTM	Both	SC	Manakov	Both
[139]	Arguëllo	2022	MLP	Reg.	SC	Manakov	Both
[4]	Diedolo	2022	MLP	Reg.	SC		Exp.
[140]	Li	2022	CNN	Both	Both	Manakov	Both
[141]	Freire	2022	DCNN, biLSTM	Reg.	SC	Manakov	Both
[142]	Ming	2022	biLSTM	Reg.	WDM		Exp.

We briefly describe these studies in the following, highlighting the essential findings and main discoveries. We have grouped the studies in sections according to the NN type. Even so, some of these works explored multiple kinds of NN for comparison purposes. In such cases, we have indicated all the NN types in Table 4.2 (in the NN column) and also in the corp of the text.

### Multilayer Perceptron

First NLI compensation techniques based on NN focus their attention on MLP since its implementation is very straightforward. However, as the MLP acts as a black box, the choice of hyperparameters was the first aspect that many works worried about. For instance, in [37], the authors proposed an MLP, termed dynamic because the input collected some past symbols apart from the Symbol of Interest (SOI) using delay blocks at the input. This approach was widely adopted in posterior works as well. The hyperparameters optimization consisted of optimizing the hyperparameters (specifically, the number of delay taps, the number of layers, and the number of units per layer) one by one while keeping the others fixed. In this work, the MLP showed to outperform a DBP 2 StPS in SC and WDM configurations using a DP-16QAM for several spans of 100 km of SSMF. On the other hand, the optimal power is almost conserved, contrary to the DBP case. The details of the DBP implementation were not provided, and we believed that an optimized DBP could work significantly better.

In [132], it was experimentally demonstrated that an NN MLP could compensate for fiber nonlinearity in transoceanic distances ( $\sim 11,017$  km) in a live-traffic carrying cable. Using a PCS 64QAM, a simple NN with two hidden layers and an input layer including supplementary nonlinear features such as the IXPM and the IFWM triplets in the input layer, the NN was capable of increasing the Achievable Information Rate (AIR) and the Q-factor in SC and WDM systems.

In [45], the NN in [132] was optimized to provide good results with the lowest complexity, which the latter was achieved by placing the MLP at the transmitter side. Also, the IXPM and IFWM triplets, used in the training phase, are obtained using an averaging process of the ASE noise and the interchannel nonlinearity in repeated sequences of training data.

In [44], the authors utilized the MLP to compensate for optical and electrical nonlinearities. Using an experimental setup of a DP-16QAM 88 Gbaud and using pilot symbols for the adaptive DSP algorithms, in a BtB scenario, the MLP showed a better performance than the VNLE. Also, this work noticed that an MLP that jointly compensates for the I and Q components is slightly worse than an MLP that processes I and Q independently. This last finding was not observed in successive works, and most of them prefer to utilize NN to compensate for the I and Q components jointly and, even more, both polarization at once.

In [38], the authors explored the case of DP-16QAM 32Gbaud in  $4 \times 100$  km of SSMF. In this study, the authors consider as target data the received data in a configuration setup with the nonlinear coefficient set  $\gamma = 0$ . This choice differs from similar works in which the target is the transmitted symbol. They also showed that using a numerical and experimental setup, an MLP working at 1 SpS after the phase recovery algorithm works better than after the MIMO equalizer.

An interesting study was done in [124] about using Turbo Equalizer based NN for nonlinearity compensation. This novel approach replaces the BCJR equalizer, which performs nonlinear equalization, by a deep NN, which, in addition to the binary information corresponding to the QAM symbols, is fed with the Forward Error Correction (FEC) soft output to enhance accuracy.

The results showed an improvement on the AIR with respect to linear equalization and classical deep NN.

The combination of PCS and an MLP was also explored in [133], using DP-64QAM and DP-256QAM. A short MLP with 24 input nodes, two hidden layers with ten units each and with Tanh activation function, and an output linear layer with four units was employed in these experiments. The performance gain was validated through the Mutual Information (MI), observing that more robust shaping shows better performance gain than uniform and moderate shaping.

In [43], the authors studied the MLP capabilities compared to other NN types. The transmission scenario was a SC DP-16QAM 34.4 Gbaud over  $9 \times 50$  of TWC fiber, which has a reduced CD and a higher nonlinear coefficient than the SSMF. They showed that an optimized MLP is adequate for limited available complexity, taking into account the limited performance gains of an MLP with respect to the other tested NN. Also, an MLP with a different number of hidden units per layer is more advantageous than with an equal number of units.

An interesting and innovative approach was presented in [134], which proposed adding random phase noise (like the one produced in the transmitted laser and the LO) to the target signal during the training phase. Indeed, the random phase noise could avoid the NN to learn the deterministic phase noise generated by the NLI that is already challenging for the ASE noise generated in the EDFA. Adding a random phase noise to the target permits the NN to concentrate in deterministic NLI. The simulation results of an SC SP-16QAM 32Gbaud over  $14 \times 50$  km of DSF show a good trade-off performance complexity using both real-valued and complex-valued NN.

In [44], a classifier MLP was studied in a BtB configuration to handle optical and electrical nonlinearities in high data baud rate systems, showing an improvement with respect to the VNLE with still lower CC.

Recently, in [138], the authors highlighted some caveats and pitfalls when using NN based nonlinear equalizers. Specifically, they employed an MLP and an bidirectional LSTM (biLSTM). Important aspects were covered, such as the importance of uncorrelated training, validation, and testing datasets or the use of large mini-batches during the training to account for a good representativeness of the whole dataset. They also addressed the phenomenon observed in the equalized signal constellations, which they called “jail window” pattern, which we extensively covered in Chapter 5.

In [139], it has been demonstrated that a low-complexity NN using an MLP architecture could be achieved using pruning and quantization techniques. The low-complexity NN was implemented in hardware units and tested with numerical data, showing a significant reduction in complexity without noticeable performance degradation.

In [4], the authors proposed a modified loss function based on the MSE called MSE-X, capable of handling with the so-called “MMSE-scatterplot”, and experimentally tested using an MLP. We delve further into this problem in chapter 5.

## **Convolutional Neural Networks**

In [39], the authors proposed a deep CNN (DCNN). The proposed DCNN takes into account SPM and XPM but not PMD or PSP rotation and was numerically tested in a WDM  $11 \times 64$  Gbaud DP-16QAM,  $40 \times 80$  km SMF, processing an SC or five channels simultaneously. The deep CNN consisted of linear layers based on FIR filters in cascade layer by layer, jointly

optimized to compensate for the accumulated CD span by span, an approach very similar to the one implemented into the VNLE. A customized nonlinear activation function based on the nonlinear operator of the enhanced SSFM that considers neighboring samples, neighboring spectral channels, and dual polarization. The DCNN performed better than the DBP at various StPS with the same complexity. On the other hand, with the same performance, the DCNN is much less complex than the DBP.

In [140], a CNN based on the perturbative analysis was used for NLI compensation and tested in an experimental setup SC 120 Gb/s DP-64QAM and a numerical setup WDM 8x120 Gb/s, both over 5x75 km SSMF. The proposed method used a feature map of the received signal. The results showed better performances than an MLP-based perturbative analysis method with reduced CC.

In [141], the authors implemented a CNN and a biLSTM in an FPGA. Results showed Q factor improvements of more than 1dB with numerical and experimental setups compared to the CDC, while  $\times 3$  and  $\times 2$  more complexity using biLSTM and CNN, respectively. In this case, the experimental setup consisted of a DP-16QAM 34Gbaud 17x70 km LEAF.

### Recurrent Neural Networks

In [40] was explored an RNN of type Long Short-Term Memory (LSTM) and tested using a DP-16QAM in C+O bands for several spans of 50 km. In SC, the LSTM showed similar performances to the DBP 4 StPS. In WDM, the LSTM outperformed DBP 6 StPS. The LSTM proved to be more efficient in WDM than in SC scenarios. Also, the LSTM was tolerant to power variations and modifications of neighboring channel modulation formats. Finally, in the computational complexity analysis, the LSTM seemed more efficient than the DBP for long distances ( $> 1000$  km).

Also, in [136], the authors proposed a bidirectional RNN (biRNN) capable of leading with nonlinear ISI generated in high-speed data transmissions, for instance, in a DP-32QAM 92Gbaud (800 Gb/s). The biRNN employed a final output dense layer to output  $m = 5$  soft-bits. Therefore, this biRNN performs a classification task and uses the binary cross-entropy loss function, showing that this function is optimal as it maximizes the achievable information rate. Using a data-aided approach with pilot symbols in the experimental setup, the authors demonstrated the superior performance of the biRNN against a classical MLP in a WDM  $5 \times 96$ Gbaud DWDM transmission over  $6 \times 100$  km of G.654D fiber.

A modified biLSTM called co-LSTM for center-oriented LSTM was proposed in [142] and tested in a WDM  $10 \times 64$ Gbaud 16QAM  $20 \times 80$  km SSMF. The co-LSTM utilizes a mechanism called “recycling mechanism”, which allows complexity reduction. The co-LSTM is at the end of the DSP stack, working at 1 StPS. The training and testing datasets were small, with only  $2 \cdot 10^4$  and  $2 \cdot 10^5$  symbols and mini-batches of 60 symbols. The co-LSTM showed similar results of a DBP 1 StPS but with  $\sim$  less 70% of real multiplications per bit, which was notable.

### Hybrid Neural Networks

Combining different NN architectures to handle the residual CD and the NLI has been another methodology explored in several works. For instance, in [43], the authors employed a CNN as a pre-processor to extract the most relevant features for subsequent processing using an MLP or a biLSTM, indicating that these combinations show better performances than a deep

CNN alone. The transmission scenario was a SC DP-16QAM 34.4 Gbaud over  $9 \times 50$  of TWC fiber. However, these combinations are hungry resources with a large number of parameters required to achieve such good performances.

The Transfer Learning (TL) technique was also explored in [137] under various transmission numerical setups. The objective was to demonstrate the capabilities of TL under changes in fiber type, symbol rate, launch power, and modulation formats. The numerical setup consisted of a DP-16QAM 34.4 Gbaud over  $18 \times 50$  km of SSMF and  $9 \times 50$  km of TWC. The authors employed a CNN followed by a biLSTM. The main finding could be summarized as follows: 1) changes in launch power and symbol rate necessitate a small number of epochs to be retrained with a smaller quantity of training data, and 2) changes in modulation formats do not necessitate retraining by TL as soon as the other parameters remain constant. Also, the TL proved to be more effective when the scenario moves from the higher nonlinearity to the lower one.

### 4.3.2 Implementation and Tests using a Numerical Setup

In order to understand the capabilities of NN as nonlinear equalizers, we use the numerical scenario presented in Section 3.1.5, i.e., including the impairments induced by the optical fiber as CD, PMD, and NLI, but also the ones due to inherent imperfections of optical devices such as the CFO and the LPN.

We started our investigation with an NN processing samples at one SpS after the Carrier Phase Recovery (CPR) algorithm. The Fig. 4.5 depicts the DSP algorithm stack, including the NN-based nonlinear equalizer.

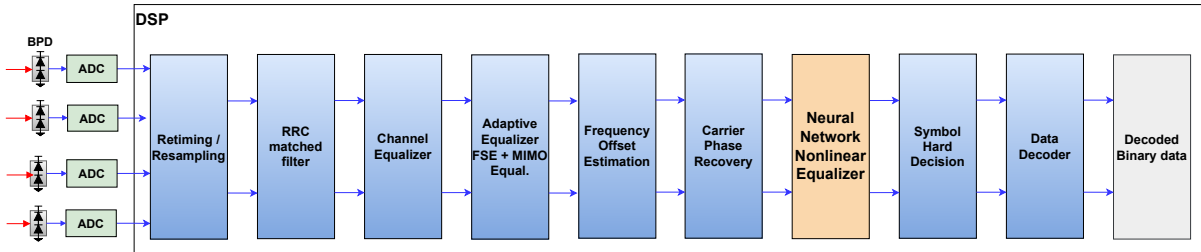


Figure 4.5 – DSP with NN nonlinear equalizer after the CPR algorithm.

The choice to place the NN after the CPR is motivated by the following reasons: i) The CD and PMD for the entire link are assumed to be already compensated, reducing the channel memory due to the ISI that provokes pulse overlapping. ii) The two polarizations are already separated, permitting a lower complexity NN (similar to a single polarization case), iii) An optimal downsampling based on the FSE algorithm has permitted to obtain samples at one SpS also reducing the processing load for the NN, iv) The CFO and random phase fluctuations due to the laser phase noise are already compensated, allowing a focus in deterministic nonlinear phase noise.

However, there are also some drawbacks to this approach: i) no considerations about the interplay between the CD, PMD and the NLI since they act together as described in Section 2.4, ii) the algorithms such as the adaptive equalization, CFO estimation, and CPR are commonly designed to work with compensated or neglected NLI, being not optimal when we account for the NLI.

In this first part, we prioritize the benefits of such a place for the NN (after the CPR) and let the study of the position of NN for Section XX. Furthermore, an NN at the end of the DSP chain, before decoding, could also be helpful for compensating all the residual impairments due to non-sub-optimal DSP algorithms.

For the training and validation, we generated two different datasets using a pseudo-random number of bit sequences for each polarization and dataset. The pseudo-random binary sequences are generated using the Mersenne Twister generator [143] with a periodicity of  $2^{19937} - 1$  and is the default generator in many programming tools, including Python and Matlab.

We focus our investigation on the simplest NN, the MLP, which theoretically could approximate any nonlinear function provided that it has sufficient capacity and was adequately built [123].

### Data pre-processing for datasets building

In supervised learning, the training and validation datasets are constituted by an input  $X$  and a target  $y$ <sup>3</sup>. Depending on the NN position,  $X$  results from previous DSP techniques, and  $y$  comes from the transmitted symbols.  $X$  is not directly the vector of complex symbols that we denoted as a vector  $\mathbf{x}$ , but a formatted representation of them. Specifically, the raw data from  $\mathbf{x}$  containing  $N_{symb}$  complex symbols are first divided into its real and imaginary parts, giving as a result a real-valued matrix of size  $(N_{symb}, 2)$ . At this part, the rows correspond to the  $N_{symb}$  symbols, and the features are the real and imaginary parts of these symbols, meaning that the unique features that permit to characterize a symbol fully are their real and imaginary parts of that symbol. As previous works show, in channels with memory (as the optical fiber), where a symbol is perturbed by its neighboring symbols due to the interplay between the CD and the NLI, we must consider the neighboring symbols as additional features for each symbol. Even if the CD is digitally pre-compensated using DSP, we must consider the residual channel memory due to this interplay. Thus, we accompanied each symbol by its  $N$  past and  $N$  future symbols, separated into their real and imaginary parts, making a matrix of size  $(N_{symb} - 2N, 2N + 1, 2)$ . When considering two polarizations, the matrix size becomes  $(N_{symb} - 2N, 2N + 1, 4)$ , where the features of the second polarization are vertically stacked next to the features of the first polarization. Therefore, the input  $X$  correspond to this matrix of size  $(N_{symb} - 2N, 2N + 1, 4)$ . Similarly, the target  $y$  comes from the vector of complex transmitted symbols denoted by  $\mathbf{y}$ . Following the same reasoning as for the input, the target  $y$  has a size  $(N_{symb} - 2N, 4)$ .

In general, for a dual-polarization case,  $X$  has the size  $(N_{symb} - 2N, 2N + 1, 2Pol_{in})$  and  $y$  the size  $(N_{symb} - 2N, 2Pol_{out})$ , where  $Pol_{in}$  and  $Pol_{out}$  stand for 1 or 2 polarization considered at the input. Clearly, when  $Pol_{in} = 1$  then  $Pol_{out} = 1$ , but when considering two polarizations at the input, we might be interested in obtaining only one polarization component ( $Pol_{in} = 2$  and  $Pol_{out} = 1$ ) or the two polarizations components at the same time ( $Pol_{in} = 2$  and  $Pol_{out} = 2$ ).

Even more generally, we cannot limit ourselves to treating data at 1 sample per symbol but with oversampled data. In this case, the input  $X$  size and the target  $y$  size become  $(N_{symb} - 2N, 2N + 1, 2S_{in}Pol_{in})$  and  $(N_{symb} - 2N, 2N + 1, 2S_{out}Pol_{out})$ , respectively, and where  $S_{in}$  and  $S_{out}$  are the oversampling factor (samples per symbol) for the input and the target.

For training and validation datasets, the input  $X$  and target  $y$  are reshaped to a size  $(N_B, B, 2N + 1, 2S_{in}Pol_{in})$  and  $(N_B, B, 2S_{out}Pol_{out})$ , respectively, where  $N_B$  is the number of

---

3. Conventionnaly, in machine learning,  $X$  and  $y$  are the denotations for the input and the target, respectively

mini-batches and  $B$  is the mini-batch size.

Concerning the testing dataset, it is composed of  $2^{18}$  symbols independent from the training and validation datasets.

### Hyperparameters optimization and Training process

Following the format used in other studies, we represent the MLP as  $N_i|N_1|f_a|\dots|N_L|f_a|N_o$ , where  $N_i$  signifies the number of neurons in the input layer,  $N_h$  denotes the number of neurons in the hidden layer  $h$  (with  $1 \leq h \leq L$ ),  $L$  signifies the total number of hidden layers, and  $N_o$  represents the number of neurons in the output layer. After each layer (linear part), we applied a nonlinear activation function  $f_a$ , except for the output layer.

The hyperparameters to be tuned are the number of neighboring symbols  $N$ , the number of hidden layers  $L$ , the number of units per layer  $N_h$  (with  $1 \leq h \leq L$ ), and the learning rate  $\epsilon$  defined in (4.2). We fixed the nonlinear activation function hyperbolic tangent. In this work, we used the Optuna [144] framework, available in Python, which utilizes the TPE algorithm. For this technique, we must define an objective function, i.e., that set of hyperparameters will be appropriate to maximize or minimize a metric. Notice that this is different from the Loss minimization used during the training. We aimed to minimize the loss between the target and the prediction during the training. The objective function in hyperparameter optimization aims to optimize a metric that could be different from the loss, with the unique purpose of selecting an optimal set of hyperparameters.

In this chapter, let us consider the objective function, error rate minimization. As an error rate metric, we choose the Symbol Error Rate (SER) as we work directly with symbols, not bits. The BER consideration will give proportional results.

Consider the case of a DP 16-QAM 32Gbaud over  $14 \times 100$  km of SSMF. Also consider the case of solving the Manakov equation (2.40) through the SSFM, i.e., without the PMD, which is random, and additionally without the LPN, which is also random. The CFO is deterministic, but normally, it is not a big challenge for the DSP and is commonly neglected. Therefore, we consider, for training, the simplified DSP shown in Fig. 4.6.

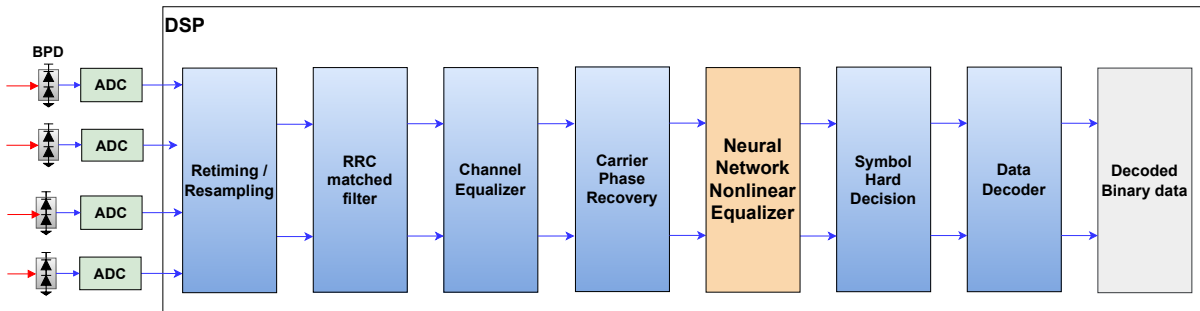


Figure 4.6 – DSP receiver used for Manakov-equation based model without CFO and LPN.

To find the optimal hyperparameters, let us choose a dataset corresponding to an input  $\mathbf{x}$  with launch power 3dBm, which is 1dB higher than the optimal power. We choose to work with two polarizations in the input  $S_{in} = 2$  and one polarization at the output  $S_{out} = 1$ .

The hyperparameter optimization was done using the following configuration:

- Number of taps  $N \in \{5, \dots, 20\}$ .

- Number of layers  $L \in \{1, 3\}$ .
- Number of hidden units per layer  $N_h \in \{50, 60, \dots, 1500\}$ .
- Learning rate  $\varepsilon \in \{10^{-4}, 5 \cdot 10^{-4}, 10^{-3}\}$ .

These options correspond to our available computational resources. Certainly, higher values of hyperparameters could potentially lead to very complex NN that could lead to overfitting problems and, more importantly, to impractical NN architectures that are hardly realizable in real-time.

We ran up to 35 trials, finding that trial 34 provided the lowest SER. Further trials provided similar SER values, showing that the TPE algorithm was at a standstill, so we stopped the process. The results per trial are shown in Fig. 4.7.

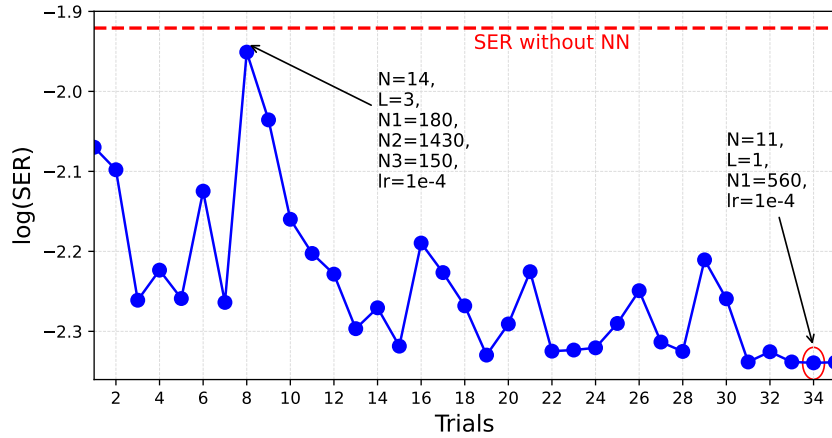


Figure 4.7 – SER per trial using the hyperparameter optimization framework Optuna in a DP-16QAM system at 3 dBm over  $14 \times 100$  km of SSMF.  $N$  represent memory taps,  $L$  is number of hidden layers,  $N_h$  is number of hidden units in layer  $h$ , and  $lr$  for learning rate. The dashed red line is the level of SER without NN.

Fig. 4.8 shows the evolution of the MSE loss function per training epoch for the training and validation datasets. In the same figure, we depict the SER calculated in the validation dataset, which serves to stop the training when it reaches 200 epochs without SER improvement.

These results also illustrate the importance of a well-chosen set of hyperparameters, where a bad choice could lead to very bad results, e.g., trial 8. Empirically, we observe that a single layer with sufficient units performs better in terms of SER than an NN with multiple layers.

## Tests and Results

We consider the Manakov-PMD equation (2.39) considering the CFO and the LPN for testing. Thus, we consider the full DSP shown in Fig. 4.5 at the receiver. For each level of launch power, we retrain the NN obtained with a P/ch = 3dBm for each launch power. The results are shown in Fig. 4.9 together with the CDC, DBP, and VNLE results.

In Fig. 4.10, we plot the IQ constellation diagrams for P/ch = 0, 1, 2, and 3 dBm using only CDC (first row) and with the MLP (second row).

In our study, we observe that an MLP is significantly less performant than the DBP or the VNLE. The MLP is not even close in such an explored scenario. Certainly, other studies

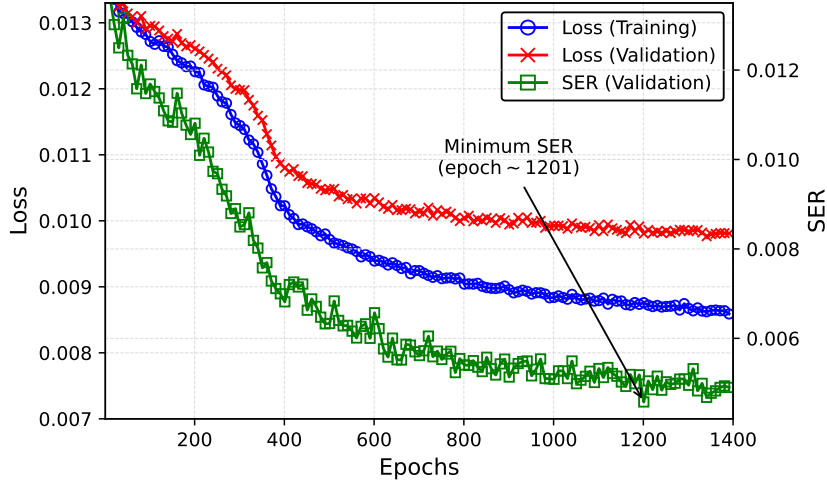


Figure 4.8 – MSE loss function in training (blue) and validation (red) datasets per epoch, and SER (green) in the validation dataset.

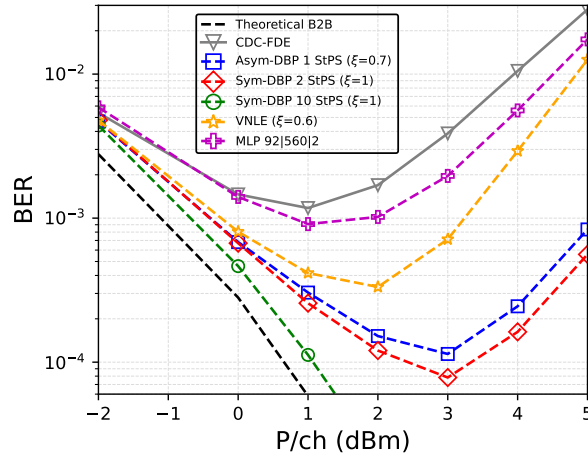


Figure 4.9 – BER vs. P/ch using the trained MLP at each P/ch for a DP-16QAM over  $14 \times 100\text{km}$  of SSMF and comparison with the DBP and the VNLE.

have shown good performances, even comparable to the DBP ones. However, the reader must consider that scenarios with shorter span lengths ( $< 100\text{km}$ ) and for different fiber types with higher nonlinearity and lower CD are more favorable to the use of NN. The reader could refer, for instance, to [46, Fig. 7], where a numerical setup using Large Effective Area Fiber (LEAF) shows better performances than a setup using the SSMF that shows even worse results than ours.

Even though, in this investigation, we are focusing on long distances optical fiber using the SSMF, with the objective to show the advantages and disadvantages of using NN, particularly for nonlinear equalization.

We must also account for an additional metric, which is the CC of the MLP. The CC of the algorithms was examined in terms of the number of real multiplications required to predict each

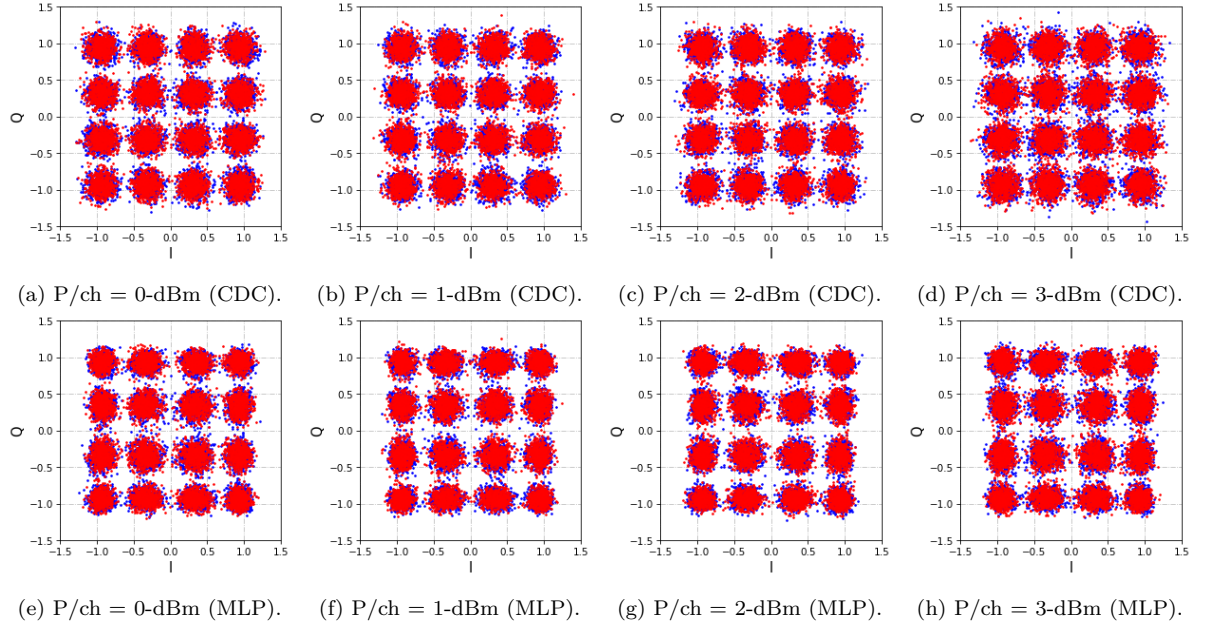


Figure 4.10 – IQ constellation diagrams using only CDC (first row) and the MLP (second row).

symbol (RMpS). We neglected the addition operations (small with respect to RMpS) and the operations associated with the nonlinear functions, assuming look-up table-based methods [43]. This CC is clearly related to the number of parameters. More formally, the CC of the MLP measured in RMpS is defined as follows:

$$CC_{MLP} = N_i \times N_1 + \sum_{h=1}^{L-1} (N_h \times N_{h+1}) + N_L \times N_o, \quad (4.11)$$

where  $N_i$  is the number of units in the input layer,  $N_h$  is the number of units of the hidden layer  $h$ ,  $1 \leq h \leq L$ , being  $L$  the number of hidden layers, and  $N_o$  is the number of units of the output layer.

However, as the MLP is equivalent to successive matrix multiplications, current processors could perform multiple tasks concurrently (threads) even if the number of multiplications is very large. Matrix multiplications could be processed with simultaneous row-by-column multiplications using multiple threads per processing unit, significantly reducing the processing time.

This can be verified by observing the processing time per recovered symbol, estimated similarly as in 3.2.3. Fig. 4.11 shows the CC in RMpS and the processing time for the MLP, where we plot the corresponding ones again using the CDC, the DBP, and the VNLE for comparison purposes. For the MLP, we added the CDC since, in our configuration, the CDC-FDE is still employed.

In our study, even if the RMpS of the MLP is largely superior to the other methods, the MLP shows a significant processing time reduction compared to the DBP and VNLE implementations, as is expected due to the previous reasoning or multi-threading capacities of processors.

A clear disadvantage of the DBP and the VNLE against the MLP (or any data-aided channel equalizer) is that both require a good knowledge of the optical link and the fiber parameters,

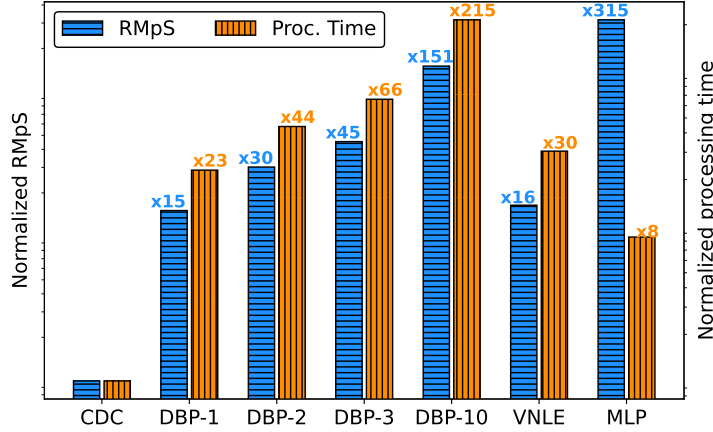


Figure 4.11 – Computational complexity in RMpS and processing time in Logarithmic scale including the MLP.

which the MLP does not need.

In this section, we have highlighted the importance of finding a good set of hyperparameters in order to provide good results using an error rate metric (BER, SER). This process involves two steps executed for different sets of hyperparameters: i) a training model using a minimization loss criterion with validation loss monitoring to avoid overfitting, and ii) in the validation dataset, calculate the error rate metric per epoch to choose the model that fits better. This process could be very time-consuming, particularly dependent on the number of sets of hyperparameters (trials) to consider and the validation dataset size.

In practice, we only rely on the training/validation metric, i.e., the loss function, without additional monitoring metrics. We repeated the hyperparameters optimization process using only step (i) and selected the model that provides the lowest loss.

The hyperparameter optimization was done using the following configuration:

- Number of taps  $N \in \{5, \dots, 20\}$ .
- Number of layers  $L \in \{1, 2\}$ .
- Number of hidden units per layer  $N_h \in \{50, \dots, 1000\}$ .
- Learning rate  $\in \{10^{-4}, 5 \cdot 10^{-4}, 10^{-3}\}$ .

The recovered lowest MSE loss per trial is shown in Fig. 4.12.

We chose trial 13, which consists of two hidden layers, opposite to the previous recovered set of hyperparameters with one hidden layer when the objective metric was the SER. In the same figure, we show the set of hyperparameters that gave the highest MSE (trial 11) and accounted for one single hidden layer. In general, a single hidden layer shows a lower capability to provide lower values of MSE loss, but that could also depend on the number of hidden units; e.g., trial 12 has two hidden layers but with a more significant number of units, resulting in a higher MSE loss.

The MSE loss per epoch using the set of hyperparameters of trial 13 is shown in Fig. 4.13. The training is stopped after 200 epochs of no MSE loss improvement in the validation dataset.

For each P/ch, we retrain the NN. The trained models are used in a testing dataset, and we calculate the BER for each P/ch. The results are shown in Fig. 4.14 with the previously

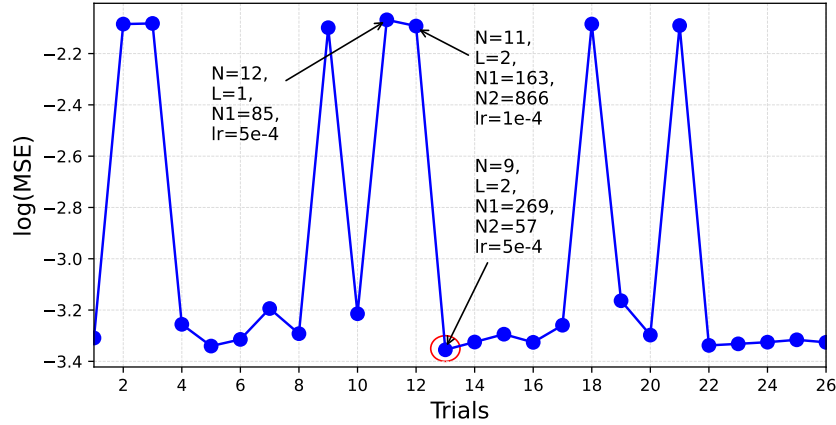


Figure 4.12 – MSE loss per trial using the hyperparameter optimization framework Optuna in a DP-16QAM system at 2 dBm over  $14 \times 100$  km of SSMF.  $N$  represent memory taps,  $L$  is number of hidden layers,  $N_h$  is number of hidden units in layer  $h$ , and  $lr$  for learning rate.

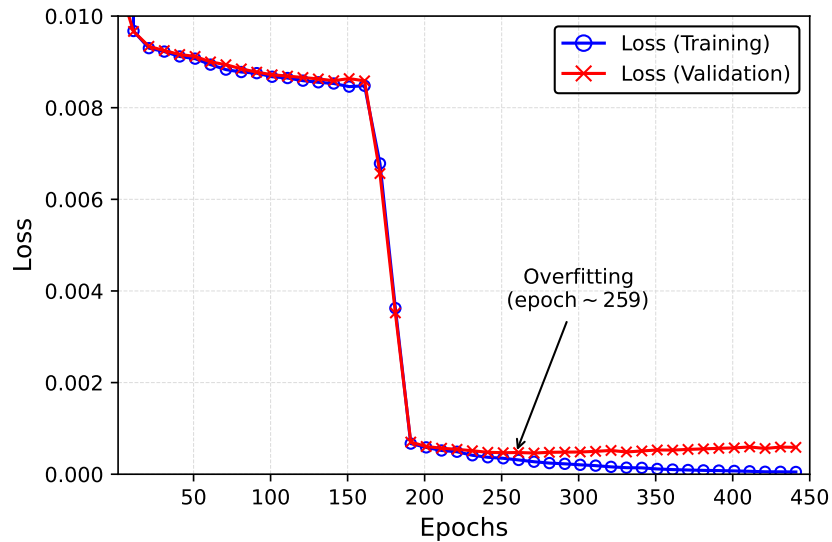


Figure 4.13 – MSE loss function in training (blue) and validation (red) datasets per epoch.

obtained results of the DBP, VNLE, and the MLP with optimized hyperparameters with SER objective function.

The IQ constellation diagrams are shown in Fig. 4.15.

Interestingly, the IQ constellation diagrams present a deformation adopting a grid shape. This observation was also noticed in a limited number of studies. The reasons why the constellation diagrams of the equalized signal when using NN (MLP in this case) are intensely studied in the following chapter.

The position of the NN was arbitrarily placed at the end of the DSP receiver before the symbol detection. We began this section by specifying that this choice has some benefits and drawbacks. In the next part, we further explore different alternatives of the position of the NN

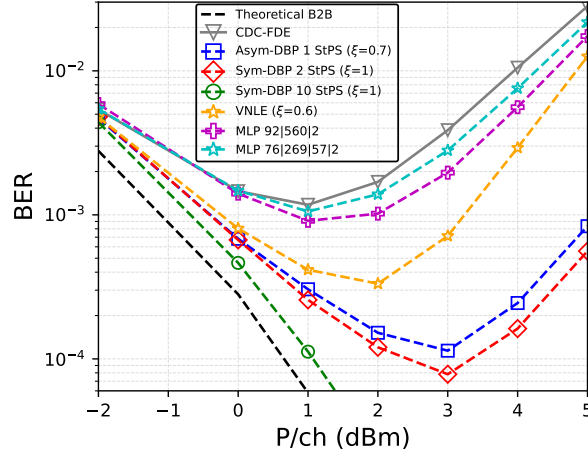


Figure 4.14 – BER vs.  $P/ch$  using the trained MLP at each  $P/ch$  for a DP-16QAM over  $14 \times 100$ km of SSMF.

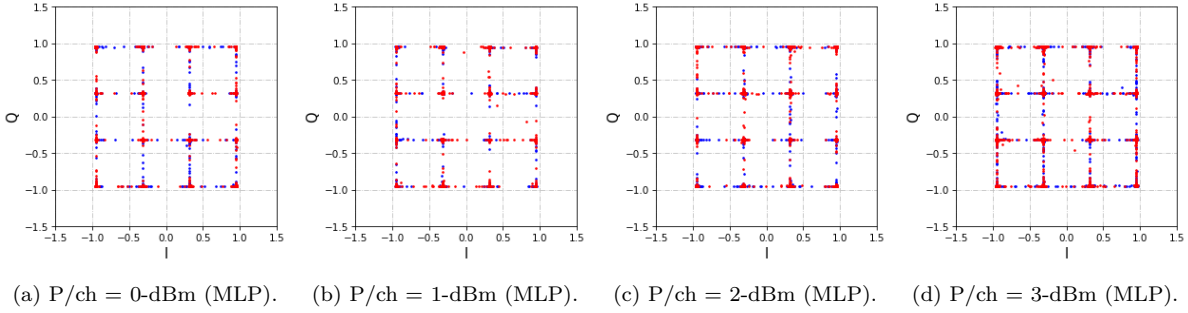


Figure 4.15 – IQ constellation diagrams using only CDC the MLP.

using the MLP.

### 4.3.3 Study of the position of the MLP

In this part, we explore two alternatives of the MLP position: i) immediately after the linear compensation with a focus on nonlinear compensation and ii) immediately after channel filtering and downsampling and comprising linear and nonlinear compensation jointly. Nevertheless, the MLP is a static algorithm (without retraining). In our dual polarization setup, the MLP would be incapable of handling time-varying impairments such as the laser phase noise and the SOP rotation due to linear birefringence. Therefore, to test the effectiveness of the MLP regarding its position in the DSP receiver, it is necessary to alleviate the setup, specifically neglecting the laser phase noise and the SOP rotation.

To simplify the tests, we can consider a single polarization scenario, only affected by the CD and NLI. These tests permitted us to observe and analyze the differences in the MLP position in terms of BER and CC.

Fig. 4.16 shows the three possible scenarios of our single polarization setup.

The red dotted square represents the entire NN with static layers RRC and Norm. RRC is the matched filter with the same parameters as in the transmitter. “Norm” is a normalization

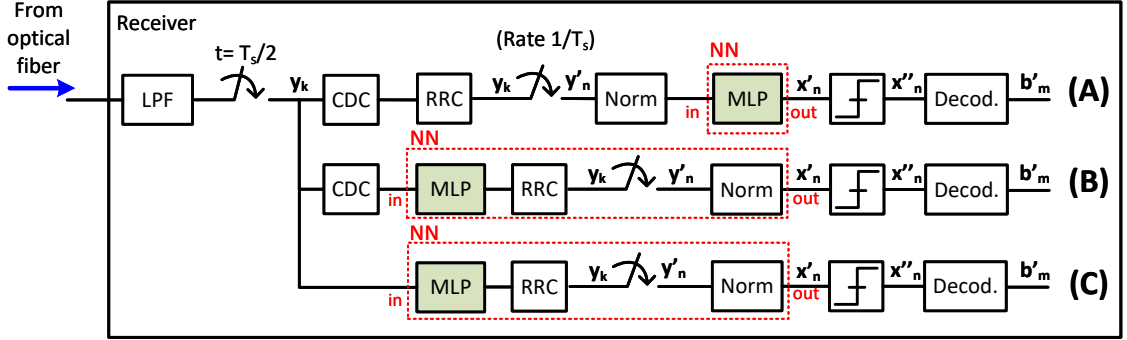


Figure 4.16 – Receiver configurations. A) MLP acting at 1sps with CD equalized signal, B) MLP acting at 2 sps with CD equalized signal, C) MLP acting at 2 sps with non-equalized signal. sps: samples/symbol, RRC: Root Raised Cosine, LPF: Low Pass Filter, CDC: Chromatic Dispersion Compensation ©2023, IEEE.

MLP	5x100 km					10x100 km				
	$N_i$	$N_1$	$N_2$	$N_o$	BER	$N_i$	$N_1$	$N_2$	$N_o$	BER
A	12	529	–	2	2.50e-6	14	242	–	2	2.66e-3
B	11	312	689	4	5.00e-6	20	583	102	4	2.89e-3
C	42	170	509	4	2.75e-5	79	301	155	4	4.03e-3

Table 4.3 – MLP architectures for  $N_{span} = 5$  and  $N_{span} = 10$  of 100km SSMF.  $n_i$ ,  $n_h$  ( $h = 1, 2$ ), and  $n_o$  are the number of neurons in the input, hidden, and output layers, respectively.

in phase and amplitude, taking the transmitted signal  $x_n$  as a reference. We placed the MLP at the last position of the stack of DSP blocks in scenario (A), letting the NN act for NLC. This is usually the case in most of the related works [37], [139]. In scenarios (B) and (C), NN were placed to process the signal at 2 SpS before the RRC filtering. This is also a natural choice concerning the classical DBP. Specifically, in (B), we considered that CD is fully compensated, while (C) treated the CD and NLI jointly. (A) and (B) tended to leverage the differences of applying the MLP for NLC at 1 sps (A) and 2 sps (B) with only CD compensation (CDC). (C) allowed comparing the benefits of the MLP for the CDC+NLC task. The three scenarios were tested using an SC SP-16QAM at 32 Gbaud for 5x100km and 10x100km SMF with no inline dispersion compensation and with an erbium-doped fiber amplifier (EDFA) to balance fiber span loss. We determined the impact of accumulated noise on the NN performance by varying the number of spans.

The number of layers and neurons per layer of the MLP were found using the TPE algorithm via the Optuna framework combined with a K-Fold Cross Validation (K=3) for better generalization. The classical “Tanh” was used as a nonlinear activation function. For the hyperparameters optimization, we chose a fixed launch power of 2.5dBm, which is  $\sim 3$ dB above the optimal power (minimal BER with only CDC), for all the MLP cases. Finally, we chose the model with low CC but still low BER calculated in the validation dataset among 50 trials. The details for those MLP are provided in Table 4.3, where  $N_i$ ,  $N_h$  ( $h = 1, 2$ ), and  $N_o$  are the number of neurons in the input, hidden, and output layers, respectively.

As can be seen, the number of input units is more significant in (C) than in (A) and (B). This

behavior was expected since CD equalization needs a large number of neighboring symbols  $M$ , increasing the input size in (C). Additionally, (A) required a single hidden layer for the scenarios with 5 and 10 spans, while (B) and (C), required both two hidden layers. This may be because there was twice as much data treated in (B) and (C) (due to the processing at 2 sps of the MLP) as in (A) (where the MLP operates at 1 sps).

We trained the MLP on 15 different datasets of 65536 symbols each (different bit generation patterns). In the MLP cases, for each dataset, we built batches of shape  $(B, S, n_s, 2)$ , where  $B$  is the batch size,  $S = 2N + 1$ ,  $n_s$  is the number of samples per symbol, and 2 corresponds to the real and imaginary parts of the complex sample, as we worked with a real-value MLP. The training and validation datasets were composed of the first 80% and the remaining 20% of batches, respectively. During the training, we randomly picked up batches of the training dataset. In general, we trained models up to 2000 epochs and chose the model with the lowest BER on the validation dataset. However, in some cases, we obtained the same BER in different epochs. For these particular cases, we chose the model with the lowest Kurtosis [145], equivalent to choosing a model that outputs a signal with Gaussian-like noise. The MLP training was done for every launch power as it was noticed that MLP could not predict the channel transfer function (CTF) for every launch power. Even though, for the linear part, it was enough to train the MLP around the optimal power for predicting the CTF in the linear regime.

For testing, a Monte-Carlo simulation of 100 runs with different random patterns was carried out at each run.

The results of the study in terms of BER are shown in Fig. 5.9a for (a) 5x100km and (b) 10x100km. Focusing on the results obtained using the MLP approaches, it can be seen in Fig. 5.9a(a) that methods (A), (B), and (C) all increased the optimal power by  $\sim 2$ dB. However, there are some observable differences between them: (A) allowed for slightly better performance than (B) and (C) around the optimal power, at the expense of a degraded behavior in the linear regime (low launch power). It can be noticed that this penalty in the linear regime can not be observable in more complex scenarios when frequency offset, laser phase noise, and polarization-dependant impairments are taken into account because NN could still mitigate the residual impairments of these accurate setups. (B) and (C) looked very similar, with slightly better results in (B). The MLP performances were between those of a 1 step/span (StPS) DBP and 2StPS DBP. In the case of 10 spans, shown in Fig. 5.9a(b), the results of MLP were quite different. Still, (A) and (B) achieved a BER improvement with respect to only CDC. On the other hand, (C) became more challenging for the MLP, probably because there were too many parameters that needed to be processed during the MLP optimization. The MLP results were, in this case, no better than a 1StPS DBP. The insets in 5.9a(b) represent the IQ constellation diagrams of the predicted signal in the optimal power.

The CC of the algorithms was examined in terms of the number of real multiplications required to predict each symbol (RMpS), similar to other studies [37], [43], [146]. We neglected here the addition operations (small with respect to RMpS) and the operations associated with the nonlinear functions assuming look-up table-based methods [43] (because it does not contribute to the CC).

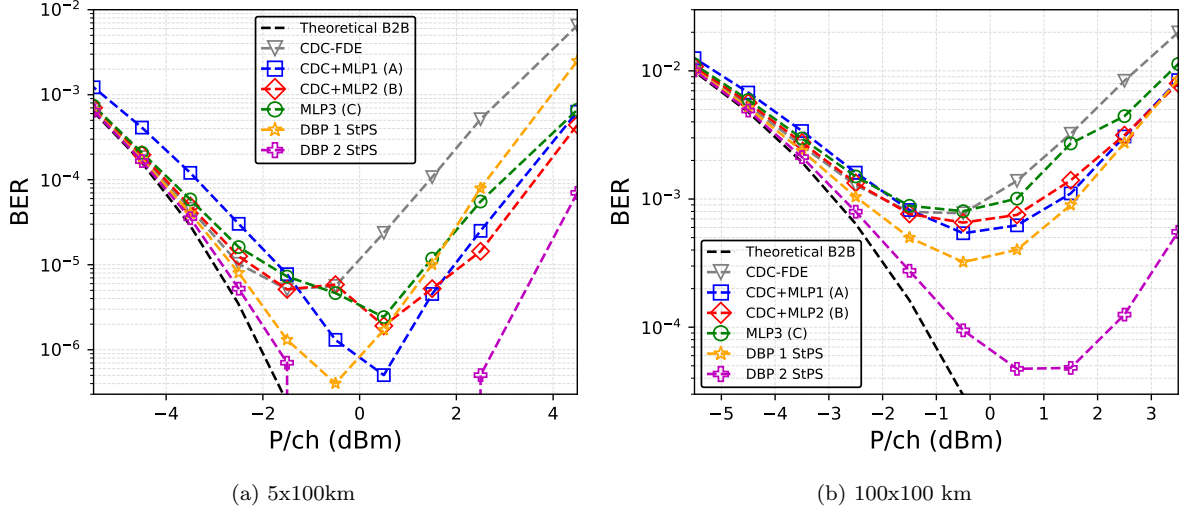


Figure 4.17 – Results BER vs.  $P/ch$  for scenarios (A),(B),(C),(D). CDC and a, 1StPS and 2StPS DBP results were added as a reference. The insets represent the IQ constellations of the predicted signal in the optimal power ©2023, IEEE.

#### 4.3.4 Implementation and Tests using the Experimental Setup

When training NN using data from an experimental setup, we must be careful about certain but important details. The data waveforms generated by software that feed the IQ modulators are commonly constituted by PRBS. This is because the PRBS reflects actual traffic with the advantage that the sequence is completely known and reproducible [7].

The PRBS is produced using Linear Feedback Shift Register (LFSR) and XOR operations. A PRBS of  $N$ -th order (hereafter PRBS- $N$ ) could be generated using LFSR with 2 or 4 inputs for the XOR operation, which output is sent to the first bit [147]. The PRBS is obtained at the end of the shift register when the process is repeated  $2^N - 1$  times. A PRBS- $N$  is characterized by having consecutive  $N - 1$  zeros and  $N$  ones and all the possible combinations of zeros and ones [148]. Fig. illustrates the LFSR-2 (1 inputs) and the LFSR-4 (4 outputs) for PRBS- $N$  generation.

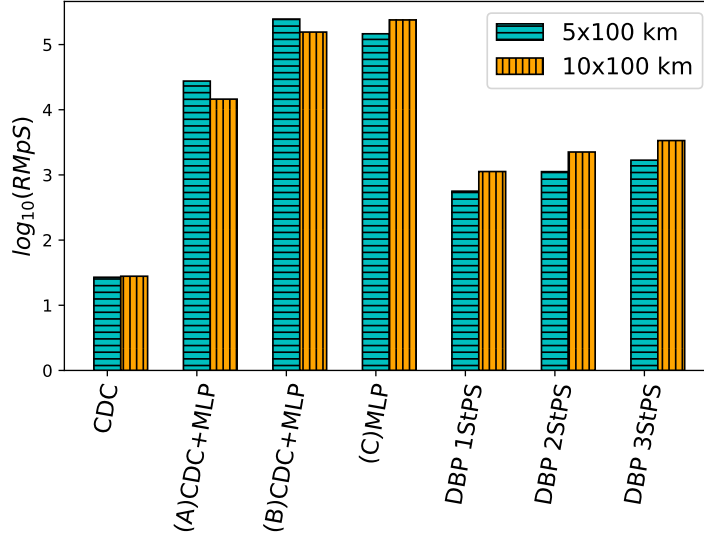
The corresponding 2 (or 4 bits) for the LFSR-2 (or LFSR-4) determines the PRBS order. For instance, a PRBS-7 utilizes the bits  $l_1 = 7$  and  $l_2 = 6$  for the LFSR-2 and the bits  $m_1 = 7, m_2 = 6, m_3 = 5, m_4 = 4$  for the LFSR-4. Similarly, the PRBS-15 utilizes the bits  $l_1 = 15$  and  $l_2 = 14$  for the LFSR-2 and the bits  $m_1 = 15, m_2 = 14, m_3 = 13, m_4 = 11$  for the LFSR-4 [147].

In the case of the LFSR-2, this is equivalent to the polynomials [128]:

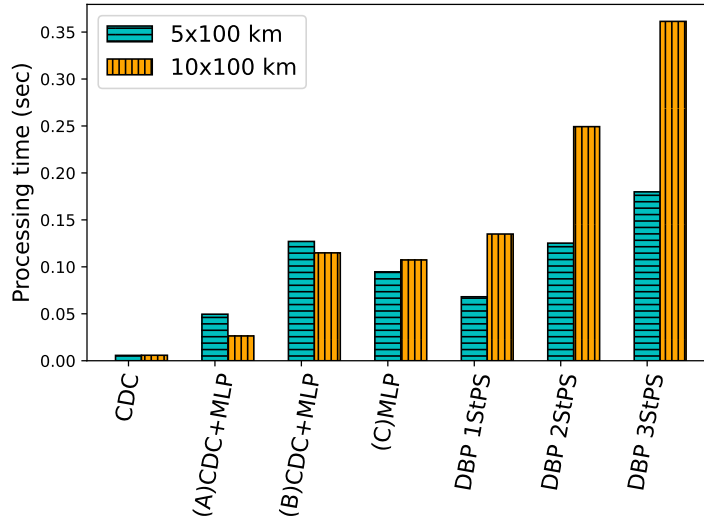
$$P_{PRBS-7}(x) = x^7 + x^6 + 1, \quad (4.12)$$

$$P_{PRBS-15}(x) = x^{15} + x^{14} + 1. \quad (4.13)$$

In the context of NN, the PRBS is a deterministic data flow whose pattern generation algorithm or periodicity could be easily retrieved by the NN given that we provide the NN a dataset whose length is greater than the PRBS length [128]. For those reasons, one must be cautious when using PRBS in the training phase. In our experiments, we could work with



(a) Real Multiplications per Symbol (RMpS)



(b) Processing time using an Intel Xeon 3.60GHz 8-core, 32GB RAM

Figure 4.18 – Computational complexity for scenarios (A),(B),(C). Results with CDC and a 1StPS DBP and 2StPS DBP were added as a reference ©2023, IEEE.

PRBS-15 continuously transmitted by the AWG. Under this scenario, we adopt the following strategy to avoid overfitting and overestimation of our results, following the recommendations given in [128], [138]:

- A PRBS-15 ( $2^{15}-1$  bits) generated by software corresponds to  $N_s \sim 8191$  16QAM symbols. The AWG continuously sends the  $N_s$  symbols several times with a sampling frequency equal to 92 GSa/s.
- At the receiver, the DSO working at 80 GSa/s, permit us to recover the transmitted samples. Using DSP, we retrieve the concatenated PRBSs synchronized with the transmitted

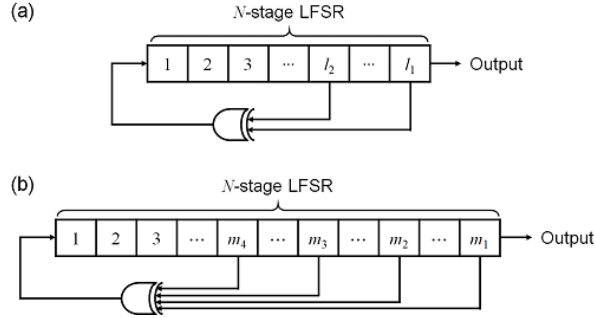


Figure 4.19 – (a) LFSR-2 and (b) LFSR-4 used to generate PRBS-N [147] © .

symbols.

- For training the NN, each PRBS is divided into 3 parts: training, validation, and testing. Inside the PRBS, we are sure the 3 parts are uncorrelated. Since a third of a PRBS-15 is  $\sim 2730$  16QAM symbols, insufficient to train an NN, we increase the training dataset by concatenating the first third of each PRBS. A similar procedure is used for the validation and testing of the dataset. This procedure is illustrated in Fig. 4.20. To avoid that, the NN always observes the same first third of the PRBS that constitute the Training dataset; at each epoch, we randomly rotate the symbols inside each third (only in the Training dataset) a multiple of  $\pi/2$ .

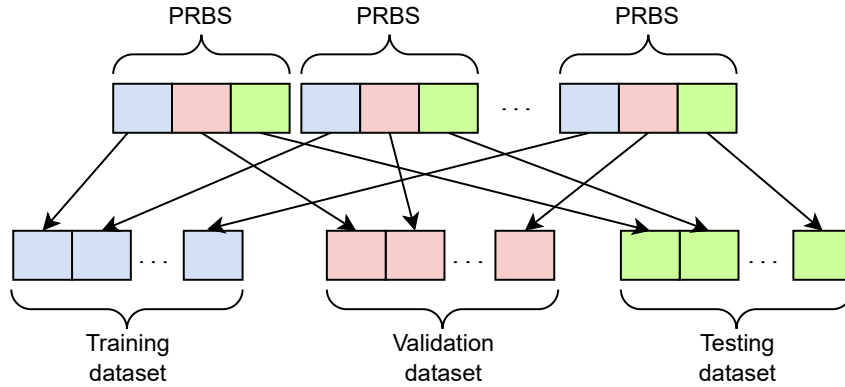


Figure 4.20 – Followed approach to train an NN using a dataset containing PRBS. To avoid the NN always observing the same first third of the PRBS that constitute the Training dataset, at each epoch, we randomly rotate the symbols inside each third (only in the Training dataset) a multiple of  $\pi/2$  ( $n, m, \dots, l$  are randomly and uniformly selected from  $\{0,1,2,3\}$ ).

The results obtained using the experimental setup could not be fully validated, and we believe the results necessitate a more extensive and exhaustive analysis in order to ensure that the NN has not learned the PRBS pattern. The problem arose because we did not have access to the transmitted data from the AWG<sup>4</sup> and instead we must rely on the cleanest back-to-back

4. The used version of the Keysight software, up to the submission of this manuscript, does not support the functionality of recovering the transmitted data.

processed data at highest OSNR to be considered as the transmitted data. This process helped us to recover the results shown in Section 3.3.3 but is less evident in the case of NN.

Our doubts surge mainly because, under some architectures, the NN seemed to converge perfectly to the target data in the training and validation datasets, surpassing the theoretical result. This is clearly a bad sign of a common pattern learned by the NN instead of the nonlinear channel transfer function.

In future works, we will be able to recover the transmitted data using an upgraded version of the Keysight software and generate data using large PRBS, not limited to a 15th order.

## 4.4 Summary

In this chapter we have seen that the use of NN as NLI equalizer has proven to be useful in numerical and experimental scenarios involving different type of fibers as well as different modulation formats and data rates in single channel and multichannel scenarios. Indeed, studies involving simple NN, such as the MLP up to more complex architectures combining different types of NN and using customized layers and nonlinear activation functions, showed that NN could retrieve more easily the nonlinear transfer function and, therefore, are good candidates for NLI compensation.

Simple NN architectures, such as the MLP, are the obvious candidates for real-time implementations. Therefore, it is crucial to study their capacities in facing typical scenarios using SSMF and longer spans. In this chapter, we have intended to cover this point of view. We consider a practical scenario consisting of  $14 \times 100$  km of SSMF and a 16-QAM modulation format, which is very realistic for modern transceivers (putting aside the recent Probabilistic Constellation shaping (PCS) technique) and a simple NN such as the MLP. In a numerical study, we noticed that an optimized MLP (taking into account the architecture that gives the lowest SER among other architectures) partially mitigates the NLI, being inferior in NLI compensation capacity to the DBP and the VNLE but with the advantage of being faster (considering a processing time metric) than the DBP (1 StPS) and the VNLE. Indeed, the accumulated ASE noise produced by the EDFA, combined with the NLI, highly perturbs the symbol phase, making the phase rotation almost random. We must highlight that we focus our study on a low-complexity MLP with at most three hidden layers and not more than 2000 neurons per layer. It is possible to obtain better results with a more significant number of parameters, as other works did (with a risk of provoking overfitting). Still, we believe such architectures are not helpful as the purpose of an NN is to operate in real-time, therefore with a limited number of parameters.

In conclusion, we believe the usage of the MLP in a real-time implementation is not advantageous as its capacity is very limited, even in single channel, playing down the interest of adding a NN block into the DSP chain if the gain is not appreciable.

# MMSE-DRIVEN SIGNAL CONSTELLATION SCATTERPLOT EFFECT

---

In the previous chapter, we highlighted a particular effect on signal constellation diagrams when using NN based nonlinear equalizers in conjunction with the MSE loss function in the learning process. This phenomenon has been observed particularly in QAM constellations, and was referred to “jail window” pattern in [138] or “MSE-grid scatterplot” in [4], [44]. These terms highlighted the rectangular nature of QAM constellations. This effect appears as a concentration of the equalized symbols around the original constellation points with some scattered along the straight lines between the neighboring points of the original constellation. This effect is called here “MMSE-driven signal constellation scatterplot” (MMSE-scatterplot) because it appears when using the minimum MSE (MMSE) criterion in the NN optimization. While the MMSE-scatterplot has been noted in multiple works on NN using the MSE loss function [37], [44], [125], [149]–[151], the focus on this phenomenon has gained more attention in recent works [4], [138], [152].

The presence of the MMSE-scatterplot can have detrimental consequences on subsequent signal processing blocks, especially on Soft-Decision (SD)-FEC schemes [4], [138], which require reliable soft information<sup>1</sup>. Furthermore, in the classical DSP coherent receiver, this soft-information is provided by the demapper based on the equalized signal but also on the optical channel law [153]. However, since this latter is usually unknown, an auxiliary memoryless AWGN channel is commonly assumed [153], which even proves to be a good assumption in the nonlinear regime [154]. Therefore, the role of the equalizer is to reconstruct the transmitted signal and provide the necessary information to the demapper in the form of constellation with Gaussian-like noise. The MMSE-scatterplot, however, completely disrupts the Gaussian-like properties expected by the demapper.

Besides this, the MMSE scatterplot also affects the AIR estimations, such as the MI and the Generalized Mutual Information (GMI), necessary for the BER after the FEC (postFEC-BER) predictions [153], [155]. Indeed, the MI and GMI, are commonly estimated through closed-form expressions using the auxiliary memoryless AWGN channel [155]–[157], proven to be lower bounds of the MI/GMI of the true channel with memory [158]. The MMSE-scatterplot effect induces a significant alteration in the equalized signal constellation, reducing the precision of these closed-form expressions<sup>2</sup>. Therefore, it is required that the noise distribution of the equalized signal approximates a Gaussian.

Some techniques have been proposed to mitigate the MMSE-scatterplot effect. Particularly,

---

1. Soft: a continuous range of probabilities of belonging to a determined class or category. Hard: a real specific value (e.g. 0 or 1 in binary codes)

2. A similar reasoning could be made for the Q-factor estimate, which is calculated using a Gaussian noise assumption, being not valid when the MMSE-scatterplot appears.

in [138] was proposed the monitoring of the MI’s lower bound (MI-LB) in a validation dataset, stopping the training when the MI-LB reaches its maximum value (early stopping). Another alternative, presented in [4], introduces a novel loss function called MSE-X, which combines the MSE with a regularization term based on the AIR maximization. This term ensures that the noise of the equalized signal follows a Gaussian distribution. However, this regularization term requires a fine-tuning of its noise variance parameter, otherwise, the loss function might fail to converge.

In this chapter we delve deeper into the MMSE-scatterplot effect, building upon previous studies’ findings [4], [138], [152], [159] and proposing an alternative solution to prevent its occurrence.

The chapter is organized as follows: In Section 5.1 we describe the MMSE-scatterplot effect. Section 5.2 explains the fundamental origin of this phenomenon and its equivalent mathematical function. Section 5.3 presents the related works and describes the proposed technique to avoid the MMSE-scatterplot effect. Section 5.4 details the numerical setup considered in this study, and Section 5.5 presents the results. The chapter concludes by summarizing key findings and suggesting future perspectives.

## 5.1 MMSE-Driven Signal Constellation Scatterplot

When employing an NN based nonlinear equalizer using the MSE loss function, it has been observed in QAM modulated signals, a phenomenon termed “jail window pattern” in [138] and “MSE-grid scatterplot” in [4]. These names were given due to the rectangular nature of QAM constellations. To illustrate this phenomenon, let us consider the case of an AWGN channel and a simple NN.

Let  $X$  be a discrete random variable that represents the sequence of transmitted symbols with an alphabet  $\mathcal{X}$  consisting of  $M$  discrete symbols, i.e.  $\mathcal{X} = \{x_1, \dots, x_M\}$ , and let  $R$  be also a discrete random variable that represents the sequence of received samples. An AWGN channel has the form:

$$R = X + Z, \quad (5.1)$$

where  $Z$  is a complex Gaussian-distributed random variable with zero mean and total variance  $\sigma^2$ ,  $Z \sim \mathcal{CN}(0, \sigma^2)$ .

Consider an NN with parameters  $\theta$ , with input  $R$  and output  $Y = f(R; \theta)$ , where  $f$  represents the NN and  $Y$  is the estimate of the transmitted sequence  $X$ . An illustration of this setup is shown in Fig. 5.1, where the equalized signal  $Y$  is the demapper input and  $Q_{X|Y}(\cdot|y)$  is the soft-information in the form of a posterior distribution that feeds the SD-FEC [4], [153].

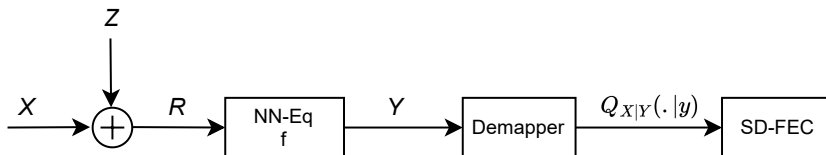


Figure 5.1 – Classical transceiver model with an NN-based nonlinear equalizer (regressor) in an AWGN channel represented by  $Z$  ©2024, IEEE.

The objective of the NN is to bring  $Y$  closer to  $X$ . The MSE is commonly used to measure the difference between  $Y$  and  $X$ , and can be expressed as [159], [160]:

$$\text{MSE}(X, Y) = \mathbb{E}[|X - Y|^2], \quad (5.2)$$

where  $\mathbb{E}[\cdot]$  is the expectation operator.

For simplicity, consider NNs using real number parameters. Therefore, the complex inputs were separated into their I and Q components. Consequently, the outputs also corresponded to the separated I and Q parts of the predicted complex symbols.

The chosen NN was the MLP because it is known that it could approximate any nonlinear function[123], but as we will see later, there are not restrictions for the NN-based nonlinear equalizer architecture. The MLP consists of an input layer, one or more hidden layers, and an output layer. Each layer comprises multiple units or neurons. Following the format used in other studies, we represent the MLP as  $N_i|N_1|f_a|\dots|N_L|f_a|N_o$ , where  $N_i$  signifies the number of neurons in the input layer,  $N_h$  denotes the number of neurons in the hidden layer  $h$  (with  $1 \leq h \leq L$ ),  $L$  signifies the total number of hidden layers, and  $N_o$  represents the number of neurons in the output layer. After each layer (linear part), we applied a nonlinear activation function  $f_a$ , except for the output layer. In the case of the regression task, the number of neurons in the output layer is fixed to  $N_o = 2$  (in the case of one polarization), as we aimed to recover the real and imaginary parts of the equalized symbol. The NN architecture utilized in this study for the AWGN channel is outlined in Table 5.1 with the specifications for the training.

Fig. 5.2a and 5.2c show  $R$  (NN input) for squared 16QAM and rectangular 8QAM, respectively. The noise variance  $\sigma^2$  was set to achieve a received BER of  $10^{-3}$ . Meanwhile, Fig. 5.2b and 5.2d show  $Y$  (NN output), that correspond to the observed phenomenon in rectangular constellations. A similar experiment was done in [159], where a pure AWGN channel with only CD was employed to show the MMSE-scatterplot emergence after some epochs using an NN-based nonlinear equalizer.

This phenomenon, to the best of our knowledge, has primarily been attributed to rectangular QAM constellations. However, this effect is not exclusive to QAM signals; a similar one also appears in PSK constellations. For example, if we used an 8PSK signal (Fig. 5.2e), using a similar NN as in the previous example, we found the outcome presented in 5.2f. For this constellation, the NN output on the right adopts the geometric shape of an octagon, corresponding to the eight points of the constellation in this case. Comparable results could be achieved with any other PSK constellation.

Table 5.1 – NN architecture and training specifications used in Section 5.1 for an AWGN channel.

NN architecture	Activation function $f_a$	Learning rate	Training epochs	Loss function
2 30  $f_a$  30  $f_a$  2	Tanh	$10^{-3}$	1000	MSE

In general, this phenomenon could be observed in any signal constellation with an equal probability of occurrence for all the symbols. For instance, in the optimal 8QAM signal constellation[59] (Fig. 5.2g), we can also note a distortion in the NN output constellation (5.2h). Once again, it is observed that the NN induces a specific alteration of the constellation.

All the previously mentioned results share a common characteristic: the NN induces a con-

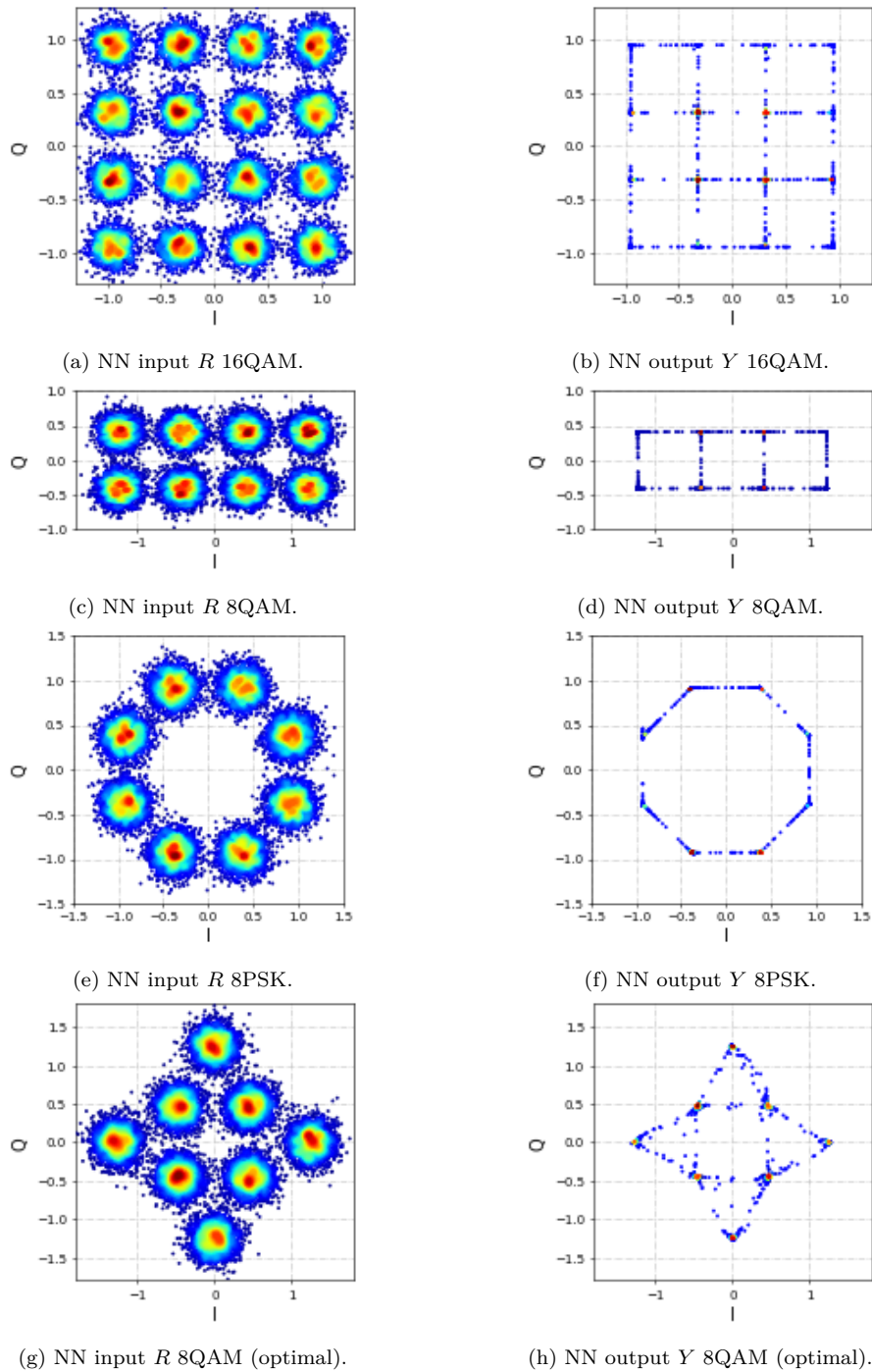


Figure 5.2 – MMSE-scatterplot effect on signal constellations in an AWGN channel ©2024, IEEE.

centration of the symbols around the original constellation points, with some scattered along straight lines connecting neighboring points of the original constellation. This effect is referred to here as the “MMSE-Driven Signal Constellation Scatterplot” (MMSE-scatterplot). Notably, this

phenomenon is consistently observed in experiments involving M-PSK ( $M = 4, 8, 16$ ), M-QAM ( $M = 4, 8, 16, 32, 64$ ), and any signal constellation with a uniform probability of occurrence for all the symbols. It is worth mentioning that this phenomenon is a direct consequence of the choice of the MSE as a loss function.

In the subsequent section, we delve into the fundamental origin of the MMSE-scatterplot effect by means of its equivalent mathematical expression.

## 5.2 Origin of the MMSE-scatterplot

The emergence of the MMSE-scatterplot effect when using the MSE loss function in NN-based nonlinear equalizers necessitated further investigations. This section aims to establish a relationship between the results obtained from the MMSE criterion and the characteristics observed in the MMSE-scatterplot.

Is not worth mentioning that the MMSE-scatterplot only appears when using nonlinear equalizers, i.e. general functions whose outputs are not linear with respect to their inputs, with the MMSE criterion. Therefore, we focus our study on nonlinear equalizers and also we restrain our study to Gaussian-like channels, which is the case of nonlinear channels that could be considered as a Gaussian noise source [154].

### 5.2.1 MSE Loss Function

The optimization criterion when training an NN using the MSE loss function is to minimize the MSE, referred to as the MMSE criterion. The rationale behind employing the MSE lies in its functional properties, as discussed in [29]: i) MSE is a differentiable function, making it suitable for gradient backpropagation during the optimization stage. ii) In the case of linear problems, MSE is a convex function, ensuring convergence to the global minima. However, it is still widely used in non-convex optimization problems, where acceptable local minima are achievable [28].

Moreover, a significant property is the relationship between the MSE and the conditional Maximum Likelihood Estimation (MLE). The conditional MLE aims to find the optimal set of parameters  $\theta$ , maximizing the posterior probability to estimate  $X$  given  $R$ ,  $P_{X|R}(x|r)$ , i.e.  $\theta_{ML} = \arg \max_{\theta} P_{X|R}(x|r)$ . Assuming that  $P_{X|R}(x|r)$  is Gaussian distributed, it has been demonstrated that the conditional MLE and the MMSE criterion are equivalent [28], [29].

### 5.2.2 MMSE estimate

The optimal estimate of  $X$ , i.e.  $Y = \hat{X}$ , under the MMSE criterion, was studied, for instance, in [161]–[163]<sup>3</sup>. It has been demonstrated that the MMSE is attained when  $Y$  is the mean of the posterior probability  $P_{X|R}(x|r)$ , i.e.

$$Y = \mathbb{E}[X|R]. \quad (5.3)$$

In the scenario where  $x \in \mathcal{X}$ , with  $P_X(x) = \frac{1}{M}$  uniform  $\forall x \in \mathcal{X}$  and zero elsewhere, and assuming  $Z \sim \mathcal{CN}(0, \sigma^2)$ , it has been shown in [164, Eq. 3.11],[163, Eq. 5] [161, Eq. 10.9] that the optimal estimate of  $X$  is given by

3. In the context of MIMO detection, the MMSE estimate has been referred to as the optimal denoiser[163].

$$Y = \mathcal{S}_{\mathcal{X}}(R; \sigma^2), \quad (5.4)$$

where  $\mathcal{S}_{\mathcal{X}}(R; \sigma^2)$  is a Soft-Thresholding (STH) projector onto  $\mathcal{X}$ . This expression is called here STH function and for  $R = r$  is defined as follows:

$$\mathcal{S}_{\mathcal{X}}(r; \sigma^2) = \frac{\sum_{x \in \mathcal{X}} x e^{-\frac{1}{\sigma^2}|r-x|^2}}{\sum_{x \in \mathcal{X}} e^{-\frac{1}{\sigma^2}|r-x|^2}}. \quad (5.5)$$

In [160, Eq 6.24], the authors analyzed the case of the optimal equalizer using the MMSE criteria. They considered no restrictions on the equalizer, i.e., not necessarily linear, and assumed Gaussian noise and BPSK symbols. They found that the MSE minimization reduces the equalizer function to

$$f(r; \sigma^2) = \tanh\left(\frac{r}{\sigma^2}\right), \quad (5.6)$$

which is equivalent to the equation (5.5) for  $x \in \{-1, +1\}$  [Eq. 3.14][164].

As the noise variance approaches zero ( $\sigma^2 \rightarrow 0$ ), one can note that the STH function reduces to the Hard-Thresholding function  $\mathcal{H}_{\mathcal{X}}(r)$ , defined by

$$\mathcal{H}_{\mathcal{X}}(r) = \lim_{\sigma^2 \rightarrow 0} \mathcal{S}_{\mathcal{X}}(r; \sigma^2) = \arg \min_{x \in \mathcal{X}} |r - x|^2. \quad (5.7)$$

Note that this function corresponds to the optimal Hard Decision (HD) detector into the signal constellation.

For illustrative purposes, the Soft and Hard-thresholding functions are depicted in Fig. 5.3 for the particular case of a PAM4 constellation. Observe that, for small values of the noise variance  $\sigma^2$ , most points will concentrate around  $x_1$ ,  $x_2$ ,  $x_3$  and  $x_4$ , whereas for large values of  $\sigma^2$ , these points will spread more along the straight lines between neighboring symbols  $x_1 - x_2$ ,  $x_2 - x_3$ , and  $x_3 - x_4$ .

Consider the inputs  $R$  of the previous examples whose constellations are depicted in Fig. 5.2a, 5.2c, 5.2e and 5.2g. When using the STH function of (5.5) with a  $\sigma^2$  equals to the AWGN variance, the outputs show the constellations depicted in Fig. 5.4 for each case. Upon simple inspection, it is clear that these results exhibit the same distribution as those when using the NN, shown in Fig. 5.2b, 5.2d, 5.2f, and 5.2h, and the MMSE criterion during the training.

Therefore, we can conclude that in an AWGN channel, a nonlinear equalizer, e.g. an NN, with the objective of minimizing MSE (MMSE criterion) simplifies to the STH function in (5.5).

It must be mentioned that the use of such a function (5.5) was also investigated in [164], but in the pursuit of a less complex NN that provides the optimal estimator for the transmitted signal, specifically for PAM constellations.

### 5.3 Mitigation Techniques of the MMSE-scatterplot effect

This section describes in detail the related works concerning the MMSE-scatterplot effect and presents another alternative to avoid its appearance.

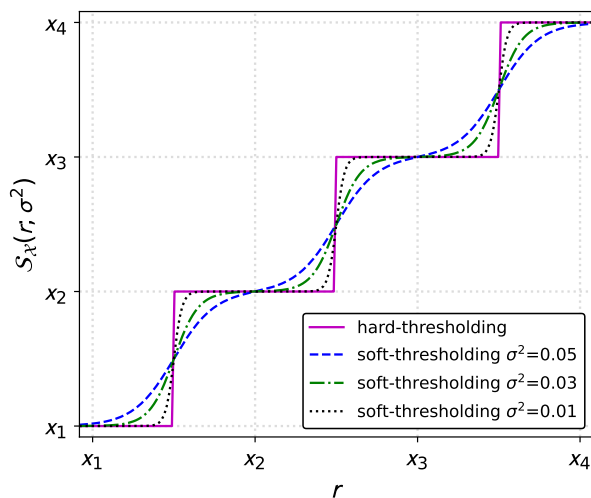


Figure 5.3 – Soft and Hard-thresholding functions for a PAM4 constellation with alphabet  $\mathcal{X} = \{x_1, x_2, x_3, x_4\}$  ©2024, IEEE.

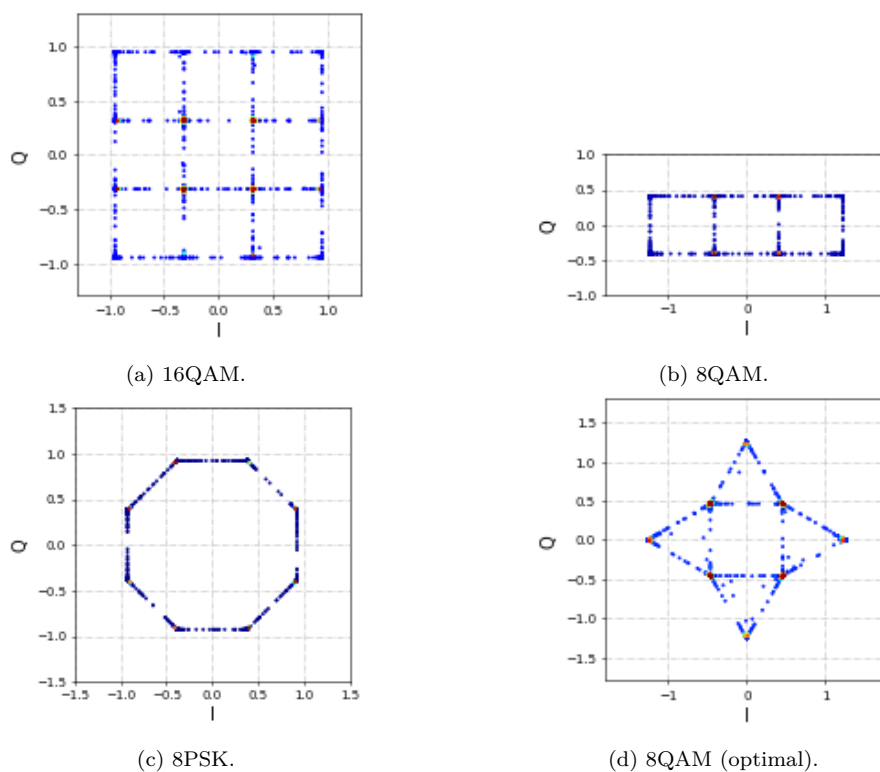


Figure 5.4 – Estimate of  $X$  using the STH function in (5.5), where  $R$  are the inputs in Fig. 5.2a, 5.2c, 5.2e and 5.2g ©2024, IEEE.

### 5.3.1 Related works

In [138], the authors provided some insights about the MMSE-scatterplot effect, which they called the “jail-window” pattern. They highlighted the fact that this phenomenon appears due to the Euclidean distance minimization between the target and predicted symbols performed by the NN when minimizing the MSE loss function. Additionally, they provided possible reasons for its appearance from an ML perspective, e.g. the mismatch between the ultimate goal of the NN-based equalizer (BER improvement) and the NN loss function (MSE), and the use of not enough large mini-batch sizes. Other important observations were made on that paper. For instance, the necessity of carefully training the NN, being aware to avoid overfitting at most, and making the different datasets employed for training/validation/test highly uncorrelated. In that work, it was also proposed the use of the  $L^2$  regularization technique to mitigate the MMSE-scatterplot effect. However, it was pointed out that it could only partially mitigate the MMSE-scatterplot effect and it still needed large mini-batch sizes.

Another study in [159], provides other solutions to mitigate the MMSE-scatterplot effect. In particular, an early stopping routine based on the maximum AIR estimated in a validation dataset. The AIR estimated in that work was the MI-LB. Indeed, monitoring the MI-LB on the validation dataset is indicated as the best approach to selecting a model that avoids the MMSE-scatterplot effect. However, a signal could still have a good AIR but not be fully equalized. From our point of view, the NN could in effect, avoid the MMSE-scatterplot effect by selecting the model with a good AIR, but not necessarily improving the BER, which is also the goal of the equalizer.

Other authors in [4] also specifically investigated how to mitigate the MMSE-scatterplot effect using a regularization term based on the *a posteriori* probability distribution  $Q_{X|Y}(x|y)$  of the demapper, where  $X$  is the transmitted data and  $Y$  is the received data after equalization. This function was called MSE-X and given by:

$$\text{MSE-X}(X, f(R)) = \text{MSE}(X, f(R)) - 2\sigma^2\mathbb{E}[-\log Q_Y(f(R))], \quad (5.8)$$

where  $Y = f(R)$ ,  $f$  represents the NN channel equalization, and  $\sigma^2$  is the noise power.

The MSE-X loss function requires to set a parameter  $\sigma^2$  related to the variance of the equalized signal. We found that this parameter is difficult to set as the expected quality of the equalized signal is unknown.

In this section, we propose an alternative approach to mitigate the MMSE-scatterplot effect, by using the STH function as a nonlinear layer at the end of the NN.

### 5.3.2 Soft Thresholding-based Output Layer

We propose a new approach that involves adding the STH function (5.5) after the NN. Instead of directly producing two real numbers as the predicted symbol, we introduce the STH function as an additional nonlinear function immediately after the output layer. A similar “staircase” function was proposed in [149], [165] as a nonlinear activation function to handle nonlinearities in M-QAM systems. They showed that this function effectively minimizes the MSE with BER improvements. However, when observing the MMSE-scatterplot in their results, is clear that the AIR is very poor.

In [164], this function was used as an optimal<sup>4</sup> NN. Indeed, the STH function can be used as a single-layer NN with only a few neurons, with the minimal number of neurons being  $\sqrt{M} - 1$  for a real-valued NN in squared M-QAM constellations. However, this ultra-short NN is not useful as it does not perform any equalization.

We require an NN that can perform equalization, thereby increasing the AIR and decreasing the BER by minimizing the MSE during the training stage. The key to adding the STH function as a nonlinear layer after the NN is the following: on the one hand, the NN addresses the equalization with MI and BER improvement. On the other hand, the STH function takes the role of the MMSE-scatterplot. Indeed, the NN alone plays both roles. Why not separate both roles if the MMSE-scatterplot expression is known?

The NN followed by the STH (NN + STH) architecture is illustrated in Fig. 5.5a. During the training stage, the output  $Y$  is the outcome of the NN + STH and is used to calculate the  $\text{MSE}(X, Y)$ . However, during the evaluation stage, the equalized signal, denoted as  $R_2$ , is the signal recovered before the STH function, and is free of the MMSE-scatterplot.

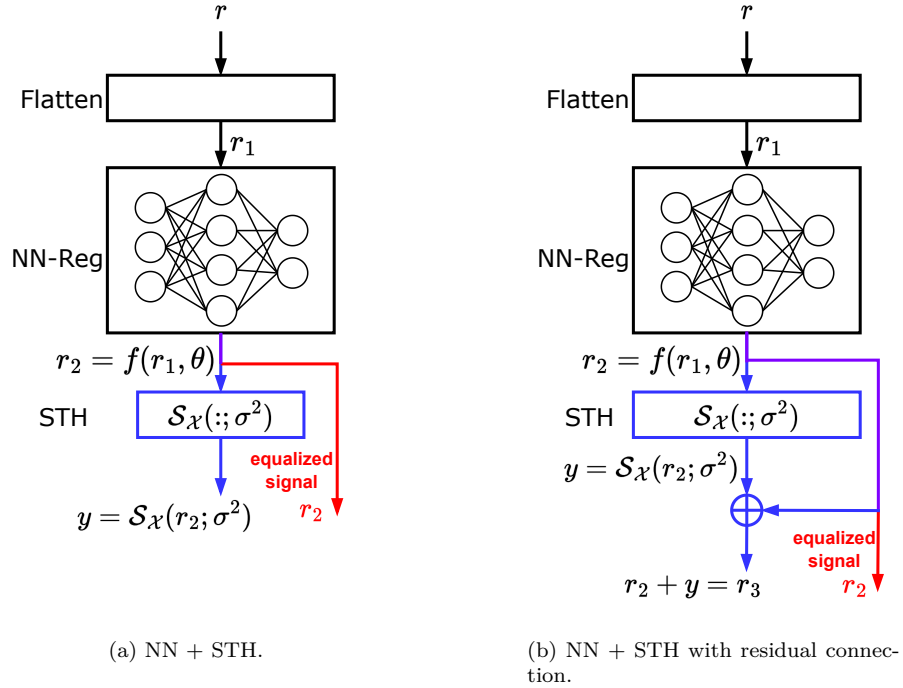


Figure 5.5 – Proposed NN followed by the STH function. Flatten: reshapes input  $r$  into a vector of shape  $(B, :)$ , where  $B$  is the mini-batch size. Color blue indicates only training mode, red indicates only evaluation mode, and purple indicates both training and evaluation modes ©2024, IEEE.

The STH-based layer relies on a parameter  $\sigma^2$ , which must be appropriately set to generate the MMSE-scatterplot. Since the gradient loss tends to become null for small  $\sigma^2$  due to this “soft staircase” function, it becomes susceptible to block the gradient backpropagation. To tackle this issue, we can employ a well-known technique, based on a residual connection[166]. Residual connections were initially introduced to alleviate the vanishing gradient issue in deep NNs. In

4. Notice that the term “optimal” referred to the minimum MSE.

this context, the vanishing gradient problem does not arise from a deep structure but rather from the STH function. A residual connection facilitates gradient propagation through two connections. A modified architecture, featuring a residual connection, is depicted in Fig. 5.5b. More formally, let  $\mathcal{L}$  be the loss, i.e.,  $\mathcal{L} = E[|R_3 - X|^2]$ , then the variation of NN parameters  $\theta$  will occur through the gradient descent of  $\mathcal{L}$  with respect to  $\theta$ :

$$\frac{\partial \mathcal{L}}{\partial \theta} = \frac{\partial \mathcal{L}}{\partial r_3} \frac{\partial r_3}{\partial \theta} \quad (5.9a)$$

$$= \frac{\partial \mathcal{L}}{\partial r_3} \left( \frac{\partial r_2}{\partial \theta} + \frac{\partial y}{\partial \theta} \right) \quad (5.9b)$$

$$= \frac{\partial \mathcal{L}}{\partial r_3} \left( \frac{\partial r_2}{\partial \theta} + \frac{\partial y}{\partial r_2} \frac{\partial r_2}{\partial \theta} \right) \quad (5.9c)$$

$$= \frac{\partial \mathcal{L}}{\partial r_3} \frac{\partial r_2}{\partial \theta} \left( 1 + \frac{\partial y}{\partial r_2} \right). \quad (5.9d)$$

In this manner, even if the gradient  $\frac{\partial y}{\partial r_2}$  becomes zero,  $\frac{\partial \mathcal{L}}{\partial \theta}$  can still propagate due to the second connection. Notice that in the first architecture (Fig. 5.5a),  $\frac{\partial \mathcal{L}}{\partial \theta}$  becomes zero when  $\frac{\partial y}{\partial r_2}$  approaches zero.

The selection of  $\sigma^2$  using the residual connection was empirically approached in two different ways:

- Calculating the value of  $\sigma^2$  for each batch by using the equalized signal before the STH function along with the transmitted signal. This method requires feeding the NN with the transmitted signal to calculate  $\sigma^2$ .
- Treating  $\sigma^2$  as a learnable parameter of the NN.

In practice, we noticed that the first option did not provide the desired results, as the calculated value of  $\sigma^2$  was too large to generate the required MMSE-scatterplot effect. Therefore, we opted for the second option. However, during the training process, there comes a point where the gradient is unable to backpropagate, due to the very small values of  $\sigma^2$ , even with the residual connection. This eventually stops the training. Nevertheless, this is not an issue as long as the equalization has been performed.

Another alternative that we explored is the use of Kurtosis as a regularization term. Indeed, Kurtosis tends to approach zero for Gaussian-distributed random variables[145], [167]. The idea was to encourage the minimization of the Kurtosis during the training. In doing so, we aimed to force the noise to be Gaussian-distributed, avoiding the MMSE-scatterplot appearance. However, we decided not to use this approach because a Kurtosis value close to zero does not necessarily indicate a Gaussian distribution. While it worked in some cases, it was not easily applicable to other cases.

## 5.4 Description of the Numerical Setup

In this section, we describe the transmission setup under study, the datasets building, the NN architecture, and the training/validation process.

### 5.4.1 Transmission setup

To investigate the conditions leading to the MMSE-scatterplot effect, we initiated a numerical study based on a dual-polarization transmission setup illustrated in Fig. 5.6. In this setup, the transmitted symbols  $X$  are oversampled to 8 samples/symbol (SpS) to simulate the digital-to-analog conversion. After pulse shaping using Root-Raised Cosine (RRC) filters, the combined dual-polarization signal propagates through the optical channel. At the receiver, DSP techniques are applied exclusively to address linear impairments. The resulting signal, denoted as  $R$ , is used as the input for the NN represented by  $f$ . We denote the output of the NN as  $Y = f(R)$ .

The optical channel consisted of 14 spans of standard single-mode fibers (SSMF) with a span length of 50 km. After each span, an erbium-doped-fiber amplifier (EDFA) fully compensates for the fiber loss. To simulate the signal's propagation, we numerically solved the Manakov-PMD equation [24], [83] using the split-step Fourier method (SSFM) [18]. The Rx-DSP low-pass filters the signal to the effective bandwidth. Subsequently, the signal undergoes an undersampling to 4 SpS for full CD compensation (CDC), or using the DBP [24], followed by an identical RRC pulse shaping to mitigate inter-symbol interference. Subsequently, a polarization demultiplexing technique based on a 2x2 Multiple-Input-Multiple-Output (MIMO) equalizer combined with a Fractionally-Spaced Equalizer (FSE) and sequentially using the Constant Modulus Algorithm (CMA) [74] and Radius-Directed Equalizer (RDE) [96], was applied to recover the signal at the symbol rate (1 SpS) [75]. This processing was followed by an estimation of frequency offset [99] and carrier phase [56]. The resulting output  $R$ , is still affected by the interplay between fiber nonlinearity, CD, PMD, and amplified spontaneous-emission (ASE) noise originated by EDFAs. Indeed, this setup allowed us to analyze the impact of significant accumulated fiber nonlinearity, in the widely deployed SMF-28 fiber type. The specific simulation parameters are outlined in Table 5.2.

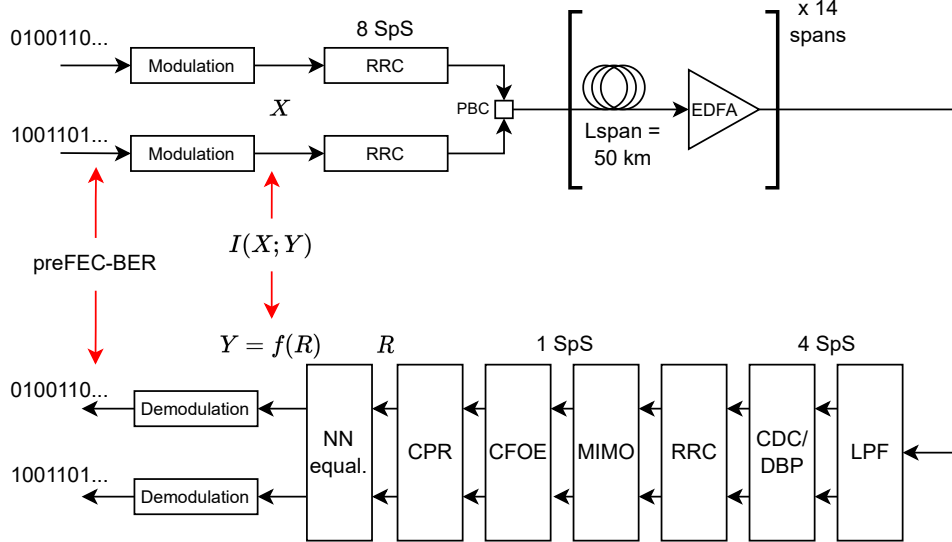


Figure 5.6 – Dual-Polarization Transmission Setup. SpS: samples per symbol, RRC: root-raised cosine, PBC: polarization beam combiner, EDFA: erbium-doped fiber amplifier, LPF: low pass filter, CDC: chromatic dispersion compensation, DBP: digital backpropagation, MIMO: multiple-input multiple-output, CFOE: carrier frequency offset estimation, CPR: carrier phase recovery ©2024, IEEE.

Table 5.2 – Parameters of numerical simulation.

PARAMETER	VALUE
System	Dual-Polarization
Modulation	64QAM
Baud Rate	32 Gbaud
Wavelength	1552 nm
Laser linewidth	100 KHz
Frequency offset	200 MHz
Pulse shaper	RRC
RRC roll-off	0.1
SpS (TX)	8
SpS (RX)	4
$N_{\text{spans}}$	14
$L_{\text{span}}$	50 km
Fiber loss	0.2 dB/km
CD coeff.	-21.7 ps <sup>2</sup> /km
PMD coeff.	0.05 ps/ $\sqrt{\text{km}}$
Fiber nonlinear coeff.	1.4 W <sup>-1</sup> .km <sup>-1</sup>
$G_{\text{EDFA}}$	10 dB
$NF_{\text{EDFA}}$	4.5 dB
LPF cutoff freq.	20 GHz
SSFM resolution	1 km/step

### 5.4.2 Datasets

For the training and validation process, we used 14 different datasets. Each dataset was generated with a different random pattern and contained 233,274 symbols, after the classical DSP described in the precedent subsection. For each dataset, 50% of the data was used for training, and the following 50% was used for validation. Then, similar to [138], we reshaped each part in the form  $(B, S, 4)$ , where  $B$  is the mini-batch size equal to 4096,  $S$  accounts for  $N$  neighboring symbols of the input symbol ( $S = 2N + 1$ ) and 4 for the real and imaginary parts of each polarization. Under this configuration, the number of neurons of the input layer  $N_i = 4S = 4(2N + 1)$ . After this distribution, the training batches of each dataset were concatenated producing a final training dataset in the form  $(N_B, B, S, 4)$ , where  $N_B$  is the number of batches. An identical procedure was done with the corresponding parts for the validation dataset. Table 5.3 details the total number of batches and symbols used during the training.

Table 5.3 – Number of batches and symbols used in training and validation.

	Training	Validation
Batches ( $N_B$ )	392	392
Batchsize ( $B$ )	4096	4096
Batches $N_B$ /epoch	192	192

However, due to limitations in computational resources, we could not use the 392 batches. Therefore, we randomly selected 192 batches from 392 batches at each epoch. For testing purposes, we used a different unseen dataset consisting of 633,177 effective symbols.

Table 5.4 – Architecture of the NN-based nonlinear equalizer.

NN architecture	Activation function $f_a$
86 646  $f_a$  319  $f_a$  365  $f_a$  4	Tanh

### 5.4.3 NN hyperparameters and Training Process

In this study, we selected an MLP architecture with carefully adjusted hyperparameters to get the lowest MSE values during training and to improve the BER as much as possible in the validation dataset. We utilized the Optuna framework for hyperparameter optimization [144] with 50 trials (candidates), setting the following ranges: the number of taps  $N$  should range from 10 to 20 symbols, the number of hidden layers should range from 1 to 3, and the number of hidden units should range from 15 to 1000.

We concur with the viewpoint outlined in [138] regarding the necessity for careful consideration of several crucial factors during NN training. In particular, the following aspects should be taken into account:

- Considering large enough datasets for highly accurate systems, as is the case of optical transport networks.
- Employing distinct data generation patterns for training, validation, and testing datasets, or using cross-fold validation. We opted for cross-fold validation using the 14 datasets.
- Utilizing large mini-batch sizes, with the mini-batch size being as large as possible to ensure it is representative of the entire dataset.

During the training, at each epoch, the training mini-batches were shuffled. This approach was adopted to prevent the NN from learning specific patterns (even if this was highly improbable due to the various datasets with different dataset generation patterns), ensuring a more generalized model. The learning process involved the minimization of the loss function, through an optimization step using Adam optimization, followed by the updating of NN parameters [29]. We found that a learning rate of  $10^{-4}$  and a large minibatch  $B = 4096$  yielded better BER improvements.

We found the NN hyperparameters indicated in Table 5.4. The numbers in the NN architecture indicate the neurons per layer, with the first and last numbers corresponding to the input and output layers, respectively. The numbers in between are the hidden units and  $f_a$  states for the activation function which is the hyperbolic tangent.

## 5.5 Results

In this section, we have compared the performance of an NN trained with MSE, an NN trained with MSE-X, an NN + STH trained with MSE, and a DBP at 1 step/span. The validation dataset was utilized to monitor the performances during the learning process. Finally, the testing dataset was used to calculate accuracy metrics on an unseen dataset.

We selected the model that provides the lowest MSE in the validation dataset for each case. We monitored the MSE in the training and validation datasets and stopped the training process if no MSE improvement was observed in the validation dataset or if we observed overfitting.

Table 5.5 – Parameter  $\sigma^2$  utilized in NNs with MSE-X and NN+STH with MSE.

P/ch (dBm)	-4	-2	0	2
$\sigma^2$ (MSE-X)	0.0027	0.0027	0.0027	0.005
$\sigma^2$ initial (STH)	0.025	0.025	0.025	0.03

The MSE-X loss function requires to set a parameter  $\sigma^2$  related to the variance of the equalized signal. We found this parameter difficult to set as the expected quality of the equalized signal is unknown. Despite that, guided by the details provided in [4], [168], we performed the following steps:

- We fixed  $\sigma^2$  and we trained the NN for a period.
- When we observed a training stabilization or overfitting, we stopped the training and calculated  $\sigma^2$  using a testing dataset.
- We updated  $\sigma^2$  with the recovered value (which corresponded to an equalized signal). The final training of the NN was then performed using this adjusted  $\sigma^2$ .

Table 5.5 provides the details of the parameters utilized for  $\sigma^2$  for both the MSE-X and the STH function.

In all configurations, we chose the model that provided the lowest loss in the validation dataset. For instance, for P/ch = 0 dBm, we obtained the curves illustrated in Fig. 5.7. As we can observe in this example, the NN using MSE shows a gradual loss descent up to eventually occurring overfitting. On the other hand, the NN with MSE-X shows lower training losses compared to the MSE case. This is due to the entropy regularization term added to the MSE, as explained in [4]. The NN + STH using MSE was early stopped owing to the blocking backpropagation. For MSE-X as well as for NN + STH with MSE, the validation losses are calculated using the MSE between the transmitted and equalized symbols.

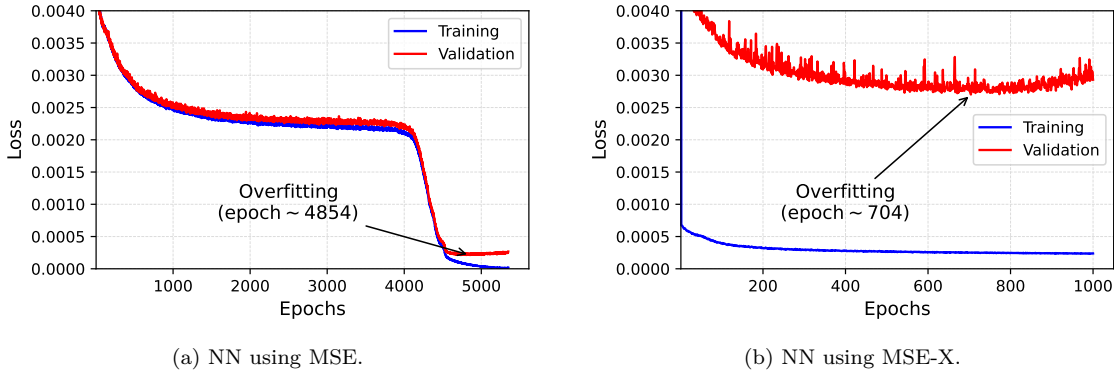
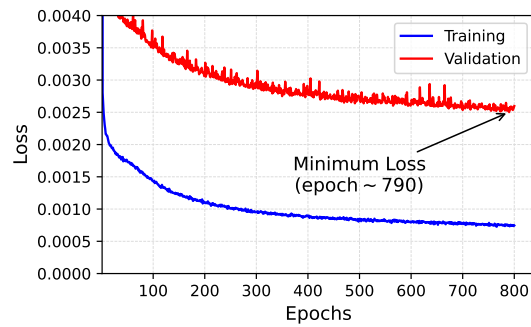
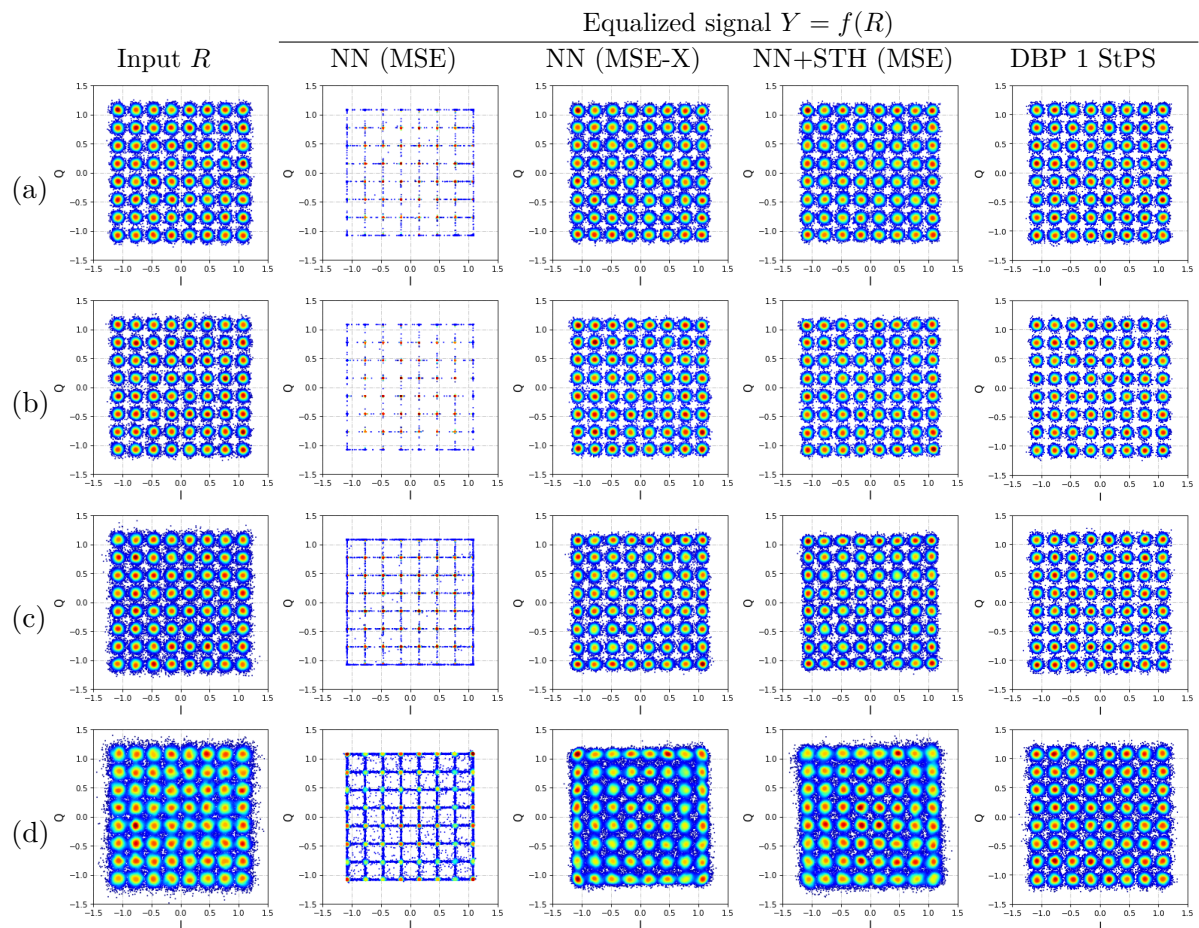


Figure 5.7 – Curve of losses (average of training batches per epoch) for each equalizer for P/ch = 0 dBm ©2024, IEEE.

In Fig. 5.8 we plot the input constellations denoted previously as  $R$ , followed by the equalized signals  $Y = f(R)$  using the NN with MSE, the NN with MSE-X, and NN + STH with MSE. Notice that both, the NN with MSE-X and NN + STH with MSE, avoid the MMSE-scatterplot. The last column corresponds to the equalized signal using the DBP 1 step/span.



(c) NN + STH using MSE.

Figure 5.7 – Curve of losses (average of training batches per epoch) for each equalizer for  $P/ch = 0$  dBm (cont.) ©2024, IEEE.Figure 5.8 – Symbol constellation diagrams of the received signal (NN input)  $R$  and constellations of equalized signal  $Y = f(R)$  for each NN-based equalizer and using a DBP 1 StPS. (a)  $P/ch = -4$ dBm, (b)  $P/ch = -2$ dBm, (c)  $P/ch = 0$ dBm, (d)  $P/ch = 2$ dBm ©2024, IEEE.

For each launch power and each equalizer, we calculated the BER and the MI-LB using (B.5). The results are depicted in Fig. 5.9a and 5.9b.

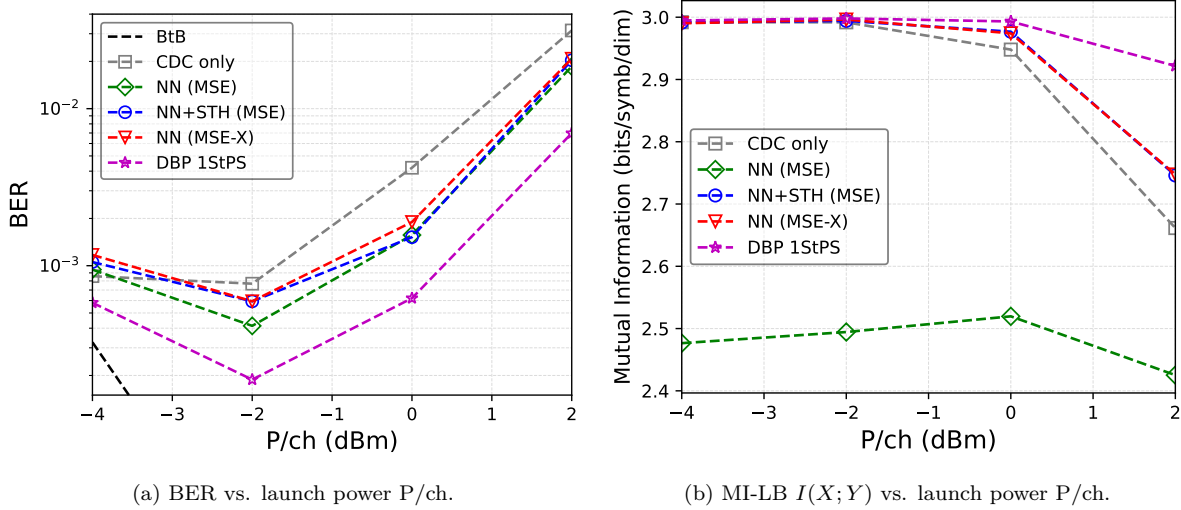


Figure 5.9 – Performances obtained for each equalizer ©2024, IEEE.

In terms of BER, all the NNs performed worse than the DBP 1 step/span. However, the reader should take into account the performance-computational complexity trade-off between the DBP and the NN. This comparison is out of the scope of the present work but the reader could refer, for instance, to [43], [169]. The NN (MSE) is slightly better in the linear regime, at  $P/ch = -4$  and  $-2$  dBm, than the NN (MSE-X) and the NN + STH (MSE), which both show similar performances, with the NN+STH (MSE) slightly outperforming the NN (MSE-X). In the linear regime, both methods hardly improve the CDC or even worsen it. This was not due to the methods themselves but because training an NN in the linear regime is very challenging, requiring a large amount of data and computational power.

Regarding the MI  $I(X;Y)$ , the NN (MSE) method results in a loss of soft information, showing a very poor MI. On the other hand, all the tested NNs increased the MI, but the DBP method was always superior.

## 5.6 Summary

In this study, our goal was to offer more insights about the MMSE-scatterplot phenomenon that occurs when using nonlinear equalizers based on NNs.

Firstly, we explained the fundamental origin of the MMSE-scatterplot and presented its equivalent mathematical expression, which is the Soft Thresholding (STH) function.

Secondly, we used the STH function as an alternative to avoid the MMSE-scatterplot. The STH function is placed after the NN during the training. In the evaluation, the equalized signal, free of the MMSE-scatterplot, is obtained before the STH function. A comparison between the NN+STH (using MSE) and the NN (using MSE-X), showed slightly better BER using the NN+STH (MSE) than using the NN (MSE-X) with similar MI. The NN+STH approach requires initializing the parameter  $\sigma^2$  with sufficiently small values capable of generating the MMSE

scatterplot. The MSE-X also requires setting a parameter  $\sigma^2$ , however it must be carefully set up. If is too small, the training loss could become negative.

Finally, other strategies could also be explored. For instance a kurtosis-based regularization term, or different hyperparameters optimization strategies with different objectives, for instance, the BER minimization or MI maximization, both requiring more in-depth justifications.



# CONCLUSION AND PERSPECTIVES

---

This study aimed to respond to the question about the real benefits of using Neural Networks (NN) as Nonlinear Impairments (NLI) compensation techniques in typical scenarios of high data bit rate and long haul coherent optical transmissions using the standard single mode fiber (SSMF). We have chosen the NN model Multilayer Perceptron (MLP) as it is a general-purpose NN that theoretically could approximate any nonlinear function. We performed the following steps, covering each of them in one chapter as follows:

- In Chapter 2, we extensively studied the typical coherent transmission system in order to understand the phenomenon of fiber nonlinearity in conjunction with Chromatic Dispersion (CD) and Polarization Mode Dispersion (PMD). For numerical simulations using the split-step Fourier method (SSFM), we must use the Manakov-PMD equation when considering larger values of fiber birefringence.
- In Chapter 3, with the knowledge acquired in the previous step, we performed a numerical simulation of different scenarios considering a single channel. We implemented some Digital Signal Processing (DSP) algorithms to handle linear and adaptive equalization as well as frequency offset compensation and carrier phase recovery. This step permitted us to observe the performance degradation, specifically in terms of Bit Error Rate (BER), when we account for the fiber nonlinearity (for a single channel, considering only the self-phase modulation (SPM), nonlinear phase noise (NLPN), and cross-polarization modulation (XPolM)). We also implemented the NLI compensation techniques: Digital Backpropagation (DBP) and the Volterra Nonlinear Equalizer (VNLE). We observed and compared the nonlinear mitigation performed by these two techniques.

We agree that a single channel is still a nonrealistic scenario as we do not transmit one channel over an optical fiber but multiple channels. However, it was necessary to start with this use case for methodology reasons. We believe we laid the groundwork for a multichannel exploration by our study group in future works.

In the same chapter, we also started to use an experimental setup that reproduces an optical coherent link, observing a similar degradation of the BER but a more limited NLI compensation capacity when using the DBP and the VNLE.

- In Chapter 4, we used the MLP in our single-channel numerical scenario, observing a limited gain performance (BER reduction) compared to the results using the DBP and the VNLE. However, this limited NLI compensation capacity is accompanied by a lower processing time. Unfortunately, we could not fully exploit the experimental setup to test the capabilities of the MLP compared to the DBP and the VNLE ones. Indeed, as our experimental setup relies on multiple PRBS-15 sent continuously, the datasets comprise these concatenated PRBS-15. The NN is trained using these datasets, being highly susceptible to learning easily retrievable deterministic patterns if they are present instead of the nonlinear channel transfer function. One must be extremely careful when presenting the results using an experimental setup when the data comprises PRBS. Unfortunately, we could not do more in-depth studies, but we let this pending work for future studies.

- 
- In Chapter 5, we faced a phenomenon observed in the constellation diagrams when using NN trained with the Mean Squared Error (MSE) loss function. This phenomenon, which we called MMSE-scatterplot, was analytically explained in this chapter by means of its mathematical expression, which we called the Soft-Thresholding (STH) function. We showed that if we add the STH function at the end of the NN, we can obtain the equalized signal without the MMSE scatterplot.

From our point of view, the question about the benefits of using NN as nonlinear equalizers is still open. To address this matter seriously, many actors must be openly involved, led by optical communication product vendors, who know precisely the additional resources we can assign to an NN. From an academic and operator perspective, we can only make assumptions. Despite that, we could respond to some aspects related to NN, such as the MMSE-scatterplot effect, which was fully covered in Chapter 5.

In our study, we also had the opportunity to explore the Learned Digital Backpropagation (LDBP) [170] in a single-channel scenario. Even if this method is not described in this manuscript, we would like to highlight its relevance regarding its superior performance. Certainly, in one of our contributions [169], we compared the LDBP and the MLP, clearly observing that the LDBP largely outperforms the MLP with optimal hyperparameters. Moreover, the LDBP requires much less implementation effort than non-parametric NN, such as the MLP. The reason is that the LDBP is built from the DBP, with a more intuitive knowledge of the number of layers, neurons per layer, and nonlinear activation function. In that work, we also observed that the computational complexity is not much higher than the MLP one. In the last years, several works have been done to reduce the computational complexity of the LDBP [47], [87], [171], [172].

The question about the position of the NN in the DSP chain was also partially covered in our study [169] for the simplest case of single channel and one polarization, concluding that an NN, such as the MLP, behaves very similarly whatever the position into the DSP chain is, as long as the NN's hyperparameters were optimized. In the case of the LDBP, its natural position is one of the first blocs, as the CDC and the DBP. For complex scenarios, the position of the LDBP could be challenging. Certainly, if we account for two polarizations and include frequency offset and laser phase noise, that means that after the LDBP there will be at least three DSP algorithms before we can recover the symbols that must be compared to the target symbols (transmitted symbols) to calculate the loss and training the LDBP. It has been proposed some alternatives in [146], [171], [173] but, in our opinion, the proposed methods could fail in avoiding reproducibility because of the complexity of the methods. In an unpublished work, we proposed a simple technique for training the LDBP using numerical data and evaluating the results using experimental data, observing good results. The key relied on using the samples after a DBP, at the largest number of steps per span, as the target for training the LDBP. The drawback is that we necessitate a good knowledge of the actual transmission setup to be simulated.

In summary, we believe that future works could be dedicated to investigating how to employ a technique such as the LDBP in real transmission setups, making sure that the proposed methods are easily reproducible and more importantly, that the proposed methods could work be tested online in hardware as the ultimate test. Another research axis is a full learnable DSP [174], where techniques such as the LDBP could be easily integrated.

# QUALITY OF TRANSMISSION ASSESSMENT METRICS

---

In communication systems, the SNR has traditionally been used as a measure of the Quality of Transmission (QoT). In optical communication systems, it was also included a more specific metric, the OSNR. Recently, it was proposed the used of a Generalized Signal-to-Noise Ratio (GSNR) to account for the nonlinearity of the channel. These metrics are typically analyzed together with the BER, perhaps the ultimate metric of a communication system. The BER is sometimes replaced by the SER due to their close relationship. Therefore, we also introduced these two concepts along with the mathematical formulas to estimate them. Finally, we discuss the Q-factor, which is often used to measure the quality of a signal. Although it is typically viewed as the BER in logarithmic scales.

## A.1 Signal-to-Noise Ratio

The SNR can be defined in two ways depending on the entity being measured: symbols or bits.

SNR per symbol, known as only SNR, is a ratio between the energy per symbol  $E$  and the level of noise. On the other hand,  $\text{SNR}_b$  measures the energy per bit  $E_b$  compared to the level of noise [60]. The  $\text{SNR}_b$  is also denoted as  $E_b/N_0$ . When the noise follows a Gaussian distribution with zero mean and variance  $\frac{N_0}{2}$ , the SNR per symbol and SNR per bit can be estimated using the following equations:

$$\text{SNR} = \frac{E}{N_0} = \frac{P}{N_0 R_s}, \quad (\text{A.1})$$

$$\text{SNR}_b = \frac{\text{SNR}}{\log_2(M)}, \quad (\text{A.2})$$

where  $R_s$  denotes the symbol rate, and  $M$  is the constellation size.

## A.2 Optical Signal to Noise Ratio

The OSNR is a measure of the energy of the optical signal in relation to the level of noise, taking into account the bandwidth of the measured noise. More formally, the OSNR measured in a reference bandwidth  $B_{ref}$  is defined as follows:

$$\text{OSNR}_{B_{ref}} = \frac{P}{2N_{ASE}B_{ref}}, \quad (\text{A.3})$$

---

where  $P$  is the total average signal power summed over the two polarizations,  $N_{ASE}$  is the spectral density of the ASE noise in one polarization, and the factor 2 accounts for the ASE noise in both polarizations [60].

More indeed, from (A.1), (A.2) and (A.3), we can relate the  $OSNR_{B_{ref}}$  to the SNR and the  $SNR_b$ :

$$OSNR_{B_{ref}} = \frac{pR_s SNR}{2B_{ref}} \quad (A.4)$$

$$= \frac{p \log_2 M R_s SNR_b}{2B_{ref}}, \quad (A.5)$$

where  $p$  equals 1 for single polarization and 2 for dual polarization.

### A.3 Generalized Signal-to-Noise Ratio

The contribution of NLI on the performances of the transmission has been analytically studied in the Gaussian Noise (GN) model. In [175] was verified that the NLI behave as a additive Gaussian noise statistically independent of the ASE whose variance increase with distance and signal power. Later, in [19] was defined a modified SNR to take into account the NLI, referred as GSNR.

$$GSNR = \frac{P_{Tx,ch}}{P_{ASE} + P_{NLI}}, \quad (A.6)$$

where  $P_{Tx,ch}$  is the per-channel power,  $P_{ASE}$  is the ASE noise, and  $P_{NLI}$  is due to the NLI, and could be estimated as:

$$P_{NLI} = \left(\frac{2}{3}\right)^3 N_s \gamma^2 L_{eff} P_{Tx,ch}^3 \frac{\log(\pi^2 |\beta_2| L_{eff} N_{ch}^2 R_s^2)}{\pi \beta_2 R_s^3} B_n, \quad (A.7)$$

where  $N_s$  is the number of spans,  $\gamma$  is the fiber nonlinearity coefficient,  $L_{eff} = (1 - \exp(-2\alpha L_s)) / (2\alpha)$  is the fiber effective length,  $N_{ch}$  means number of channels (odd),  $\alpha$  the fiber loss coefficient,  $L_s$  the span length,  $R_s$  the baud rate assuming a rectangular spectrum per channel and spacing  $\Delta f = R_s$ ,  $\beta_2 [ps^2/km]$  is the CD coefficient, and  $B_{ref}$  is the reference noise bandwidth equals to 12.5 GHz (0.1 nm).

### A.4 Symbol Error Rate

The SER measures the ratio of symbol errors to the total number of transferred symbols. It is useful to have closed-form expressions for the SER from a statistical point of view, which we can use later in this work.

Let us denote the received signal as  $r$  and given by:

$$r = s_m + n, \quad (A.8)$$

where  $s_m$  is the transmitted signal that belongs to  $M$  discrete symbols, where  $1 \leq m \leq M$ . The

---

additive noise  $n$  corrupts the transmitted signal  $s_m$ . We assume that all  $M$  discrete symbols are sent with equal probability  $P_m$ , i.e.,  $P_m = \frac{1}{M}$ .

The receiver takes a decision of the received signal  $r$  by means of a function  $g(r)$ . To this effect, the output space is divided into  $M$  decision regions denoted by  $D_1, D_2, \dots, D_M$ , where  $s_m \in D_m; \forall 1 \leq m \leq M$ .

The SER is defined as follows:

$$\text{SER} = \sum_{m=1}^M P_m P[r \notin D_m | s_m], \quad (\text{A.9})$$

where  $P[r \notin D_m | s_m]$  means the probability that the decision taken by the receiver  $g(r) \neq s_m$  given that  $s_m$  was sent [59].

When  $n$  follows a zero-mean Gaussian distribution with variance  $\frac{N_0}{2}$ . We get the following closed expression for the SER for PSK and QAM signals:

$$\text{SER}_{\text{BPSK}} = Q\left(\sqrt{2\text{SNR}_b}\right), \quad (\text{A.10})$$

$$\text{SER}_{\text{QPSK}} = 2Q\left(\sqrt{2\text{SNR}_b}\right) \left[1 - \frac{1}{2}Q\left(\sqrt{2\text{SNR}_b}\right)\right], \quad (\text{A.11})$$

$$\text{SER}_{\text{M-PSK}} \approx 2Q\left(\sqrt{2\log_2 M \sin^2\left(\frac{\pi}{M}\right) \text{SNR}_b}\right); M > 4, \quad (\text{A.12})$$

$$\text{SER}_{\text{M-QAM}} \approx 4\left(1 - \frac{1}{\sqrt{M}}\right) Q\left(\sqrt{\frac{3\log_2 M}{M-1} \text{SNR}_b}\right); M > 4, k = \log_2 M \text{ even}, \quad (\text{A.13})$$

where the Q function is defined as  $Q(x) = \frac{1}{\sqrt{2\pi}} \int_x^\infty e^{-\frac{t^2}{2}} dt = \frac{1}{2} \text{erfc}\left(\frac{x}{\sqrt{2}}\right)$ , erfc is the complementary error function, and  $\text{SNR}_b$  is the SNR per bit.

## A.5 Bit Error Rate

The BER is a metric that calculates the number of bit errors divided by the total number of bits transferred. The specific encoding scheme used to translate bits to symbols affects the BER. Therefore, to obtain closed-form expressions, it is necessary to consider the specific encoding scheme in most cases. Assuming Gray encoding and that the noise follows a zero-mean Gaussian distribution with variance  $\frac{N_0}{2}$ , we can derive the following closed-form expressions for the BER for PSK and QAM signals:

$$\text{BER}_{\text{BPSK}} = \text{BER}_{\text{QPSK}} = Q\left(\sqrt{2\text{SNR}_b}\right), \quad (\text{A.14})$$

$$\text{BER}_{\text{M-PSK Gray}} \approx \frac{\text{SER}_{\text{M-PSK}}}{\log_2 M}; M > 4, \quad (\text{A.15})$$

$$\text{BER}_{\text{M-QAM Gray}} \approx \frac{\text{SER}_{\text{M-QAM}}}{\log_2 M}; M > 4, k = \log_2 M \text{ even}, \quad (\text{A.16})$$

In the case of Differential encoding, we can derive a closed-form expression for the QPSK as follows [59]:

$$\text{BER}_{\text{BPSK,diff}} = \text{BER}_{\text{QPSK,diff}} = 2Q\left(\sqrt{2\text{SNR}_b}\right)\left(1 - Q\left(\sqrt{2\text{SNR}_b}\right)\right). \quad (\text{A.17})$$

## A.6 Q-Factor

Is a metric initially proposed for binary signals to facilitate the quality of signal measurement in an operative system when BER can be hardly obtained. It results as a measure of the electrical signal levels [176], [177] in an oscilloscope and is calculated as follows:

$$\text{Q-factor} = \frac{u_1 - u_0}{\sigma_1 + \sigma_0}, \quad (\text{A.18})$$

where  $u_1$  and  $u_0$  represent mean voltage to get a level 1 and 0, respectively. Similarly,  $\sigma_1$  and  $\sigma_0$  are the standard deviations of those distributions, as shown in Fig A.1.

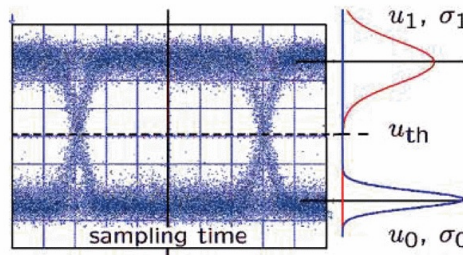


Figure A.1 – Eye diagram for Q-factor computation in binary signals using (A.18), where  $u_{1,0}$  and  $\sigma_{1,0}$  are the mean and standard deviations, respectively for level 1 and level 0 [177] ©2012, IEEE.

Assuming that the distributions of high and low levels are Gaussian, it is possible to calculate the Q-factor from the BER and vice-versa [52] as follows:

$$\text{Q-factor} = 20\log\left[\sqrt{2}\text{erfc}^{-1}(2\text{BER})\right] \text{ (dB)}. \quad (\text{A.19})$$

Although the derivation of this equation was for binary signals, it has extensively been used for multilevel signals such as QAM. One of the main reasons for this is that the Q-factor provides an easy way to express the performance of a system in comparison to the BER. For QPSK, it was proposed an averaged Q-factor for each of the two BPSK constituting the QPSK [178]. An interesting study about the Q-factor can be found in [179].

In this study, we use BER instead of Q-factor since the latter must be still generalized for higher orders of constellations [180].

# INFORMATION THEORY

---

In the early stage of the communication era, it was asked what could be the maximum capacity of a transmission system in the presence of noise [12]. Since then, the efforts have been focused on reaching the maximum theoretical capacity. To measure the capacity that could be reliably transmit over a channel, it was developed a mathematical theory [12] that we summarized here in this subsection. We also, present the two important concepts in communication systems to quantify the reliable transmission capacity over a channel: the MI and GMI.

Let  $X$  be the transmitted data from an information source, belonging to a discrete alphabet  $\mathcal{X}$  and with probability mass function  $p_X(x)$ , and let  $Y$  be the received data with probability density function  $f_Y(y)$ <sup>1</sup>.

## B.1 Entropy

The entropy of  $X$  measures the amount of information generated by the source [12] in bits per symbol or bits per second. It is also interpreted as the amount of information (bits) needed to describe  $X$  [183]. The entropy of  $X$ ,  $H(X)$ , is calculated as follows,

$$\begin{aligned}
 H(X) &= \mathbb{E}[-\log_2 p_X(x)] \\
 &= - \sum_{x \in \mathcal{X}} p_X(x) \log_2 p_X(x) \\
 &\approx - \frac{1}{K} \sum_{i=1}^K \log_2 p_X(x_i),
 \end{aligned} \tag{B.1}$$

where  $\mathbb{E}$  is the real expectation and the third equation is the empirical expectation for  $K$  samples from  $p_X(x)$ [160].

The entropy of  $Y$  (differential entropy for the continuous case) is denoted as  $h(Y)$  and is calculated as follows,

$$\begin{aligned}
 h(Y) &= \mathbb{E}[-\log_2 f_Y(y)] \\
 &= - \int_{y \in \mathcal{Y}} f_Y(y) \log_2 f_Y(y) dy \\
 &\approx - \frac{1}{K} \sum_{i=1}^K \log_2 f_Y(y_i).
 \end{aligned} \tag{B.2}$$

---

1. Here we considered  $Y$  continuous, though it could be also considered discrete as in [181], [182] by means of an ADC.

---

Nevertheless, the meaning of the differential entropy is different from the entropy of the discrete case, as it does not represent an amount of information to describe a random variable. Indeed, the differential entropy could even be negative [12]. The meaning of the differential entropy is related to the log-scale of the smaller set that contains most of the probability [183], meaning a low entropy (more negative) a more confined set, and high entropies (less negative) a more dispersed set.

## B.2 Conditional Entropy

The conditional entropy of  $X$  knowing  $Y$  (also called equivocation),  $H(X|Y)$ , measures the uncertainty of  $X$  by the knowledge of  $Y$ .

$$\begin{aligned} H(X|Y) &= \mathbb{E}[-\log_2 p_{X|Y}(x|y)] \\ &\approx -\frac{1}{K} \sum_{i=1}^K \log_2 p_{X|Y}(x_i|y_i). \end{aligned} \quad (\text{B.3})$$

Similarly, the equivocation of  $Y$  given  $X$  is defined as,

$$\begin{aligned} h(Y|X) &= \mathbb{E}[-\log_2 f_{Y|X}(y|x)] \\ &\approx -\frac{1}{K} \sum_{i=1}^K \log_2 f_{Y|X}(y_i|x_i). \end{aligned} \quad (\text{B.4})$$

## B.3 Mutual Information

The reduction in uncertainty of  $X$  due to the knowledge of  $Y$  is the MI,  $I(X;Y)$  which is defined as [12], [183], [184],

$$I(X;Y) = \log_2 \left( \frac{P_{X|Y}(x|y)}{P_X(x)} \right) \quad (\text{B.5})$$

$$= H(X) - H(X|Y) \quad (\text{B.6})$$

$$= h(Y) - h(Y|X), \quad (\text{B.7})$$

where (B.5) is the ratio between the a posteriori probability to get the transmitted symbol  $X = x$  given that we receive  $Y = y$  and the prior probability of  $X = x$ , (B.6) means the amount of information sent less the uncertainty of this information regarding the received data, and (B.7) is obtained because of the symmetry and means the amount of information received less the uncertainty corresponding to the noise of the channel [12], [183].

In an AWGN channel, the MI could be estimated using the following expression [185]:

---


$$I(X;Y) \approx m - \frac{1}{MN_s} \sum_{i=1}^M \sum_{n=1}^{N_s} \log_2 \sum_{j=1}^M \exp \left( -\frac{|x_i - x_j|^2 + 2\Re\{(x_i - x_j)^* z[n]\}}{\sigma_z^2} \right), \quad (\text{B.8})$$

where  $M$  is the constellation size,  $m = \log_2 M$  is the number of bits per symbol,  $N_s$  is the total number of symbols, and  $\Re\{\cdot\}$  means the real part.

The channel capacity is  $\max I(X;Y)$ .

In an AWGN channel, this definition leads to the maximization of the SNR [12].



# BIBLIOGRAPHY

---

- [1] E. Agrell, M. Karlsson, F. Poletti, *et al.*, « Roadmap on optical communications », *Journal of Optics*, vol. 26, 9, p. 093 001, Jul. 2024. DOI: 10.1088/2040-8986/ad261f. [Online]. Available: <https://dx.doi.org/10.1088/2040-8986/ad261f>.
- [2] M. Shtaif, C. Antonelli, A. Mecozzi, and X. Chen, « Challenges in estimating the information capacity of the fiber-optic channel », *Proceedings of the IEEE*, vol. 110, 11, pp. 1655–1678, 2022. DOI: 10.1109/JPROC.2022.3197188.
- [3] L. Liu, L. Li, Y. Huang, *et al.*, « Intrachannel nonlinearity compensation by inverse volterra series transfer function », *Journal of Lightwave Technology*, vol. 30, 3, pp. 310–316, 2012. DOI: 10.1109/JLT.2011.2182038.
- [4] F. Diedolo, G. Böcherer, M. Schädler, and S. Calabró, « Nonlinear equalization for optical communications based on entropy-regularized mean square error », in *European Conference on Optical Communication (ECOC) 2022*, Optica Publishing Group, 2022, We2C.2. [Online]. Available: <https://opg.optica.org/abstract.cfm?URI=ECEOC-2022-We2C.2>.
- [5] Ericsson. « Mobile data traffic outlook ». (2023), [Online]. Available: <https://www.ericsson.com/en/reports-and-papers/mobility-report/dataforecasts/mobile-traffic-forecast>. (accessed: 29.08.2023).
- [6] Cisco. « Cisco annual internet report (2018–2023) white paper ». (2023), [Online]. Available: <https://www.cisco.com/c/en/us/solutions/collateral/executive-perspectives/annual-internet-report/white-paper-c11-741490.html>. (accessed: 29.08.2023).
- [7] ITU. « Facts and figures 2023 ». (2023), [Online]. Available: <https://www.itu.int/itu-d/reports/statistics/2023/10/10/ff23-internet-traffic/>. (accessed: 16.05.2024).
- [8] Orange. « 6g : préparer aujourd’hui les réseaux mobiles du futur ». (2024), [Online]. Available: <https://hellofuture.orange.com/fr/grand-format/6g-preparer-aujourd'hui-les-reseaux-mobiles-du-futur#introduction>. (accessed: 04.06.2024).
- [9] G. P. Agrawal, *Fiber-optic communication systems*. John Wiley & Sons, 2012.
- [10] Y. Chen, M. Petrovich, E. N. Fokoua, *et al.*, « Hollow core dnanf optical fiber with <math>0.11\text{ dB/km}</math> loss », in *Optical Fiber Communication Conference (OFC) 2024*, Optica Publishing Group, 2024, Th4A.8. DOI: 10.1364/OFC.2024.Th4A.8. [Online]. Available: <https://opg.optica.org/abstract.cfm?URI=OFC-2024-Th4A.8>.
- [11] H. Sun, K.-T. Wu, and K. Roberts, « Real-time measurements of a 40 gb/s coherent system », *Opt. Express*, vol. 16, 2, pp. 873–879, Jan. 2008. DOI: 10.1364/OE.16.000873. [Online]. Available: <https://opg.optica.org/oe/abstract.cfm?URI=oe-16-2-873>.
- [12] C. E. Shannon, « A mathematical theory of communication », *The Bell System Technical Journal*, vol. 27, 3, pp. 379–423, 1948. DOI: 10.1002/j.1538-7305.1948.tb01338.x.

- 
- [13] A. Napoli, N. Costa, J. K. Fischer, *et al.*, « Towards multiband optical systems », in *Advanced Photonics 2018 (BGPP, IPR, NP, NOMA, Sensors, Networks, SPCom, SOF)*, Optica Publishing Group, 2018, NeTu3E.1. DOI: 10.1364/NETWORKS.2018.NeTu3E.1. [Online]. Available: <https://opg.optica.org/abstract.cfm?URI=Networks-2018-NeTu3E.1>.
- [14] J. K. Fischer, M. Cantono, V. Curri, *et al.*, « Maximizing the capacity of installed optical fiber infrastructure via wideband transmission », in *2018 20th International Conference on Transparent Optical Networks (ICTON)*, 2018, pp. 1–4. DOI: 10.1109/ICTON.2018.8473994.
- [15] F. Buchali, G. Böcherer, W. Idler, L. Schmalen, P. Schulte, and F. Steiner, « Experimental demonstration of capacity increase and rate-adaptation by probabilistically shaped 64-qam », in *2015 European Conference on Optical Communication (ECOC)*, 2015, pp. 1–3. DOI: 10.1109/ECOC.2015.7341688.
- [16] F. Pittalà, R.-P. Braun, G. Böcherer, *et al.*, « 1.71 tb/s single-channel and 56.51 tb/s dwdm transmission over 96.5 km field-deployed ssmf », *IEEE Photonics Technology Letters*, vol. 34, 3, pp. 157–160, 2022. DOI: 10.1109/LPT.2022.3142538.
- [17] T. Duthel, C. R. Fludger, B. Liu, *et al.*, « Dsp design for point-to-multipoint transmission », in *2023 Optical Fiber Communications Conference and Exhibition (OFC)*, 2023, pp. 1–3. DOI: 10.1364/OFC.2023.W1E.1.
- [18] G. P. Agrawal, « Nonlinear fiber optics », in *Nonlinear Science at the Dawn of the 21st Century*, Springer, 2000, pp. 195–211.
- [19] P. Poggiolini, A. Carena, V. Curri, G. Bosco, and F. Forghieri, « Analytical modeling of nonlinear propagation in uncompensated optical transmission links », *IEEE Photonics Technology Letters*, vol. 23, 11, pp. 742–744, 2011. DOI: 10.1109/LPT.2011.2131125.
- [20] A. Carena, V. Curri, G. Bosco, P. Poggiolini, and F. Forghieri, « Modeling of the impact of nonlinear propagation effects in uncompensated optical coherent transmission links », *Journal of Lightwave Technology*, vol. 30, 10, pp. 1524–1539, 2012. DOI: 10.1109/JLT.2012.2189198.
- [21] A. Amari, O. A. Dobre, R. Venkatesan, O. S. S. Kumar, P. Ciblat, and Y. Jaouën, « A survey on fiber nonlinearity compensation for 400 gb/s and beyond optical communication systems », *IEEE Communications Surveys & Tutorials*, vol. 19, 4, pp. 3097–3113, 2017. DOI: 10.1109/COMST.2017.2719958.
- [22] X. Li, X. Chen, G. Goldfarb, *et al.*, « Electronic post-compensation of wdm transmission impairments using coherent detection and digital signal processing », *Opt. Express*, vol. 16, 2, pp. 880–888, Jan. 2008. DOI: 10.1364/OE.16.000880. [Online]. Available: <https://opg.optica.org/oe/abstract.cfm?URI=oe-16-2-880>.
- [23] E. Ip and J. M. Kahn, « Compensation of dispersion and nonlinear impairments using digital backpropagation », *Journal of Lightwave Technology*, vol. 26, 20, pp. 3416–3425, 2008. DOI: 10.1109/JLT.2008.927791.
- [24] E. Ip, « Nonlinear compensation using backpropagation for polarization-multiplexed transmission », *Journal of Lightwave Technology*, vol. 28, 6, pp. 939–951, 2010. DOI: 10.1109/JLT.2010.2040135.

- 
- [25] F. P. Guiomar, J. D. Reis, A. L. Teixeira, and A. N. Pinto, « Digital postcompensation using volterra series transfer function », *IEEE Photonics Technology Letters*, vol. 23, 19, pp. 1412–1414, 2011. DOI: 10.1109/LPT.2011.2162229.
- [26] A. Vannucci, P. Serena, and A. Bononi, « The rp method: a new tool for the iterative solution of the nonlinear schrodinger equation », *Journal of Lightwave Technology*, vol. 20, 7, pp. 1102–1112, 2002. DOI: 10.1109/JLT.2002.800376.
- [27] L. B. Du, D. Rafique, A. Napoli, *et al.*, « Digital fiber nonlinearity compensation: toward 1-tb/s transport », *IEEE Signal Processing Magazine*, vol. 31, 2, pp. 46–56, 2014. DOI: 10.1109/MSP.2013.2288110.
- [28] C. M. Bishop and N. M. Nasrabadi, *Pattern recognition and machine learning*. Springer, 2006, vol. 4.
- [29] I. Goodfellow, Y. Bengio, and A. Courville, *Deep Learning*. MIT Press, 2016, <http://www.deeplearningbook.org>.
- [30] P. Baldi and R. Vershynin, « The capacity of feedforward neural networks », *Neural Networks*, vol. 116, pp. 288–311, 2019, ISSN: 0893-6080. DOI: <https://doi.org/10.1016/j.neunet.2019.04.009>. [Online]. Available: <https://www.sciencedirect.com/science/article/pii/S0893608019301078>.
- [31] Z. Xiang and G. Bi, « Complex neuron model with its applications to m-qam data communications in the presence of co-channel interferences », in *[Proceedings] ICASSP-92: 1992 IEEE International Conference on Acoustics, Speech, and Signal Processing*, vol. 2, 1992, 305–308 vol. 2. DOI: 10.1109/ICASSP.1992.226059.
- [32] G. Kechriotis, E. Zervas, and E. Manolakos, « Using recurrent neural networks for adaptive communication channel equalization », *IEEE Transactions on Neural Networks*, vol. 5, 2, pp. 267–278, 1994. DOI: 10.1109/72.279190.
- [33] W. R. Kirkland and D. Taylor, « Neural network channel equalization », in *Neural networks in telecommunications*, Springer, 1994, pp. 143–171.
- [34] A. Patnaik, D. Anagnostou, R. Mishra, ChristodoulouCG, and J. Lyke, « Applications of neural networks in wireless communications », *IEEE Antennas and Propagation Magazine*, vol. 46, 3, pp. 130–137, 2004. DOI: 10.1109/MAP.2004.1374125.
- [35] T. O’Shea and J. Hoydis, « An introduction to deep learning for the physical layer », *IEEE Transactions on Cognitive Communications and Networking*, vol. 3, 4, pp. 563–575, 2017. DOI: 10.1109/TCCN.2017.2758370.
- [36] W. Tong and G. Y. Li, « Nine challenges in artificial intelligence and wireless communications for 6g », *IEEE Wireless Communications*, vol. 29, 4, pp. 140–145, 2022.
- [37] O. Sidelnikov, A. Redyuk, and S. Sygletos, « Equalization performance and complexity analysis of dynamic deep neural networks in long haul transmission systems », *Opt. Express*, vol. 26, 25, pp. 32 765–32 776, Dec. 2018. DOI: 10.1364/OE.26.032765. [Online]. Available: <https://opg.optica.org/oe/abstract.cfm?URI=oe-26-25-32765>.
- [38] C. Catanese, R. Ayassi, E. Pincemin, and Y. Jaouën, « A fully connected neural network approach to mitigate fiber nonlinear effects in 200g dp-16-qam transmission system », in *2020 22nd International Conference on Transparent Optical Networks (ICTON)*, 2020, pp. 1–4. DOI: 10.1109/ICTON51198.2020.9203197.

- 
- [39] O. Sidelnikov, A. Redyuk, S. Sygletos, M. Fedoruk, and S. Turitsyn, « Advanced convolutional neural networks for nonlinearity mitigation in long-haul wdm transmission systems », *Journal of Lightwave Technology*, vol. 39, 8, pp. 2397–2406, 2021. DOI: 10.1109/JLT.2021.3051609.
- [40] S. Deligiannidis, A. Bogris, C. Mesaritakis, and Y. Kopsinis, « Compensation of fiber nonlinearities in digital coherent systems leveraging long short-term memory neural networks », *Journal of Lightwave Technology*, vol. 38, 21, pp. 5991–5999, 2020. DOI: 10.1109/JLT.2020.3007919.
- [41] X. Liu, Y. Wang, X. Wang, H. Xu, C. Li, and X. Xin, « Bi-directional gated recurrent unit neural network based nonlinear equalizer for coherent optical communication system », *Opt. Express*, vol. 29, 4, pp. 5923–5933, Feb. 2021. DOI: 10.1364/OE.416672. [Online]. Available: <https://opg.optica.org/oe/abstract.cfm?URI=oe-29-4-5923>.
- [42] A. Shahkarami, M. I. Yousefi, and Y. Jaouen, « Efficient deep learning of nonlinear fiber-optic communications using a convolutional recurrent neural network », in *2021 20th IEEE International Conference on Machine Learning and Applications (ICMLA)*, 2021, pp. 668–673. DOI: 10.1109/ICMLA52953.2021.00112.
- [43] P. J. Freire, Y. Osadchuk, B. Spinnler, *et al.*, « Performance versus complexity study of neural network equalizers in coherent optical systems », *Journal of Lightwave Technology*, vol. 39, 19, pp. 6085–6096, 2021. DOI: 10.1109/JLT.2021.3096286.
- [44] M. Schaedler, C. Bluemm, M. Kuschnerov, F. Pittalà, S. Calabrò, and S. Pachnicke, « Deep neural network equalization for optical short reach communication », *Applied Sciences*, vol. 9, 21, 2019, ISSN: 2076-3417. DOI: 10.3390/app9214675. [Online]. Available: <https://www.mdpi.com/2076-3417/9/21/4675>.
- [45] S. Zhang, F. Yaman, K. Nakamura, *et al.*, « Field and lab experimental demonstration of nonlinear impairment compensation using neural networks », *Nature communications*, vol. 10, 1, p. 3033, 2019. DOI: 10.1038/s41467-019-10911-9.
- [46] P. J. Freire, V. Neskornuik, A. Napoli, *et al.*, « Complex-valued neural network design for mitigation of signal distortions in optical links », *Journal of Lightwave Technology*, vol. 39, 6, pp. 1696–1705, 2021. DOI: 10.1109/JLT.2020.3042414.
- [47] C. Häger and H. D. Pfister, « Physics-based deep learning for fiber-optic communication systems », *IEEE Journal on Selected Areas in Communications*, vol. 39, 1, pp. 280–294, 2021. DOI: 10.1109/JSAC.2020.3036950.
- [48] Q. Fan, C. Lu, and A. P. T. Lau, « Combined neural network and adaptive dsp training for long-haul optical communications », *Journal of Lightwave Technology*, vol. 39, 22, pp. 7083–7091, 2021. DOI: 10.1109/JLT.2021.3111437.
- [49] J. Zhang and Z. Jia, « Coherent passive optical networks for 100g/ $\lambda$ -and-beyond fiber access: recent progress and outlook », *IEEE Network*, vol. 36, 2, pp. 116–123, 2022. DOI: 10.1109/MNET.005.2100604.
- [50] C. Laperle and M. O’Sullivan, « Advances in high-speed dacs, adcs, and dsp for optical coherent transceivers », *Journal of Lightwave Technology*, vol. 32, 4, pp. 629–643, 2014. DOI: 10.1109/JLT.2013.2284134.

- 
- [51] X. Zhou and C. Xie, « Introduction », in *Enabling Technologies for High Spectral-efficiency Coherent Optical Communication Networks*. 2016, pp. 1–12. DOI: 10.1002/9781119078289.ch1.
- [52] B. Mukherjee, I. Tomkos, M. Tornatore, P. Winzer, and Y. Zhao, « Springer handbook of optical networks », 2020.
- [53] R. Tkach and A. Chraplyvy, « Phase noise and linewidth in an ingaasp dfb laser », *Journal of Lightwave Technology*, vol. 4, 11, pp. 1711–1716, 1986. DOI: 10.1109/JLT.1986.1074677.
- [54] M. Tur, B. Moslehi, and J. Goodman, « Theory of laser phase noise in recirculating fiber-optic delay lines », *Journal of Lightwave Technology*, vol. 3, 1, pp. 20–31, 1985. DOI: 10.1109/JLT.1985.1074163.
- [55] E. Ip, A. P. T. Lau, D. J. F. Barros, and J. M. Kahn, « Coherent detection in optical fiber systems », *Opt. Express*, vol. 16, 2, pp. 753–791, Jan. 2008. DOI: 10.1364/OE.16.000753. [Online]. Available: <https://opg.optica.org/oe/abstract.cfm?URI=oe-16-2-753>.
- [56] T. Pfau, S. Hoffmann, and R. Noe, « Hardware-efficient coherent digital receiver concept with feedforward carrier recovery for  $M$ -qam constellations », *Journal of Lightwave Technology*, vol. 27, 8, pp. 989–999, 2009. DOI: 10.1109/JLT.2009.2010511.
- [57] T. Sasai, A. Matsushita, M. Nakamura, S. Okamoto, F. Hamaoka, and Y. Kisaka, « Laser phase noise tolerance of uniform and probabilistically shaped qam signals for high spectral efficiency systems », *Journal of Lightwave Technology*, vol. 38, 2, pp. 439–446, 2020. DOI: 10.1109/JLT.2019.2945470.
- [58] I. Fatadin, D. Ives, and S. J. Savory, « Blind equalization and carrier phase recovery in a 16-qam optical coherent system », *J. Lightwave Technol.*, vol. 27, 15, pp. 3042–3049, Aug. 2009. [Online]. Available: <https://opg.optica.org/jlt/abstract.cfm?URI=jlt-27-15-3042>.
- [59] J. G. Proakis, *Digital communications*. McGraw-Hill, Higher Education, 2008.
- [60] R.-J. Essiambre, G. Kramer, P. J. Winzer, G. J. Foschini, and B. Goebel, « Capacity limits of optical fiber networks », *Journal of Lightwave Technology*, vol. 28, 4, pp. 662–701, 2010. DOI: 10.1109/JLT.2009.2039464.
- [61] M. Kuschnerov, K. Piyawanno, B. Spinnler, *et al.*, « Data-aided vs. blind single-carrier coherent receivers », in *Optical Fiber Communication Conference*, Optica Publishing Group, 2010, OMR5. DOI: 10.1364/OFC.2010.OMR5. [Online]. Available: <https://opg.optica.org/abstract.cfm?URI=OFC-2010-OMR5>.
- [62] W. Weber, « Differential encoding for multiple amplitude and phase shift keying systems », *IEEE Transactions on Communications*, vol. 26, 3, pp. 385–391, 1978. DOI: 10.1109/TCOM.1978.1094074.
- [63] Y. Wang, Z. Wu, X. Li, *et al.*, « Non-data-aided cycle slip self-correcting carrier phase estimation for qpsk modulation format of coherent wireless optical communication system », *IEEE Access*, vol. 7, pp. 110 451–110 462, 2019. DOI: 10.1109/ACCESS.2019.2934224.
- [64] M. Magarini, L. Barletta, A. Spalvieri, *et al.*, « Pilot-symbols-aided carrier-phase recovery for 100-g pm-qpsk digital coherent receivers », *IEEE Photonics Technology Letters*, vol. 24, 9, pp. 739–741, 2012. DOI: 10.1109/LPT.2012.2187439.

- 
- [65] B. Châtelain, C. Laperle, K. Roberts, *et al.*, « A family of nyquist pulses for coherent optical communications », *Opt. Express*, vol. 20, 8, pp. 8397–8416, Apr. 2012. DOI: 10.1364/OE.20.008397. [Online]. Available: <https://opg.optica.org/oe/abstract.cfm?URI=oe-20-8-8397>.
- [66] E. Cubukcu, « Root raised cosine (rrc) filters and pulse shaping in communication systems », in *AIAA Conference*, 2012.
- [67] Y. Frignac, « Contribution à l'ingénierie des systèmes de transmission terrestres sur fibre optique utilisant le multiplexage en longueur d'onde de canaux modulés au débit de 40 Gbit/s. », Theses, Télécom ParisTech, Apr. 2003. [Online]. Available: <https://pastel.hal.science/pastel-00000688>.
- [68] S. J. Savory, « Digital filters for coherent optical receivers », *Opt. Express*, vol. 16, 2, pp. 804–817, Jan. 2008. DOI: 10.1364/OE.16.000804. [Online]. Available: <https://opg.optica.org/oe/abstract.cfm?URI=oe-16-2-804>.
- [69] J. Gordon and H. Kogelnik, « Pmd fundamentals: polarization mode dispersion in optical fibers », *Proceedings of the National Academy of Sciences*, vol. 97, 9, pp. 4541–4550, 2000. DOI: <https://doi.org/10.1073/pnas.97.9.454>.
- [70] H. Kogelnik, L. E. Nelson, and J. P. Gordon, « The inverse pmd problem », in *Polarization Mode Dispersion*, A. Galtarossa and C. R. Menyuk, Eds. New York, NY: Springer New York, 2005, pp. 70–85, ISBN: 978-0-387-26307-6. DOI: 10.1007/0-387-26307-1\_5. [Online]. Available: [https://doi.org/10.1007/0-387-26307-1\\_5](https://doi.org/10.1007/0-387-26307-1_5).
- [71] R. M. Büttler, C. Häger, H. D. Pfister, G. Liga, and A. Alvarado, « Model-based machine learning for joint digital backpropagation and pmd compensation », *Journal of Lightwave Technology*, vol. 39, 4, pp. 949–959, 2021. DOI: 10.1109/JLT.2020.3034047.
- [72] P. K. A. Wai, C. R. Menyuk, and H. H. Chen, « Stability of solitons in randomly varying birefringent fibers », *Opt. Lett.*, vol. 16, 16, pp. 1231–1233, Aug. 1991. DOI: 10.1364/OL.16.001231. [Online]. Available: <https://opg.optica.org/ol/abstract.cfm?URI=ol-16-16-1231>.
- [73] C. Xie, « Polarization and nonlinear impairments in fiber communication systems », in *Enabling Technologies for High Spectral-Efficiency Coherent Optical Communication Networks*. John Wiley & Sons, Ltd, 2016, ch. 6, pp. 201–246, ISBN: 9781119078289. DOI: <https://doi.org/10.1002/9781119078289.ch6>. eprint: <https://onlinelibrary.wiley.com/doi/pdf/10.1002/9781119078289.ch6>. [Online]. Available: <https://onlinelibrary.wiley.com/doi/abs/10.1002/9781119078289.ch6>.
- [74] S. J. Savory, « Digital coherent optical receivers: algorithms and subsystems », *IEEE Journal of Selected Topics in Quantum Electronics*, vol. 16, 5, pp. 1164–1179, 2010. DOI: 10.1109/JSTQE.2010.2044751.
- [75] E. Ip and J. M. Kahn, « Digital equalization of chromatic dispersion and polarization mode dispersion », *Journal of Lightwave Technology*, vol. 25, 8, pp. 2033–2043, 2007. DOI: 10.1109/JLT.2007.900889.
- [76] C. Menyuk and B. Marks, « Interaction of polarization mode dispersion and nonlinearity in optical fiber transmission systems », *Journal of Lightwave Technology*, vol. 24, 7, pp. 2806–2826, 2006. DOI: 10.1109/JLT.2006.875953.

- 
- [77] M. Eiselt, M. Shtaif, and L. Garrett, « Contribution of timing jitter and amplitude distortion to xpm system penalty in wdm systems », *IEEE Photonics Technology Letters*, vol. 11, 6, pp. 748–750, 1999. DOI: 10.1109/68.766806.
- [78] K. Inoue, « Four-wave mixing in an optical fiber in the zero-dispersion wavelength region », *Journal of Lightwave Technology*, vol. 10, 11, pp. 1553–1561, 1992. DOI: 10.1109/50.184893.
- [79] M. Maeda, W. Sessa, W. Way, *et al.*, « The effect of four-wave mixing in fibers on optical frequency-division multiplexed systems », *Journal of Lightwave Technology*, vol. 8, 9, pp. 1402–1408, 1990. DOI: 10.1109/50.59171.
- [80] S. L. Woodward, M. R. Phillips, and R. L. Smith, « Cross-polarization modulation: theory and experiment of a multiple-wavelength system », in *Optical Fiber Communication Conference and Exposition and The National Fiber Optic Engineers Conference*, Optica Publishing Group, 2006, OWI15. [Online]. Available: <https://opg.optica.org/abstract.cfm?URI=OFC-2006-OWI15>.
- [81] M. Phillips and S. Woodward, « Cross-polarization modulation: theory and measurement of a two-channel wdm system », *IEEE Photonics Technology Letters*, vol. 17, 10, pp. 2086–2088, 2005. DOI: 10.1109/LPT.2005.856325.
- [82] G. P. Agrawal, *Fiber-optic communication systems*. John Wiley & Sons, 2012.
- [83] D. Marcuse, C. Menyuk, and P. Wai, « Application of the manakov-pmd equation to studies of signal propagation in optical fibers with randomly varying birefringence », *Journal of Lightwave Technology*, vol. 15, 9, pp. 1735–1746, 1997. DOI: 10.1109/50.622902.
- [84] C. R. Menyuk, « Solitons in birefringent optical fibers and polarization mode dispersion », *Optics Communications*, vol. 550, p. 129 841, 2024, ISSN: 0030-4018. DOI: <https://doi.org/10.1016/j.optcom.2023.129841>. [Online]. Available: <https://www.sciencedirect.com/science/article/pii/S0030401823005898>.
- [85] P. Wai and C. Menyuk, « Polarization mode dispersion, decorrelation, and diffusion in optical fibers with randomly varying birefringence », *Journal of Lightwave Technology*, vol. 14, 2, pp. 148–157, 1996. DOI: 10.1109/50.482256.
- [86] K. Kikuchi, « Fundamentals of coherent optical fiber communications », *Journal of Lightwave Technology*, vol. 34, 1, pp. 157–179, 2016. DOI: 10.1109/JLT.2015.2463719.
- [87] V. Oliari, S. Goossens, C. Häger, *et al.*, « Revisiting efficient multi-step nonlinearity compensation with machine learning: an experimental demonstration », *Journal of Lightwave Technology*, vol. 38, 12, pp. 3114–3124, 2020. DOI: 10.1109/JLT.2020.2994220.
- [88] M. Oerder and H. Meyr, « Digital filter and square timing recovery », *IEEE Transactions on Communications*, vol. 36, 5, pp. 605–612, 1988. DOI: 10.1109/26.1476.
- [89] J. G. Proakis and D. G. Manolakis, *Digital signal processing (3rd ed.): principles, algorithms, and applications*. USA: Prentice-Hall, Inc., 1996, ISBN: 0133737624.
- [90] B. Spinnler, « Equalizer design and complexity for digital coherent receivers », *IEEE Journal of Selected Topics in Quantum Electronics*, vol. 16, 5, pp. 1180–1192, 2010. DOI: 10.1109/JSTQE.2009.2035931.

- 
- [91] M. Secondini, D. Marsella, and E. Forestieri, « Enhanced split-step fourier method for digital backpropagation », in *2014 The European Conference on Optical Communication (ECOC)*, 2014, pp. 1–3. DOI: 10.1109/ECOC.2014.6964122.
- [92] A. Eghbali, H. Johansson, O. Gustafsson, and S. J. Savory, « Optimal least-squares fir digital filters for compensation of chromatic dispersion in digital coherent optical receivers », *Journal of Lightwave Technology*, vol. 32, 8, pp. 1449–1456, 2014. DOI: 10.1109/JLT.2014.2307916.
- [93] J. W. Cooley and J. W. Tukey, « An algorithm for the machine calculation of complex fourier series », *Mathematics of computation*, vol. 19, 90, pp. 297–301, 1965.
- [94] J. Treichler, I. Fijalkow, and C. Johnson, « Fractionally spaced equalizers », *IEEE Signal Processing Magazine*, vol. 13, 3, pp. 65–81, 1996. DOI: 10.1109/79.489269.
- [95] D. Godard, « Self-recovering equalization and carrier tracking in two-dimensional data communication systems », *IEEE Transactions on Communications*, vol. 28, 11, pp. 1867–1875, 1980. DOI: 10.1109/TCOM.1980.1094608.
- [96] F. P. Guiomar, S. B. Amado, A. Carena, *et al.*, « Fully blind linear and nonlinear equalization for 100g pm-64qam optical systems », *Journal of Lightwave Technology*, vol. 33, 7, pp. 1265–1274, 2015. DOI: 10.1109/JLT.2014.2386653.
- [97] M. Morelli and U. Mengali, « Feedforward frequency estimation for psk: a tutorial review », *European Transactions on Telecommunications*, vol. 9, 2, pp. 103–116, 1998.
- [98] A. Leven, N. Kaneda, U.-V. Koc, and Y.-K. Chen, « Frequency estimation in intradyne reception », *IEEE Photonics Technology Letters*, vol. 19, 6, pp. 366–368, 2007. DOI: 10.1109/LPT.2007.891893.
- [99] M. Selmi, Y. Jaouen, and P. Ciblat, « Accurate digital frequency offset estimator for coherent polmux qam transmission systems », in *2009 35th European Conference on Optical Communication*, 2009, pp. 1–2.
- [100] M. Selmi, « Outils avancés de traitement de signal pour les systèmes de communications optiques utilisant les formats qam », Thèse de doctorat dirigée par Jaouën, Yves et Ciblat, Philippe Electronique et communications Paris, Télécom ParisTech 2011, Ph.D. dissertation, 2011, 1 vol. (LII–111 p.) [Online]. Available: <http://www.theses.fr/2011ENST0028>.
- [101] A. J. Viterbi and A. M. Viterbi, « Nonlinear estimation of psk-modulated carrier phase with application to burst digital transmission », *IEEE Transactions on Information Theory*, vol. 29, 4, pp. 543–551, 1983. DOI: 10.1109/TIT.1983.1056713.
- [102] D.-S. Ly-Gagnon, S. Tsukamoto, K. Katoh, and K. Kikuchi, « Coherent detection of optical quadrature phase-shift keying signals with carrier phase estimation », *Journal of Lightwave Technology*, vol. 24, 1, pp. 12–21, 2006. DOI: 10.1109/JLT.2005.860477.
- [103] C. Fludger, D. Nuss, and T. Kupfer, « Cycle-slips in 100g dp-qpsk transmission systems », in *Optical Fiber Communication Conference*, Optica Publishing Group, 2012, OTu2G.1. DOI: 10.1364/OFC.2012.OTu2G.1. [Online]. Available: <https://opg.optica.org/abstract.cfm?URI=OFC-2012-OTu2G.1>.

- 
- [104] F. Yaman and G. Li, « Nonlinear impairment compensation for polarization-division multiplexed wdm transmission using digital backward propagation », *IEEE Photonics Journal*, vol. 2, 5, pp. 816–832, 2010. DOI: 10.1109/JPHOT.2010.2071860.
- [105] C. B. Czegledi, G. Liga, D. Lavery, *et al.*, « Digital backpropagation accounting for polarization-mode dispersion », *Opt. Express*, vol. 25, 3, pp. 1903–1915, Feb. 2017. DOI: 10.1364/OE.25.001903. [Online]. Available: <https://opg.optica.org/oe/abstract.cfm?URI=oe-25-3-1903>.
- [106] J. Zhang, X. Li, and Z. Dong, « Digital nonlinear compensation based on the modified logarithmic step size », *Journal of Lightwave Technology*, vol. 31, 22, pp. 3546–3555, 2013. DOI: 10.1109/JLT.2013.2285648.
- [107] A. Napoli, Z. Maalej, V. A. J. M. Sleiffer, *et al.*, « Reduced complexity digital back-propagation methods for optical communication systems », *Journal of Lightwave Technology*, vol. 32, 7, pp. 1351–1362, 2014. DOI: 10.1109/JLT.2014.2301492.
- [108] C. Fougstedt, M. Mazur, L. Svensson, H. Eliasson, M. Karlsson, and P. Larsson-Edefors, « Time-domain digital back propagation: algorithm and finite-precision implementation aspects », in *Optical Fiber Communication Conference*, Optica Publishing Group, 2017, W1G.4. DOI: 10.1364/OFC.2017.W1G.4. [Online]. Available: <https://opg.optica.org/abstract.cfm?URI=OFC-2017-W1G.4>.
- [109] K. Peddanarappagari and M. Brandt-Pearce, « Volterra series transfer function of single-mode fibers », *Journal of Lightwave Technology*, vol. 15, 12, pp. 2232–2241, 1997. DOI: 10.1109/50.643545.
- [110] M. Schetzen, « Theory of pth-order inverses of nonlinear systems », *IEEE Transactions on Circuits and Systems*, vol. 23, 5, pp. 285–291, 1976. DOI: 10.1109/TCS.1976.1084219.
- [111] F. P. Guiomar, J. D. Reis, A. L. Teixeira, and A. N. Pinto, « Mitigation of intra-channel nonlinearities using a frequency-domain volterra series equalizer », *Opt. Express*, vol. 20, 2, pp. 1360–1369, Jan. 2012. DOI: 10.1364/OE.20.001360. [Online]. Available: <https://opg.optica.org/oe/abstract.cfm?URI=oe-20-2-1360>.
- [112] A. Bakhshali, W.-Y. Chan, J. C. Cartledge, *et al.*, « Frequency-domain volterra-based equalization structures for efficient mitigation of intrachannel kerr nonlinearities », *Journal of Lightwave Technology*, vol. 34, 8, pp. 1770–1777, 2016. DOI: 10.1109/JLT.2015.2510607.
- [113] A. M. Turing, « Computing machinery and intelligence », in *Parsing the Turing Test: Philosophical and Methodological Issues in the Quest for the Thinking Computer*, R. Epstein, G. Roberts, and G. Beber, Eds. Dordrecht: Springer Netherlands, 2009, pp. 23–65, ISBN: 978-1-4020-6710-5. DOI: 10.1007/978-1-4020-6710-5\_3. [Online]. Available: [https://doi.org/10.1007/978-1-4020-6710-5\\_3](https://doi.org/10.1007/978-1-4020-6710-5_3).
- [114] A. K. Jain, M. N. Murty, and P. J. Flynn, « Data clustering: a review », *ACM Comput. Surv.*, vol. 31, 3, pp. 264–323, Sep. 1999, ISSN: 0360-0300. DOI: 10.1145/331499.331504. [Online]. Available: <https://doi.org/10.1145/331499.331504>.

- 
- [115] A. K. Jain, « Data clustering: 50 years beyond k-means », *Pattern Recognition Letters*, vol. 31, 8, pp. 651–666, 2010, Award winning papers from the 19th International Conference on Pattern Recognition (ICPR), ISSN: 0167-8655. DOI: <https://doi.org/10.1016/j.patrec.2009.09.011>. [Online]. Available: <https://www.sciencedirect.com/science/article/pii/S0167865509002323>.
- [116] V. Chandola, A. Banerjee, and V. Kumar, « Anomaly detection: a survey », *ACM Comput. Surv.*, vol. 41, 3, Jul. 2009, ISSN: 0360-0300. DOI: 10.1145/1541880.1541882. [Online]. Available: <https://doi.org/10.1145/1541880.1541882>.
- [117] Y. LeCun, Y. Bengio, and G. Hinton, « Deep learning », *Nature*, vol. 521, pp. 436–44, May 2015. DOI: 10.1038/nature14539.
- [118] Q. Wang, Y. Ma, K. Zhao, and Y. Tian, « A comprehensive survey of loss functions in machine learning », *Annals of Data Science*, pp. 1–26, 2020.
- [119] D. P. Kingma and J. Ba, *Adam: a method for stochastic optimization*, 2017. arXiv: 1412.6980 [cs.LG]. [Online]. Available: <https://arxiv.org/abs/1412.6980>.
- [120] E. Pincemin, Y. Loussouarn, A. Sotomayor, *et al.*, « 927-km end-to-end interoperable 400-gb ethernet optical communications through 2-km 400gbase-fr4, 8x100-km 400g-openroadm and 125-km 400-zr fiber lines », in *Optical Fiber Communication Conference (OFC) 2022*, Optica Publishing Group, 2022, Th4A.3. DOI: 10.1364/OFC.2022.Th4A.3. [Online]. Available: <https://opg.optica.org/abstract.cfm?URI=OFC-2022-Th4A.3>.
- [121] J. Bergstra, R. Bardenet, Y. Bengio, and B. Kégl, « Algorithms for hyper-parameter optimization », in *Advances in Neural Information Processing Systems*, J. Shawe-Taylor, R. Zemel, P. Bartlett, F. Pereira, and K. Weinberger, Eds., vol. 24, Curran Associates, Inc., 2011. [Online]. Available: [https://proceedings.neurips.cc/paper\\_files/paper/2011/file/86e8f7ab32cfd12577bc2619bc635690-Paper.pdf](https://proceedings.neurips.cc/paper_files/paper/2011/file/86e8f7ab32cfd12577bc2619bc635690-Paper.pdf).
- [122] S. Haykin, *Neural networks: a comprehensive foundation*. Prentice Hall PTR, 1998.
- [123] M. Leshno, V. Y. Lin, A. Pinkus, and S. Schocken, « Multilayer feedforward networks with a nonpolynomial activation function can approximate any function », *Neural Networks*, vol. 6, 6, pp. 861–867, 1993, ISSN: 0893-6080. DOI: [https://doi.org/10.1016/S0893-6080\(05\)80131-5](https://doi.org/10.1016/S0893-6080(05)80131-5). [Online]. Available: <https://www.sciencedirect.com/science/article/pii/S0893608005801315>.
- [124] T. Koike-Akino, Y. Wang, D. S. Millar, K. Kojima, and K. Parsons, « Neural turbo equalization: deep learning for fiber-optic nonlinearity compensation », *Journal of Lightwave Technology*, vol. 38, 11, pp. 3059–3066, 2020. DOI: 10.1109/JLT.2020.2976479.
- [125] M. A. Jarajreh, E. Giacoumidis, I. Aldaya, *et al.*, « Artificial neural network nonlinear equalizer for coherent optical ofdm », *IEEE Photonics Technology Letters*, vol. 27, 4, pp. 387–390, 2015. DOI: 10.1109/LPT.2014.2375960.
- [126] E. Giacoumidis, S. T. Le, M. Ghanbarisabagh, *et al.*, « Fiber nonlinearity-induced penalty reduction in co-ofdm by ann-based nonlinear equalization », *Opt. Lett.*, vol. 40, 21, pp. 5113–5116, Nov. 2015. DOI: 10.1364/OL.40.005113. [Online]. Available: <https://opg.optica.org/ol/abstract.cfm?URI=ol-40-21-5113>.

- 
- [127] J. Estaran, R. Rios-Mueller, M. A. Mestre, *et al.*, « Artificial neural networks for linear and non-linear impairment mitigation in high-baudrate im/dd systems », in *ECOC 2016; 42nd European Conference on Optical Communication*, 2016, pp. 1–3.
- [128] T. A. Eriksson, H. Bülow, and A. Leven, « Applying neural networks in optical communication systems: possible pitfalls », *IEEE Photonics Technology Letters*, vol. 29, 23, pp. 2091–2094, 2017. DOI: 10.1109/LPT.2017.2755663.
- [129] R. Rios-Müller, J. M. Estarán, and J. Renaudier, « Experimental estimation of optical nonlinear memory channel conditional distribution using deep neural networks », in *2017 Optical Fiber Communications Conference and Exhibition (OFC)*, IEEE, 2017, pp. 1–3.
- [130] C. Catanese, A. Triki, E. Pincemin, and Y. Jaouën, « A survey of neural network applications in fiber nonlinearity mitigation », in *2019 21st International Conference on Transparent Optical Networks (ICTON)*, 2019, pp. 1–4. DOI: 10.1109/ICTON.2019.8840355.
- [131] F. Zhang, X. Fang, and X. Chen, « Neural network-based fiber nonlinearity mitigation in high-speed coherent optical transmission systems », in *Optical Fiber Communication Conference (OFC) 2022*, Optica Publishing Group, 2022, M1H.1. DOI: 10.1364/OFC.2022.M1H.1. [Online]. Available: <https://opg.optica.org/abstract.cfm?URI=OFC-2022-M1H.1>.
- [132] V. Kamalov, L. Jovanovski, V. Vusirikala, *et al.*, « Evolution from 8qam live traffic to ps 64-qam with neural-network based nonlinearity compensation on 11000 km open sub-sea cable », in *Optical Fiber Communication Conference Postdeadline Papers*, Optica Publishing Group, 2018, Th4D.5. DOI: 10.1364/OFC.2018.Th4D.5. [Online]. Available: <https://opg.optica.org/abstract.cfm?URI=OFC-2018-Th4D.5>.
- [133] T. T. Nguyen, T. Zhang, E. Giacomidis, *et al.*, « Coupled transceiver-fiber nonlinearity compensation based on machine learning for probabilistic shaping system », *Journal of Lightwave Technology*, vol. 39, 2, pp. 388–399, 2021. DOI: 10.1109/JLT.2020.3029336.
- [134] T. Kamiyama, H. Kobayashi, and K. Iwashita, « Neural network nonlinear equalizer in long-distance coherent optical transmission systems », *IEEE Photonics Technology Letters*, vol. 33, 9, pp. 421–424, 2021. DOI: 10.1109/LPT.2021.3067341.
- [135] M. Schädler, G. Böcherer, and S. Pachnicke, « Soft-demapping for short reach optical communication: a comparison of deep neural networks and volterra series », *Journal of Lightwave Technology*, vol. 39, 10, pp. 3095–3105, 2021. DOI: 10.1109/JLT.2021.3056869.
- [136] M. Schädler, G. Böcherer, F. Pittalà, *et al.*, « Recurrent neural network soft-demapping for nonlinear isi in 800gbit/s dwdm coherent optical transmissions », *Journal of Lightwave Technology*, vol. 39, 16, pp. 5278–5286, 2021. DOI: 10.1109/JLT.2021.3102064.
- [137] P. J. Freire, D. Abode, J. E. Prilepsky, *et al.*, « Transfer learning for neural networks-based equalizers in coherent optical systems », *Journal of Lightwave Technology*, vol. 39, 21, pp. 6733–6745, 2021. DOI: 10.1109/JLT.2021.3108006.
- [138] P. J. Freire, A. Napoli, B. Spinnler, N. Costa, S. K. Turitsyn, and J. E. Prilepsky, « Neural networks-based equalizers for coherent optical transmission: caveats and pitfalls », *IEEE Journal of Selected Topics in Quantum Electronics*, vol. 28, 4: *Mach. Learn. in Photon. Commun. and Meas. Syst.* Pp. 1–23, 2022. DOI: 10.1109/JSTQE.2022.3174268.

- 
- [139] D. Arguello Ron, P. Freire, J. Prilepsky, M. Kamalian, A. Napoli, and S. Turitsyn, « Experimental implementation of a neural network optical channel equalizer in restricted hardware using pruning and quantization », *Scientific Reports*, vol. 12, May 2022. DOI: 10.1038/s41598-022-12563-0.
- [140] C. Li, Y. Wang, J. Wang, *et al.*, « Convolutional neural network-aided dp-64 qam coherent optical communication systems », *Journal of Lightwave Technology*, vol. 40, 9, pp. 2880–2889, 2022. DOI: 10.1109/JLT.2022.3146839.
- [141] P. J. Freire, M. Anderson, B. Spinnler, *et al.*, « Towards fpga implementation of neural network-based nonlinearity mitigation equalizers in coherent optical transmission systems », in *European Conference on Optical Communication (ECOC) 2022*, Optica Publishing Group, 2022, We1C.2. [Online]. Available: <https://opg.optica.org/abstract.cfm?URI=ECEOC-2022-We1C.2>.
- [142] H. Ming, X. Chen, X. Fang, L. Zhang, C. Li, and F. Zhang, « Ultralow complexity long short-term memory network for fiber nonlinearity mitigation in coherent optical communication systems », *Journal of Lightwave Technology*, vol. 40, 8, pp. 2427–2434, 2022. DOI: 10.1109/JLT.2022.3141404.
- [143] M. Matsumoto and T. Nishimura, « Mersenne twister: a 623-dimensionally equidistributed uniform pseudo-random number generator », *ACM Trans. Model. Comput. Simul.*, vol. 8, 1, pp. 3–30, Jan. 1998, ISSN: 1049-3301. DOI: 10.1145/272991.272995. [Online]. Available: <https://doi.org/10.1145/272991.272995>.
- [144] T. Akiba, S. Sano, T. Yanase, T. Ohta, and M. Koyama, « Optuna: a next-generation hyperparameter optimization framework », in *Proceedings of the 25th ACM SIGKDD International Conference on Knowledge Discovery and Data Mining*, 2019.
- [145] A. Mansour and C. Jutten, « What should we say about the kurtosis? », *IEEE Signal Processing Letters*, vol. 6, 12, pp. 321–322, 1999. DOI: 10.1109/97.803435.
- [146] B. I. Bitachon, A. Ghazisaeidi, M. Eppenberger, B. Baeuerle, M. Ayata, and J. Leuthold, « Deep learning based digital backpropagation demonstrating snr gain at low complexity in a 1200 km transmission link », *Optics Express*, vol. 28, 20, pp. 29 318–29 334, 2020. DOI: 10.1364/OE.401667. [Online]. Available: <https://opg.optica.org/oe/abstract.cfm?URI=oe-28-20-29318>.
- [147] J. Kim and H. Kim, « Length of pseudorandom binary sequence required to train artificial neural network without overfitting », *IEEE Access*, vol. 9, pp. 125 358–125 365, 2021. DOI: 10.1109/ACCESS.2021.3111092.
- [148] ITU. « O.150 : digital test patterns for performance measurements on digital transmission equipment ». (1993), [Online]. Available: <https://www.itu.int/rec/T-REC-O.150-199210-S>. (accessed: 16.05.2024).
- [149] C. You and D. Hong, « Adaptive equalization using the complex backpropagation algorithm », in *Proceedings of International Conference on Neural Networks (ICNN'96)*, vol. 4, 1996, 2136–2141 vol.4. DOI: 10.1109/ICNN.1996.549232.

- 
- [150] J. Patra, R. Pal, R. Baliarsingh, and G. Panda, « Nonlinear channel equalization for qam signal constellation using artificial neural networks », *IEEE Transactions on Systems, Man, and Cybernetics, Part B (Cybernetics)*, vol. 29, 2, pp. 262–271, 1999. DOI: 10.1109/3477.752798.
- [151] S. Liu, P.-C. Peng, C.-W. Hsu, S. Chen, H. Tian, and G.-K. Chang, « An effective artificial neural network equalizer with s-shape activation function for high-speed 16-qam transmissions using low-cost directly modulated laser », in *2018 International Conference on Network Infrastructure and Digital Content (IC-NIDC)*, 2018, pp. 269–273. DOI: 10.1109/ICNIDC.2018.8525619.
- [152] A. Sotomayor, E. Pincemin, V. Choqueuse, and M. Morvan, « Optimized cost function of multi-layer perceptron for fibre non-linear impairment mitigation in coherent 200-gbps dp-16qam transmission system », in *Optica Advanced Photonics Congress 2022*, Optica Publishing Group, 2022, JTU2A.41. [Online]. Available: <https://opg.optica.org/abstract.cfm?URI=SPPCom-2022-JTu2A.41>.
- [153] A. Alvarado, E. Agrell, D. Lavery, R. Maher, and P. Bayvel, « Replacing the soft-decision fec limit paradigm in the design of optical communication systems », *Journal of Lightwave Technology*, vol. 33, 20, pp. 4338–4352, 2015. DOI: 10.1109/JLT.2015.2450537.
- [154] P. Poggiolini, « The gn model of non-linear propagation in uncompensated coherent optical systems », *Journal of Lightwave Technology*, vol. 30, 24, pp. 3857–3879, 2012. DOI: 10.1109/JLT.2012.2217729.
- [155] A. Alvarado, « Information rates and post-fec ber prediction in optical fiber communications », in *Optical Fiber Communication Conference*, Optica Publishing Group, 2017, Th3F.3. DOI: 10.1364/OFC.2017.Th3F.3. [Online]. Available: <https://opg.optica.org/abstract.cfm?URI=OFC-2017-Th3F.3>.
- [156] P. P. Mitra and J. B. Stark, « Nonlinear limits to the information capacity of optical fibre communications », *Nature*, vol. 411, 6841, pp. 1027–1030, 2001. DOI: <https://doi.org/10.1038/35082518>.
- [157] A. Alvarado, T. Fehenberger, B. Chen, and F. M. J. Willems, « Achievable information rates for fiber optics: applications and computations », *J. Lightwave Technol.*, vol. 36, 2, pp. 424–439, Jan. 2018. [Online]. Available: <https://opg.optica.org/jlt/abstract.cfm?URI=jlt-36-2-424>.
- [158] T. Fehenberger, A. Alvarado, P. Bayvel, and N. Hanik, « On achievable rates for long-haul fiber-optic communications », *Opt. Express*, vol. 23, 7, pp. 9183–9191, Apr. 2015. DOI: 10.1364/OE.23.009183. [Online]. Available: <https://opg.optica.org/oe/abstract.cfm?URI=oe-23-7-9183>.
- [159] P. J. Freire, J. E. Prilepsky, Y. Osadchuk, S. K. Turitsyn, and V. Aref, « Deep neural network-aided soft-demapping in coherent optical systems: regression versus classification », *IEEE Transactions on Communications*, vol. 70, 12, pp. 7973–7988, 2022. DOI: 10.1109/TCOMM.2022.3213284.
- [160] G. Böcherer. « Lecture notes on machine learning for communications ». (2022), [Online]. Available: <http://georg-boecherer.de/mlcomm>. (accessed: 31.10.2023).

- 
- [161] S. M. Kay, *Fundamentals of statistical signal processing: estimation theory*. Prentice-Hall, Inc., 1993.
- [162] D. Taylor, « The estimate feedback equalizer: a suboptimum nonlinear receiver », *IEEE Transactions on Communications*, vol. 21, 9, pp. 979–990, 1973. DOI: 10.1109/TCOM.1973.1091791.
- [163] M. Khani, M. Alizadeh, J. Hoydis, and P. Fleming, « Adaptive neural signal detection for massive mimo », *IEEE Transactions on Wireless Communications*, vol. 19, 8, pp. 5635–5648, 2020.
- [164] W. R. Kirkland, « On the application of multi-layered perceptrons to nonlinear equalization for frequency selective fading channels and nonlinear prediction for time selective rayleigh fading channels », Ph.D. dissertation, 1994. DOI: <http://hdl.handle.net/11375/7802>.
- [165] C. You and D. Hong, « Nonlinear blind equalization schemes using complex-valued multilayer feedforward neural networks », *IEEE Transactions on Neural Networks*, vol. 9, 6, pp. 1442–1455, 1998. DOI: 10.1109/72.728394.
- [166] K. He, X. Zhang, S. Ren, and J. Sun, « Deep residual learning for image recognition », in *Proceedings of the IEEE conference on computer vision and pattern recognition*, 2016, pp. 770–778.
- [167] H. Mathis, « On the kurtosis of digitally modulated signals with timing offsets », in *2001 IEEE Third Workshop on Signal Processing Advances in Wireless Communications (SPAWC'01). Workshop Proceedings (Cat. No.01EX471)*, 2001, pp. 86–89. DOI: 10.1109/SPAWC.2001.923850.
- [168] F. Diedolo. « Nonlinear equalization for optical communications based on entropy-regularized mean square error ». (2022), [Online]. Available: [http://www.georg-boecherer.de/diedolo2022nonlinear\\_slides.pdf](http://www.georg-boecherer.de/diedolo2022nonlinear_slides.pdf). (accessed: 20.06.2023).
- [169] A. Sotomayor, E. Pincemin, V. Choqueuse, and M. Morvan, « A comparison of machine learning techniques for fiber non-linearity compensation: multilayer perceptron vs. learned digital backpropagation », in *2023 23rd International Conference on Transparent Optical Networks (ICTON)*, 2023, pp. 1–4. DOI: 10.1109/ICTON59386.2023.10207458.
- [170] C. Häger and H. D. Pfister, « Nonlinear interference mitigation via deep neural networks », in *Optical Fiber Communication Conference*, Optica Publishing Group, 2018, W3A.4. DOI: 10.1364/OFC.2018.W3A.4. [Online]. Available: <https://opg.optica.org/abstract.cfm?URI=OFC-2018-W3A.4>.
- [171] Q. Fan, G. Zhou, T. Gui, C. Lu, and A. P. T. Lau, « Advancing theoretical understanding and practical performance of signal processing for nonlinear optical communications through machine learning », *Nature Communications*, vol. 11, 1, p. 3694, 2020.
- [172] P. Jain, L. Lampe, and J. Mitra, « Joint pmd tracking and nonlinearity compensation with deep neural networks », *Journal of Lightwave Technology*, vol. 41, 12, pp. 3957–3966, 2023. DOI: 10.1109/JLT.2023.3276373.
- [173] C. Häger and H. D. Pfister, « Physics-based deep learning for fiber-optic communication systems », *IEEE Journal on Selected Areas in Communications*, vol. 39, 1, pp. 280–294, 2021. DOI: 10.1109/JSAC.2020.3036950.

- 
- [174] A. Frunză, V. Choqueuse, F. Miron, and S. Azou, « A parametric state-space network for global impairments compensation in optical systems », in *2024 15th International Conference on Communications (COMM)*, 2024, pp. 1–6. DOI: 10.1109/COMM62355.2024.10741393.
- [175] A. Carena, G. Bosco, V. Curri, P. Poggiolini, M. T. Taiba, and F. Forghieri, « Statistical characterization of pm-qpsk signals after propagation in uncompensated fiber links », in *36th European Conference and Exhibition on Optical Communication*, 2010, pp. 1–3. DOI: 10.1109/ECOC.2010.5621509.
- [176] N. Bergano, F. Kerfoot, and C. Davidsion, « Margin measurements in optical amplifier system », *IEEE Photonics Technology Letters*, vol. 5, 3, pp. 304–306, 1993. DOI: 10.1109/68.205619.
- [177] W. Freude, R. Schmogrow, B. Nebendahl, *et al.*, « Quality metrics for optical signals: eye diagram, q-factor, osnr, evm and ber », in *2012 14th International Conference on Transparent Optical Networks (ICTON)*, 2012, pp. 1–4. DOI: 10.1109/ICTON.2012.6254380.
- [178] F. Zhang, Y. Luo, Y. Wang, *et al.*, « Experimental comparison of different ber estimation methods for coherent optical qpsk transmission systems », *IEEE Photonics Technology Letters*, vol. 23, 18, pp. 1343–1345, 2011. DOI: 10.1109/LPT.2011.2160718.
- [179] R. Hui and M. O’Sullivan, *Fiber-Optic Measurement Techniques*. Academic Press, 2022.
- [180] P. Jennevé, P. Ramantanis, J.-C. Antona, *et al.*, « Pitfalls of error estimation from measured non-gaussian nonlinear noise statistics over dispersion-unmanaged systems », in *2014 The European Conference on Optical Communication (ECOC)*, IEEE, 2014, pp. 1–3.
- [181] T. Fehenberger and N. Hanik, « Mutual Information as a Figure of Merit for Optical Fiber Systems », *arXiv e-prints*, arXiv:1405.2029, arXiv:1405.2029, Apr. 2014. DOI: 10.48550/arXiv.1405.2029.
- [182] L. Hanzo, S. X. Ng, W. Webb, and T. Keller, *Quadrature amplitude modulation: From basics to adaptive trellis-coded, turbo-equalised and space-time coded OFDM, CDMA and MC-CDMA systems*. IEEE Press-John Wiley, 2004.
- [183] T. M. Cover, *Elements of information theory*. John Wiley & Sons, 1999.
- [184] R. G. Gallager, *Information theory and reliable communication*. Springer, 1968, vol. 588.
- [185] R. Maher, A. Alvarado, D. Lavery, and P. Bayvel, « Increasing the information rates of optical communications via coded modulation: a study of transceiver performance », *Scientific Reports*, vol. 6, pp. 1–10, 2016, ISSN: 2045-2322. DOI: 10.1038/srep21278.



**Titre :** Etude et Implémentation des Egaliseurs Non-linéaires utilisant des Réseaux de Neurones Artificiels pour les Systèmes de Transmission Optique Cohérente.

**Mot clés :** systèmes cohérents, non-linéarité, égalisation non-linéaire, réseaux de neurones

**Résumé :** Dans les systèmes optiques cohérents utilisant des schémas de modulation par déplacement de phase, la non-linéarité de la fibre constitue le principal obstacle à l'atteinte de la capacité de Shannon. En pratique, la propagation non-linéaire dans la fibre introduit un bruit de phase qui ne peut pas être complètement compensé par des égaliseurs DSP linéaires. Pour compenser ces non-linéarités, des égaliseurs non-linéaires plus performants, basés sur la Digital Backpropagation ou sur les séries de Volterra, sont souvent trop gourmands en calculs pour leur déploiement en temps réel dans les récepteurs actuels. Dans ce contexte, une alternative prometteuse aux égaliseurs non linéaires classiques réside dans l'utilisation des réseaux de neurones artificiels lesquels, par rapport aux égaliseurs non-linéaires, présentent l'avantage d'une complexité calculatoire maîtrisée. En utilisant des simulations numériques d'un DP-16QAM sur

14×100 km de fibre monomode standard, nous avons montré que, pour de longues distances, des réseaux de neurones simples potentiellement implémentables dans un récepteur ne compensent pas le bruit de phase non-linéaire aussi efficacement que les techniques classiques. De plus, ce travail montre que l'utilisation d'une fonction de coût basée sur l'erreur quadratique moyenne lors de l'entraînement introduit une déformation non-linéaire du diagramme de constellation en sortie de réseau. En particulier, pour les constellations QAM quadratiques, cette déformation se traduit géométriquement sous la forme d'une grille. Ce phénomène, que nous avons nommé MMSE-scatterplot, peut affecter significativement les traitements DSP ultérieurs de la chaîne de réception. Après une analyse théorique de ce phénomène, ce travail présente une technique innovante pour atténuer cet effet et améliorer les performances de la chaîne.

**Title:** Study and Implementation of Nonlinear Equalizers Using Artificial Neural Networks for Coherent Optical Transmission Systems

**Keywords:** coherent systems, fiber nonlinearity, nonlinear equalization, neural networks

**Abstract:** The fiber nonlinearity is considered the ultimate barrier to reaching the Shannon capacity, particularly relevant in coherent systems that rely on phase shift modulation schemes. In effect, the fiber nonlinearity introduces a nonlinear phase noise making ineffective the DSP linear equalizers. To compensate for the fiber nonlinearity, DSP-based nonlinear equalizers, such as the Digital Backpropagation or the Volterra series nonlinear equalizer, are commonly considered computationally heavy solutions that do not fit into the limited resources of current transceivers. Under such a scenario, artificial neural networks surge as an option to efficiently perform nonlinear equalization with limited computational complexity. Using numerical simulations of a DP-16QAM over 14×100 km of standard single-mode fiber and considering a simple

neural network promising to be implemented in a transceiver, we have shown that for long distances, simple neural networks potentially implementable in a transceiver do not compensate for nonlinear phase noise as effectively as classical DSP techniques. Even more, when using the mean squared error cost function to train the neural network, it has been seen that the diagram constellation exhibits a deformation that adopts a grid shape in the case of quadratic QAM constellations. This phenomenon, which we named MMSE-scatterplot, potentially affects the subsequent DSP and has been deeply studied in this work, elucidating the mathematical model equivalent to the MMSE-scatterplot. Based on this mathematical equation, we also have proposed an innovative technique to mitigate this effect.